Dielectric metasurfaces for integrated imaging devices and active optical elements

Thesis by

Hyounghan Kwon

In Partial Fulfillment of the Requirements for the
Degree of
Doctor of Philosophy

CALIFORNIA INSTITUTE OF TECHNOLOGY
Pasadena, California

2021
Defended April 26, 2021

Hyounghan Kwon
ORCID: 0000-0002-9257-687X

To my wife, Min Kyung Kang,

and

my parents, Jongkook Kwon and Soon-ki Yoon.

ACKNOWLEDGEMENTS

First and foremost, I would like to express tremendous gratitude to my advisor, Prof. Andrei Faraon. He has always been devoted to serve his role not only as an academic mentor, but also as a good human being and a close friend. His broad expertise and interests in several distinct subjects such as quantum science, nanophotonics, and optical engineering have always inspired me. He gave me freedom to explore diverse ideas I liked, and helped me to become self-confident. His positive attitude and trust in his students helped me to push research projects forward when I faced numerous failures. I deeply appreciate everything I learned from him over my Ph.D. as well as the friendly and collaborative atmosphere he created within the group.

I was fortunate to have opportunities to interact with great professors at Caltech and UMass Amherst. I want to thank Prof. Chanhuei Yang, Prof. Lihong Wang, Prof. Babak Hassibi, Prof. Alireza Marandi, and Prof. Harry Atwater for their service as committee members of my candidacy exam or doctoral defense. Their insightful feedback improved my research and this thesis. I also want to thank Prof. Amir Arbabi at UMass Amherst for being a great mentor and a collaborator during the DARPA project. I would like to express my appreciation for his insightful feedback and supports. I am also grateful to Prof. Hyuck Choo, who currently works as a SVP at Samsung Advanced Institute of Technology, for helping me to settle at Caltech. His passion for technology toward real-world application was truly inspiring.

None of the works in this thesis would have been possible without great supports in KNI at Caltech. I would like to thank all the KNI staff, Guy DeRose, Bert Mendoza, Nathan Lee, Alex Wertheim, and Matthew Sullivan Hunt (now at Amazon). I am also grateful to Cecilia Gamboa and Tanya Owen for their administrative support.

It was fortunate to become a member of the Faraon group. All of the group members have always been friendly, open, collaborative, and helpful. Especially, I would like to thank Ehsan Arbabi for teaching me many fundamental things, which include nanofabrication, optical measurements, idea development, problem solving, writing, presentation, and so on. I was always surprised by his broad knowledge and insights on physics, and grateful to him for answering my numerous questions on various topics. I also want to thank Mahsa Kamali for teaching me many things in the KNI and the lab, and giving fruitful feedback in the subgroup meetings. I appreciate Ehsan and Mahsa for being good mentors as well as good friends. I want to thank MohammadSadegh Faraji-Dana. I really enjoyed our discussions, collaborations, and casual conversations. The time that we learned nanofabrication and experiment together in 2017 was one of my greatest experiences at Caltech. In the last two years, I was very happy to work closely with Tianzhe Zheng on active metasurface projects. All of your passion, hard work, friendship, and positive feedback have helped me to keep my focus on the research. I also enjoyed numerous discussions we had over Zoom or in the lab. Personally, it is such a shame that we couldn't have more fun time together due to the pandemic. I would like to express my gratitude to Philip Camayd-Munoz, Conner Ballew, and Greg Roberts for their friendship and positive attitudes. They offered opportunities to learn the inverse-designed 3D metamaterials. In addition to the brilliant research, I have sincerely thought that all of you spread positive vibes in the group, and more importantly are globally-optimized in many aspects of life. I also thank Bilgehan Baspinar, Suki Gu, and Ian Foo for being good friends and giving fresh viewpoints. I also thank their friendships to all members in quantum subgroup. Especially, I am very grateful to the GaAs folks, Daniel Riedel and Chu-ju Wu. I learned a lot during our trials and errors in fabrication and experiment. Also, I really enjoyed many dinners and drinkings we had together. I am grateful to Jake Rochman, who gave me a lot of help during cleanroom fabrication. In addition, I thank Ioana Craiciu and Andrei Ruskuc for answering my random questions about rare earth projects. Finally, I am grateful to Ding Zhong for being a good friend and doing many transfers for our TMDC-based metasurface projects. It was a good opportunity for me to learn the novel materials from an expert.

I also want to thank my friends at Caltech, Ju-hyun Kim, Jin-soo Park, Areum Kim, Jeongmin Kim, Changsoon-choi, Youngjun Choi, Hyunjun Cho, Haeri Park, Jeong Oen Lee, Radwanul Hasan Siddique, Kai Narita, and Peter Lee, who made me feel relaxed and helped my research through insightful discussions. I also thank Donghyeon Won for being a good friend in Korea and LA over the years.

Finally, my deepest gratitude goes to my family. My wife, Min Kyung Kang, has supported all aspects of my life, encouraged me when I faced many failures, and made our life happy and meaningful. This thesis would not have been possible without your unconditional support. I am deeply thankful to my father, Jongkook Kwon, my mother, Soon-Ki Yoon, and my sister, Bohye Kwon, for always being there, staying healthy, and encouraging me. My family's unquestioning love and support have been crucial in finishing this thesis.

ABSTRACT

Optical dielectric metasurfaces have shown great advances in the last two decades and become promising candidates for next-generation free-space optical elements. In addition to their compatibility with scalable semiconductor fabrication technology, metasurfaces have provided new and efficient ways to manipulate diverse characteristics of light. In this thesis, we demonstrate the potential of dielectric metastructures in the realization of compact imaging devices, reconfigurable optical elements, and multi-layer inverse-designed metasurfaces. With the metasurfaces' extreme capability to simultaneously control phase and polarization, we first showcase their potential toward optical field imaging applications. In this regard, we demonstrate a system of dielectric metasurfaces and designed random metasurfaces for single-shot phase gradient microscopes and computational complex field imaging system, respectively. Then, we propose nano-electromechanically tunable resonant dielectric metasurfaces as a general platform for active metasurfaces. For example, we demonstrate two different types of the phase and amplitude modulators. While one utilizes resonant eigenmodes in the lattice such as leaky guided mode resonances and bound-states in the continuum modes, the other is based on the high-Q Mie resonances in the dielectric nanostructures where symmetry is broken. In addition to the modulation of the phase and amplitude, we also show tuning of strong chiroptical responses in dielectric chiral metasurfaces. Next, we experimentally demonstrate inverse-designed multi-layer metasurfaces. Not only do they provide increased degree of freedom in the design space, but also overcome limits of conventional design methods of the metasurfaces. Finally, we summarize the presented works and conclude this thesis with a brief outlook on what aspects of the metasurfaces can be important for their real-world applications in the future and what challenges and opportunities remain.

PUBLISHED CONTENT AND CONTRIBUTIONS

[1]H. Kwon*, T. Zheng*, and A. Faraon, "Nano-electro-mechanical tuning of dual-mode resonant dielectric metasurfaces for dynamic amplitude and phase modulation", Nano Letters **21**, 2817–2823 (2021) 10.1021/acs.nanolett.0c04888,
H.K. has participated in the conception of the experiments, design, fabrication, and measurement of the samples, analysis of the data, and writing of the manuscript. *:equal contribution.

[2]H. Kwon, E. Arbabi, S. M. Kamali, M. Faraji-Dana, and A. Faraon, "Single-shot quantitative phase gradient microscopy using a system of multifunctional metasurfaces", Nature Photonics **14**, 109–114 (2020) 10.1038/s41566-019-0536-x,
H.K. has participated in the conception of the experiments, design, fabrication, and measurement of the samples, analysis of the data, and writing of the manuscript.

[3]M. Mansouree*, H. Kwon*, E. Arbabi, A. McClung, A. Faraon, and A. Arbabi, "Multifunctional 2.5 d metastructures enabled by adjoint optimization", Optica **7**, 77–84 (2020) 10.1364/OPTICA.374787,
H.K. has participated in the conception of the experiments, fabrication, and measurement of the samples, analysis of the data, and writing of the manuscript. *:equal contribution.

[4]M. Faraji-Dana, E. Arbabi, H. Kwon, S. M. Kamali, A. Arbabi, J. G. Bartholomew, and A. Faraon, "Hyperspectral imager with folded metasurface optics", ACS Photonics **6**, 2161–2167 (2019) 10.1021/acsphotonics.9b00744,
H.K. has participated in the fabrication, analysis of the data, and writing of the manuscript.

[5]S. M. Kamali, E. Arbabi, H. Kwon, and A. Faraon, "Metasurface-generated complex 3-dimensional optical fields for interference lithography", Proceedings of the National Academy of Sciences **116**, 21379–21384 (2019) 10.1364/10.1021/10.1073/pnas.1908382116,
H.K. has participated in the fabrication, experiments, and writing of the manuscript.

[6]M. Faraji-Dana, E. Arbabi, A. Arbabi, S. M. Kamali, H. Kwon, and A. Faraon, "Compact folded metasurface spectrometer", Nature communications **9**, 4196 (2018) 10.1038/s41467-018-06495-5,
H.K. has participated in the fabrication, analysis of the data, and writing of the manuscript.

[7]H. Kwon, E. Arbabi, S. M. Kamali, M. Faraji-Dana, and A. Faraon, "Computational complex optical field imaging using a designed metasurface diffuser", Optica **5**, 924–931 (2018) 10.1364/OPTICA.5.000924,
H.K. has participated in the conception of the experiments, design, fabrica-

tion, and measurement of the samples, analysis of the data, and writing of the manuscript.

TABLE OF CONTENTS

LIST OF ILLUSTRATIONS

LIST OF TABLES

Chapter 1

INTRODUCTION TO METASURFACES

In the last decade, there have been remarkable progresses in the field of optical metasurfaces. Especially, the metasurfaces have not only provided unprecedented optical functionality and scalable free-space optical platforms, but also introduced novel underlying physics. In this Chapter, we review the field of optical metasurfaces from various viewpoints. First, we introduce the concept of optical metasurfaces. Next, we focus on high-contrast dielectric metasurfaces that constitute the basis of several Chapters of this thesis. In particular, we review high-contrast metasurfaces' unprecedented ability to control polarization and phase. Finally, beyond the passive optical metasurfaces, progress and challenges in active optical metasurfaces are briefly discussed. At the end of this Chapter, a short outline of this thesis is introduced.

1.1 Introduction to optical metasurfaces

Metasurfaces are two-dimensional arrays of subwavelength structures which locally manipulate multiple properties of light [1–7]. The spatially distributed subwavelength structures locally capture and scatter incident light. Multiple characteristics of the scattered light can be judiciously controlled by selecting proper designs of the nanostructures. As a result, the metasurfaces have not only enabled conventional optical elements such as lenses, waveplates, gratings, and beam-splitters, but also provided a novel optical functionality which is very challenging to achieve with any kind of single conventional optical element. Furthermore, the metasurfaces can be fabricated by using standard semiconductor fabrication processes, enabling potential low-cost production especially for applications that are of high volume.

In the long history of optical elements, there have been two categories of optical elements that are conceptually and technically similar to optical metasurfaces. One is a reflect- or a transmit- array in the microwave domain, and the other is conventional diffractive optical elements such as Fresnel lenses. Especially, the early demonstration of the metasurfaces based on plasmonic nanoantennas [8] is very similar to the reflect-array in microwave [9, 10]. In this thesis, we define (high-contrast) dielectric metasurfaces as a new type of the diffractive optical elements, providing several advantages over the conventional counterparts. For instance, well-designed metasurfaces outperform the conventional diffractive optical elements when the numerical aperture (NA) of the devices or the incident angle of the light is large [11, 12]. In addition, the metasurfaces can offer new optical functionalities such as control of polarization and phase [13], dispersion engineering [14, 15], distinct angular control [16], edge-detection [17], free-space coupled high-Q resonances [18, 19], and so on. Furthermore, detailed discussions about the optical metasurfaces from historical perspectives can be found in [11].

In the last two decades, the research field of the metasurfaces have shown great advances. Initially, plasmonic metasurfaces have been extensively explored thanks to their thin form factor and great interests in plasmonics [3, 8]. However, optical loss from metallic structures fundamentally limits the optical performance for transmissive devices. To circumvent the limits of the plasmonic structures, various types of dielectric metasurfaces have been investigated. First, dielectric geometric phase metasurfaces have been demonstrated for efficient wavefront shaping [20]. Specifically, the geometric phase metasurfaces consist of nanostructures working as local half waveplates and the rotation of each half waveplate determines local phase response. However, not only do the geometric phase metasurfaces work with one circular polarized light, but they also suffer from low efficiency for high NA devices because of considerable coupling between the nanostructures [21]. On the other hand, thin dielectric Huygens' metasurfaces have been proposed in order to enable high efficient transmissive metasurfaces [22, 23]. In the Huygens' metasurfaces, electric and magnetic dipole modes are equally and simultaneously excited in dielectric nanostructures and the two modes are overlapped in spectral domain. The spectral overlap of the modes enables high transmission and enhanced phase response close to 2π at the resonance. However, the coupling between adjacent meta-atoms is severe in the Huygens' metasurfaces, and this coupling significantly degrades the performance of the devices having large deflection angles. Detailed discussion about the fundamental limits of the Huygens' metasurfaces can be found in [24].

Due to the limits of the metasurfaces mentioned above, many researchers have investigated the high-contrast dielectric metasurfaces [25–28]. The high-contrast metasurfaces consist of relatively tall high index nanostructures. It is worth noting that the earliest demonstration of the high-contrast metasurfaces can be found at least two decades ago [25]. These structures were called by blazed binary optical elements. Nevertheless, the high-contrast metasurfaces outperform other types of the metasurfaces mentioned above. In the following section, we will introduce the operating principles and review the recent advances of the high-contrast metasurfaces.

Although the optical metasurfaces have been briefly introduced from the perspectives of the wavefront control, the general concepts of the metasurfaces include large categories of optical elements such as absorbers [29], filters [30, 31], chiral elements [32–34], nonlinear optical elements [35–37], and so on. Among these various kinds of optical elements, a brief introduction to the chiral metasurfaces can be found in Chapter 6. However, we note that most of the work presented in this thesis is related to the metasurfaces that manipulate wavefronts.

1.2 High-contrast dielectric metasurfaces and their capabilities to control phase and polarization

Here, we introduce high-contrast dielectric metasurfaces, which form the central basis of the work presented in Chapter 2, 3, and 7. Especially, we discuss their unprecedented ability to control phase and polarization at the same time [13].

The high-contrast metasurfaces consist of subwavelength nanostructures with a large refractive index contrast. The thickness of the nanostructures are usually between 0.5λ to 1λ, where λ is a wavelength in free space. The optimal thickness depends on the materials, type of the device (i.e. reflective or transmissive type), and operating wavelengths. The periodic high-contrast structures are known to provide high transmission or reflection in broadband, enabling highly efficient transmissive or reflective devices [38]. The physical origin of the broadband property can be found in multiple Bloch modes hosted by the high-contrast structures [38]. More surprisingly, various nanostructures can have spatially varying cross-sections in the metasurface plane to manipulate the wavefronts efficiently [26, 27]. Even with the non-periodicity, each structure locally controls the phase of light while its high efficiency remains well. This is because the light is captured inside the high-index nanostructure and scattered in the desired manner. Intuitively, each nanoscatterer can be considered as a waveguide giving a desired phase response. Thus, the coupling between the posts is not considerable.

In a standard design method of the high-contrast metasurfaces, transmission (or reflection) coefficients for a periodic array of the nano-posts are extracted. Then, the extracted coefficients are directly exploited to design aperiodic devices by using the desired phase profile. In other words, an arbitrary 2D (or 1D) phase map can be realized by adjusting the cross-sections of the nanostructures. Also, the lattice is often selected to be periodic for simplicity. This design method basically assumes that the sampling is local. Namely, there is no considerable coupling between the structures, so the transmission (or reflection) phase and amplitude remain the same despite the introduction of the non-periodicity. There are several important aspects in the design process of the high-contrast metasurfaces. First, the lattice constant should satisfy the Nyquist sampling criteria in order to avoid unwanted diffractions and to control the wavefront efficiently [39]. For polarization-independent operation under normal incidence, the cross-sections of the nano-scatterers must be symmetric such as circles, squares, etc [27]. For large incident angle, optimized anisotropic structures such as ellipses or rectangles can support nearly polarization insensitive phase controls [40]. In addition, the validity of local sampling starts to break at large deflection angles and contributes to the lower efficiency of the devices at such angles. Therefore, a few novel methods have been proposed to improve the efficiencies of the devices having high NA [41–43].

The high-contrast metasurfaces provide unprecedented ability to control polarization and phase simultaneously. Although we briefly review this exceptional ability here, the detailed discussion can be found in [13]. Considering that nanostructures having symmetric cross-sections achieve a polarization insensitive optical function, one can also extend the idea to the case of anisotropic structures. If the metasurfaces are composed of the nanoposts with anisotropic cross-sections such as rectangles or ellipses, they allow the capabilities to control the polarization and phase simultaneously. This type of the metasurfaces realizes two categories of novel optical devices. In the first category, given any kind of two orthogonal input polarizations including linear, circular, and elliptical polarizations, their phases can be independently controlled. The second category transforms any input field with a desired phase and polarization. This property has been extensively explored to achieve different kinds of vector beams or vectorial holograms. In this thesis, the first and second categories were used for the devices in Chapters 2 and 3, respectively. In detail, the nanoposts having the rectangular cross-sections have been exploited in both Chapter 2 and Chapter 3 (see Figs. 2.A.4, 3.2, and 3.A.1). Mathematically, the single metasurface allows for a two-dimensional map of unitary and symmetric Jones matrices which are written by

$$T = \begin{pmatrix} T_{xx} & T_{xy} \\ T_{yx} & T_{yy} \end{pmatrix} = R(\theta) \begin{pmatrix} e^{i\phi_x} & 0 \\ 0 & e^{i\phi_y} \end{pmatrix} R(-\theta), \tag{1.1}$$

where ϕ_x, ϕ_y, and $R(\theta)$ denote a transmitted phase for x-polarization, a transmitted phase for y-polarization, and the rotation matrix by an angle θ in the counter-clockwise direction, respectively. For each nanopost, its two side lengths and orientation can be selected as functions of desired ϕ_x, ϕ_y, and θ in Eq 1.1. In other words, the metasurfaces enable arbitrary two-dimensional distribution of the Jones matrices satisfying Eq. 1.1. Very recently, it has been shown that the spatially varying Jones matrices enabled by the metasurfaces lead to various types of spatially varying Jones matrices in the far-field [44]. This design method is beneficial if the metasurfaces are designed for output functions without given bases of input polarization states.

1.3 Progresses and challenges in active metasurfaces

Despite the great advancement of the passive metasurfaces discussed above, active metasurfaces can open up new opportunities because they offer a new degree of freedom in time domain [45]. Here, active metasurfaces represent the devices that can change their optical functions in time. In particular, fast control of wavefronts in subwavelength scale is of significant interest. Compared to conventional spatial light modulators using micromechanical systems or liquid crystals, the active metasurfaces potentially offer a wide field of view, compact form factor, fast modulation speed, and new optical functionality. To achieve the dynamic manipulation of the wavefront, many seminal works have exploited various tunable platforms or materials that include transparent conducting oxides [46–48], micromechanical actuators [49], 2D materials [50, 51], phase change materials [52, 53], semiconductors [54], and liquid crystals [55]. Among these various methods, electrically tunable metasurfaces can be of significant interests from practical perspectives thanks to their potentials for on-chip integration. In particular, the plasmonic metasurfaces using the transparent conducting oxides have demonstrated arbitrary wavefront control, modulation speed close to a a few MHz, and ranging experiment with continuous beam steering [47, 48]. However, absolute efficiencies of the plasmonic metasurfaces are inherently limited by the loss of metals. Specifically, plasmonic metasurfaces using the transparent conducting oxides operate close to the critical coupling regime or epsilon-near-zero regime in which the light is mostly absorbed. Even with noble metals such as gold or silver, its absolute efficiency is close to 0% to 2% [48]. Use of scalable metals such as aluminium or copper may further degrade the efficiency due to their high optical loss. Thus, none of the previous active metasurfaces can still compete with commercially available spatial light modulators based on liquid crystal. Highly efficient, high-speed, and scalable phase-modulated metasurfaces have remained the holy grail. In addition, it is worth noting here that a company in the USA (Lumotive) has recently commercialized the active metasurfaces LIDARs by combing mature liquid-crystal technology with metasurface technology. In addition to the spatial light phase modulator, novel active metasurfaces can be proposed. Considering the metasurfaces' exotic capabilities to control polarization of light, a novel polarization modulator can be of great interests.

1.4 Thesis outline

The main goal of this thesis is to demonstrate the potentials of the dielectric metastructures in the realization of compact imaging devices, active optical elements, and multi-layer metasurfaces. Chapters 2 and 3 focus on optical field imaging devices using high-contrast dielectric metasurfaces. Chapters 4, 5, and 6 showcase nano-electromechanically tunable metasurfaces for dynamic controls of the metasurfaces' unprecedented optical responses. Chapter 7 focuses on inverse-designed multi-layer metasurfaces for the realization of efficient multifunctional optical components. Specifically, in Chapter 2, we demonstrate single-shot quantitative phase gradient microscopes based on cascaded two layers of dielectric metasurfaces. The high-contrast metasurfaces' extreme ability to control polarization and phase enables a quantitative phase gradient imager of which size is in millimeter scale. Chapter 3 introduces a computational complex field imaging system using the concept of random metasurfaces. In Chapter 4, we demonstrate nano-electromechanical tuning of dual-mode resonant metasurfaces for dynamic amplitude and phase modulation. The concept relies on two kinds of resonant eigenmodes hosted by the dielectric metasurfaces, which are leaky guided modes and bound states in the continuum. Chapter 5 introduces dielectric metasurfaces having asymmetry in z-axis. With the asymmetric metasurfaces and nano-electromechanical system (NEMS), we showcase electrically controllable wavefront engineering with a wavelength-scale pixel size. In particular, reconfigurable beam splitting and beam steering are experimentally demonstrated. Chapter 6 discusses NEMS-tunable strong chiroptical effects in a single-layer dielectric metasurfaces. With CMOS level voltage, the devices achieve the dynamic transition from strong to negligible chiroptical states. Chapter 7 introduces inverse-designed multi-layer metasurfaces, which potentially overcome fundamental limits of single layer metasurfaces. Chapter 8 concludes thesis with summary and outlook.

Chapter 2

SINGLE-SHOT QUANTITATIVE PHASE GRADIENT MICROSCOPY USING A SYSTEM OF MULTIFUNCTIONAL METASURFACES

The material in this Chapter was in part presented in [56].

Quantitative phase imaging (QPI) of transparent samples plays an essential role in multiple biomedical applications, and miniaturizing these systems will enable their adoption into point-of-care and *in-vivo* applications. We propose a novel quantitative phase gradient microscope (QGPM) based on two dielectric metasurface layers inspired by a classical differential interference contrast (DIC) microscope. Owing to the multi-functionality and compactness of the dielectric metasurfaces, the QPGM simultaneously captures three DIC images to generate a quantitative phase gradient image in a single shot. We demonstrate two different QPGM systems, one based on metasurfaces on two separate substrates, and one composed of two metasurface layers monolithically integrated on the same substrate. The volumes of the metasurface optical systems are on the order of 1-mm^3 cubic volume. Imaging experiments with both systems and various phase resolution samples verify their capability to capture quantitative phase gradient data, with phase gradient sensitivity better than 92.3 mrad/μm and single cell resolution. The results showcase potentials of metasurfaces for developing miniaturized QPI systems for label-free *in-vivo* cellular imaging and point-of-care devices.

2.1 Introduction

Optical phase microscopy techniques have been widely investigated for imaging transparent specimens like cells [57–60]. For these weakly scattering samples, phase information represents the optical path difference of light passing through the cell, which is usually directly related to its morphological and chemical properties [59]. Moreover, phase imaging techniques do not require contrast agents and avoid several issues faced in fluorescence microscopy such as photobleaching and phototoxicity [61]. While conventional phase imaging methods such as phase contrast [57] and differential interference contrast (DIC) microscopy [58] only capture qualitative phase information, quantitative phase imaging (QPI) has been rapidly growing in the past two decades [59, 60, 62]. For instance, techniques like digital holographic microscopy [63], tomographic QPI [64, 65], Fourier ptychography [66], and lens-less imaging [67] overcome limitations of qualitative phase imaging methods to acquire quantitative phase data.

Miniaturized microscopes have garnered great interest in recent decades [68–70] since they enable and facilitate *in-vivo* biological imaging in freely moving objects [70] and in portable applications. Miniaturized systems have only been demonstrated as different forms of amplitude imaging modules such as single [68] or two-photon [69] fluorescence microscopes. This is mainly because QPI systems usually require an interference "setup" to retrieve the phase information, and such setups need complicated and bulky optical systems. This had left miniaturized QPI microscopes that are of interest in various fields such as biomedicine [60] out of reach until now.

Dielectric metasurfaces are a category of diffractive optical elements consisting of nano-scatterers [4, 7] that enable the control of light in sub-wavelength scales [13–15, 20, 25, 71]. In addition, metasurfaces can simultaneously provide multiple distinct functionalities through various schemes such as spatial multiplexing [72, 73] or more sophisticated designs of the nano-scatterers [16, 74]. These capabilities, compactness, low weight, and compatibility with conventional nano-fabrication processes have made them suitable candidates for miniaturized optical devices such as miniaturized microscopes [75], on-chip spectrometers [40, 76], and endoscopes [77]. In addition, vertical integration of multiple metasurfaces has been introduced to achieve enhanced functionalities [78–81]. Despite these vast advances, applications of metasurfaces for quantitative phase imaging have not previously been explored. Although different types of spatial field differentiators, that may be regarded as qualitative phase imaging devices, have been proposed, their investigation has been limited to optical computing and optical signal processing [82, 83].

Here, we propose a miniaturized quantitative phase gradient microscope (QPGM) inspired by the classical DIC microscope and based on an integrated system of multifunctional dielectric metasurfaces. As we fully exploit the two unique properties of metasurfaces which are compactness and multi-functionality via both polarization and spatial multiplexing methods, two metasurface layers that are cascaded vertically operate as a miniaturized QPGM. We experimentally demonstrate that the millimeter-scale optical device can capture quantitative phase gradient images (PGIs) from phase resolution targets and biological samples.

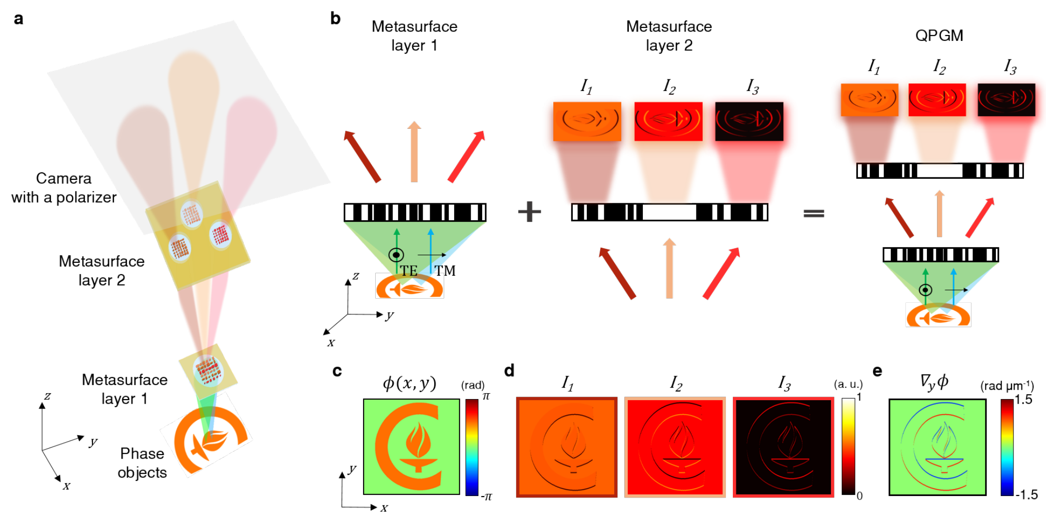

Figure 2.1: **Schematic illustration of a metasurface-based QPGM and its operation principle.** **a** Schematic of the QPGM employing two metasurface layers, where the second layer is composed of three separate metasurface lenses. The first metasurface together with each of the lenses in the second metasurface layer forms a different image of the object. A polarizer and the polarization sensitive metasurfaces then result in three interference patterns. **b** Illustration of the roles of the two metasurface layers. Metasurface 1 makes two sheared focuses for TE and TM polarizations and splits the field in three different directions towards the three lenses in the second layer. With the polarizer, the three metasurface lenses in layer 2 form three DIC images (I_1, I_2, and I_3) having different phase offsets between the TE and TM polarizations. The combination of the two layers forms the QPGM shown on the right. **c** A binary phase sample with a unity amplitude used as an example target. **d** Set of three DIC images of the phase sample shown in c. **e** PGI formed from combining I_1, I_2, and I_3 from d, showing the phase gradient along the y axis. The y axis lies along the shear direction of the system.

2.2 Concept of the metasurface-based QPGM

Figure 2.1**a** illustrates the concept of a miniaturized QPGM consisting of two cascaded metasurface layers. The roles of each layer is visually explained in Fig. 2.1**b**. Metasurface layer 1 captures two images for TE and TM polarizations with focal points that are separated along the y axis. In addition, it splits the captured light equally into three separate directions towards the three metasurface lenses in layer 2. To implement this multi-functionality, polarization [13] and spatial multiplexing techniques [72, 73] are employed in the design of metasurface layer 1 (see Appendix 2.1 for details). Metasurface layer 2, which is composed of three birefringent off-axis lenses, forms three DIC images with three different phase offsets between the TE and TM polarizations. Effectively, each metasurface of the second layer constitutes a separate DIC microscope system with the metasurface layer 1. With two linear polarizers at the input and output aligned to 45° and -45°, respectively, the two metasurface layers capture three separate DIC images with different phase offsets. As an example, a binary phase target is shown in Fig. 2.1**c**, which has optical fields with a unity amplitude, $U(x, y) = e^{i\phi(x,y)}$. The QPGM simultaneously captures three DIC images (I_1, I_2, and I_3) as shown in Fig. 2.1**d**. Specifically, I_1, I_2, and I_3 are written as:

$$I_j = |U(x, y) - \mathrm{e}^{\mathrm{i}\phi_j} U(x, y - \Delta y)|, \tag{2.1}$$

where $\phi_j = \phi_0 + \frac{2\pi}{3}(j - 1)$, and Δy is the sheared distance between TE and TM polarizations at the object plane. I_1, I_2, and I_3 in Fig. 2.1**d** show a strong contrast at the top and bottom edges of the sample because each DIC image results from the interference of the two sheared optical fields along the y-axis by Eq. 2.1. Using I_1, I_2, and I_3, one can calculate the unidirectional gradient of the phase sample with respect to y, $\nabla_y \phi(x, y)$, through the three-step phase shifting method [84]:

$$\nabla_y \phi = \frac{1}{\Delta y} arctan(\sqrt{3} \frac{I_2 - I_3}{2I_1 - I_2 - I_3}) - \nabla_y \phi_{\mathrm{cali}}. \tag{2.2}$$

Here, $\nabla_y \phi_{\mathrm{cali}}$ is the PGI calculated in the absence of the sample that is used for calibration (see Appendix 2.3 for details about the three-step phase shifting method). Figure 2.1**e** shows the PGI calculated from the three DIC images in Fig. 2.1**d**.

The QPGM consists of the two multi-functional metasurface layers for two main reasons (see Appendix 2.1 and Fig. 2.A.1 for detailed discussion based on wave propagation simulation). First, at least two polarization sensitive bifocal lenses are needed to capture clear DIC images. In other words, a single birefringent metasurface lens with a regular refractive lens is not capable of capturing the DIC images clearly (see Appendix 2.2 and Fig. 2.A.2 for theoretical and experimental results with the single metasurface lens). Second, the vertical integration of the two multi-functional metasurface layers uniquely enables capturing the PGI in a single shot with compact implementation of the system.

We should mention that while single polarization sensitive bifocal metasurface lenses have been demonstrated before for polarization splitting and imaging [13, 85], their potential application for phase imaging has not been explored. Moreover, the working principle used here is conceptually similar to the gradient light interference microscopy, as in both methods several DIC images are utilized to calculate the quantitative phase gradient image along one axis [86]. Various devices also have been proposed to develop compact QPI techniques [87–91]. However, they are designed as the add-on devices to a conventional microscope system and their imaging performance mainly rely on the microscope which is fundamentally hard to miniaturize. The system demonstrated here is mainly different from the previous approaches as the highly miniaturized system replaces the bulky phase or phase gradient microscope systems and captures the phase gradient information in a single shot without additional phase shifting elements like variable liquid crystal retarders or spatial light modulators.

In the following, we discuss two implementations of the QPGM, one based on metasurfaces on two separate substrates and one composed of metasurfaces on both sides of a single substrate. While the first implementation provides large aperture size and field of view, the second implementation provides compactness and mechanical robustness.

2.3 Implementation of the QPGM by two separate dielectric metasurface layers

To implement the two metasurface layers, we utilized the high-contrast transmitarray platform consisting of rectangular amorphous silicon nano-posts on a fused silica substrate shown in Fig. 2.2**a** (see Method and Fig. 2.A.4 for details) [13]. We designed the metasurfaces for an operation wavelength of 850 nm. In Figs. 2.2**b** and 2.2**c**, the schematics of the metasurface-based QPGM are illustrated. In particular, the left and right images correspond to the metasurface layers 1 and 2 in Figs. 2.1**a** and 2.1**b**, respectively. To minimize the effects of geometric aberrations, the phase profiles of the metasurfaces are further optimized using the ray tracing method (Zemax OpticStudio) over a field of view (FOV) of 140 μm in diameter (see Methods, Appendix 2.1, Table 2.A.1, and Fig. 2.A.5 for the details of the optimized phase profiles and corresponding point spread functions).

Conventional nano-fabrication techniques are used to fabricate the metasurfaces (see Methods for the process details). All four metasurface lenses have identical diameters of 600 μm. To block the stray light caused by the imperfect operation of metasurfaces and limit the device aperture, circular gold apertures are patterned through photo-lithography. Figures 2.2**d** and 2.2**e** show the optical and scanning electron microscope images of the two layers of the fabricated metasurfaces, respectively. In this design, the whole QPGM system would fit within a cube that is 1.92×1.26×2.70 mm^3, including the space between the metasurfaces. The magnification and objective numerical aperture (NA) of the QPGM are 1.98× and 0.4,

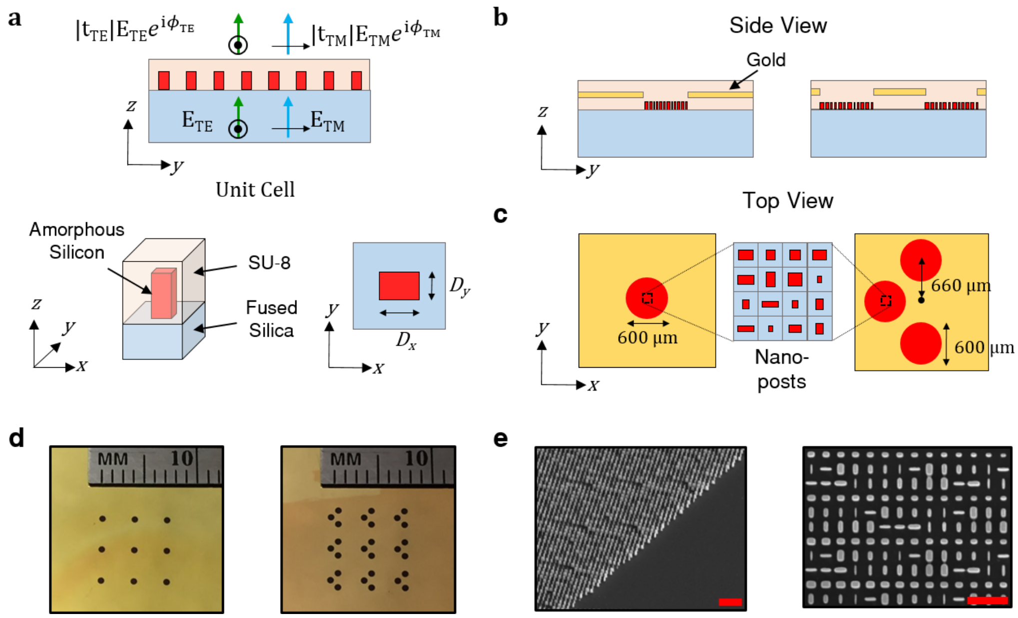

Figure 2.2: **Design and fabrication of the metasurfaces.** **a** Schematics of a uniform array of rectangular nano-posts (top) and a single unit cell (bottom), showing the parameter definitions. The rectangular amorphous silicon (α-Si) nano-posts are on a fused silica substrate, cladded by a 8-μm thick SU-8 layer for protection. The transmission phase of the two orthogonal polarizations can be independently controlled using the nano-posts. The α-Si layer is 664 nm thick, and the lattice constant is 380 nm. **b** Schematic illustration of the side views of metasurface layers 1 (left) and 2 (right), showing the gold apertures used to block unwanted diffraction and the external noise. **c** Top view schematics of the metasurface layers 1 (left) and 2 (right). The magnified array of the nano-posts is shown at the center. **d** Optical images of the fabricated metasurfaces. Nine copies of the fabricated metasurface-based QPGM system are shown. **e** Scanning electron microscope images of a portion of the fabricated metasurfaces. Scale bars denote 2 μm and 1 μm in the left and right images, respectively.

respectively. Although the phase map is optimized for the central area of 140 μm in diameter, the total FOV of the system is 336 μm in diameter. In addition, the separation between the optical axes for TE and TM polarizations is 1.5 μm, which results in a derivation step Δy = 2.25 μm (see Fig. 2.A.3 for the details about Δy). Δy is larger than 1.06-μm of theoretical diffraction-limit of the imaging system, and it imposes a constraint on the resolution along y-axis. However, we should point out that Δy can easily be adjusted to below the diffraction limited resolution by reducing the optical axis separation accordingly.

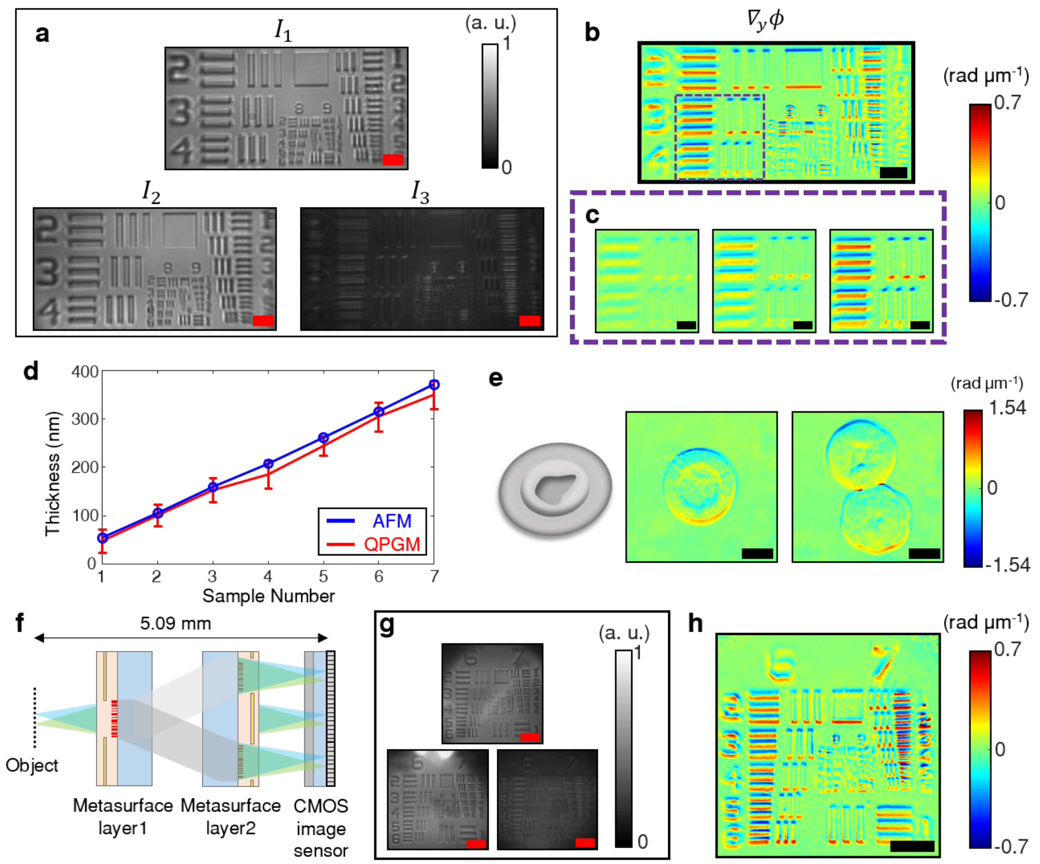

Figure 2.3: **Imaging experiment with the QPGM based on metasurfaces fabricated on two separate substrates.** **a** Three DIC images of a 314-nm thick QPI 1951-USAF resolution target captured by the QPGM. Scale bars: 25 μm. **b** The PGI calculated from the measured DIC images in a. Scale bar: 25 μm. **c** The PGIs captured for three parts of the phase target with 105 nm, 207 nm, and 314 nm thickness from left to right, respectively. Scale bars: 15 μm. **d** Thicknesses of seven different the phase targets calculated by the QPGM, and those measured by AFM. The plotted estimated thicknesses through QPGM are averaged over 100 arbitrarily chosen points on the sample edges. Error bars represent standard deviations of the estimated values. **e** Schematic of a sea urchin cell, and its corresponding PGIs captured by the QPGM. Scale bars: 40 μm. **f** Schematic of the miniaturized optical setup with a CMOS image sensor. The microscope consists of the two metasurfaces shown in Fig. 2.2, the sensor, and a linear polarizer on top of the sensor. **g** Three DIC images captured by the setup in f. The 314-nm thick resolution target used in a is imaged here. Scale bars: 50 μm. **h** The PGI calculated from the measured DIC images in g. Scale bar: 50 μm.

2.4 Imaging with the QPGM based on two separate metasurface layers

We characterize the QPGM consisting of the fabricated metasurfaces with a commercially available 1951 USAF phase resolution target (Quantitative Phase Microscopy Target, Benchmark Technologies). As shown in Fig. 2.3**a**, the QPGM captures three DIC images of the 314-nm-thick resolution target in a single shot (see Method and Fig. 2.A.6 for the details of the optical setup). The resulting PGI shown in Fig. 2.3**b** is calculated from the DIC images in Fig. 2.3**a** using Eq. 2.2. As expected in the ideal cases in Figs. 2.1**d** and 2.1**e**, the unidirectional phase gradient imaging in the y direction causes a strong contrast only at the top and bottom edges and very weak contrast at left and right edges in the measurement results shown in Figs. 2.3**a** and 2.3**b**. To verify the quantitative phase microscopy capability, we used seven parts of the resolution target with thicknesses ranging from 54 to 371 nm. Figure 2.3**c** shows the resulting PGIs for 105-nm, 207-nm, and 314-nm thick resolution targets (see Fig. 2.A.7 for the four remaining PGIs). The results show a clear increase of the phase gradient as the thickness of the structures increases. For a more rigorous analysis, Fig. 2.3**d** shows the target thicknesses estimated from the PGIs, in addition to the values measured using atomic force microscopy (AFM). The agreement between these measurements shows the ability of the system to retrieve quantitative phase data. In order to estimate the target thickness, the phase gradient is integrated at the edges of the targets along the y axis to calculate the phase. Then, the thickness is estimated from the phase, refractive index of the polymer constituting target, and the wavelength. Especially, the QPGM can clearly capture phase gradient information as small as 92.3 mrad/μm, which corresponds to a phase of 207 mrad (see Fig. 2.A.7**a** for details). In addition, the measured spatial and temporal noise levels are 36.9±0.7 and 11.4 mrad/μm, respectively (see Fig. 2.A.8 for details). Furthermore, the lateral resolutions achieved in the experiment along the x- and y- axes are 2.76 μm and 3.48 μm, respectively (see Fig. 2.A.9 for details). Comparing with the 1.06-μm theoretical diffraction limit, the reduced resolutions result from the geometric aberration of the device, misalignment in the optical setup, and imperfect fabrication. Besides, to compare our results with one of the state of the art QPI techniques, the resolution targets are also characterized by the Fourier Ptychography techniques [66] (see Fig. 2.A.10 for details). Finally, to demonstrate the capability of the QPGM to image biological samples, we imaged several sea urchin samples. As seen in a few sample PGIs plotted in Fig. 2.3**e**, the QPGM can capture the edges of the sea urchin as well as the detailed morphology inside the cells. Thus, the QPGM is able to measure the phase gradient information of the biological samples, which is directly related to cellular mass transport [86].

To demonstrate further miniaturization of the system, we performed additional measurements with an off-the-shelf CMOS image sensor. Figure 2.3**f** shows the schematic of the optical system. The distance from the object plane to the CMOS image sensor is just 5.09 mm (see Figs. S11a and S11b for details of the compact optical setup). Figure 2.3**g** shows three raw DIC images captured by the setup in Fig. 2.3**f** when using the imaging target shown in Fig. 2.3**a**. Using Eq. 2.2, the three DIC images in Fig. 2.3**g** result in the PGI plotted in Fig. 2.3**h**. The edges and the measured phase gradient of the PGI in Fig. 2.3**h** are comparable to the results shown in Fig. 2.3**b** (see Figs. 2.A.11**c** and 2.A.11**d** for additional measurement results).

2.5 QPGM based on monolithically integrated double-sided metasurfaces

To further miniaturize the device, we designed and fabricated a monolithically integrated double-sided metasurface QPGM. Figure 2.4**a** schematically illustrates the double-sided QPGM. While conceptually similar to the system discussed in the previous section, the double-sided QPGM is more compact, mechanically robust, and does not need further alignment after fabrication. The two metasurface layers are based on the same platform discussed in the previous section, but they are fabricated on the two sides of a 1-mm-thick fused silica substrate (see Method, Appendix 2.1, and Table 2.A.2 for details about the design and fabrication). The optical images of the device are shown in Fig. 2.4**b**. The total volume of the QPGM is $0.62\times0.41\times1.00$ mm^3. Also, it has a magnification of $1.60\times$ and a field of view of 140 μm in diameter. To verify the capability of the double-sided QPGM, we used the same resolution targets as in Figs. 2.3**c** and 2.3**d**. The results, shown in Figs. 2.4**c** and 2.4**d**, verify that the double-sided metasurface QPGM generates PGIs that are comparable to those of the QPGM based on the two separate metasurface layers. Particularly, the estimated thicknesses of the phase samples plotted in Fig. 2.4**d** are in good agreement with the values measured by AFM. Phase images of sea urchin samples captured by the double-sided metasurface QPGM are shown in Fig. 2.A.12.

2.6 Discussion

One limitation of the proposed system, especially for the double-sided metasurface device, is its FOV. The small FOV mostly results from the fact that our system is close to 4-f configuration that requires the sum of the focal lengths of the two lenses to be comparable to their separation. To increase the FOV, a possible solution is the recently reported folded metasurface platform [40] that might be able to

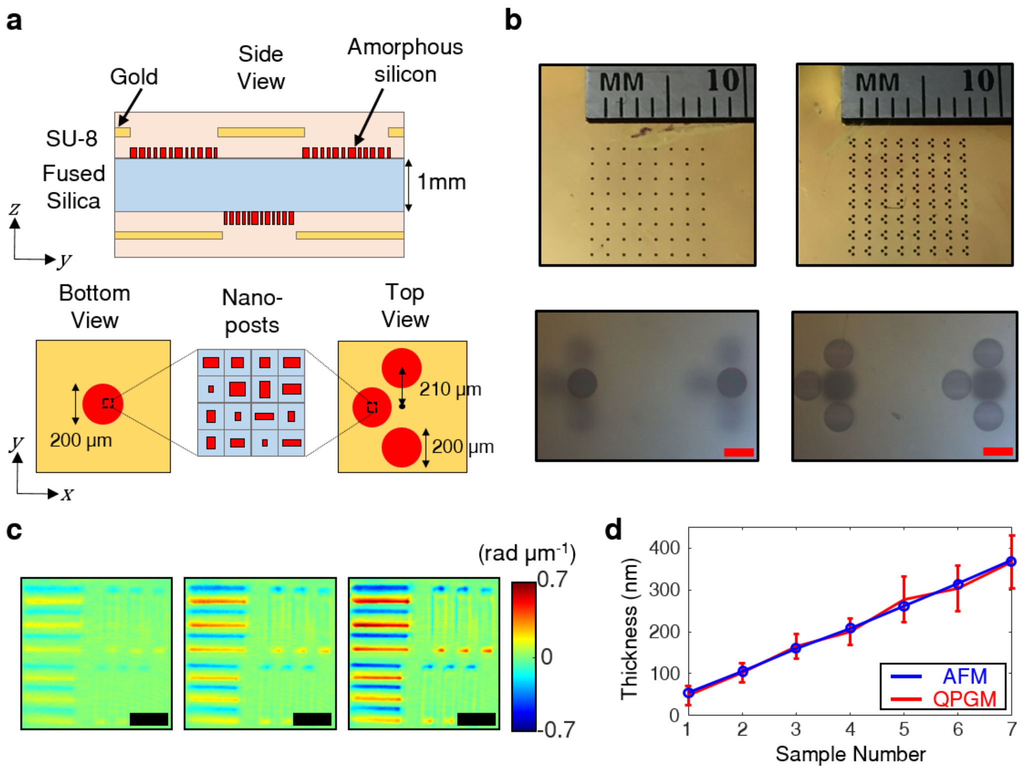

Figure 2.4: **Imaging with the doublet QPGM formed from monolithic integration of two metasurface layers on the same substrate.** **a** Schematic drawing of the miniaturized QPGM using the double-sided metasurface from different viewing angles. The two metasurface layers are patterned on the two sides of a 1-mm-thick fused silica substrate. **b** Optical images of bottom (left) and top (right) views of the 8 by 8 array of the doublet QPGM, in addition to zoomed-in images for portions of the devices. Scale bars: 200 μm **c** PGIs captured using the doublet QPGM from the same parts of the resolution target used in Fig. 2.3**c**. Scale bars: 15 μm **d** Thicknesses of seven different parts of the phase target calculated from the PGIs captured by the metasurface QPGM, and those measured by AFM. The plotted estimated thicknesses through QPGM are averaged over 100 arbitrarily chosen points on the sample edges. Error bars represent standard deviations of the estimated values.

achieve a large FOV and a small footprint simultaneously. In this platform, the propagation space between the two lenses is folded inside the substrate through multiple reflections, and therefore the effective distance between the lenses can be significantly larger than the substrate thickness. Furthermore, adding another metasurface layer can be used to mitigate the geometric aberrations further and increase the FOV [78].

The QPGM system is sensitive to the equality of optical axis separation for TE and TM polarizations in the two metasurface lenses. Nevertheless, this separation can be controlled very precisely since metasurfaces allow for implementation of almost arbitrary phase profiles in sub-wavelength scales. If the separations between the optical axes are identical for the two metasurfaces, the structure becomes robust against lateral and axial misalignment (see Fig. 2.A.13).

2.7 Outlook and Summary

It is worth noting that the multi-functionality via both polarization and spatial multiplexing schemes, that is the key property for the design of the miniaturized quantitative phase gradient microscope, is very hard to achieve in any other platform if at all possible. We envision that these and other versatile properties of metasurfaces enable various types of quantitative phase imaging devices. For example, three different images at different axial positions can be captured to calculate the phase information rather than the phase gradient information through the transport-of-intensity equation [67, 92]. In addition, different focus scanning schemes can be integrated with the quantitative phase gradient microscope to achieve a tomographic quantiative phase imaging device with fast axial scanning [39, 93, 94]. Moreover, we expect that around ten to a hundred of miniaturized microscopes could be integrated on a single CMOS sensor for highly parallelized microscopy. Finally, a synergistic combination of metasurfaces and computational optics is an emerging area to enhance the potentials of metasurface optical systems. Considering the computational aspects of quantitative phase imaging, we believe that new kinds of miniaturized quantitative phase imaging devices which benefit from novel properties and enhanced optical control of metasurfaces can be proposed.

In conclusion, we utilized two multi-functional metasurface layers to realize miniaturized quantitative phase gradient microscopes. A novel design and working principle were proposed and investigated both through simulation and experiment. Exploiting vertically integrated multi-functional metasurfaces, we experimentally captured phase gradient images of several transparent samples and verified the quantitative phase imaging capability of the systems. This work clearly demonstrates potentials of dielectric metasurface platforms in quantitative phase imaging systems to make miniaturized imaging devices such as miniaturized microscopes or endoscopes [77]. With the great interest in quantitative phase imaging and the miniaturized microscopes, we envision that the metasurfaces will play a significant role in the development of these technologies.

2.8 Methods

Simulation and design

The simulation results presented in Fig. 2.A.4 were obtained by finding the transmission coefficients of corresponding periodic metasurfaces using the rigorous coupled wave analysis technique [95]. The amorphous silicon nano-posts were assumed to be 664 nm tall and the square lattice constant was 380 nm. The nano-posts are capped with an 8-μm-thick SU-8 polymer layer. Refractive indices of amorphous silicon, fused silica, and SU-8 for the operation wavelength of 850 nm in the simulations were 3.56, 1.44, and 1.58, respectively. Side lengths of the nano-posts, D_x and D_y, were varied in simulations to achieve full and independent phase control over the 2π range for x and y polarizations (see Figs. 2.A.4**a**-2.A.4**d** for the simulation results) [13]. Next, we optimized D_x and D_y as functions of ϕ_{TE} and ϕ_{TM} to provide high transmission and desired phase shifts. The optimized maps of the side lengths as functions of the phase delays for TE and TM polarized light are plotted in Figs. 2.A.4**e** and 2.A.4**f** (see Figs. 2.A.4**g** and 2.A.4**h** for the simulated transmittance corresponding to TE and TM polarizations). For the double-sided metasurface device, while the metasurface layer 2 is designed by the same lookup table in Figs. S4e and S4f, the metasurface layer 1 was composed of nano-posts having a 60-nm-thick Al_2O_3 layer on top of the amorphous silicon layer. To consider the presence of the Al_2O_3 layer, we performed additional simulations with the new condition. In particular, the refractive index of Al_2O_3 for the operation wavelength in the simulation was 1.76. The optimized results are plotted in Figs. 2.A.4**i**-2.A.4**l**.

We used the wave propagation method for the numerical studies of Fig. 2.A.1 to calculate the optical fields for TE and TM polarized light. Then, the interference intensity patterns at the image plane can be directly calculated from the TE and TM polarized fields. Metasurfaces are treated as phase plates in simulations, and their phase profiles used in the numerical simulations are given in Appendix 2.1. It is worth noting explicitly that the optimal phase profiles of the two metasurface layers in

Fig. 2.A.1**e** were obtained through optimization with the ray-tracing technique using a commercial optical design software (Zemax OpticStudio, Zemax) to minimize geometric aberrations.

Device fabrication

The metasurface layers 1 and 2 shown in Fig. 2.2**d** were fabricated on two different 1-mm-thick fused silica substrates. A 664-nm-thick layer of amorphous silicon was deposited using the plasma enhanced chemical vapor deposition technique. For nano-patterning, a ~300-nm-thick positive electron resist (ZEP-520A) was used. In addition, a ~60-nm-thick water soluble conductive polymer (aquaSAVE, Mitsubishi Rayon) was spin-coated for charge dissipation. The patterns were generated using electron-beam lithography (EBPG-5000+, Raith). The conductive polymer was then dissolved in water and the resist was developed in a resist developer solution (ZED-N50, Zeon Chemicals). A 60-nm-thick Al_2O_3 layer was deposited by electron beam evaporation. The pattern was transferred to the Al_2O_3 layer by a lift-off process in a solvent (Remover PG, MicroChem). The patterned Al_2O_3 layer worked as a hard mask to etch the amorphous silicon layer. The dry etching step was performed in a mixture of SF_6 and C_4F_8 plasmas using an inductively coupled plasma reactive ion etching process. The Al_2O_3 mask was dissolved in a 1:1 mixture of ammonium hydroxide and hydrogen peroxide heated to 80 °C.

The double-sided metasurfaces shown in Fig. 2.4**b** are patterned on both sides of a 1-mm thick fused silica substrate. Two 664-thick layers of amorphous silicon were deposited on both sides of the substrate using the plasma enhanced chemical vapor deposition technique. Then, the metasurface layer 2 was first fabricated using the same process employed for the single-sided metasurfaces. Then, metasurface 2 was cladded by an SU-8 polymer layer (SU-8 2002, MicroChem), which served to protect metasurface 2 during the fabrication of the metasurface 1. A 4-μm-thick layer of SU-8 was spin-coated on the sample, baked at 90 °C for 4 minutes, and reflowed at 200 °C for 5 minutes to achieve a completely planarized surface. The SU-8 polymer was then exposed with ultraviolet light and cured by baking at 200 °C for another 90 minutes. To align the metasurface layers 1 and 2, a second set of alignment marks were patterned on the side of the metasurface 1 and aligned to the alignment marks on the side of the metasurface layer 2 using optical lithography. Next, metasurface 1 was fabricated by the same method as the single-sided metasurfaces. However, the Al_2O_3 mask was not removed from the top of the metasurface layer 1 because a mixture of ammonia and hydrogen peroxide at 80 °C would damage the SU-8 cladding layer of the metasurface layer 2. It should be noted that the 60-nm thick Al_2O_3 layer was considered as an integral part of metasurface layer 1 in the design process. Like the metasurface layer 2, the metasurface layer 1 was also cladded by a 4-μm-thick SU-8 layer. Next, the circular apertures on both sides were patterned by photo-lithography, deposition of chrome and gold (10 nm/ 100 nm) layers, and lift-off. Finally, additional 4-μm-thick SU-8 polymer layers were spin coated on both sides to protect the apertures.

Measurement procedure

The imaging performance of the QPGM was characterized using the setups shown schematically in Fig. 2.A.6. An 850-nm LED (Thorlabs LED851L) was exploited as the light source. A linear polarizer (Thorlabs, LPVIS100-MP2) was placed in front of the LED and set at 45° to confirm the polarization state of the input light. The sample image was captured by the two metasurface layers which are mounted on three-axis translation stages to enable alignment. The field at the image plane of the QPGM was captured by a custom-built optical microscope. The microscope consists of an objective lens (Olympus, LMPlanFL 10×) and a tube lens (Thorlabs AC254-150-B-ML, focal length of 15 cm). The second linear polarizer, set at -45°, was inserted between the objective lens and the tube lens to form interference between x- and y- polarized light. An optical band pass filter (Thorlabs, FL850-10) in front of the camera was used to limit the bandwidth of the LED and remove the background. For the double-sided metasurface devices, the optical system is almost the same as the one used for the two separated metasurface layers. The double-sided metasurface device was mounted on one three-axis translation stage instead of two.

For the setup shown in Fig. 2.A.11**a**, a CMOS image sensor (MT9J001, Arducam) replaces the custom-built microscope. A 260-μm-thick linear polarizer (LPVIS100-MP2, Thorlabs) is attached on top of a glass substrate protecting the CMOS image sensor by a double-sided tape. As shown in Fig. 2.A.11**a**, the band-pass filter is placed between a LED and a lens (LB1761-C, Thorlabs).

2.9 Appendix

Wave propagation simulation and phase maps of the metasurfaces

In this section we present numerical analysis results of the QPGM. First, it is worth explaining why the QPGM consists of two metasurface layers, and a single layer is not capable of doing so. Then, we verify that the QPGM based on the two metasurface layers addresses the issues faced in the system using a single metasurface. We used wave-propagation simulations to analyze the systems in Fig. 2.A.1. In the simulations, the metasurfaces and the conventional lens are modeled as ideal phase plates. Moreover, the thickness of all fused silica substrates is fixed at 1 mm. For all metasurfaces, the distance between the optical axes for TE and TM polarizations, Δs, is fixed at 1.5 μm along the y-axis. Finally, the phase sample shown in Fig. 2.1**c** is used for all the simulations.

Figure 2.A.1**a** shows a schematic of a DIC system based on a single birefringent metasurface lens and a regular refractive lens, forming a 4-f imaging system. To implement the single metasurface layer system, we use the thin lens equation for the phase profiles of the metasurface lens ($\mathrm{ML}_{1,a}$) and the conventional lens (Lens_2, a). More specifically, $\mathrm{ML}_{1,a}$ has two different phase profiles for TE and TM polarizations, ($\phi_{\mathrm{ML}_{1,a},\mathrm{TE}}$ and $\phi_{\mathrm{ML}_{1,a},\mathrm{TM}}$), given by:

$$\phi_{\mathrm{ML}_{1,a},\mathrm{TE}} = -\frac{\pi}{\lambda f_1}(x^2 + (y + \frac{\Delta s}{2})^2), \tag{2.3}$$

$$\phi_{\mathrm{ML}_{1,a},\mathrm{TM}} = -\frac{\pi}{\lambda f_1}(x^2 + (y - \frac{\Delta s}{2})^2), \tag{2.4}$$

where x and y are Cartesian coordinates from the center of $\mathrm{ML}_{1,a}$ and λ is the operating wavelength in vacuum. Moreover, the polarization-insensitive phase profile of $\mathrm{Lens}_{2,a}$ is written as, $\phi_{\mathrm{Lens}_{2,\mathrm{a}}} = -\frac{\pi}{\lambda f_2}(x^2 + y^2)$. While one might expect that the configuration in Fig. 2.A.1**a** works similar to a conventional DIC microscope, an additional spurious intensity gradient shows up in the formed interference pattern, I_{single}, as seen in Fig. 2.A.1**b**. The reason is that despite the 4-f imaging system, the two slightly separated optical axes for the TE and TM polarizations cause the intensity gradient not present in the original target (see Appendix 2.2 and Fig. 2.A.2 for experimental results of the single metasurface system and theoretical analysis about the degradation). Another clear issue with the system shown in in Fig. 2.A.1**a** which undermines its miniature size is that it would require a variable phase retarder to retrieve quantitative phase gradient information.

To resolve the spurious intensity gradient issue first, we replace the refractive lens with a second birefringent metasurface lens in Fig. 2.A.1**c**. For the system based on the two bifocal metasurface lenses shown in Fig.2.A.1**c**, the metasurface lens 1, $ML_{1,c}$, is the same as $ML_{1,a}$ shown in Fig.2.A.1**a**. A second birefringent metasurface lens, $ML_{2,c}$, is used in the system shown in Fig. 2.A.1**c** instead of $Lens_{2,a}$ in Fig. 2.A.1**a**. The two phase profiles of $ML_{2,c}$ for TE and TM polarizations, ($\phi_{ML_{2,c},TE}$ and $\phi_{ML_{2,c},TM}$), are given by:

$$\phi_{ML_{2,c},TE} = -\frac{\pi}{\lambda f_2}(x^2 + (y + \frac{\Delta s}{2})^2), \tag{2.5}$$

$$\phi_{ML_{2,c},TM} = -\frac{\pi}{\lambda f_2}(x^2 + (y - \frac{\Delta s}{2})^2) + \phi_o, \tag{2.6}$$

where ϕ_o is the phase offset between the two orthogonal polarizations. ϕ_o is fixed at $\frac{3\pi}{4}$ for the simulations. As a result, the simulated interference intensity map shown in Fig. 2.A.1**d**, I_{double}, is a clear DIC image of the transparent object with no intensity artifacts (see Appendix 2.2 for theoretical explanation about the system of the two birefringent metasurface lenses). In the experimental implementation, the values of ϕ_o are $\frac{3\pi}{4}$ and $\frac{\pi}{4}$ for the QPGM using two separate substrates and the double-sided QPGM, respectively.

In addition to birefringence, the capability of metasurfaces to simultaneously perform multiple independent functions allows us to eliminate the requirement of a variable retarder, since several images with different phase offsets can be captured simultaneously as shown schematically in Fig. 2.A.1**e**. Moreover, we employed the ray tracing method instead of the thin lens equation to mitigate geometric aberrations. In other words, the phase profiles are optimized for the metasurface layers 1 and 2 in Fig.2.A.1**e**, $Layer_{1,e}$ and $Layer_{2,e}$, to minimize the off-axis aberrations and increase the field of view. Specifically, the phase profiles of the metasurfaces are defined by two terms. One is a sum of even-order polynomials of radial coordinates (mostly implementing the focusing), and the other is a linear phase gradient term associated with the three-directional splitting of light. The phase profiles of $Layer_{1,e}$ for TE and TM polarizations, $\phi_{Layer_{1,e},TE}$ and $\phi_{Layer_{1,e},TM}$, are given by:

$$\phi_{Layer_{1,e},TE} = \sum_{n=1}^{5} \frac{a_n}{R^{2n}}(x^2 + (y + \frac{\Delta s}{2})^2)^n - k_{grat,1}y, \tag{2.7}$$

$$\phi_{Layer_{1,e},TM} = \sum_{n=1}^{5} \frac{a_n}{R^{2n}}(x^2 + (y - \frac{\Delta s}{2})^2)^n - k_{grat,1}y, \tag{2.8}$$

$$\phi_{Layer_{1,e},TE} = \sum_{n=1}^{5} \frac{a_n}{R^{2n}}(x^2 + (y + \frac{\Delta s}{2})^2)^n - k_{grat,1}x, \tag{2.9}$$

$$\phi_{\text{Layer}_{1,e},\text{TM}} = \sum_{n=1}^{5} \frac{a_n}{R^{2n}}(x^2 + (y - \frac{\Delta s}{2})^2)^n - k_{grat,1}x, \tag{2.10}$$

$$\phi_{\text{Layer}_{1,e},\text{TE}} = \sum_{n=1}^{5} \frac{a_n}{R^{2n}}(x^2 + (y + \frac{\Delta s}{2})^2)^n + k_{grat,1}y, \tag{2.11}$$

$$\phi_{\text{Layer}_{1,e},\text{TM}} = \sum_{n=1}^{5} \frac{a_n}{R^{2n}}(x^2 + (y - \frac{\Delta s}{2})^2)^n + k_{grat,1}y, \tag{2.12}$$

where a_n are the optimized coefficients of the even-order polynomials in the shifted radial coordinates, $k_{grat,1}$ is the linear phase gradient, and R denotes the radius of the metasurfaces. Detailed information about a_n, $k_{grat,1}$, and R is given in Table 2.A.1. Since a single set of rectangular nano-posts can only implement one pair of the birefringent phase maps, three different sets of rectangular nano-posts are designed to achieve the three pairs of phase maps in (Eqs. 2.7 and 2.8), (Eqs. 2.9 and 2.10), and (Eqs. 2.11 and 2.12). Then, the three maps of the rectangular nano-posts are interleaved along the x-axis using the spatial multiplexing method [72, 73, 96]. With the phase profiles in Eqs. 2.7-2.12, the $\text{Layer}_{1,e}$ in Fig. 2.A.1**e** plays the role of a lens and a three directional beam-splitter at the same time, at the cost of a drop in efficiency.

$\text{Layer}_{2,e}$ has three different birefringent metasurfaces which are identically displaced from the center of $\text{Layer}_{2,e}$. The distance from the center of the $\text{Layer}_{2,e}$ to the center of each lens, ΔD, is 660 μm. The three coordinates of the centers of the lenses measured from the center of the $\text{Layer}_{2,e}$ are (0,-ΔD) (-ΔD,0) and (0,ΔD). The six phase profiles of the three lenses for TE and TM polarizations are written as:

$$\phi_{\text{Layer}_{2,e},\text{TE}} = \sum_{n=1}^{5} \frac{b_n}{R^{2n}}(x^2 + (y + \Delta D + \frac{\Delta s}{2})^2)^n + k_{grat,2}y, \tag{2.13}$$

$$\phi_{\text{Layer}_{2,e},\text{TM}} = \sum_{n=1}^{5} \frac{b_n}{R^{2n}}(x^2 + (y + \Delta D - \frac{\Delta s}{2})^2)^n + k_{grat,2}y + \phi_o, \tag{2.14}$$

$$\phi_{\text{Layer}_{2,e},\text{TE}} = \sum_{n=1}^{5} \frac{b_n}{R^{2n}}((x + \Delta D)^2 + (y + \frac{\Delta s}{2})^2)^n + k_{grat,2}x, \tag{2.15}$$

$$\phi_{\text{Layer}_{2,e},\text{TM}} = \sum_{n=1}^{5} \frac{b_n}{R^{2n}}((x + \Delta D)^2 + (y - \frac{\Delta s}{2})^2)^n + k_{grat,2}x + \phi_o + \frac{2\pi}{3}, \tag{2.16}$$

$$\phi_{\text{Layer}_{2,e},\text{TE}} = \sum_{n=1}^{5} \frac{b_n}{R^{2n}}(x^2 + (y - \Delta D + \frac{\Delta s}{2})^2)^n - k_{grat,2}y, \tag{2.17}$$

$$\phi_{\mathrm{Layer}_{2,e},\mathrm{TM}} = \sum_{n=1}^{5} \frac{b_n}{R^{2n}}(x^2 + (y - \Delta D - \frac{\Delta s}{2})^2)^n - k_{grat,2}y + \phi_o + \frac{4\pi}{3}, \tag{2.18}$$

where b_n are the optimized coefficients of the even-order polynomials of the shifted radial coordinates and $k_{grat,2}$ is the linear phase gradient. The detailed information about b_n and $k_{grat,2}$ is given in Table 2.A.1. As a result, the two layers form the three different DIC images at the image plane. Specifically, combinations of (Eqs. 2.7, 2.8, 2.13, and 2.14), (Eqs. 2.9, 2.10, 2.15, and 2.16), and (Eqs. 2.11, 2.12, 2.17, and 2.18) result in the three phase-shifted DIC images in Fig. 2.A.1**f**, I_1, I_2, and I_3, respectively. To be specific, the desired phase offsets for the three-step phase shifting are achieved by the phase maps of the second metasurface layer in Eqs. 2.13-2.18. Moreover, we should point out that I_1, I_2, and I_3 in Fig. 2.A.1**f** are comparable to the ideal results shown in Fig. 2.1**d**. Figure 2.A.1**g** shows the PGI calculated from the three DIC images in Fig. 2.A.1**f** by using Eq.**2**, and is in good agreement with the ideal PGI shown in Fig. 2.1**e**.

As shown in Figs. 2.4**a** and Fig. 2.4**b**, the QPGM is also implemented using double-sided metasurfaces on a 1-mm thick fused silica wafer. The double-sided metasurface QPGM is designed through an identical process used for the design of the QPGM based on two metasurface layers on two separate substrates. The phase profiles of the double-sided metasurfaces are determined by Eqs. 2.7-2.18 with the optimized phase profile parameters such as a_n, b_n, R, ΔD, Δs, $k_{grat,1}$, and $k_{grat,2}$ given in Table 2.A.2. The distances from the object plane to the metasurface layer 1 and from the image plane to the metasurface layer 2 are 317 μm and 397 μm, respectively.

Experimental and theoretical results with a single bifocal metasurface lens

We fabricated a single bifocal metasurface and measured its performance. The phase map of the device is determined by Eqs. 2.3 and 2.4. For the fabricated single bifocal metasurface lens, the diameter, focal length, and separation of the focal points are 900 μm, 1.2 mm, and 2 μm, respectively. The two focal points are characterized through the optical setup shown in Fig.2.A.2**a**. An 850-nm semiconductor laser (Thorlabs, L850P010) is coupled to a single mode fiber and a laser collimator for illumination. The linear polarizer in front of the laser collimator is aligned to 0° (for TE), 90° (for TM), and 45° for characterization of the bifocal metasurface lens. The measured intensity maps shown in Fig.2.A.2**b** clearly show the polarization dependent bifocal property. The intensity profiles on the black dashed lines in Fig.2.A.2**b** are shown in Fig.2.A.2**c**. In Fig.2.A.2**c**, the FWHM of the two focal points and the distance between the two focal points are 1.21-1.35 μm and 2 μm, respectively. Moreover, the measured focusing efficiencies through a pin-hole with a diameter of about 4×FWHM at the focal plane are ~78% for both TE and TM polarizations.

We performed imaging experiments with the single bifocal metasurface lens using the optical setup schematically shown in Fig.2.A.2**d**. We employed a variable retarder to capture three different DIC images. Moreover, oblique illumination from an LED was used to avoid saturation at the central pixels of the camera resulting from undiffracted light. To limit the bandwidth, we employed a band-pass filter with a center wavelength and bandwidth of 850 nm and 10 nm, respectively. The three captured DIC images, I_1, I_2, and I_3, are shown in Fig.2.A.2**e**. The results clearly show that the spurious graded intensity patterns degrade the DIC images as expected from Fig. 2.A.1**b**. In Fig.2.A.2**f**, the PGI is calculated from the three DIC images in Fig. 2.A.2**e** through the three-step phase shifting method [84]. The graded phase gradient in the background in Fig. 2.A.2**f** also indicates the imperfect imaging performance of the single bifocal metasurface lens.

The degradation exists both in the simulation results shown in Fig. 2.A.1**b** and the measurement in Figs. 2.A.2**e** and 2.A.2**f**. The degradation can be explained using Fourier optics. If we consider the optical system consisting of one metasurface bi-focal lens and a normal thin lens as in Fig. 2.A.1**a** such that the z-axis passes through the center of the second lens (i.e. the optical axes of the first lens for TE and TM polarizations are Δs/2 distant from the z-axis), we can write down the relations between the field at the object plane (U) and the fields at the Fourier plane ($U_{F,TE}$

and $U_{F,TM}$) through the Fresnel diffraction. For simplicity, let us assume that the focal lengths of the two lenses in Fig. 2.A.1**a** are identical. In this case, the two optical fields formed by the first metasurface lens, $U_{F,TE}$ and $U_{F,TM}$ are no longer simple Fourier transforms of U, but would instead be written as:

$$
\begin{aligned}
U_{F,TE}(x,y) = \iint \iint & U(x'',y'')exp[i\tfrac{\pi}{\lambda f}((x'-x'')^2+(y'-y'')^2)]dx''dy'' \\
& \times exp[-i\tfrac{\pi}{\lambda f}(x'^2+(y'+\tfrac{\Delta s}{2})^2))])exp[i\tfrac{\pi}{\lambda f}((x-x')^2+(y-y')^2)]dx'dy' \\
& = A_1 \iint U(x'',y'')exp[i\tfrac{\pi}{\lambda f}(x^2+x''^2+y^2+y''^2)] \\
& \times \iint exp[i\tfrac{\pi}{\lambda f}(x'^2+y'^2-2(x+x'')x'-2(y+y''+\tfrac{\Delta s}{2})y']dx'dy'dx''dy'' \\
& = A_2 exp(-i\tfrac{2\pi}{\lambda f}\tfrac{\Delta s}{2}y) \iint U(x'',y'')exp[-i\tfrac{2\pi}{\lambda f}(xx''+(y+\tfrac{\Delta s}{2})y'')]dx''dy'' \\
& = A_2 exp(-i\tfrac{2\pi}{\lambda f}\tfrac{\Delta s}{2}y)\widetilde{U}(\tfrac{x}{\lambda f},\tfrac{y+\frac{\Delta s}{2}}{\lambda f})
\end{aligned}
$$

$$
U_{F,TM}(x,y) = A_2 exp(i\tfrac{2\pi}{\lambda f}\tfrac{\Delta s}{2}y)\widetilde{U}(\tfrac{x}{\lambda f},\tfrac{y-\frac{\Delta s}{2}}{\lambda f}),
$$

where λ, f, and Δs are the wavelength, focal length of the two lenses, and the separation between the optical axes of the metasurface lens, respectively. Also, $\widetilde{U}$ represents the 2D Fourier transform of U. A_1 and A_2 are complex constants. Then, the fields at the image plane ($U_{i,TE}$ and $U_{i,TM}$) can be written through the 2D Fourier transform of $U_{F,TE}$ and $U_{F,TM}$:

$$
\begin{aligned}
U_{i,TE}(x,y) &= \iint U_{F,TE}(x',y')exp[-i\tfrac{2\pi}{\lambda f}(xx'+yy')]dx'dy' \\
&= B_1 exp(+i\tfrac{2\pi}{\lambda f}\tfrac{\Delta s}{2}y)U(-x,-(y+\tfrac{\Delta s}{2})), \\
U_{i,TM}(x,y) &= \iint U_{F,TM}(x',y')exp[-i\tfrac{2\pi}{\lambda f}(xx'+yy')]dx'dy' \\
&= B_1 exp(-i\tfrac{2\pi}{\lambda f}\tfrac{\Delta s}{2}y)U(-x,-(y-\tfrac{\Delta s}{2})),
\end{aligned}
$$

where B_1 is a complex constant. We should point out that the fields at the image plane are not only shifted laterally by the separation Δs, but also accompanied with a different phase gradient for TE and TM polarizations. The different phase gradients for TE and TM polarizations cause the spurious degradation shown in Figs. 2.A.1**b**, 2.A.2**e**, and 2.A.2**f**. Considering that Δs is close to the diffraction-limit scale, the simulation result in Fig. 2.A.1**b** and the measurement in Figs. 2.A.2**e** and 2.A.2**f** clearly reveal that the system is very sensitive to even very small values of Δs. Furthermore, the inevitable axial misalignment between the double axes of the metasurface lens and the single axis of the normal lens results in the phase gradient difference at the image plane. In other words, lens-based DIC microscopy typically necessitates at least three optical elements which are two lenses and a birefringent crystal such as a Wollaston prism between the two lenses. Although one might suppose that the different linear phase gradients can be employed instead of the lateral shifts along the y-axis in Eqs. 2.3 and 2.4 to remove the spurious degradation, it is worth pointing out that both schemes are mathematically equivalent with a different complex constant and result in a similar degradation.

In contrast, the two metasurface layers can avoid the unwanted degradation because the two lenses have independent optical axes for both polarizations. For the system in Fig. 2.A.1**c**, the fields at the image plane can be written as the Fourier transform with respect to the optical axis of each polarization. As a result, the fields at the image plane $U_{i,TE}$ and $U_{i,TM}$ can be written as:

$$U_{i,TE}(x,y) = U(-Mx, -M(y + \tfrac{\Delta s}{2}) - \tfrac{\Delta s}{2}),$$
$$U_{i,TM}(x,y) = U(-Mx, -M(y - \tfrac{\Delta s}{2}) + \tfrac{\Delta s}{2}),$$

where M is the magnification of the system and is mainly determined by the phase maps of the two bi-axial lenses. These equations clearly show that the two birefringent metasurface lenses are able to capture the conventional DIC images with two polarizers. More interestingly, the simulation results based on the wave propagation in Fig. 2.A.13 reveal that the proposed bi-axial system becomes very robust against other kinds of misalignments in the fabrication or optical alignment procedures once the separations of the optical axes for the both lenses are identical. As explained previously, it is worth noting that the metasurfaces uniquely admit arbitrary phase maps in subwavelength scale for both polarizations. Thus, the separation is one of the most accurately controllable variables in the design process of the metasurfaces. This is one of the reasons why our system performs adequately in the experiments. Furthermore, we remark that bi-focal lenses having an accurate separation close to the diffraction-limit are difficult to implement using any conventional birefringent optics.

Three-step phase shifting method for unidirectional quantitative phase gradient imaging

Phase-shifting is a widely known technique for phase retrieval in common interferometers. Moreover, it has been also used for quantitative phase gradient imaging by modifying the classical DIC microscope [97]. The technique utilizes multiple phase-shifted interference patterns to retrieve the phase information. To be specific, a captured differential interference contrast (DIC) image at the object plane is effectively written as:

$$I_j = |U(x,y) - U(x, y-\Delta y)e^{i\phi_j}|^2 = B(x,y) - C(x,y)cos(\theta(x,y) - \phi_j), \quad (2.19)$$

where $U(x,y) = A(x,y)e^{i\phi(x,y)}$, $B(x,y) = |A(x,y)|^2 + |A(x,-\Delta y)|^2$, $C(x,y) = 2|A(x,y)A(x,-\Delta y)|$, $\theta(x,y) = \phi(x,y) - \phi(x, y-\Delta y)$, and ϕ_j is a phase offset. Since $B(x,y)$, $C(x,y)$, and $\theta(x,y)$ are unknown, it can be seen that a minimum of three independent measurements are required for unambiguous retrieval of all unknowns. This is why the second metasurface layer in the current work consists of three different polarization sensitive off-axis lenses. Moreover, it is worth noting here that extensive investigations have previously been done to develop two-step phase shifting algorithms with additional assumption, some form of a priori knowledge, or complicated computations [98–100]. In the three-step phase shifting techniques, ϕ_1, ϕ_2, and ϕ_3 are usually set to 0, $\frac{2\pi}{3}$, and $\frac{4\pi}{3}$. Using the Eq. 2.19, I_1, I_2, and I_3 are written as:

$$I_1 = B(x,y) - C(x,y)cos(\theta(x,y)),$$
$$I_2 = B(x,y) - C(x,y)cos(\theta(x,y) - \tfrac{2\pi}{3}), \text{ and}$$
$$I_3 = B(x,y) - C(x,y)cos(\theta(x,y) - \tfrac{4\pi}{3}).$$

With further calculations, one can see that $\theta(x,y)$ can be expressed in terms of I_1, I_2, and I_3:

$$\theta(x,y) = arctan(\sqrt{3}\tfrac{I_2 - I_3}{2I_1 - I_2 - I_3}).$$

Considering that $\theta(x,y) = \phi(x,y) - \phi(x, y-\Delta y) \approx \nabla_y \phi \times \Delta y$ and Δy is small compared to the sample feature sizes, $\nabla_y \phi$ can be calculated as:

$$\nabla_y \phi \approx \tfrac{1}{\Delta y}\ arctan(\sqrt{3}\tfrac{I_2 - I_3}{2I_1 - I_2 - I_3}).$$

In Eq. 2, a calibration term, $\nabla_y \phi_{cali}$, is added to remove any kind of unwanted background coming from imperfect experimental conditions. Specifically, $\nabla_y \phi_{cali}$ is the background signal measured without any sample. The calibration process also allows for arbitrarily choosing three phase offsets with the same difference of $\frac{2\pi}{3}$.

For example, ϕ_1 is set to $\frac{3\pi}{4}$ and $\frac{\pi}{4}$ for the device using the two separate metasurface layers and the device based on the double-sided metasurfaces, respectively.

Metasurface	R (μm)	ΔD (μm)	Δs (μm)	a_1	a_2	a_3	a_4	a_5	$k_{grat,1}$ (rad/μm)
Layer1	300	660	1.5	-4.70×10^{2}	2.05×10^{1}	-3.88×10^{0}	7.69×10^{-1}	-7.30×10^{-2}	2.23
Metasurface	R (μm)	ΔD (μm)	Δs (μm)	b_1	b_2	b_3	b_4	b_5	$k_{grat,2}$ (rad/μm)
Layer2	300	660	1.5	-2.37×10^{2}	3.58×10^{-1}	1.07×10^{1}	-7.58×10^{0}	1.92×10^{1}	2.22

Table 2.A.1: **Phase profile parameters for the two separate metasurface layers.**

Metasurface	R (μm)	ΔD (μm)	Δs (μm)	a_1	a_2	a_3	a_4	a_5	$k_{grat,1}$ (rad/μm)
Layer1	100	210	1.5	-1.29×10^{2}	7.96×10^{0}	-1.17×10^{1}	6.98×10^{0}	-1.34×10^{0}	2.21
Metasurface	R (μm)	ΔD (μm)	Δs (μm)	b_1	b_2	b_3	b_4	b_5	$k_{grat,2}$ (rad/μm)
Layer2	100	210	1.5	-7.88×10^{1}	-5.19×10^{0}	4.53×10^{0}	-1.43×10^{0}	1.61×10^{-1}	2.19

Table 2.A.2: **Phase profile parameters for the double-sided metasurface QPGM.**

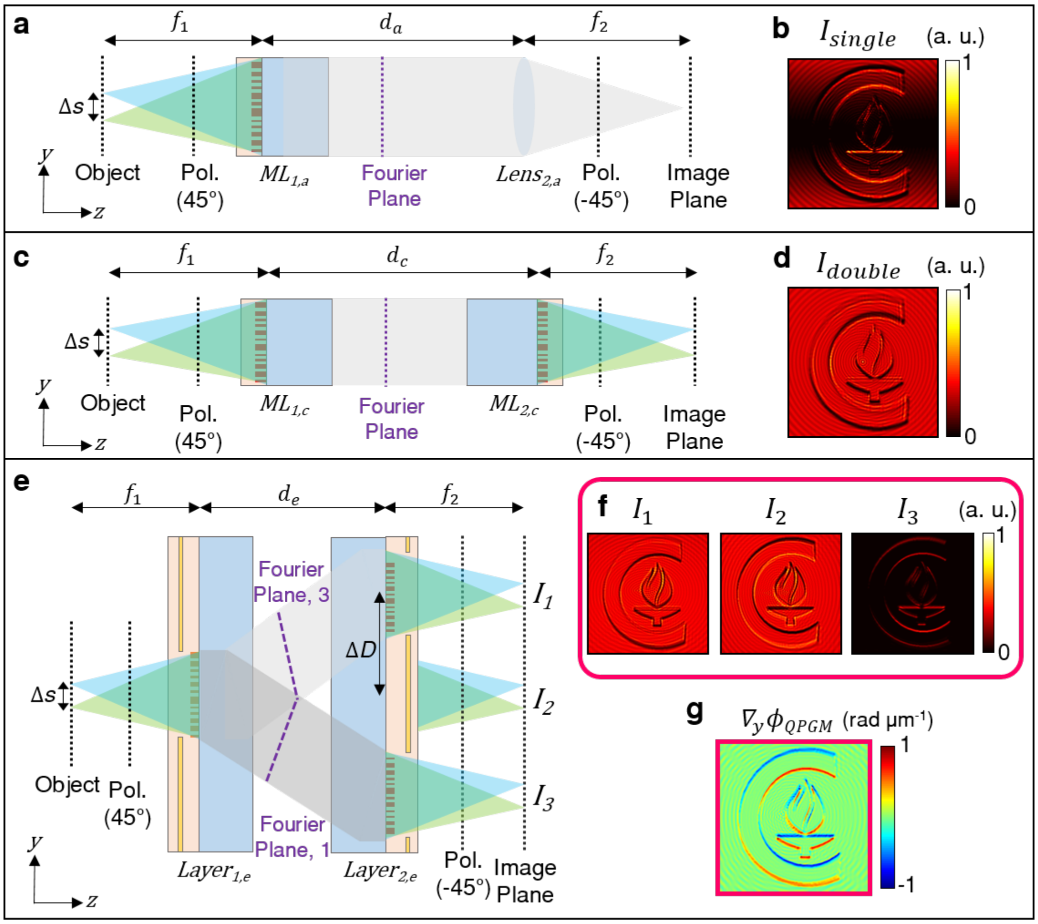

Figure 2.A.1: **System-level design and numerical analysis of the QPGM. a** Schematic of an optical system consisting of a single metasurface and a conventional thin lens. The metasurface works as a bifocal lens with two focal points for TE and TM polarizations separated along the y axis. **b** Simulated intensity map at the image plane formed by the system shown in **a**. **c** Schematic of an optical system consisting of two birefringent metasurfaces. Each metasurface acts as a bifocal lens with two focal points for TE and TM polarizations separated along the y axis. **d** Simulated intensity map formed in the image plane by the system shown in **c**. **e** Schematic of the optical system composed of one multi-functional metasurface and three bifocal lenses. As mentioned in Fig. 2.1**b**, the first metasurface collimates light from two focal points for the TE and TM polarizations that are separated in the y direction and splits it in three directions towards the three metasurfaces on the second layer. Similarly to the system in **c**, the first metasurface forms a separate imaging system with each of the metasurface lenses on layer 2. **f** Three simulated DIC images at the image plane using the system shown in **e**. **g** The PGI calculated from the three DIC images in **f**. Pol.: linear polarizer; ML: metasurface lens; d_a: 2.20 mm; d_c: 2.81 mm; d_e: 2.70 mm ; f_1: 687 μm; and f_2: 1.51 mm.

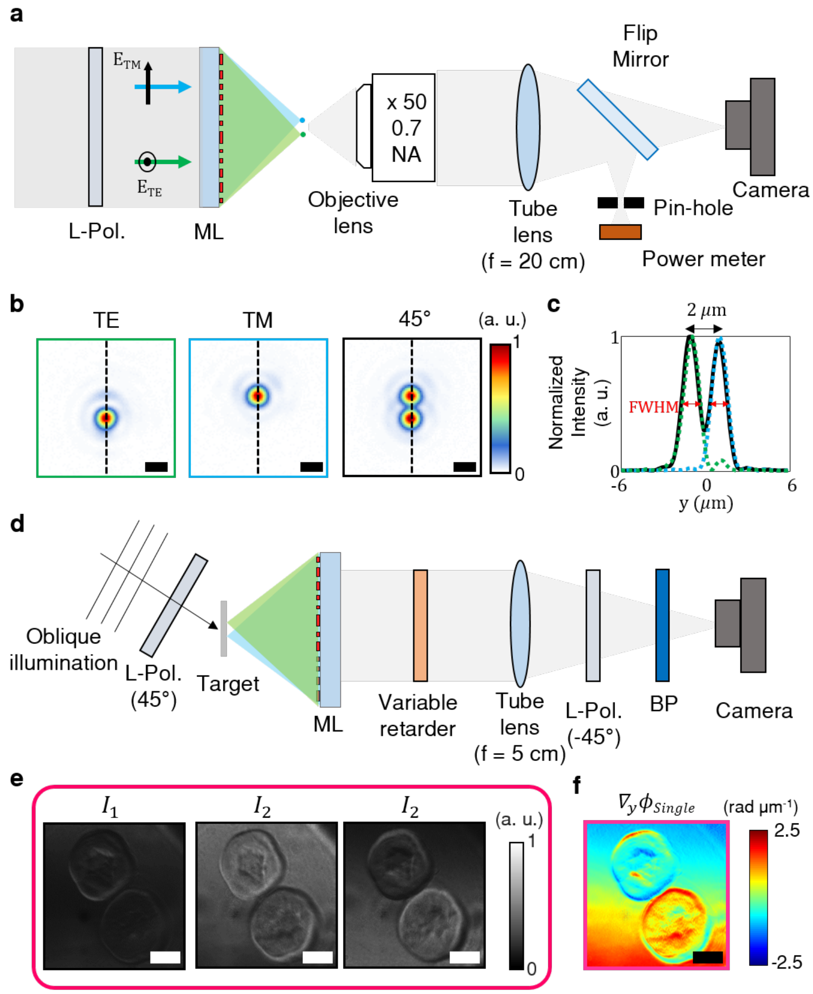

Figure 2.A.2: **Phase gradient imaging with a single bifocal metasurface lens. a** Schematic illustration of the optical setup used for capturing focuses of the single bifocal metasurface lens and measuring focusing efficiencies. The linear polarizer (L-Pol.) in front of the laser collimator is accordingly adjusted to confirm the input polarization states. **b** Measured focal points for different input polarization states. Left, center, and right images are the measured intensity maps at the focal plane with the linear polarizer aligned to 0° (TE), 90° (TM), and 45°, respectively. Scale bars: 2 μm. **c** Normalized intensity profiles at the focal plane on the three black dashed lines in **b**. Green and blue dashed lines are the intensity profiles for TE and TM polarized input light, respectively. The black line is the intensity profile with the 45° linear polarized light. **d** Schematic illustration of the optical setup capturing the three interference intensity patterns with a single bifocal metasurface and a variable retarder. An LED is used for the oblique illumination. BP: bandpass filter. **e** Measured interference intensity patterns, I_1, I_2, and I_3 that have phase offsets of 0, $\frac{2\pi}{3}$, and $\frac{4\pi}{3}$ between the TE and TM polarizations, respectively. **f** PGI calculated through the three-step phase shifting method from the three interference intensity maps in **e**. Scale bars: 30 μm.

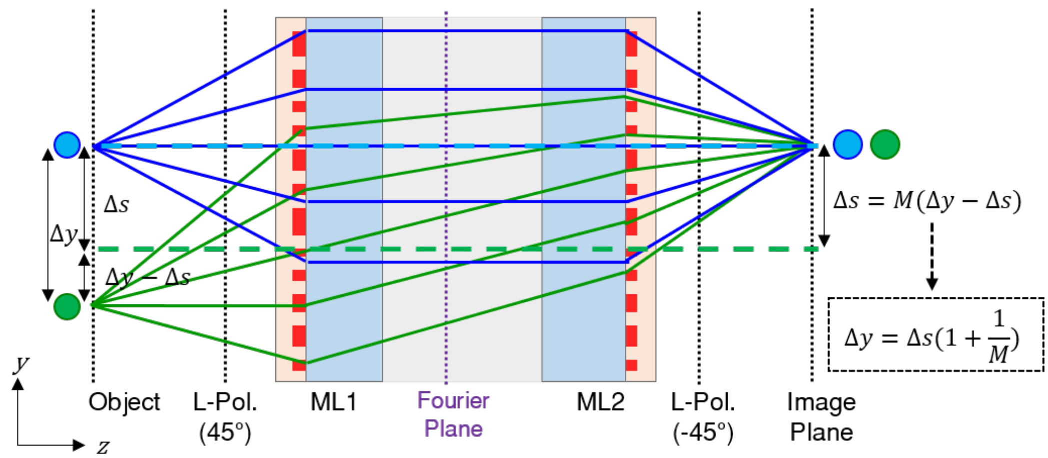

Figure 2.A.3: **Schematic illustration showing the relation between Δs and Δy.** Δs is the separation between the two optical axes for TE and TM polarizations. The green and blue dashed lines denote the optical axes for TE and TM polarizations, respectively. Δy is the effective shearing distance at the object plane. In other words, two points that are Δy apart along the y-axis in the object plane, are imaged to the same points at the image plane for the two different polarizations. The green and blue solid lines represent the rays coming from the green and blue points at the object plane, respectively. While the blue dot in the object plane is imaged along the blue dashed line representing the optical axis of TM polarization, the green dot is actually off-axis imaged at the position of the blue dot with respect to the green dashed line showing the optical axis of TE polarization. The black dashed box shows the relation between Δs and Δy given by $\Delta y = \Delta s(1 + \frac{1}{M})$, where M is the magnification of the optical system.

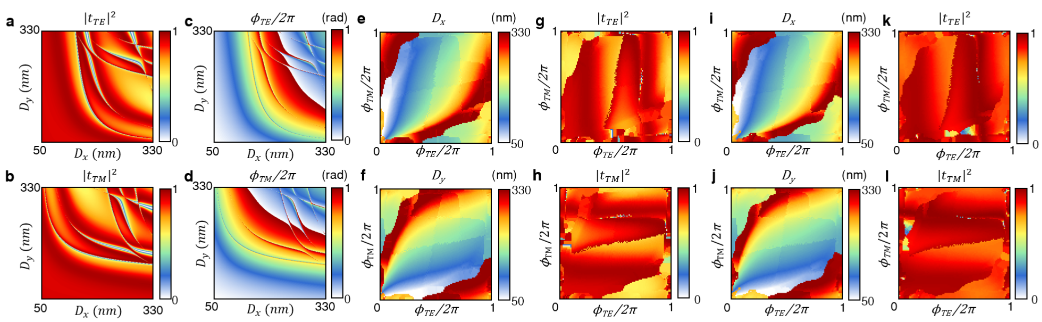

Figure 2.A.4: **Simulation results of the nano-posts at the wavelength of 850 nm.** **a**-**d** Simulated transmittance and transmitted phase of TE and TM polarized light for periodic arrays of meta-atoms as functions of D_x and D_y. The amorphous silicon layer is 664 nm thick, and the lattice constant is 380 nm. **a** and **b**: transmittance, **c** and **d**: transmitted phase **e**-**h** The optimized simulation results calculated from **a**-**d** for complete polarization and phase control. Calculated optimal D_x and D_y as functions of the required ϕ_{TE} and ϕ_{TM} are shown in **e** and **f**, respectively. Simulated transmittance of TE and TM polarized light as functions of ϕ_{TE} and ϕ_{TM} are shown in **g** and **h**, respectively. **i-l** The optimized simulation results of the nano-posts composed of 664-nm thick amorphous silicon and 60-nm thick Al_2O_3 on the fused silica substrate. The nano-posts are arranged on a square lattice with a 390-nm lattice constant and cladded by an ~8-μm-thick SU-8 layer. Calculated optimal D_x and D_y as functions of the required ϕ_{TE} and ϕ_{TM} are shown in **i** and **j**, respectively. Simulated transmittance of TE and TM polarized light as functions of ϕ_{TE} and ϕ_{TM} are shown in **k** and **l**, respectively.

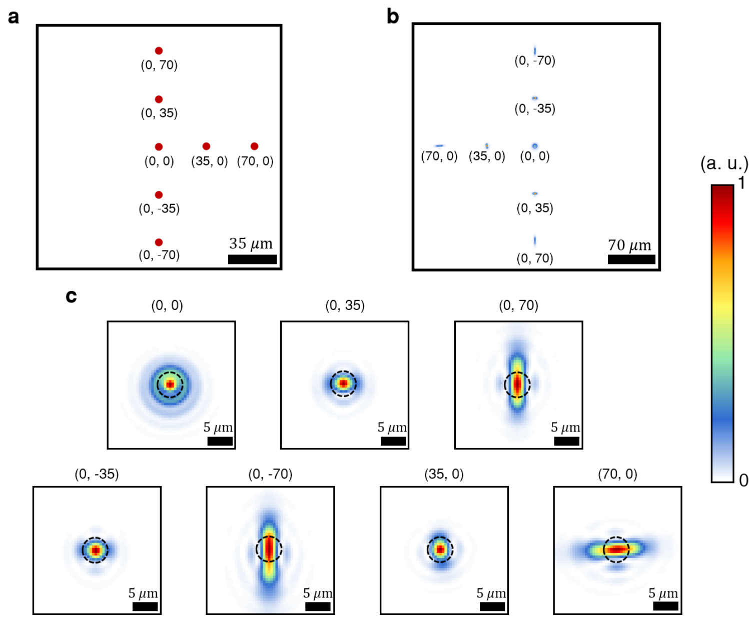

Figure 2.A.5: **Simulated point spread functions of the QPGM. a** Schematic showing the locations of point sources used at the object plane for characterizing the point spread functions (PSFs). Cartesian coordinates of each point are given under it. The coordinates are calculated from the center of the metasurface layer 1. **b** The normalized PSFs at the image plane for TE polarization of the optical system shown in Fig. 2.A.1**e**. The coordinates under the PSFs are the coordinates of the corresponding point sources. It is assumed that the PSFs are identical for TE and TM polarizations. **c** The magnified intensity maps of the normalized PSFs in **b**. The coordinates of the corresponding point sources are shown above the intensity maps. The dashed black circles are airy disks whose radii are 2.54 μm at the image plane. All coordinates in the figures are given in microns.

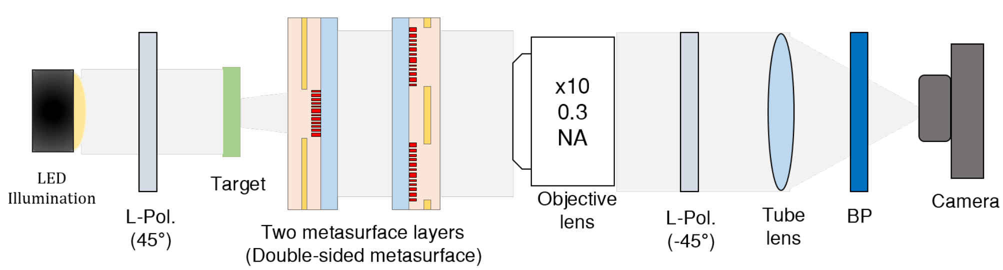

Figure 2.A.6: **Schematic of the measurement setup.** Schematics of the custom-built microscope setup used to measure the three DIC images captured by the QPGMs. L-Pol.: linear polarizer; BP: band-pass filter.

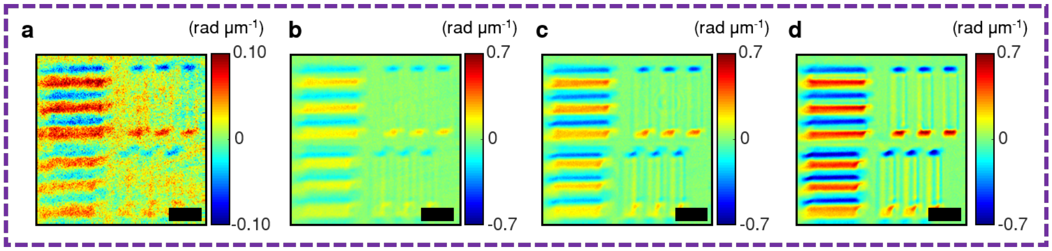

Figure 2.A.7: **Magnified PGIs of the phase resolution targets having different thicknesses.** The thicknesses of the targets are as follows; **a**: 54 nm; **b**: 159 nm; **c**: 261 nm; and **d**: 371 nm. Note that the color bar scale in **a** is different from the other panels. Scale bars: 15 μm.

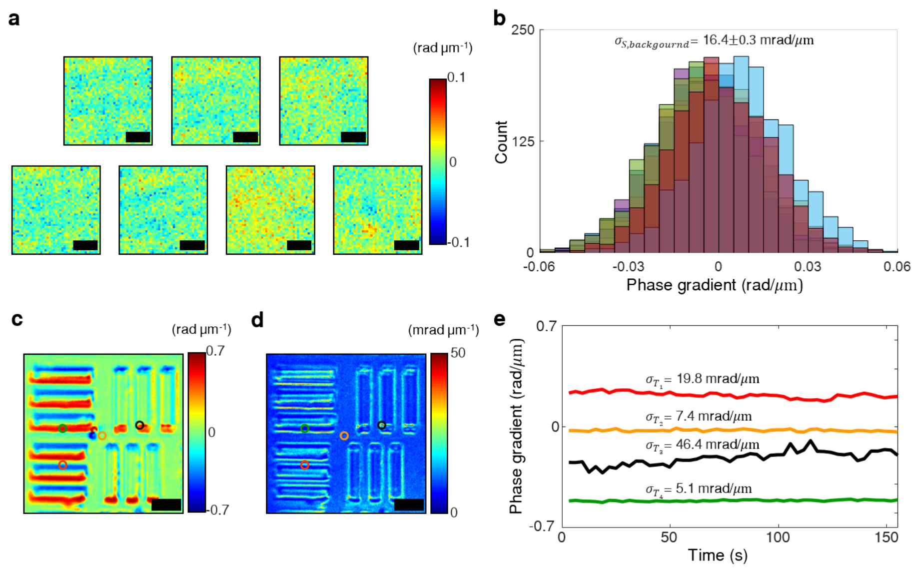

Figure 2.A.8: **Measurement of spatial and temporal noise levels.** **a** Background phase gradient images captured in an area with dimensions of 17.6×17.6 μm^2 in the central part of the seven different measurements with the seven different phase resolution targets used in Fig. 3d. Scale bars: 5 μm. **b** Phase gradient histograms of the phase gradient images in **a**. Each image in a has 1681 points. The spatial noise level is 16.4±0.3 mrad/μm calculated by measuring the standard deviation of the phase gradients in **b**. **c** and **d** The 371-nm thick resolution target used in Fig. 2.A.7**d** is measured 50 times during 155 seconds. **c** The first phase gradient image at t = 3.1s. **d** Map of the standard deviations over 50 frames. The average standard deviation over the map is 11.4 mrad/μm. **e** Plots of the temporal phase gradient signals at the different points marked with red, orange, black and green circles in **c** and **d**. The colors of the plots are matched with the colors of the circles in **c** and **d**. The corresponding standard variations are noted over the plots. Especially, the black line shows the maximum fluctuation having a standard deviation of 46.4 mrad/μm in the map.

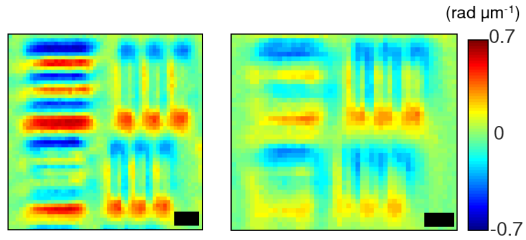

Figure 2.A.9: **Investigation of the lateral resolution.** PGIs of the smallest resolution groups that the QPGM based on the two separate metasurface layers was able to resolve. The measured lateral resolutions along the x and y directions are 2.76 μm and 3.48 μm, respectively. The thickness of the resolution target is 374 nm. Left: elements 2 and 3 in group 8; Right: elements 4 and 5 in group 8. Scale bars: 2 μm.

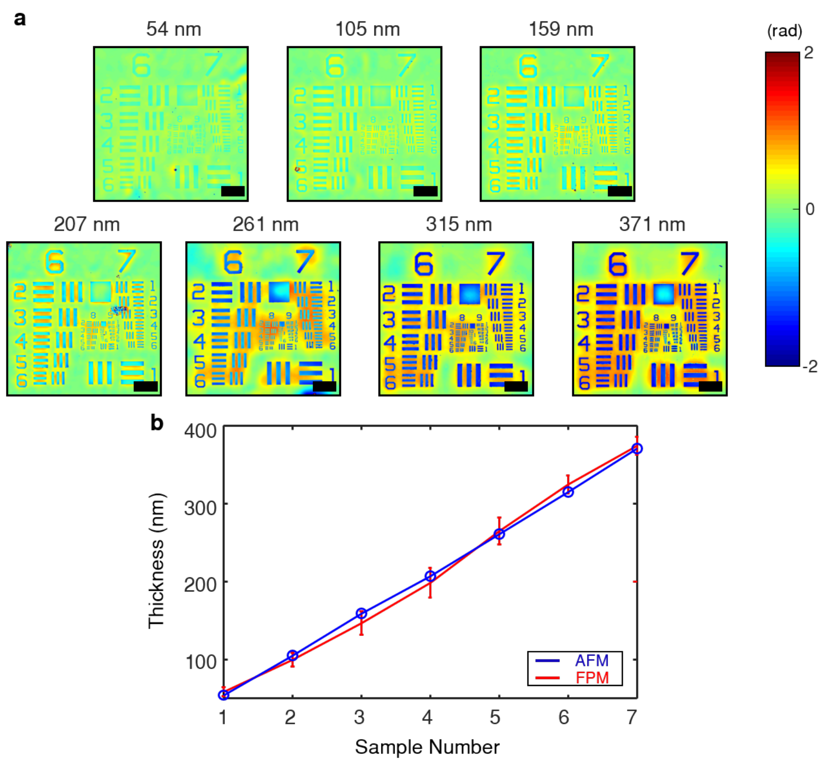

Figure 2.A.10: **Phase maps of the USAF 1951 phase resolution targets measured by Fourier ptychography.** **a** Measured phase maps of the seven USAF 1951 phase resolution targets through the Fourier ptychography method (FPM). An array of green LEDs with an operation wavelength of 522 nm was utilized for Fourier ptychography. Scale bars: 40 μm. **b** Thicknesses of seven different parts of the phase target calculated from the phase maps captured by Fourier ptychography (red), and those measured by AFM (blue). The plotted estimated height values through Fourier ptychography are averaged over 100 arbitrarily chosen points. Error bars represent standard deviations of the estimated values.

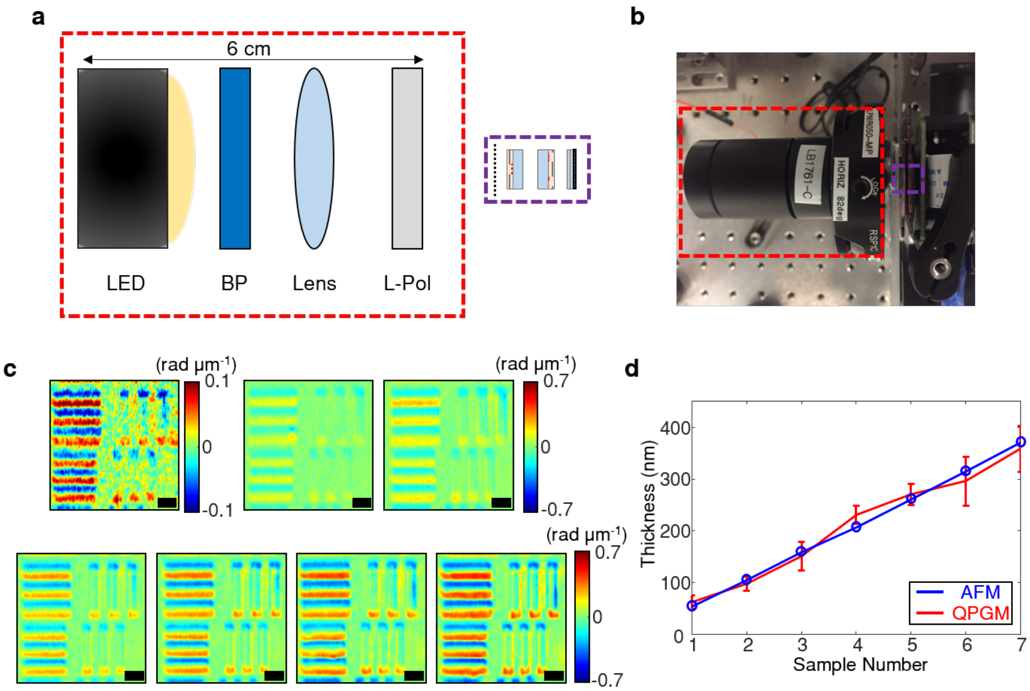

Figure 2.A.11: **Compact QPGM setup and measurement results using a CMOS image sensor.** **a** Schematics of the custom-built miniaturized microscope setup using a CMOS image sensor. The red and purple dashed boxes illustrate the illumination and detection parts of the setup, respectively. The magnified schematic of the detection part is shown in Fig. **3f**. L-Pol.: linear polarizer; BP: band-pass filter. **b** Optical image of the setup in **a**. The illumination and detection parts are represented by the red and purple dashed boxes, respectively. **c** Phase gradient images captured for the same parts of the phase target used in Figs. 3c and S7. The thicknesses of the three targets from top left to top right and the four targets from bottom left to bottom right are as follows: Top: 54 nm; 105nm; and 159 nm. Bottom: 207 nm; 261 nm; 314 nm; and 371 nm. Note that the color bar scale for the thinnest sample is different from the other panels. Scale bars: 15 μm. **d** Thicknesses of the phase targets calculated from the PGIs in **c** and those measured by AFM. The plotted estimated thickness values through QPGM are averaged over 100 arbitrarily chosen points at the sample edges. Error bars represent standard deviations of the estimated values.

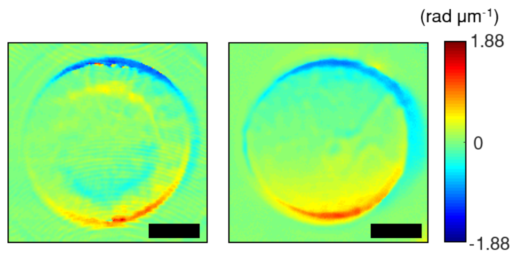

Figure 2.A.12: **PGIs of the sea urchin samples captured by the doublet QPGM.** PGIs of two sea urchin samples measured using the double-sided metasurface QPGM shown in Fig. **4b** of the main text. Scale bars: 25 μm.

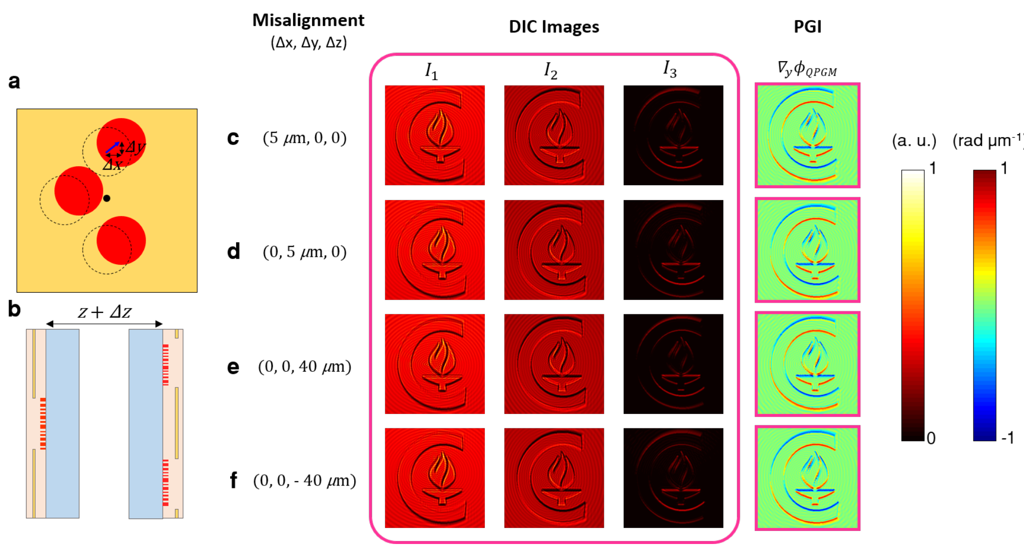

Figure 2.A.13: **Numerical investigation of the effects of misalignment between the two metasurface layers. a** Schematic illustration of the top view of the metasurface layer 2. The lateral misalignments along x and y directions, Δx and Δy, are shown. **b** Schematic illustration of the side view of the QPGM. The axial misalignment along the z axis, Δz, is shown. We assumed that the thicknesses of the two substrates is identically changed by $\frac{\Delta z}{2}$. **c-f** Simulated DIC images and PGIs for four different types of misalignment. In simulation, the QPGM is based on the system shown in Fig.2.A.1**e** with the phase profile parameters given in Table 2.A.1. Left: misalignment vectors, (Δx, Δy, Δz). Center: three different DIC images at the image plane corresponding to misalignment vectors shown on the left. Right: PGIs calculated from the DIC images at the center. For calibration, we subtract the PGI calculated in the absence of the sample with each misalignment from the PGI calculated from the three DIC images at the center.

Chapter 3

COMPUTATIONAL COMPLEX OPTICAL FIELD IMAGING USING A DESIGNED METASURFACE DIFFUSER

The material in this Chapter was in part presented in [101].

In this section, we experimentally demonstrate a computational imaging system with the ability to retrieve complex field values using a metasurface diffuser (MD) and the speckle-correlation scattering matrix method. We explore the mathematical properties of the MD transmission matrix such as its correlation and singular value spectrum to expand the understanding about both MDs and the speckle-correlation scattering matrix approach. In addition to a large noise tolerance, reliable reproducibility, and robustness against misalignments, using the MD allows for substituting the laborious experimental characterization procedure of the conventional scattering media (CSM) with a simple simulation process. Moreover, dielectric MDs with identical scattering properties can easily be mass-produced, thus enabling real world applications. Representing the first bridge between metasurface optics and speckle-based computational imaging, this work paves the way to extend the potentials of diverse speckle-based computational imaging methods for various applications such as biomedical imaging, holography, and optical encryption.

3.1 Introduction

Imaging through scattering media is one of the most challenging problems in optics, as the passage of coherent light through scatterers leads to complicated speckle patterns. Various methods for imaging objects through scattering media, such as optical coherence tomography [102], wavefront engineering [103], speckle correlation based on the memory effect [104, 105], and the transmission matrix [106], have been reported.

In the past few years, various computational techniques that retrieve hidden information from changes in complicated speckle patterns have been proposed [104, 107–122]. These speckle-based computational imaging techniques, which utilize the benefits of scattering instead of considering it an obstacle, have unique merits in capturing various types of hidden information that are otherwise challenging to obtain with conventional imaging systems, or require a higher degree of complexity in the optical system. For example, progress has been made toward developing diverse speckle-based computational imaging techniques for retrieving depth or three-dimensional information. These techniques include phase-space measurements [107, 108], speckle holography with a reference point source [109], compressed sensing techniques with speckle patterns [110, 111], deconvolution with the manipulated point spread function based on the memory effect [112], the speckle-correlation scattering matrix (SSM) [113, 114], and wavefront sensing with the Demon algorithm [104]. Based on the spectral decorrelation characteristics of the speckle pattern, various methods to retrieve spectral information have also been explored [115–118]. Moreover, speckle-based computational imaging methods allow for retrieval of more diverse information about the light, such as its polarization [119] or orbital angular momentum [120], and also can lead to retrieval of images with enhanced resolution [121, 122].

In particular, the SSM method has recently been proposed to enable complex field measurements without a reference signal [113, 114, 119, 120]. However, the previous works focus only on the optical methods or computational aspects, leaving out the scattering medium as an integral part of the scheme. Similarly to other scattering-based techniques, the use of conventional scattering media (CSM) has many drawbacks that significantly limit the potential of this technique for real applications. For example, the instability of the optical properties [123], the fluctuation in transmittance of diffusive CSM [124], and the trade-off between memory-effect range and maximum scattering angular range [125] could be critical drawbacks from a practical point of view. Most important, the cumbersome experimental characterization procedure that should be individually repeated for every scattering medium is an important barrier that will be extremely challenging to overcome if systems employing such techniques are to be mass-produced and commercialized.

Optical metasurfaces, composed of nano-scatterers or meta-atoms, can manipulate the phase, amplitude, and polarization of light at subwavelength scales [3–7]. Various conventional optical components [23, 27, 28, 126, 127] as well as newer optical devices [79, 128] have already been demonstrated using metasurfaces. In addition, concepts of computational optics with metasurfaces were recently proposed in the context of full-color imaging [129] and optical encryption [130]. Moreover, several investigations about the statistical or physical properties of random metasurfaces, such as the far-field response [131, 132] or the random Rashba effect [133], have been reported. Recently, the concept of the metasurface diffuser (MD) was also proposed for wavefront control with a spatial light modulator, demonstrating wide field of view (FOV) and high-resolution bio-imaging [125]. However, the investigation focused on wavefront shaping rather than computational imaging based on the properties of the speckle patterns.

Here we propose the use of designed MDs that replace CSMs for the purpose of complex field and three-dimensional imaging. The performance of the complex field imager is demonstrated in both simulation and experiment. In particular, measurements of amplitude samples and holographic imaging with numerical backpropagation verify the MD's capability for complex field retrieval with real objects. In addition, several benefits of the MD such as replacing the laborious characterization procedure of the CSM with a significantly simpler simulation process, reproducibility, stability, high noise tolerance, and robustness against misalignments are also demonstrated and discussed. Moreover, we explore the mathematical properties of the transmission matrix (T), such as the correlation between its columns and the randomness of its entries indicated by the singular value spectrum. These properties give important insight into the optical properties of the MD as a scattering medium and clarify the required operating conditions of the SSM method.

3.2 Metasurface diffuser design

Figure 3.1 schematically illustrates the concept of the MD-based complex field imager. Light from the object is scattered by the MD and leads to a speckle pattern that is captured by an image sensor. Using the computed T matrix of the designed MD and the captured intensity of the speckle pattern, the complex fields of the object can be retrieved. The MD works as a cross-polarized random phased array that scatters light with greater efficiency than amplitude masks, which are widely used in compressed sensing schemes [134–136]. In other words, the MD is designed to operate as a half-wave plate (HWP), and at the same time to scatter light uniformly.

The MD, schematically shown in Fig. 3.2**a**, is composed of high-contrast birefringent amorphous silicon (α-Si) meta-atoms [13]. The meta-atoms are 652 nm tall and rest on a square lattice with a lattice constant of 500 nm. The design wavelength is 850 nm. The meta-atoms shown in Fig. 3.2**b** have rectangular cross sections with side lengths D_x and D_y along the x and y axes, respectively. With proper design, the meta-atoms provide independent 2π phase coverage for x- and y-polarized light. The meta-atom side lengths versus the phase delays for two orthogonal polarizations (ϕ_x and ϕ_y) are plotted in Fig. 3.2**c** (see Appendix S1 and Fig. 3.A.1 for details of

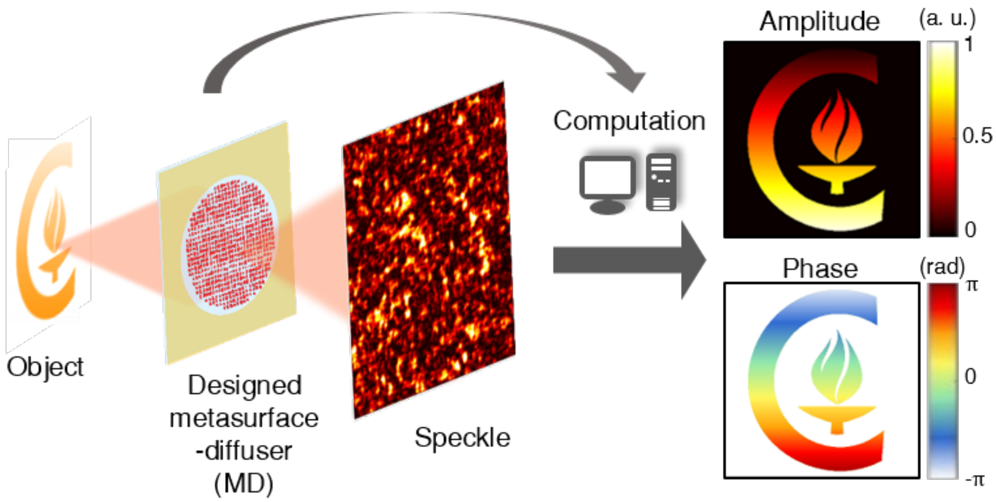

Figure 3.1: **Schematic illustration of computational complex field retrieval using a designed MD** Light from the object is scattered by the metasurface, resulting in a speckle pattern. The known phase profile of the MD is then used in a computational procedure based on the SSM method to retrieve the complex fields of the object from the captured speckle pattern.

the simulation results, design, and fabrication).

To suppress the power of the unscattered light after the MD (which is inevitable due to the finite scattering efficiency and fabrication imperfections), we designed and used the MD in a cross-polarized configuration. To this end, each meta-atom operates as a HWP whose optical axis makes a 45 deg angle with the x and y directions [Fig. 3.2**a**, right]. As a result, the x-polarized input light will be scattered to the y-polarized output. The unscattered light is then rejected using a linear polarizer. We should note here that this is an important additional benefit of the capabilities of MDs, not achievable with CSM.

In the MD design process, the data in Fig. 3.2**c** act as a lookup table, with the dashed black lines corresponding to the HWP meta-atoms. Similarly to other local dielectric metasurfaces, the MD acts as a phase mask characterized by a two-dimensional complex transmission function. In order for the MD to scatter light isotropically, we designed the phase mask to have uniform amplitude in the Fourier domain. As shown in the simulation results in Fig. 3.2**d**, the numerical aperture of the MD is set to 0.6, which means that it scatters light to a maximum angle of ~37 deg. The Gerchberg–Saxton (GS) algorithm [137–139] is used to design the phase profile of the diffuser (see Appendix for details). An optical image of an array

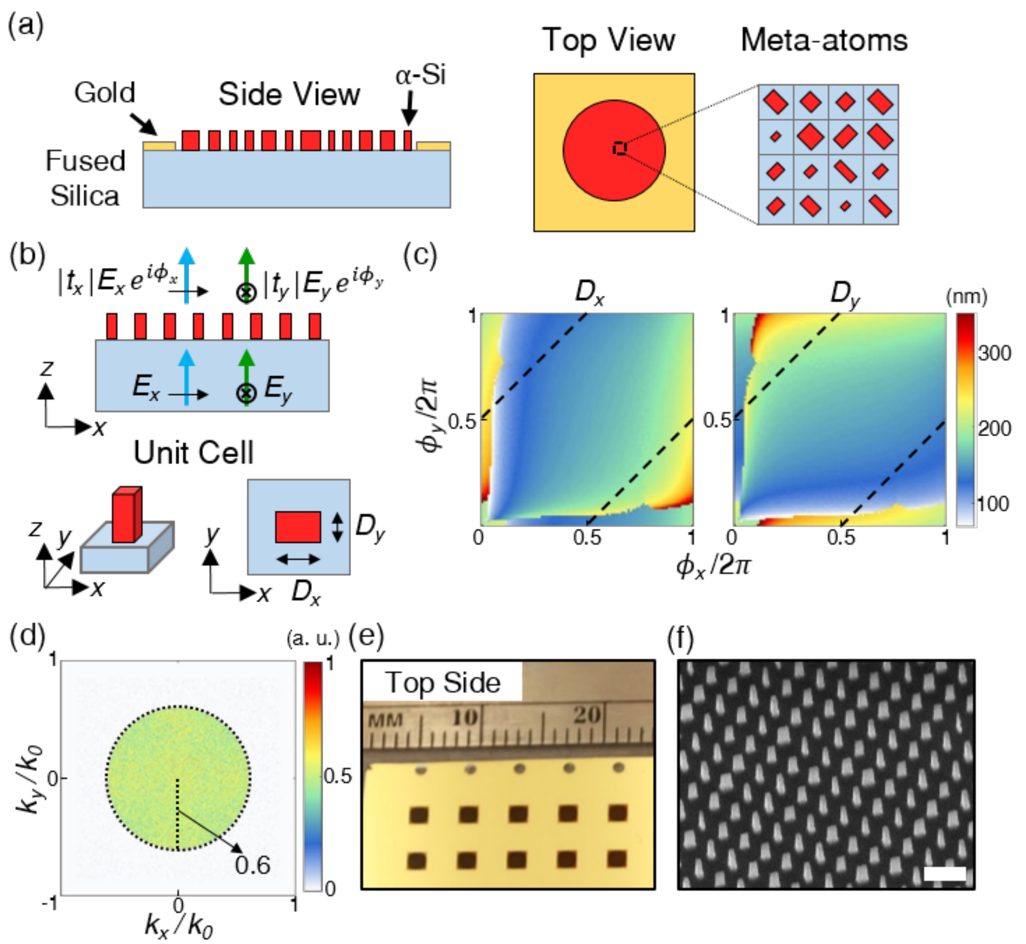

Figure 3.2: **MD structure and design. a** Schematic illustration of the side and top views of the MD. The α-Si meta-atoms are arranged in a square lattice on a fused silica substrate. A gold layer is deposited to block the light outside the diffuser aperture. **b** Schematics of a uniform array (top) and a unit cell of the metasurface (bottom), showing the parameter definitions. The transmission phase of the two orthogonal polarizations can be manipulated using the meta-atoms. **c** Calculated in-plane dimensions of the meta-atoms (D_x and D_y) as functions of the required transmission phases for x- and y-polarized light (ϕ_x and ϕ_y, respectively). The black dashed lines show the meta-atoms that work as a half-wave plate (i.e., $|\phi_x - \phi_y| = \pi$). **d** Calculated amplitude of the Fourier transform of the MD's phase mask. **e** Optical image of the fabricated MD array. **f** Bird's-eye-view scanning electron microscope image of a portion of the metasurface. The scale bar is 1 μm.

of fabricated MDs, each 1.6 mm in diameter, is shown in Fig. 3.2**e**. A scanning electron microscope image of the meta-atoms is shown in Fig. 3.2**f**. Moreover, a gold aperture is deposited around the MDs to block the unwanted light to increase the signal-to-noise ratio (SNR).

3.3 Theory and simulation results

Theory

In linear optical systems, the T matrix can describe the relationship between an input field (x) and an output field (y) through a linear equation, $y = Tx$. In this section, the properties of the T matrix of the MD are explored for two reasons. First, knowing T is a prerequisite of the SSM method, which we utilized to directly retrieve the input complex field x from the output intensity of the speckle pattern, y^*y. Second, the mathematical properties of T can be utilized not only for better characterization of the MD as a scattering medium, but also to improve our understanding of the operating conditions of the SSM method.

To compute the T matrix, we performed a numerical study using the designed MD phase mask and the wave propagation method (see Appendix and Fig. 3.A.2 for the detailed procedure and the flow graph showing the computation of T). To limit the matrix dimensions and make the calculations manageable in a regular workstation, we limited the input and output space. At the input plane, we limited the object to a 60×60 array of 2.5 μm pixels. For each input pixel, the field is then calculated at the output space. After downsampling the output field to compensate for the oversampling caused by the microscope magnification, the effective output space in our system becomes a 210×210 array of 1.06 μm pixels (see Appendix for details). Each input/output pixel corresponds to an input/output mode. Therefore, this choice sets the number of input and output modes, N and M, at 3600 and 44,100, respectively. The simulated amplitude and phase of the speckle patterns on the output space for the 1st, 2nd, and Nth input modes are shown in Fig. 3.3**a**.

The calculated complex speckle pattern for the ith input mode, t_i, can be written as an M $\times$ 1 vector. This vector then constitutes the ith column of T, which is an M $\times$ N matrix. The SSM, Z, is then computed from T and the intensity of the speckle pattern resulting from a certain object, y^*y,

$$Z_{ij} = \frac{1}{\sum_i \sum_j} [< t_i^* t_j y^* y > - < t_i^* t_j >< y^* y >], \tag{3.1}$$

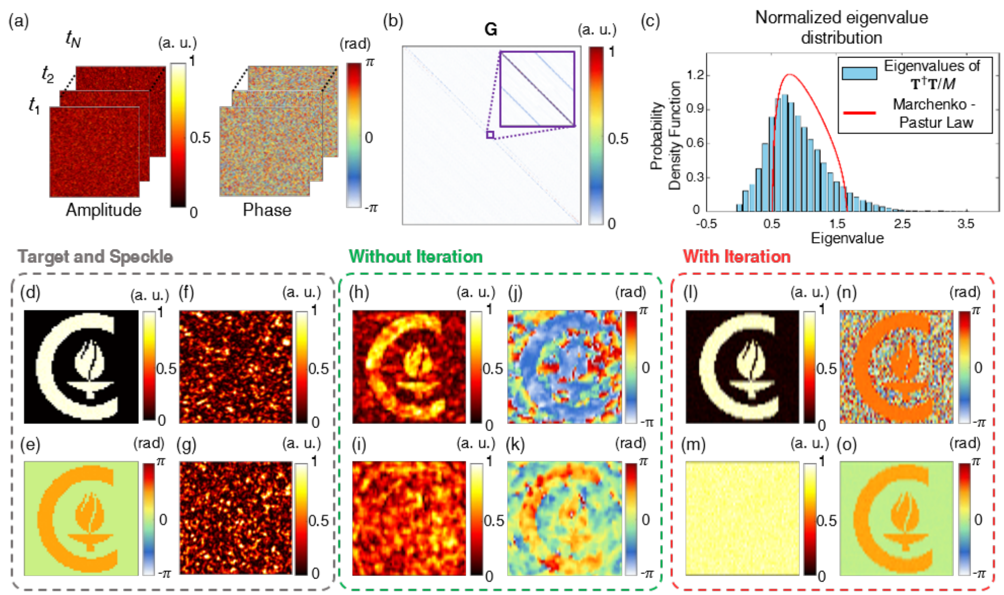

Figure 3.3: **Numerical investigation of the ability of the MD to retrieve complex fields.** **a** Simulated speckle amplitudes and phases for sample input modes, which are then shaped as complex M $\times$ 1 vectors and form the columns of T. **b** The G matrix formed from the inner product mapping of the normalized vectors of T. G_{ij} represents the absolute value of the inner product of normalized t_i and t_j. The 130 $\times$ 130 elements located at the center of G are magnified in the inset. **c** Eigenvalue distribution of the $T^{\dagger}T/M$ matrix. The solid red line is the Marchenko-Pastur law prediction for a random M $\times$ N matrix. **d**, **e** The sample amplitude and phase objects. **f**, **g** Simulated speckle patterns of the amplitude and phase objects. **h–k** Amplitude and phase maps of the initially retrieved complex fields. **h**, **j** Amplitude object. **i**, **k** Retrieved fields for the phase object. **l–o** Amplitude and phase maps of the retrieved complex fields after 20 iterations.

using [113] where $< \cdot >$ indicates spatial averaging and $\sum_p =< |t_p|^2 >$. Z plays a key role in the complex field retrieval if three conditions are met. First, the M/N ratio, denoted by γ, should be much larger than 1. In this case, the rank of Z becomes one and its eigenvector forms the initial retrieved complex field. In our case γ is 12.25, which is sufficiently larger than 1, as our system performs well in both simulation and experiment. If a system works well with a low γ, it is beneficial in terms of computational cost and performance. That is because a low γ means a wide FOV for a fixed M (i.e., higher performance) or a small-sized T matrix for a fixed N (i.e., less computation required).

Second, the columns of T should be orthogonal to each other (i.e., the speckle patterns for different input modes should be uncorrelated). To investigate the orthogonality, we formed a symmetric matrix G whose elements are the correlation of normalized columns of T ($G_{ij} =< t_i^* t_j > / \sum_i \sum_j$). The elements of G are plotted in Fig. 3.3**b**, which shows an approximately diagonal matrix with all diagonal elements equal to 1. There are some nonzero off-diagonal elements (with values close to 0.18) corresponding to the speckle field–field correlation between neighboring input modes [140, 141]. The correlation drops quickly to negligible amounts for input modes that are farther apart (see Fig. 3.A.3 for details about the correlation between the columns of T). The almost uncorrelated columns of T could be explained by the fact that the MD is a subwavelength-thick diffractive layer with a high scattering power. Also, computing the T matrix avoids additional correlation caused by any type of noise during the experimental characterization procedure. From an engineering viewpoint, it is possible to design the MDs to minimize the correlation between columns of T for given optical setup conditions. This could be a key advantage of the MD for the purpose of various speckle-based imaging methods based on the T matrix [106, 140]. Nevertheless, as the following numerical and experimental results show, the achieved level of orthogonality works well for the field retrieval. It is also worth noting here that even if the vectors (t_i and t_j) are not orthogonal, one can in principle form and use an orthogonal basis with them using the Gram–Schmidt process [see Figs. 3.A.4**a** and 3.A.4**b** for details].

As the third condition for accurate complex field retrieval, the MD should be designed to scatter light in random directions. To investigate the randomness more rigorously, an eigenvalue analysis of $T^\dagger T/M$ was performed, where † denotes the conjugate transpose. It has previously been shown that because of multiple scattering, the distribution of the normalized singular value spectrum of the square T matrix of a thick CSM follows a quartercircle law, which is a special case of the Marchenko–Pastur law [140, 142, 143]. As shown in Fig. 3.3**c**, the distribution of the normalized eigenvalues of $T^\dagger T/M$ for the MD deviates from the Marchenko Pastur law, indicating dependence between the entries of T [141, 144]. This is because unlike with a thick CSM, the MD consists of a single layer of scatterers. Also, the dependence between the entries is consistent with a large memory-effect range for the MD [125]. However, our experimental and numerical results verify that this level of randomness is enough to implement the SSM method.

Simulation Results

To numerically investigate the operation of the MD, we performed simulations using amplitude and phase samples. Figures 3.3**d** and 3.3**e** show sample amplitude and phase objects, respectively, along with their corresponding simulated speckle patterns [Figs. 3.3**f** and 3.3**g**, respectively]. Using the speckle patterns and the precalculated T matrix, the Z matrix is calculated for each speckle pattern. The first estimate of the complex field is the eigenvector of Z corresponding to the eigenvalue with the largest absolute value. The amplitude and phase of these initial estimated fields are shown in Figs. 3.3**h** and 3.3**j**, respectively, for the amplitude object in Fig. 3.3**d**, and in Figs. 3.3**i** and 3.3**k** for the phase object in Fig. 3(e). An iteration method based on the modified GS algorithm (originally proposed by Lee and Park [113]) is then applied to improve the SNR (see Appendix for the detailed computational procedure). The results after 20 iterations are shown in Figs. 3.3**l**– 3.3**o**, demonstrating the ability of the MD to retrieve the complex fields very accurately. Furthermore, to investigate the effects of the orthogonality between the columns of T, we also performed the complex field retrieval of the same amplitude and phase targets with the transmission matrix modified through the Gram–Schmidt process (T_{GRAM}). We could not discern any noticeable difference between the fields retrieved using either matrix, and therefore we conclude that the achieved level of orthogonality is high enough to allow near-ideal operation of the SSM method [see Figs. 3.A.4**c**– 3.A.4**f** for details]. The iteration process converged quickly, showing negligible changes after 20 iterations. Therefore, we used the same number of iterations (20) in the experimental studies as well. On average, calculating the initial retrieved fields and performing the 20 iterations takes less than 30 s in total on our workstation (Intel Xeon E5-2640 CPU; 96.0 Gbytes RAM). Most of the computation time is consumed by multiplication of the large matrices, and thus we expect that the time would significantly decrease with parallel computing.

3.4 Experimental complex field retrieval with amplitude targets

To experimentally test the MD and the method, we use two different parts of the 1951 USAF resolution test target as amplitude objects in the measurement setup shown in Fig. 3.A.5**a**. Figures 3.4**a** and 3.4**b** show images of the amplitude objects captured using the conventional microscope (i.e., with the MD and the polarizers removed). The speckle patterns generated by the objects through the MD are plotted in Figs. 3.4**c** and 3.4**d**. Then, proper downsampling of the speckle pattern is performed to compensate the oversampling caused by the microscope magnification and image sensor pixel size. The Z matrix can then be computed via Eq. 3.1 using the downsampled speckle intensity patterns and the precalculated T matrix. The retrieved amplitudes and phases of the two amplitude objects are shown in

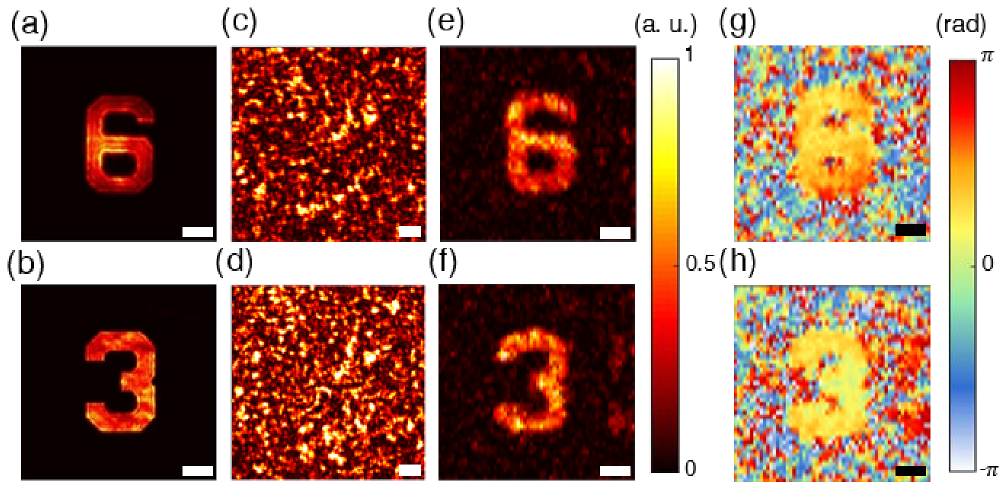

Figure 3.4: **Experimental retrieval of amplitude objects. a**, **b** in-focus images of targets captured by a custom-built microscope; **c**, **d** The resulting speckle patterns of the samples after passing through the MD; **e**, **f** The retrieved object amplitudes; **g**, **h** phases from the captured speckle patterns. The scale bars are 25 μm.

Figs. 3.4**e**– 3.4**h** after 20 iterations [see Figs. 3.A.5**b** and 3.A.5**c** for the retrieved fields before performing iterations].

Unlike with CSM, changing the measurement setup or the input/output mode conditions (distances, pixel sizes and numbers, etc.) does not require the MD to be characterized again. Instead, the new T matrix is calculated using the designed phase mask and the new conditions. To examine the reproducibility of the results under such changes, further measurements were performed with different distances and pixel sizes. We were able to reproduce the results under various conditions by just updating the T matrix accordingly (see Fig. 3.A.6 for details). Moreover, the retrieval process is successful despite the experimental noise. To show the effect of a large γ, we also performed the complex field retrieval for a γ value of 69.4. The large γ results in improved accuracy of the initial retrievals and retrievals after 20 iterations, as well as in an increased computation time from 30 s to 3 min on average (see Fig. 3.A.7 for details). In addition, the optical properties of the MD are stable over time, and no noticeable change was observed in more than five months. It is also worth noting here that a thin linear polarizer and a compact image sensor can replace the custom-built microscope for miniaturization.

3.5 Numerical noise tolerance analysis

We performed a numerical noise tolerance study using the computed T matrix of the MD. Various intensity noises with a Gaussian distribution and different energies were added numerically to the simulated and measured speckle intensity patterns to adjust the SNR. We focused on incoherent intensity noise, because the employed cross-polarized scheme cuts almost all of the coherent noise from the laser. The results of the noise tolerance study are summarized in Fig. 3.5. First, we investigated the noise tolerance with the calculated speckle intensity patterns. The initially retrieved fields for various SNR values are plotted in Figs. 3.5**a** and 3.5**b** for an amplitude object, and Figs. 3.5**c** and 3.5**d** for a phase object. The retrieval process works for SNR values greater than 1, and the initially retrieved fields look almost identical for SNR values larger than 5.

Figures 3.5**e**– 3.5**h** show the retrieved fields after 20 iterations. As expected, the retrieval accuracy improves as the SNR value increases. The same analysis can be performed using the measured speckle patterns. To this end, the Gaussian intensity noise was numerically added to the experimentally measured speckle pattern shown in Fig. 3.4**c**. We should note here that the actual SNR value of the noisy speckle pattern is less than the numerically controlled SNR, since the measured speckle pattern already includes the measurement noise and errors arising from imperfections in the fabricated MD. The results shown in Figs. 3.5**i**– 3.5**l** are comparable to the amplitude target shown in Fig. 3.4**a**. If the SNR is less than 1, it is better to avoid iterations, since the iteration process automatically assumes a high SNR in the speckle pattern.

It is worth noting the differences between the noise tolerance analysis in this work and the study performed by Lee and Park [113]. Here, we used the computed transfer matrix of the actual MD instead of the randomly generated complex matrix used in [113]. The randomly generated transfer matrix has almost perfectly uncorrelated columns, and its corresponding eigenvalue spectrum follows the Marchenko–Pastur law (i.e., it is almost ideal for the SSM method). Nevertheless, our results for the MD show better noise tolerance and similar retrieval performance in comparison to the randomly generated transfer matrix (see Section S2 and Fig. 3.A.8 for details). In addition, here the noise tolerance was investigated using both simulated and measured speckle patterns, and we observed that the complex fields can be retrieved in both cases, even for a low γ value of 12.25 and an SNR value as low as 1.

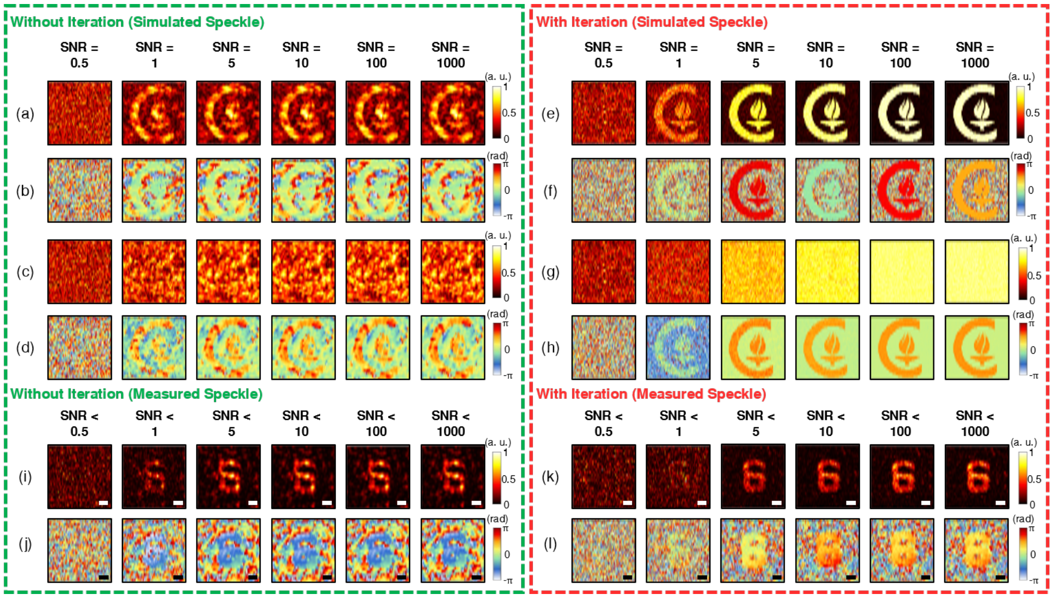

Figure 3.5: **Numerical noise tolerance analysis.** **a–d** Retrieved amplitudes and phases for the amplitude and phase objects in Figs. 3.3**d** and 3.3**e** for SNR values from 0.5 to 1000. A Gaussian noise is added to the simulated speckle patterns to test the noise tolerance. **e–h** Reconstructed objects after performing 20 iterations of the GS algorithm using the results in **a–d** as initial points. **i**, **j** Retrieved intensity and phase maps for the object shown in Fig. 3.4**a** when changing the SNR from 0.5 to 1000. A Gaussian noise is added to the measured speckle pattern shown in Fig. 3.4**c**. **k**, **l** Reconstructed intensity and phase maps after conducting 20 iterations of the GS algorithm using **i** and **j**. The scale bars in **i–l** are 25 μm.

3.6 Holographic imaging experiment and numerical analysis of robustness against misalignment

To further demonstrate the ability of the MD and the method to retrieve complex fields, we performed holographic imaging experiments. To this end, the complex fields are retrieved at a 150 μm aperture behind the MD [Fig. 3.6**a**]. The fields are then numerically backpropagated to the desired distance to reconstruct the object behind the aperture. We imaged several target objects at different distances from the aperture, as shown in Fig. 3.6**a**. The reconstructed objects are shown in Figs. 3.6**b** and 3.6**c** for different targets and distances. For comparison, we also imaged the objects through the same aperture using the microscope shown in Fig. 3.6**d**. The results are plotted in Figs. 3.6**e** and 3.6**f**, showing good agreement with the MD results. The retrieved complex fields for all images at the aperture are shown in Fig. 3.A.9. In both Figs. 3.6**c** and 3.6**f**, the image resolution decreases as the object distance to the aperture increases. This is due to the smaller effective NA of the

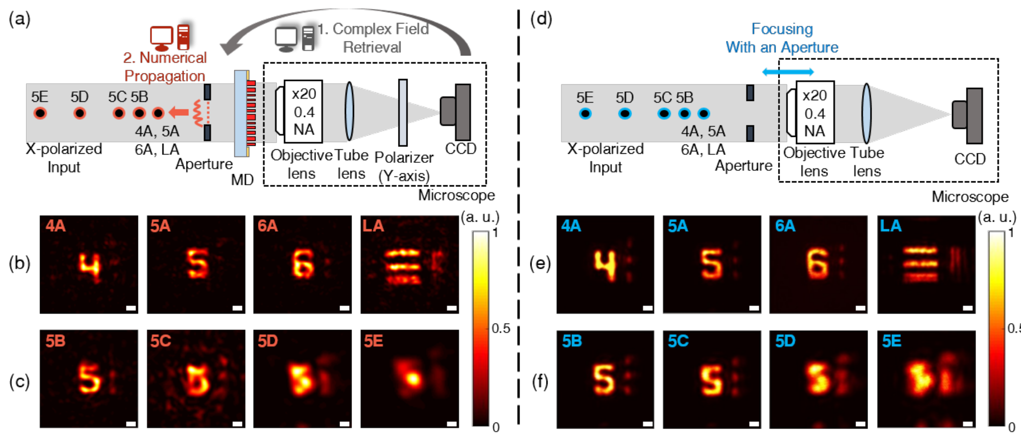

Figure 3.6: **Experimental results of complex field retrieval for holographic imaging. a** Schematic drawing of the measurement setup showing the computational steps. The complex field is retrieved at the 150 μm aperture using the captured speckle pattern. The field is then backpropagated to reconstruct the object at different distances from the aperture. **b** Reconstructed images for different objects at point A. **c** Reconstructed images for a target shaped like the number 5 at different distances from the aperture. **d** Schematic drawing of a microscope setup that images the target through the same aperture for comparison. **e** Captured in-focus images with the microscope for the same objects as in **b**. **f** Captured in-focus images with the microscope for the same object and distances as in **c**. The distances between the points and the aperture are as follows: A, 1.5 mm; B, 2 mm; C, 2.5 mm; D, 3.5 mm; and E, 4.5 mm The scale bars are 25 μm.

system in imaging farther objects as the aperture diameter is kept constant. We also numerically investigated the performance of the MD and the method under axial and transverse misalignments. Not only is the method robust to the MD displacement in the axial and transverse directions, but also some misalignments can be corrected or exploited in the alignment of the optical system (see Section S3 and Fig. 3.A.10 for details).

3.7 Discussion and conclusion

In summary, we demonstrated computational complex field imaging using dielectric MDs. We investigated the mathematical properties of the T matrix of the MD and demonstrated its performance as a scattering medium in the SSM method. In addition, we discussed the advantages of MDs for computational imaging over the CSM. A key benefit is the replacement of the difficult and time-consuming characterization process with a single simulation. The MD provides reliable reproducibility, long-term stability, high noise tolerance even for small γ values, and robustness against misalignments. CSM usually suffer from the trade-off between the light efficiency and maximum scattering angle, because both are highly dependent on the thickness of the CSM. In contrast, the MD can achieve high transmission and a large maximum scattering angle at the same time. This could be a noteworthy property for future investigations based on the MDs. Another important property of the MDs is the possibility of massproducing designed MDs with almost identical optical properties. Avoiding the required case-by-case characterization could be a key factor in applying scattering-medium-based computational imaging techniques in real-life applications.

Similarly to some other lensless techniques, speckle-based computational imaging systems can overcome some of the limits of conventional lens-based imaging systems, such as the trade-off between resolution and FOV [145]. In addition, it is worth noting that the lensless imaging systems inherently suffer less from various monochromatic and chromatic optical aberrations, which are major challenges faced by metasurface lenses [14, 15, 78, 146–149]. Even though the relatively heavy computational load is generally one of the main drawbacks for computational imaging systems, recent investigations based on deep learning have shown not only a significant decrease in the computational load but also improved imaging performance [150–152].

This work can be extended to various existing speckle-based computational optics schemes and may be beneficial for a diverse set of applications. For example, endoscopes for *in-vivo* quantitative phase imaging can be realized by using the MD and thin linear polarizers in existing image-sensor-based endoscopes with a laser light source [59, 62, 153]. Due to the compactness of the MD and its compatibility with semiconductor fabrication processes, it might be possible to integrate the MD-based holographic camera into smartphones or other electronic devices for the purpose of point-of-care diagnostics [154] and holography [155]. Furthermore, we expect that the versatile metasurface platform, which enables scattering media with tailored properties, can be exploited for speckle-based optical encryption [156, 157].

3.8 Methods

Simulation and design

The transmitted amplitude and phase of the meta-atoms with normally incident light were calculated using the rigorous coupled wave analysis technique [95]. The α-Si meta-atoms were 652 nm tall, and the square lattice constant was 500 nm. Given the high numerical aperture of the designed MD, a smaller lattice constant could be used to increase the scattering efficiency and reduce unwanted diffraction into the substrate [39]. Refractive indices of α-Si and fused silica for the operating wavelength of 850 nm in the simulation were 3.56 and 1.44, respectively. Side lengths of the meta-atoms, D_x and D_y, were varied in the simulation to achieve independent phase control to cover the full 2π range for x and y polarizations. Figures 3.A.1**b** and 3.A.1**c** show transmittance and transmission phase for both polarizations for a periodic array of the meta-atoms as functions of D_x and D_y. Then, we optimized D_x and D_y as functions of ϕ_x and ϕ_y [Fig. 3.2**c** of the main text] to provide high transmission and the desired phase shifts. Since the MD is designed to operate in cross-polarization mode, only meta-atoms operating as HWPs are required (corresponding to the dashed black lines in Fig. 3.A.1**a** and main text Fig. 3.2**c**). The meta-atoms are rotated 45 degrees (with respect to the x and y axes) to change the state of polarization from horizontal to vertical, and modulate the phase through the method explained in the supplementary material of Ref. [13].

Design of the phase profile of the MD

To design the phase profile of the MD, the GS algorithm was exploited [125, 137]. We performed 100 repetitions to get the phase profile of the MD. The initial phase profile was determined by random number generation with a uniform distribution in the 0-2π range. Each repetition process consists of four steps. First, the Fourier transform of the phase profile is calculated. Second, the amplitude in the Fourier domain is updated to be uniform inside the disk with a radius of NAk_0, where NA is 0.6 and k_0 is the propagation constant in vacuum. Third, the inverse Fourier transform of the updated Fourier domain distribution is performed. Fourth, we update the phase profile to have unity transmission inside the MD aperture. The final phase profile of the MD is acquired after 100 repetitions. Figure 3.2**d** shows the amplitude distribution of the finalized MD design in the Fourier domain.

Device fabrication

A 652-nm-thick layer of α-Si was deposited using plasma-enhanced chemical vapor deposition on a ~500-μm-thick fused silica substrate. For nano-patterning, a positive electron-beam (e-beam) resist (ZEP520A) was spin-coated on the sample (~300 nm). To avoid electrostatic charging during the e-beam lithography, a charge-dissipating polymer (aquaSave, Mitsubishi Rayon) was spin-coated on the e-beam resist layer. The metasurfaces were patterned by an e-beam lithography system

(Vistec EBPG5000+) and developed in the ZED-N50 developer. A 70-nm Al_2O_3 layer was deposited and then the nano-pattern was transferred to the Al_2O_3 layer by a lift-off process. The Al_2O_3 layer was exploited as a hard mask to etch the α-Si layer in a mixture of C_4F_8 and SF_6 gases, and was then removed by a mixture of ammonium hydroxide and hydrogen peroxide. The metallic aperture was patterned by photo-lithography, deposition of a 100-nm-thick gold layer with a 10-nm chromium adhesion layer, and a lift-off process. To avoid confusion about the shape of the MDs shown in Fig. 3.2**e**, it is necessary to note here that the MDs are square-shaped with 1.6-mm side lengths, and the gold apertures are circular with 1.6-mm diameters (i.e. the transmittance in the overlapping region is negligible, so the final device aperture is determined by the gold aperture). For all results, we treated the MD as circularly shaped with a 1.6-mm diameter.

Computational procedure

The transmission matrix of the MD (T) in each specific condition was computed using the wave propagation method [158] and the calculated phase mask of the MD. The flow graph in Fig. 3.A.2 shows the procedure for a certain optical setup. The phase mask of the MD, distances between the optical elements, magnification and NA of the custom-built microscope, and the input/output mode conditions were used to compute T. First, each input mode is propagated by z_1 to find its corresponding field distribution at the MD plane. Passing through the MD is modeled by multiplying the field and the a priori known phase mask of the MD. The fields are then propagated by z_2 to the working distance of the objective lens. The microscope is modeled as a Fourier domain filter (with the 0.4 NA of the objective lens) followed by a Fourier domain up-sampling to take into account the magnification and the NA of the objective lens. Oversampling can happen because of the microscope if $p_c/Mag < \lambda/2NA$ where p_c is the camera pixel period, Mag denotes magnification, and λ is the wavelength. The oversampling effect can be compensated by a proper Fourier domain down-sampling. In our case, the speckle intensity pattern captured on a 500×500 array of 7.4-μm pixels centered at the optical axis are utilized in the retrieval process. Considering the 16.7× magnification and the diffraction-limited spot size of 1.06 μm (determined by the NA of the optical system), the fields on the 500×500 camera pixel array can be effectively down-sampled to a 210×210 array of 17.6-μm pixels at the camera plane. The 210×210 array at the camera plane corresponds to a 210×210 array of 1.06-μm pixels at a plane far from the objective lens by the working distance of the lens. Finally, the simulated complex fields on the 210×210 output array form the columns of T, with each column corresponding to a single input mode (for a 60×60 array of input modes). The filtering and the up-sampling processes will be eliminated if a miniaturized CMOS image sensor and a thin linear polarizer are used instead of the microscope to capture the speckle pattern. Also, the down-sampling process can be eliminated by adjusting the magnification of the optical system. Using parallel processing on 6 cores of a multi-core CPU (Intel Xeon E5-2640), it took almost 2 hours to compute T. We expect the time to be reduced significantly with GPU and advanced parallel computing. We should also note that for each specific set of input/output parameters T should only be calculated once.

The speckle correlation scattering matrix Z was used to retrieve the complex fields [113]. The definition of Z is shown in Eq. 3.1. Before calculating Z, it is necessary to perform the down-sampling for the speckle intensity patterns captured by the image sensor so that the oversampling effect is compensated. When Z has a rank of one (approximately), a single eigenvector constitutes the initial field retrieval estimate. In practice, the eigenvector corresponding to the largest eigenvalue forms the initial estimate. The first retrieval process (including the computation of Z) takes most of the retrieval time (22 seconds without parallel computing). To reduce the noise, we then performed the iteration procedure based on the modified GS algorithm proposed by Lee and Park [113]. Before the iterations, the pseudo-inverse of T (T^{-1}) was calculated by singular value decomposition. Using T, T^{-1}, the first estimate of the target, and the captured intensities of the speckle pattern, the 20 iterations based on the GS algorithm were performed. The 20 iterations take 8 seconds on average without any parallel computing.

Measurement procedure

Schematic of the optical setup used to measure the speckle patterns with the amplitude targets is shown in Fig. 3.A.5**a**. An 850-nm semiconductor laser (Thorlabs, L850P010) was coupled to a single mode fiber for illumination. The fiber was connected to a collimator package (Thorlabs, F220APC-850). A linear polarizer (Thorlabs, LPVIS100-MP2) was placed in front of the collimator to confirm the horizontal (x) polarization state of the input, and a fiber polarization controller was used to maximize the power passing through the polarizer. A bi-convex lens with a 5 cm focal distance (Thorlabs, LB1471-B-ML) was used to confine the illuminated region on the targets. We used a custom-built microscope setup to capture the speckle pattern, which consisted of a 20× objective lens (Olympus, LMPlanFL) with an NA of 0.4, a tube lens with a focal distance of 15 cm (Thorlabs, AC254-150-B-ML), a linear polarizer aligned along the y axis (Thorlabs, LPVIS100-MP2) to reject unscattered light, and a CCD camera (CoolSNAP K4, Photometrics). In front of the camera, an optical band pass filter (Thorlabs, FL850-10) was used to decrease the background noise and limit the bandwidth. Schematics of the optical setup used for holographic imaging with the MD are shown in Fig. 3.A.5**a**. The optical setup was mostly similar to the setup described above and shown in Fig. 3.A.5**a**. The bi-convex lens used to confine the illumination region was removed. Also, an aperture with a 150-μm diameter (Thorlabs, P150H) was inserted at the position between the sample and the MD, where the complex field was retrieved. The schematics of the optical setup used to capture the reference images for comparison with the holographic images is shown in Fig. 3.5**d**. Compared with the setup shown in Fig. 3.5**a**, the MD and the linear polarizer in the custom-built microscope are removed. In addition, the objective lens was moved to bring the sample in focus.

3.9 Appendix

Mathematical properties and noise tolerance of a randomly generated matrix

We investigated the noise tolerance of a randomly generated T matrix for comparison. The random transmission matrix T_R was generated using the code in the supplementary materials of Ref. [113]. Similarly to the results shown in Fig. 3.3**b** and 3.3**c**, the G_R matrix generated from T_R and the eigenvalue spectrum of $T_R^\dagger T/M$ are shown in Figs. 3.A.8**a** and 3.A.8**b**, respectively. As seen in Fig. 3.A.8**a**, the columns of T_R are almost perfectly uncorrelated. Moreover, Fig. 3.A.8**b** shows that the entries of T_R are statistically independent [8,9]. Using T_R, we investigated the noise tolerance in the same way used for noise tolerance study of the MD. Gaussian intensity noise with various energies was added to the speckle pattern generated by T_R to adjust the SNR value. The results shown in Fig. 3.A.8**c-j** verify that the complex fields could be retrieved when the SNR value is equal to or greater than 5 when using T_R. Comparing the noise tolerance shown in Fig. 3.A.8 to the results shown in Fig. 3.5 for the MD, one can see that the complex fields can be retrieved for an SNR value of 1 only with the MD. This shows that despite the existing correlation between the neighboring input modes and the dependence between entries of T, the MD demonstrates higher noise tolerance compared to the randomly generated transmission matrix.

Numerical analysis of robustness against misalignment

We numerically investigated the performance of the MD and the method with axial and transverse misalignments. The location of the meta-diffuser shown in Fig. 3.A.10**a** is changed transversely or axially to study the effect of the misalignment. Thanks to the large memory-effect range of the meta-diffuser [125], the misalignment leads to relatively small changes in the speckle patterns. Referring to Figs. 3.A.10**b** and 3.A.10**c**, the axial and transverse misalignments cause magnification/demagnification and parallel shift of the speckle patterns, respectively [111]. Thus, these changes in the speckle pattern affect the retrieved complex fields. A difference in the estimated and the actual distance between the aperture and the object results in an out-of-focus retrieved image as shown in Fig. 3.A.10**e**. Figure 3.A.10**f** shows that the out-of-focus images can be corrected simply through numerical propagation. In Fig. 3.A.10**g**, the case of an error in the estimation of the distance between the MD and the image sensor degrades the results, but it has still almost negligible results if the error is less than 10 μm. As the results in Fig. 3.A.10**h** show, a transverse misalignment of the MD approximately results in a transverse displacement of the speckle pattern and the retrieved image along with a gradient in the phase. It is worth noting that this shift itself can help in aligning the system by showing the misalignment type and direction. Also, Fig. 3.A.10**i** demonstrates that the images can be corrected and the phase gradient can be mitigated by cropping the speckle patterns in the corresponding shifted region if the image sensor has additional pixels. In summary, the numerical investigation demonstrates that our system is robust against axial and transverse types of misalignment and the results can be corrected or exploited for the aligning process. Moreover, the MD could be manufactured monolithically on top of a CMOS image sensor in the fabrication to minimize these types of misalignment, particularly the axial error between the MD and the CMOS image sensor.

Effect of the number of iteration on complex field retrieval

To explore how the number of iterations affects the complex field retrieval, we performed additional simulations by changing the number of iterations from 5 to 100 (i.e. 5/10/20/30/50/100 iterations) for both the numerically generated amplitude and phase targets [shown in Figs. 3.3**d** and 3.3**e**, respectively], and the experimental target [shown in Fig. 3.4**a**]. In Figs. 3.A.11**a**-3.A.11**f**, it is clearly shown that there is no considerable difference after 20 iterations for both the numerically generated and the experimental targets. For the numerically generated amplitude and phase targets, we have also plotted the correlations between the original targets shown in Figs. 3.3**d** and 3.3**e** and the retrieved complex field maps shown in Figs. 3.A.11**a-d** versus the number of iterations. In Fig. 3.A.11**g**, the plot clearly shows that the correlation is saturated after 20 iterations and reaches 0.986 just after 5 iterations.

Effect of the numerical aperture and the magnification/field of view of the objective lens in complex field retrieval

We have performed additional experiments to investigate the effects of the objective lens on field retrieval quality. We used 10× (0.3 NA) and 50× (0.7 NA) objective lenses to compare with the results based on the 20× (0.4 NA) objective lens shown in Fig. 3.4. The NA of the objective lens determines the diffraction limited spot size corresponding to the effective sampling pixel size for the speckle pattern (i.e. effective output pixel size). In other words, the effective sampling pixel size of the 10× and 50× objective lenses are 1.42 μm and 0.57 μm, respectively. In order for the comparison of the results to be fair, we fixed not only the input pixel size at 2.5 μm, but also the number of output modes (M) and input modes (N) at 44100 and

3600, respectively. With the 10× objective lens, a large 280×280 μm^2 central area of speckle pattern is sampled by a 210×210 array of 1.42-μm pixels. On the other hand, a smaller central area of 120×120 μm^2 of the speckle pattern is sampled by a 210×210 array of 0.57-μm pixels with the 50× objective lens. The targets shown in Fig. 3.4**a** and 3.4**b** were exploited again to compare with the results based on the 20× objective lens shown in Figs. 3.4**e**-3.4**h**. First of all, the retrieved complex maps based on the 10× objective lens shown in Fig. 3.A.12**a** are comparable with the targets shown in Fig. 3.4**a** and 3.4**b**, as well as the retrieved results based on the 20× objective lens shown in Fig. 3.4**e**-3.4**h**. However, the retrieved amplitude and phase maps based on the 50× objective lens shown in Fig. 3.A.12**b** verify that the targets cannot be retrieved well with the 50× objective lens under these conditions. The experimental results with the three different objective lenses shown in Figs. 3.4**e**-3.4**h**, 3.A.12**a**, and 3.A.12**b** clearly demonstrate that it is better to capture a large area of the speckle pattern with lower resolution than a small area of the speckle pattern with higher resolution (assuming fixed numbers of input and output modes). Finally, we increased the number of the output modes from 44100 to 176400, keeping the input pixel size the same for the 50× objective lens. This means that the 240×240 μm^2 central area of the speckle pattern is sampled by a 420×420 array of 0.57-μm pixels. In these new conditions, the complex fields are successfully retrieved using the 50× objective as shown in Fig. 3.A.12**c**. Thus, if the sampling area is determined, it is better to increase the number of output modes with smaller output pixel size. In this case, the ratio between the number of output and input modes increases, resulting in a more accurate field retrieval as well as a rise in the computational time.

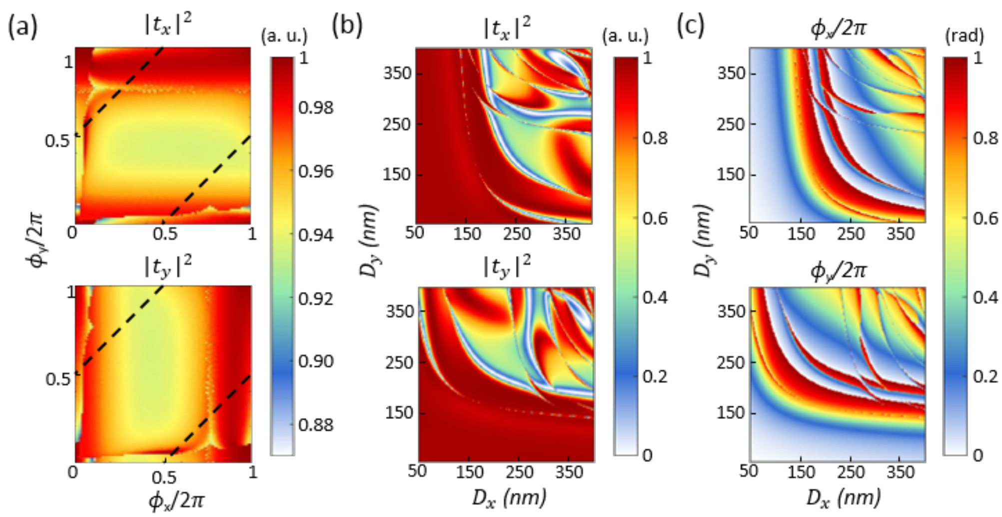

Figure 3.A.1: **Simulation results of the meta-atoms at the wavelength of 850 nm.** **a** The simulated transmittance of x- and y-polarized light ($|t_x|^2$ and $|t_y|^2$) corresponding to Fig. 3.2**c** as functions of ϕ_x and ϕ_y. The black dashed denote the meta-atoms that work as half wave-plates. **b** Simulated transmission amplitudes, and **c** phases for periodic arrays of meta-atoms as functions of D_x and D_y. The data in **b** and **c** is utilized to derive a and Fig. 3.2**c**. The meta-atoms are 652-nm tall and the lattice constant is 500 nm. The simulations are performed with a normally incident plane-wave source.

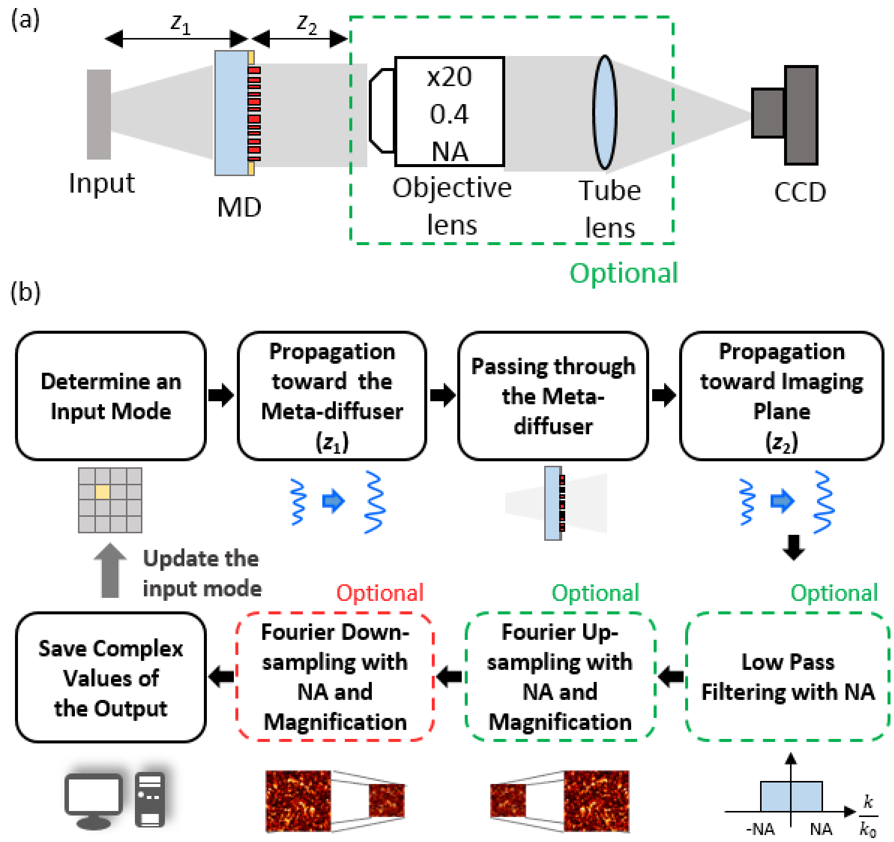

Figure 3.A.2: **Schematics of the setup and flow graph of the numerical calculation process of the transmission matrix T. a** The virtual optical setup used to calculate T. z1 and z2 represent the distances between the MD and the input and output planes, respectively. The optical components in the green dashed box (that magnify the speckle pattern and image it onto the image sensor) are optional and can be dropped for miniaturization. **b** Flow graph of the process used to calculate T. The speckle pattern corresponding to each input mode (pixel) is calculated using the wave propagation technique and the phase mask of the MD. The objective and tube lens are modeled as a low pass filter and a Fourier up-sampling. If there is an oversampling effect caused by high magnification, Fourier down-sampling can be performed to compensate the oversampling effect. The complex field of the speckle pattern corresponding to each input mode constitutes a column in T. The low pass filtering and up-sampling processes in green dashed box will be eliminated if the optical components in green dashed box in **a** are dropped. Moreover, the down-sampling process in red dashed box will be eliminated if the magnification of the optical system is adjusted to prevent the oversampling effect.

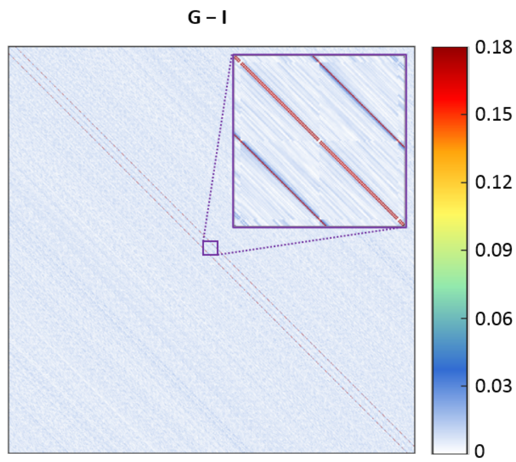

Figure 3.A.3: **Visualization of $G-I$ matrix.** The main diagonal of G is always a unit diagonal by definition. Thus, the main diagonal part is removed for visualization. It clearly shows that the correlations between neighboring modes are close to the 0.18 and the correlations between further modes are suppressed quickly. The average of the correlations between two arbitrary input modes is 0.006.

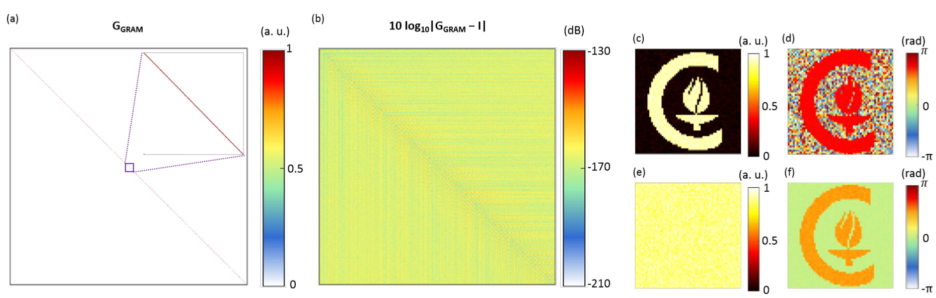

Figure 3.A.4: **Orthogonality properties between the columns of the transmission matrix (T_{GRAM}) and the capability to retrieve complex fields with T_{GRAM}. a** The G_{GRAM} matrix formed from the inner product mapping of the normalized vectors of the T_{GRAM} matrix. The entry G_{GRAMij} represents the absolute value of the inner product of normalized t_{GRAMi} and t_{GRAMj}, which are i-th and j-th columns of the T_{GRAM} matrix, respectively. The 130×130 elements located at the center of G_{GRAM} are magnified in the inset. (b) Plot of ($G_{GRAM} - I$) in log scale. We removed the main diagonal elements of G_{GRAM} which are always unit by definition. Thus, it clearly shows that all of the correlations between any two arbitrary input modes are eliminated (<10^{-13}). (c-f) Retrieved amplitude and phase maps for the numerically generated amplitude and phase objects of Figs. 3.3**d** and 3.3**e** of the main manuscript using T_{GRAM} after 20 iterations.

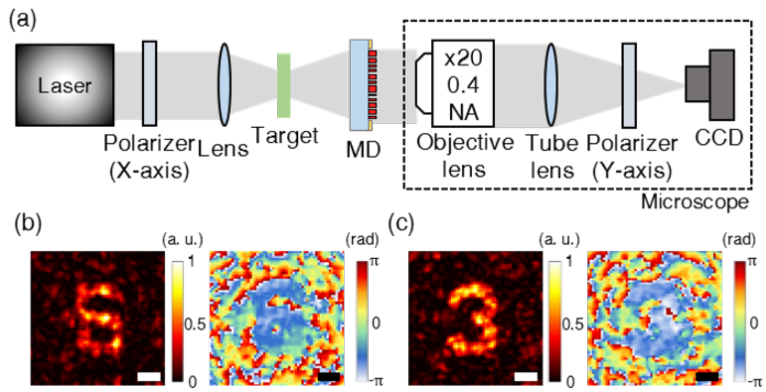

Figure 3.A.5: **Measurement setup and the initially retrieved complex fields before iterations.** **a** Schematic illustration of the measurement setup. The distance between the targets and the MD is 3 mm, and the speckle pattern is imaged 1.5 mm after the MD. **b** and **c** Intensity and phase maps of the first retrieved complex fields from the objects shown in Figs. 3.4**a** and 3.4**b**, respectively. Scale bars are 25 μm.

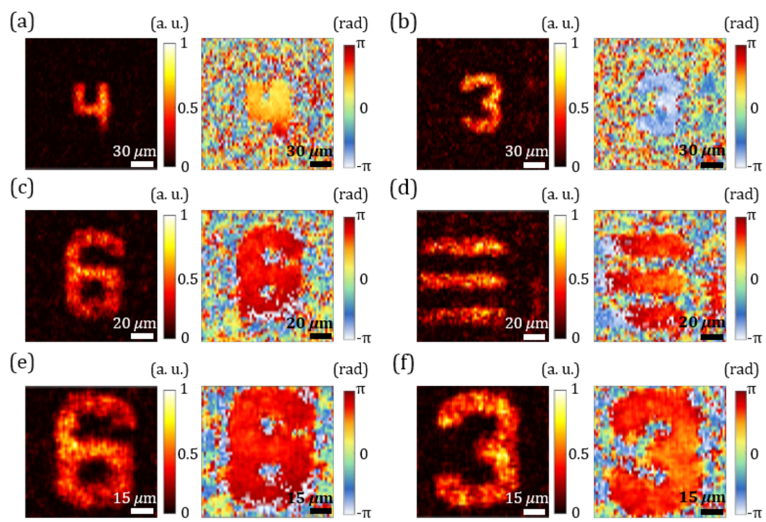

Figure 3.A.6: **Testing the reproducibility of the results under different input/output conditions and setup parameters.** Complex fields are retrieved using parts of the 1951 USAF test target as amplitude objects. The speckle patterns are captured under different conditions and the corresponding T matrix is used for each one to retrieve the complex field. The same MD (i.e. phase mask) was used for all images, and we kept the number of input pixels and the distance between the MD and the samples fixed at 60 and 3 mm, respectively. **a** and **b** Intensity and phase maps of retrieved complex fields for two different objects when the distance between the MD and the speckle plane is 1 mm, and the input pixel size is 3 μm. **c**-**f** Intensity and phase maps of retrieved complex fields when the distance between the MD and the speckle plane is 1.5 mm. The input pixel size is 2 μm in **c** and **d**, and 1.5 μm in **e** and **f**. 20 iterations were used for all retrievals.

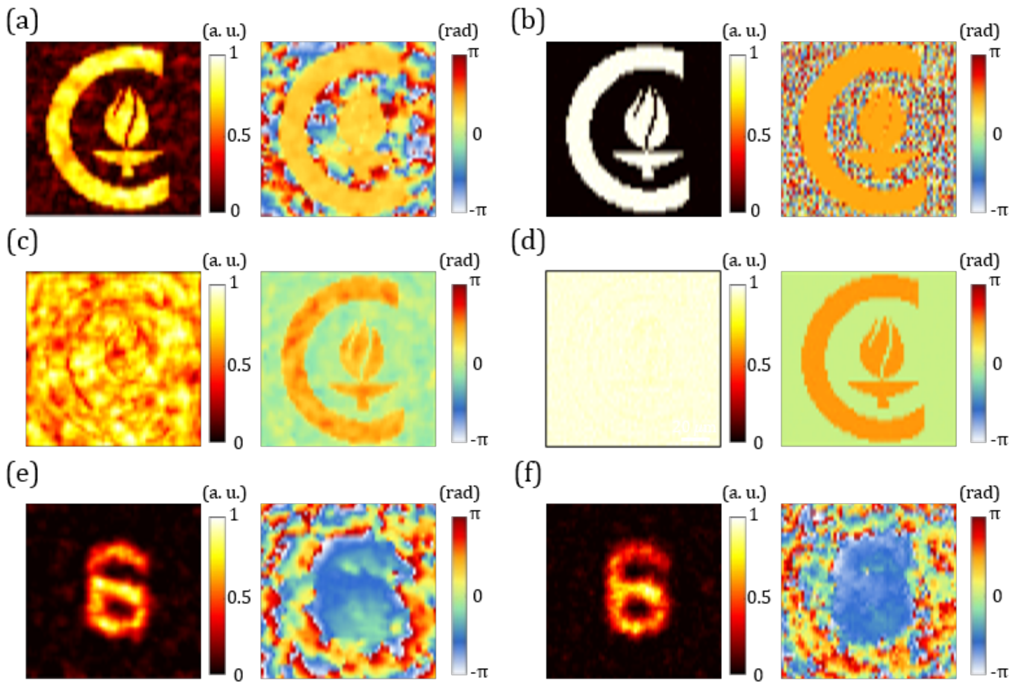

Figure 3.A.7: **Complex field retrieval with a γ value of 69.44.** Compared to the T matrix used in Fig. 3.4 of the main text, the only difference is the number of the effective output modes changed from 44100 to 250000. **a-d** Numerical field retrieval with amplitude and phase targets. **a** and **b** Amplitude and phase maps of retrieved complex fields for the amplitude target shown in Fig. 3.3**d** before and after iterations, respectively. **c** and **d** Amplitude and phase maps of retrieved complex field for the phase target shown in Fig. 3.3**e** before and after iterations, respectively. **e** and **f** Intensity and phase maps of retrieved complex fields for the measured amplitude object shown in Fig. 3.4**a**.

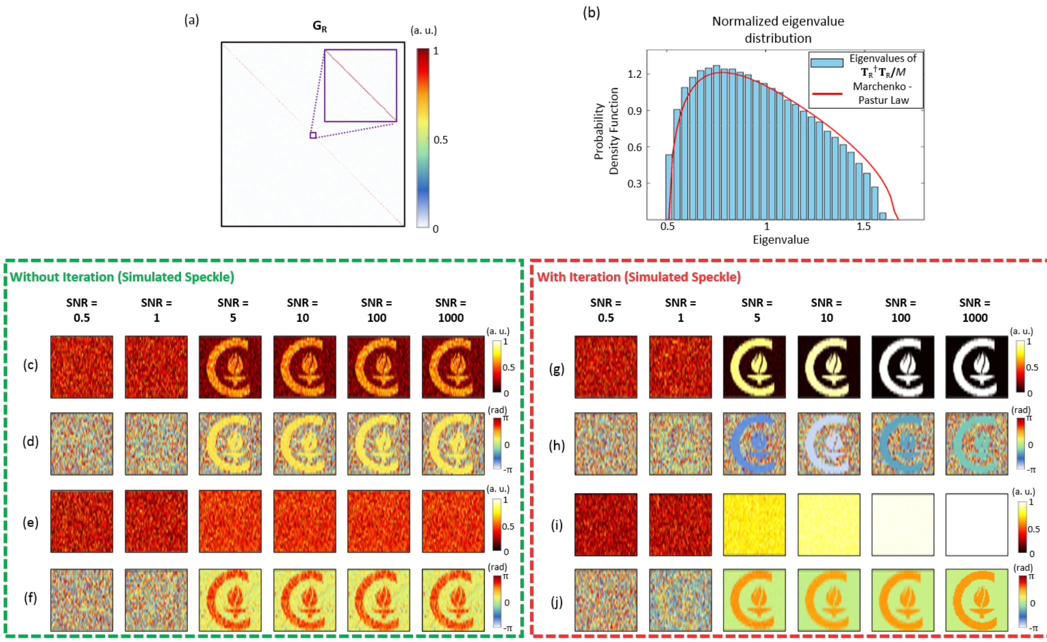

Figure 3.A.8: **Mathematical properties and noise tolerance of the randomly generated transmission matrix.** **a** The G_R matrix formed from the inner product mapping of the normalized vectors of the randomly generated T_R matrix. The entry G_{Rij} represents the absolute value of the inner product of normalized tRi and tRj, which are i-th and j-th columns of the T_R matrix, respectively. The 130×130 elements located at the center of GR are magnified in the inset. **b** Eigenvalue distribution of the. The red solid line is the Marchenko-Pastur law prediction for M×N random matrices. **c-f** Retrieved amplitude and phase maps for the amplitude and phase objects of Figs. 3.3**d** and 3**e** when changing the SNR from 0.5 to 1000. A white Gaussian noise is added to the simulated speckle pattern intensity to investigate the noise tolerance. **g-j** Reconstructed objects after 20 iterations of the GS algorithm.

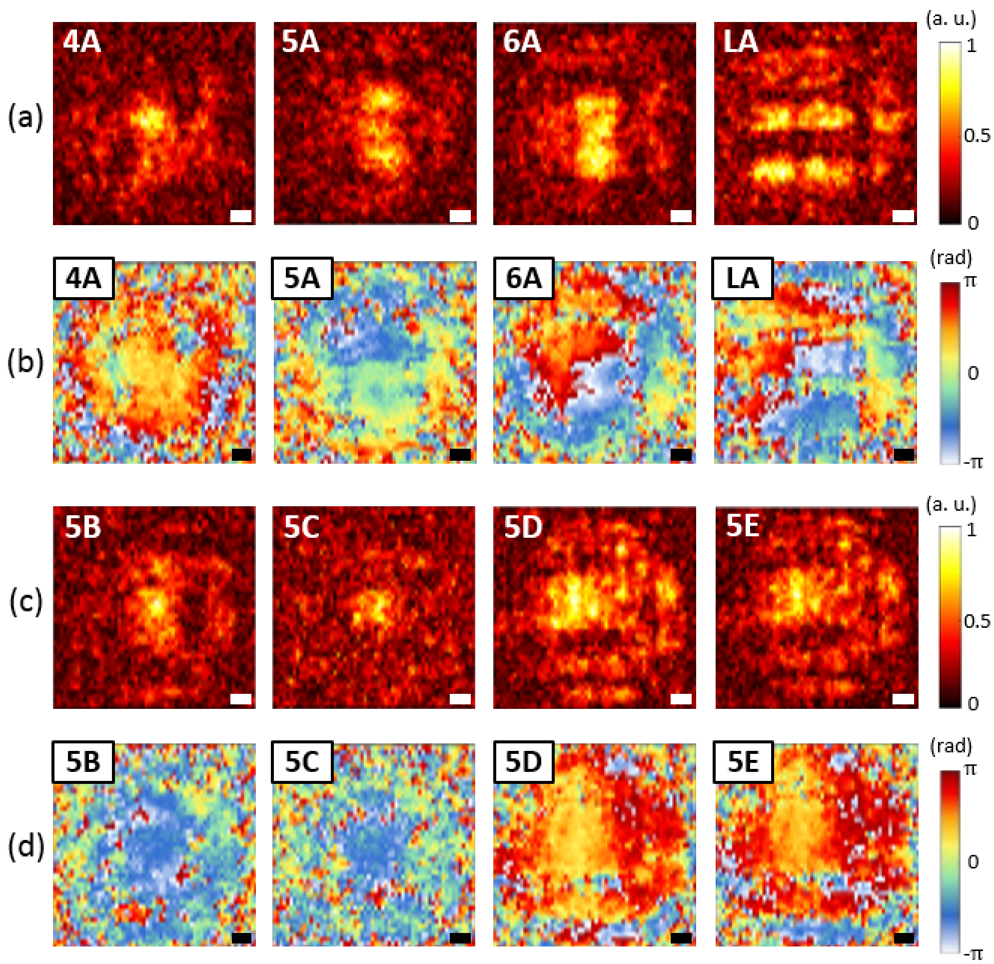

Figure 3.A.9: **Retrieved amplitude and phase distributions at the 150-μm aperture used to reconstruct the intensity images shown in Figs. 3.6b and 3.6c a** and **c** Retrieved amplitude maps. **b** and **d** Retrieved phase maps. Scale bares are 25 μm.

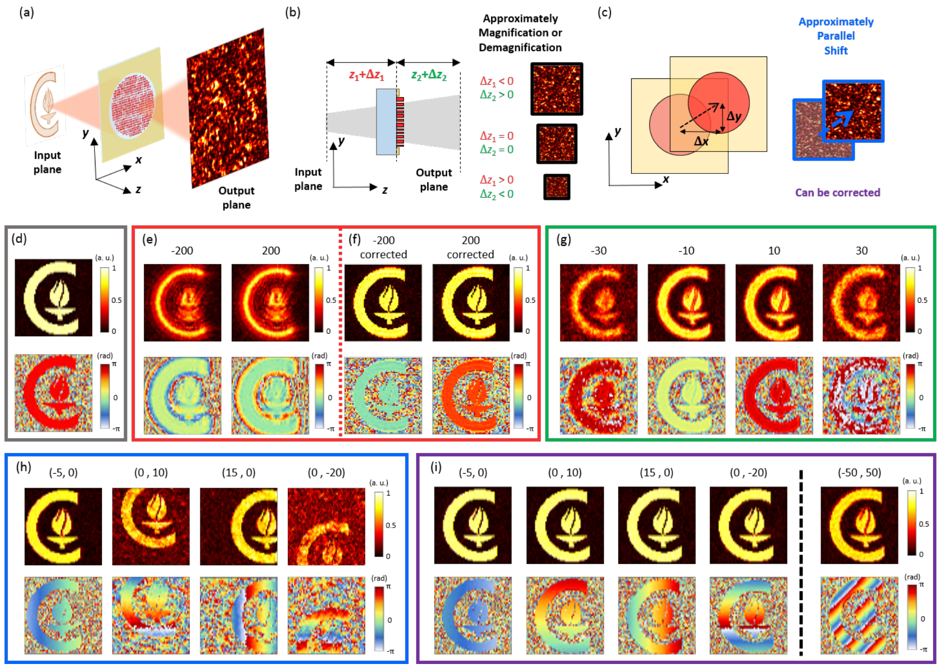

Figure 3.A.10: **Numerical investigation of robustness against axial and transverse misalignments.** **a** Schematic illustration of the utilized system showing the object, the MD, the speckle patterns and their relation to the coordinate systems. **b** Schematic drawing of the axial misalignment and its effect on speckle pattern. Δz_1 and Δz_2 are the errors in estimated distances between the input plane, the MD, and the speckle plane. Right: illustration represents that the speckle is approximately magnified or de-magnified as a result of the axial misalignment. **c** Schematic drawing of the transverse misalignment and its effect on the speckle pattern. Right: illustration represents that the transverse misalignment leads to an approximate shift of the speckle pattern parallel to the misalignment direction. **d**-**i** Retrieved amplitude (top) and phase (bottom) distributions. The SNR value is fixed at 100 to account for the noise in real systems. An amplitude mask is used as the target for the analysis. All coordinates and numbers in the figure are given in microns. **d** Retrieved complex field without any misalignment **e** Retrieved results for $\Delta z_1 \neq 0$. The numbers above the images denote the value of Δz_1. **f** Corrected results from the fields in **e** through numerical propagation. **g** Retrieved results for $\Delta z_2 \neq 0$. The numbers above the images denote the value of Δz_2. **h** Retrieved results at $(\Delta x, \Delta y) \neq (0, 0)$. The coordinates above the images show the values of Δx and Δy. **i** Corrected results for $(\Delta x, \Delta y) \neq (0, 0)$. The correction is achieved by cropping the speckle patterns in the properly shifted regions at the output plane. From the first to the fourth, the results are the corrected images from the results shown in **h**, in the same order. The fifth column of images shows the corrected results for the case of $(\Delta x, \Delta y) = (-50, 50)$. Although the amplitudes are corrected well by cropping the speckle patterns in the shifted region, the correction process is accompanied with a relieved linear gradation in the phase maps.

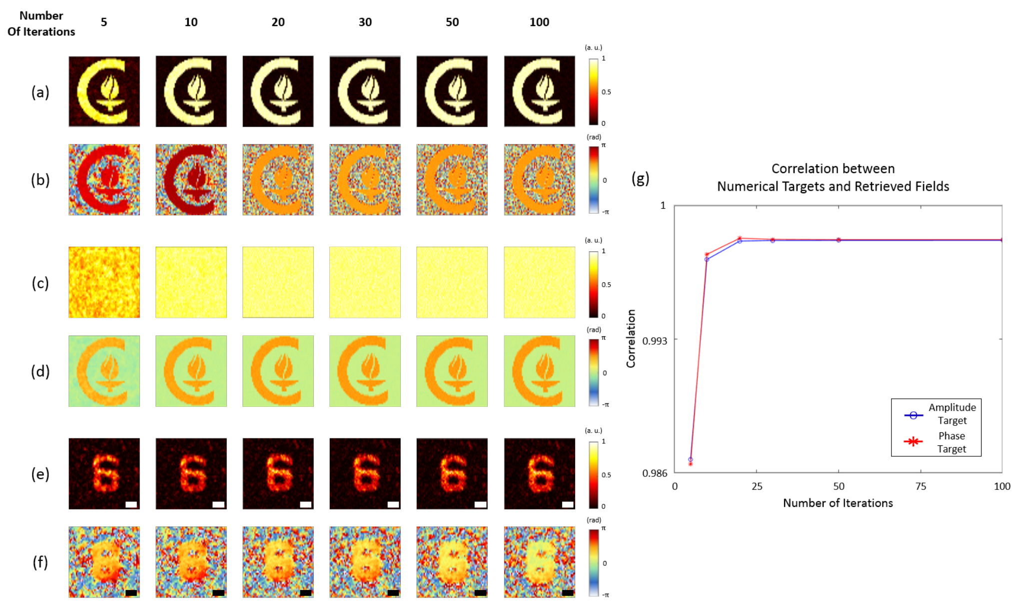

Figure 3.A.11: **Studying the effect of the number of iterations on complex field retrieval.** **a**-**f** Retrieved amplitude and phase maps for the numerically generated amplitude and phase targets of Figs. 3.3**d** and 3.3**e** and experimental target of Fig. 3.4**d** while the number of iterations changes from 5 to 100. The scale bars in **e** and **f** are 25 μm. **g** Correlation between the numerically generated amplitude and phase targets of Figs. 3.3**d** and 3.3**e** and retrieved complex maps of **a**-**d** versus the number of iterations. Blue line: Correlation between the numerically generated amplitude target of Fig. 3.3**d** and the retrieved complex maps shown in **a** and **b**. Red line: Correlation between the numerically generated phase target of Fig. 3.3**e** and the retrieved complex maps shown in **c** and **d**.

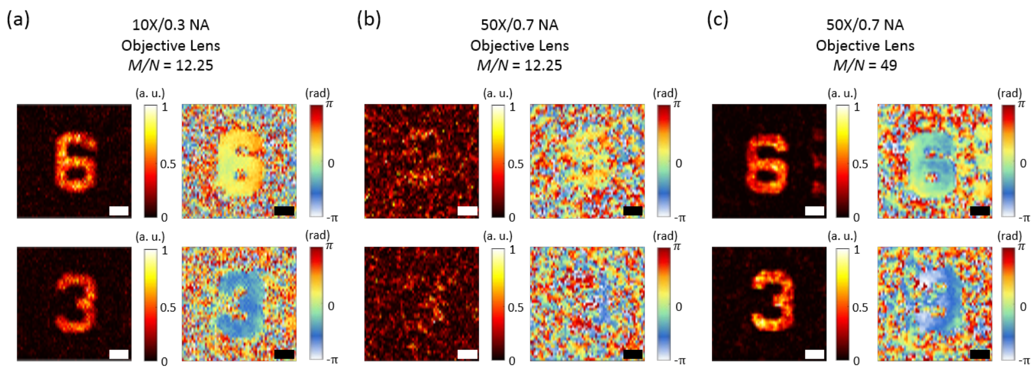

Figure 3.A.12: **Experimental investigation of the effects of the objective lens for complex field retrieval.** **a** and **b** Retrieved amplitude and phase maps for the experimental amplitude targets shown [in Figs. 3.4**a** and 3.4**b**] with the 10× (0.3 NA) and 50× (0.7 NA) objective lenses. The number of input (N) and output modes (M) are 3600 and 44100, respectively. **c** Retrieved amplitude and phase maps for the experimental amplitude targets shown [in Figs. 3.4**a** and 3.4**b**] with the 50× (0.7 NA) objective lens when the N and M are 3600 and 176400, respectively. 20 iterations were used for all retrievals. The scale bars are 25 μm.

Chapter 4

NANO-ELECTROMECHANICAL TUNING OF DUAL-MODE RESONANT DIELECTRIC METASURFACES FOR DYNAMIC AMPLITUDE AND PHASE MODULATION

The material in this Chapter was in part presented in [159].

Planar all-dielectric photonic crystals or metasurfaces host various resonant eigenmodes including leaky guided mode resonance (GMR) and bound states in the continuum (BIC). Engineering these resonant modes can provide new opportunities for diverse applications. Particularly, electrical control of the resonances will boost development of the applications by making them tunable. Here, we experimentally demonstrate nano-electromechanical tuning of both the GMR and the quasi-BIC modes in the telecom wavelength range. With electrostatic forces induced by a few voltages, the devices achieve spectral shifts over 5 nm, absolute intensity modulation over 40%, and modulation speed exceeding 10 kHz. We also show that the interference between two resonances enables the enhancement of the phase response when two modes are overlapped in spectrum. A phase shift of 144° is experimentally observed with a bias of 4V. Our work suggests a direct route towards optical modulators through the engineering of GMRs and quasi-BIC resonances.

4.1 Introduction

Photonic crystals or metasurfaces composed of low-loss dielectric materials are known to host highly resonant modes including leaky guided mode resonances (GMR) [19, 160, 161] and bound state in the continuum (BIC) modes [18, 162]. GMR is a leaky resonance offering a large optical signal via efficient coupling between leaky radiation and free-space light. Since the GMR can provide resonances that can be easily accessed from free-space, there has been a large volume of work focusing on how GMR can be used for diverse optical elements such as optical filters, polarizers, and bio-sensors [19, 160, 161]. Recently, the BIC mode has received significant interests because these exotic resonant states could still be perfectly trapped in the extended structures despite its existence within the energy spectrum of the continuum [18, 162]. While the GMR has large coupling to free-space modes, the quasi-BIC modes enable sophisticated control of the radiative lifetime through a symmetry-lowering perturbation, which provides a versatile platform for various applications such as lasers [163, 164], nonlinear light generation [165, 166], modulators [167–170], and sensors [171]. Complementary to GMR and BIC concepts, passive metasurfaces have shown an extraordinary capability for controlling diverse aspects of light such as phase, amplitude, polarization, and spectrum [1, 2]. Furthermore, reconfigurable metasurfaces can exploit new degrees of the freedom to manipulate light in time domain [45]. To achieve substantial tunability of the optical properties, the required optical response should generally be sensitive to small perturbations. Both the GMR and the quasi-BIC mode are not only highly resonant, but also efficiently coupled to free-space modes. Thus, the two resonant modes can potentially play a pivotal role in the realization of active metasurfaces. Over the past decades, reconfigurable devices hosting the GMR have been demonstrated through various platforms, such as microelectromechanical tuning [172], thermal tuning [173], carrier injection [174], and electro-optic polymer [175]. However, to the best of our knowledge, none of the works has been related to the concept of the BIC mode. Thanks to the highly resonant characteristic of BIC mode, tuning with the quasi-BIC mode can be superior in the quality factor (Q-factor) compared to GMR in similar device size. In contrast to the devices hosting a single GMR mode, devices hosting both the GMR and the quasi-BIC modes can be beneficial in exhibiting a larger phase response. Until now, the experimental demonstration of the reconfigurable BIC mode was mostly limited to all-optical tuning [167–169] or global thermal tuning [170]. In contrast to the previous tuning methods, electro-mechanical tuning can be advantageous in terms of power efficiency, high modulation speed, and integration with electronic circuits [49, 176, 177]. Moreover, the previous experimental demonstrations of the reconfigurable BIC modes mostly focused on modulation of intensity rather than phase [167–170]. In this work, we experimentally demonstrate nano-electromechanical tuning of both the GMR and the quasi-BIC modes hosted by suspended silicon gratings. With a few volts, the devices achieve reconfigurable spectral shifts, large reflection modulation, and modulation speed over 10 kHz in air. It is also shown that the electrical tuning of the interference between the GMR and the quasi-BIC mode can offer continuous tuning with large phase response.

4.2 Results

The schematic of nano-electromechanically tunable gratings is illustrated in Fig. 4.1**a**. The gratings consist of two sets of pairs of doped silicon nanobars. Throughout this paper, all structures are based on arrays of 500 nm thick and 30 μm long silicon

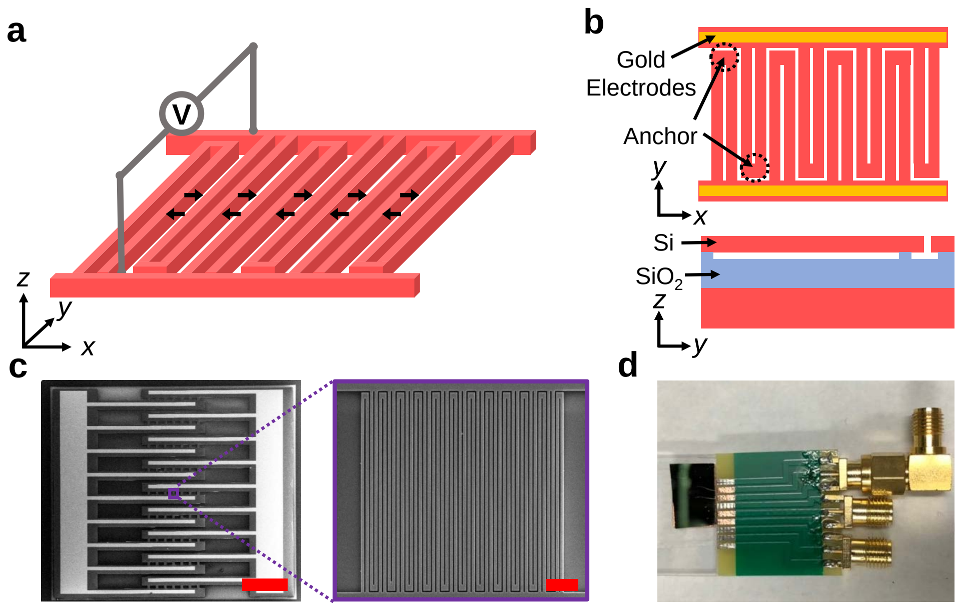

Figure 4.1: **Nano-electromechanical tunable suspended gratings.** **a** Schematic illustration of the nano-electromechanically tunable gratings. The grating is composed of pairs of silicon nanobars. The nanobars are connected to electrodes for actuation through electrostatic force. Black arrows show the directions of the actuation. **b** Schematic illustration of top (top) and side (bottom) views of the grating. Top: Two gold electrodes are deposited on top of the doped-silicon layers. Anchors and the gold electrodes are marked. Bottom: Buffered silicon oxide layer under the silicon nanobars is partially etched by 300 nm for the suspension while the anchors are supported by the oxide layer. **c** Scanning electron microscope images of the fabricated devices. Left: An array of the gratings and two gold electrodes are shown. One of the gratings is marked by a purple box. Right: Zoom-in scanning electron microscope image of the grating marked with the purple box in the left image. The grating consists of 23 pairs of silicon nanobars. Scale bars in left and right denote 500 μm and 5 μm, respectively. **d** Optical images of the fabricated device. The device is wire-bonded to a custom printed circuit board that is connected to an external source by a SMA cable.

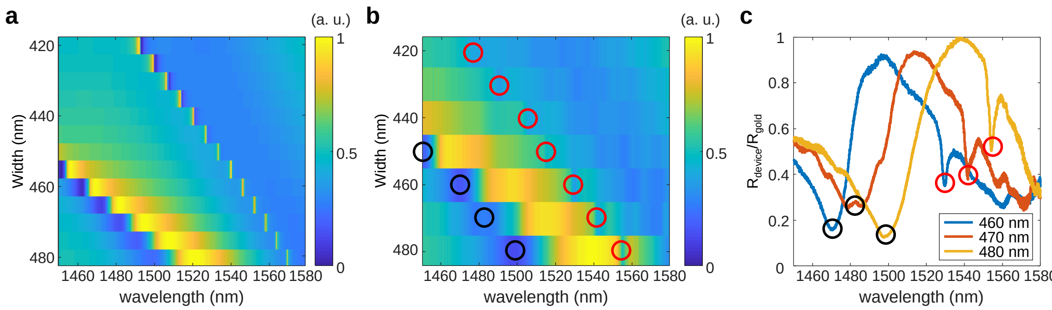

Figure 4.2: **Calculated and measured reflection spectra of the GMR and the quasi-BIC modes hosted by the gratings.** **a** Calculated reflection spectra (TE-polarized light) for gratings where widths of the nanobars vary from 420 nm to 480 nm by 5 nm. Period of the grating and incidence angle of light are 700 nm and 6 degree, respectively. **b** Measured reflection of TE-polarized light for the fabricated gratings with 6 degree tilted incident light. The reflection is normalized by the measured reflection from the gold electrode. The widths vary from 420 nm to 480 nm by 10 nm. **c** Three example spectra of the measured reflection spectra shown in b. The widths of the nanobars are 460, 470 and 480 nm and noted in legend. In b and c, black and red circles denote resonances of the GMR and the quasi-BIC modes, respectively.

bars. We also ensure that the lattice constant of the pair of the nanobars is smaller than the wavelength of interests to avoid unwanted diffraction. Figure 4.1**b** shows top and side views of illustrative schematics of the gratings. One end of the suspended nanobars is connected to the large silicon layer on which gold electrodes are deposited. To prevent bending or buckling of the suspended structures, the other end of the suspended nanobars is connected to the anchors marked in Fig. 4.1**b**. The gold electrodes are used to induce the Coulomb forces between the nanobars thus enabling the actuation. The silicon gratings and the electrodes are fabricated by sequential conventional nanofabrication procedures (see Methods for details). Figure 4.1**c** shows the scanning electron microscope images of the fabricated device, which consists of two electrodes and an array of the gratings. The device is wire-bonded to a custom-made printed circuit board so that it allows for connection to an external voltage source. The optical image of the fabricated device and the printed circuit board is shown in Fig. 4.1**d**.

First, the optical characterization of the gratings is performed. The finite-sized gratings are known to host both GMR and quasi-BIC modes that allow for coupling with free-space light [18, 178]. Figure 4.2**a** shows calculated reflection spectra for 6° tilted TE-polarized input light (see Methods for details). With a lattice constant of 700 nm, the widths of the nanobars vary from 420 nm to 480 nm. A non-zero incident angle is chosen for efficient coupling with the quasi-BIC mode. In other words, the coupling is achieved by breaking of the even symmetry of the incident beam. Moreover, it is worth noting here that breaking the odd symmetry of the mode can also result in efficient coupling at normal incidence [179]. In Fig. 4.2**a**, two distinct resonant modes can be found. One mode at the shorter wavelength is the leaky GMR mode and the other mode at the longer wavelength is the quasi-BIC mode. We fabricated and measured seven corresponding devices with nanobar widths varying from 420 nm to 480 nm by 10 nm. A custom-built microscope setup is utilized to measure the reflection spectra of the grating samples (See Method and Fig. 4.A.1 for details about the measurement). The spectrum is normalized by the reflection from the gold layer to remove fluctuations resulting from polarization variations of the input light. Thus, the actual reflection values should be a few percentages lower than the plotted reflection spectra presented in this paper considering the reflection loss of the 95 nm thick gold layer. The measured reflection spectra for the six degree tilted TE polarized light are plotted in Fig. 4.2**b** showing good agreement with the simulation results in Fig. 4.2**a**. The black and red circles show the positions of the GMR and quasi-BIC modes, respectively. Furthermore, three examples of the measured reflection spectra are shown in Fig. 4.2**c**. As shown in Figure 4.2**b**, two distinct modes, GMR and quasi-BIC mode, are observed at the three spectra shown in Fig. 4.2**c** and also marked by black and red circles. While broad dips below 1510 nm show dips of the low-Q fano-shape GMRs, other narrow dips over 1520 nm represent high-Q quasi-BIC modes. If the incident angle decreases from six to zero degree, the BIC will be protected by symmetry [18, 179]. As a result, the radiation channels of the quasi-BIC mode are gradually closed, which increases Q-factor and decreases the amplitude of the resonant signal (see Fig. 4.A.2 for two measured reflection spectra for normal and 6° tilted TE-polarized input light).

To demonstrate nano-electromechanical tuning of the devices, static voltage is applied to the electrodes and the induced changes in the optical reflection are evaluated. The shape and position of both the GMR and the quasi-BIC mode highly depend on the gap size between the nanobars, which can be continuously controlled as a function of the external bias. Specifically, in the configuration shown in Fig. 4.3**a** every two nanobars are connected to one electrode and biased by an external source or ground, so bars connected to different electrodes will attract each other. In Fig.4.3**a**, g_1 (g_2) is the gap between the nanobars having different (same) voltages.

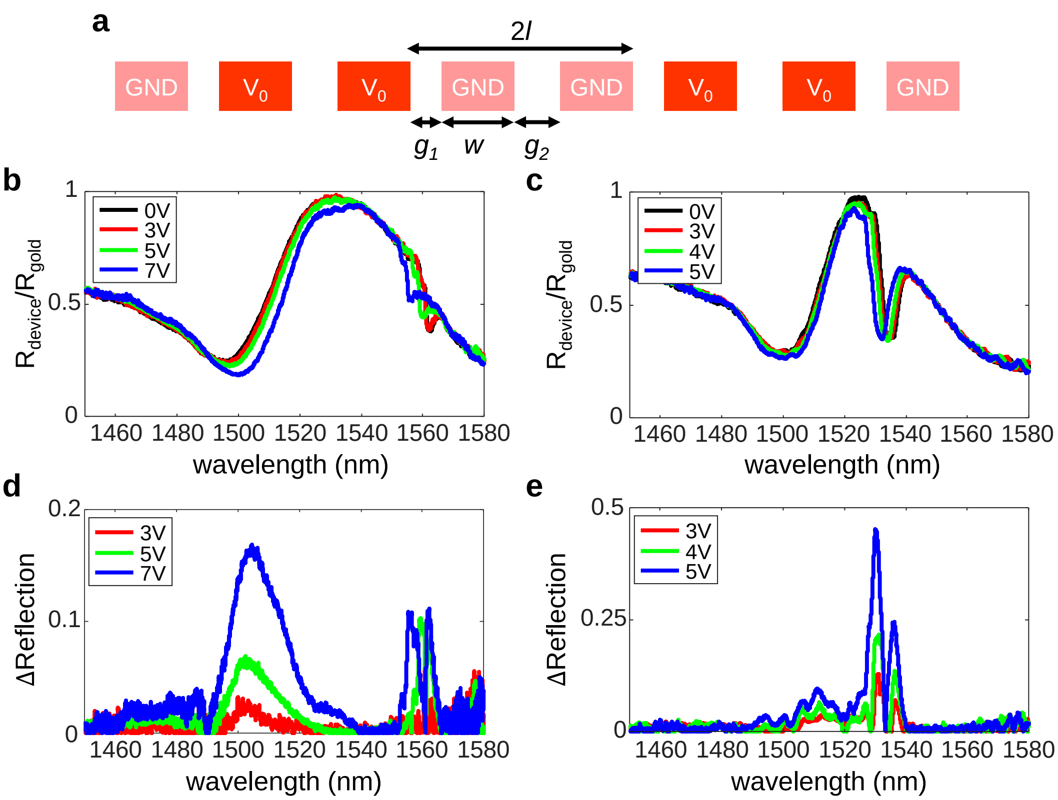

Figure 4.3: **nano-electromechanical tuning of the resonances for intensity modulation.** **a** Schematic illustration of an array of pairs of the silicon nanobars. The grating consists of periodic pairs of the silicon bars. Pink and red colors represent ground, GND, and external bias, V_0, respectively. Parameter definitions are shown in the illustration where l, w, g_1, and g_2 are the lattice constant of the grating, the width of the nanobar, the gap between the nanobars having a different bias, and the gap between the nanobars having the same bias, respectively. **b** and **c** Measured reflection spectra of TE-polarized lights for two different structures (see Table. 4.A.1 for detailed design parameters). The spectra are measured under four different biases and plotted in different colors. The applied bias for each color is shown in legends. **d** and **e** Spectra of absolute modulation in reflection calculated from b and c. The applied bias for each color is shown in legends.

As the external bias is applied, g_1 and g_2 will decrease and increase, respectively. Consequently, this nanomechanical actuation enables continuous shifts of the resonances. It is worth noting here that similar laterally movable actuators have been investigated with single-mode low-Q grating resonators [176, 180]. The measured reflection spectra under several bias voltages are shown in Figs. 4.3**b** and 4.3**c**. For the devices used in Figs. 4.3**b** and 4.3**c**, it should be mentioned that g_1 and g_2 are adjusted in the fabrication process to make g_1 smaller than g_2 such that the nano-electromechanical tuning of the gaps efficiently results in a large shift of the resonances (See Table. 4.A.1 for the detailed information about the device). In Figs. 4.3**b** and 4.3**c**, the static bias causes the red shift of the GMR mode and blue shift of the quasi-BIC mode. The observed directions of the spectral shifts show good agreement with the simulated results (see Fig. 4.A.3 for the numerical investigation about spectral shifts of the resonances induced by the actuation). With the external bias of 7 V, the peak shifts of the GMR and the quasi-BIC mode shown in Fig. 4.3**b** are as large as 5 nm and -6 nm, respectively. The absolute spectral shifts over 5 nm indicate that the required Q-factor for the spectral shift corresponding to the bandwidth of the resonance is around 300, which is readily achievable with quasi-BIC mode resonance even in a small array [165]. In general, the large spectral shift is beneficial in terms of robustness, stability, and operating bandwidth. To illustrate the capability of reflection intensity modulation of the presented devices, the absolute changes in reflection over spectrum are plotted in Figs. 4.3**d** and 4.3**e**. In Fig. 4.3**e**, the maximum absolute change in the reflection is as high as 0.45. As we treat the reflection of the 95nm thick gold electrode as 1 and use it as the normalization constant, the reflection change induced by the nanomechanical tuning will be larger than 0.4 if a few percentage loss from the gold surface is considered. It is also worth noting that the modulation can be readily improved by increasing the coupling between the resonant mode and the free space light by using the structural symmetry-breaking perturbation. Moreover, the measured values are not the real limit but the lower bound of the performance as the spectral shifts and the intensity modulation are measured with the external bias below pull-in voltage.

The temporal and frequency responses of the gratings are investigated in air. To explore temporal responses first, a periodic square-wave signal with a modulation frequency of 3 kHz, amplitude of 6V, and duty cycle of 0.5 is applied to the electrodes (see Methods for details). The device used for Fig. 4.3**b** is measured with input light at 1562 nm. The measured output signals are plotted in Fig. 4.4**a** having the corresponding frequency of 3 kHz. Fig. 4.4**b** shows measured rise time (up to 90%

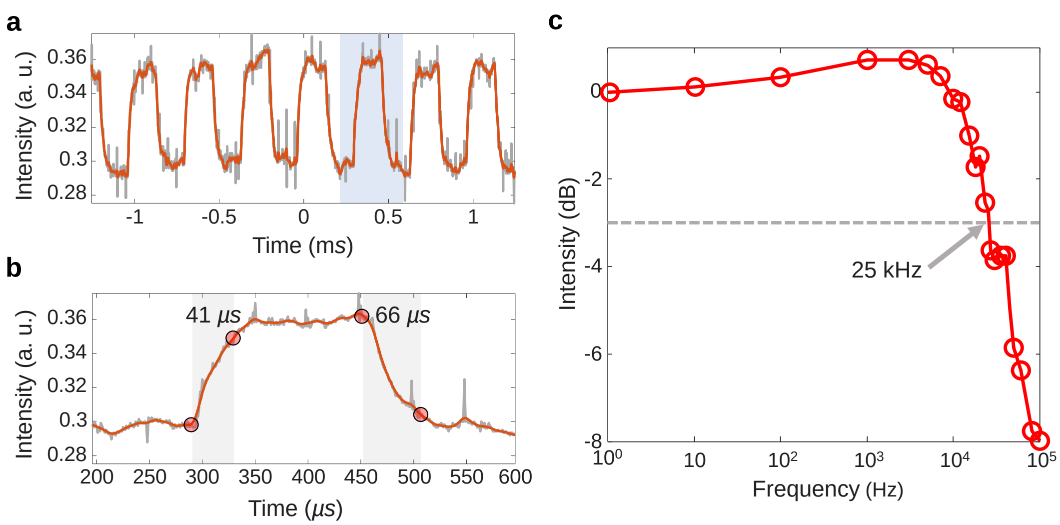

Figure 4.4: **Temporal and frequency response of the nano-electromechanically tunable grating.** **a** Measured time response of the grating with a 3-kHz square wave signal of which duty cycle and amplitude are 0.5 and 6V, respectively. Raw and filtered reflection signals are plotted by grey and orange curves, respectively. **b** Magnified temporal signal marked by sky-blue color in a. Measured rise and fall times are 41 and 66 μs, respectively. **c** Measured frequency response of the grating. The 3 dB frequency cutoff is 25 kHz.

power) and fall times (down to 10% power) of 41 and 66 μs, respectively. The rise and fall times indicate the speed limit of 15.2 kHz which is dominantly limited by air damping. The frequency response is measured and plotted in Fig. 4.4**c** showing the 3 dB frequency cutoff of 25 kHz. In addition, the mechanical resonant frequency in vacuum can be calculated by COMSOL® (see Methods for details). The mechanical resonance frequency of the devices presented in this paper is estimated to be around 4.5MHz that could be observed with proper vacuum packaging [176, 181]. Thus, our device has the potential to operate in a few MHz regime with decreased driving voltage.

Finally, we investigate enhanced phase modulation based on the interference of the two resonant modes. Temporal coupled mode theory can generally describe the optical response of eigenmodes through ports [182]. With coupled mode equations describing a single mode and a single port, it is known that large phase shift close to 2π can only be achieved when the resonant mode is over-coupled to the input port [183–185]. Specifically, coupling coefficient between the mode and the input is larger than intrinsic loss of the mode in the over-coupled regime [184, 185]. Furthermore, the over-coupling is often achieved by the presence of the bottom

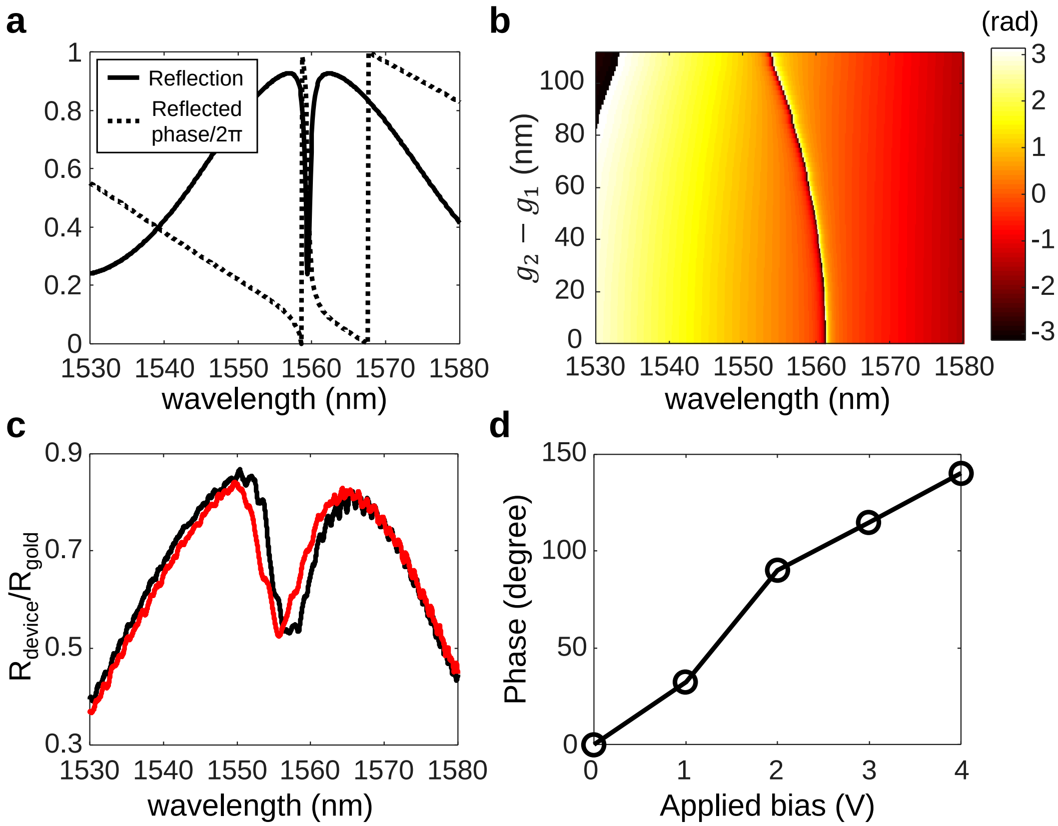

Figure 4.5: **Overlap of the GMR and quasi-BIC mode resonances for enhanced phase modulation.** **a** Calculated reflection and reflected phase spectra. The quasi-BIC mode is placed near the peak of the GMR. **b** Calculated spectra of reflection phase. The spectra are plotted as a function of the nanomechanical tuning, $g_2 - g_1$. **c** Measured reflection spectra with applied biases of 0V (black) and 4V (red). **d** Measured phase shift of the metasurface at the wavelength of 1556 nm as a function of the applied biases from 0V to 4V.

mirrors, that ensure the radiation of the mode is matched with the direction of the input [184, 185]. The silicon nanobars shown here are surrounded by air so the structure is nearly symmetric in z-axis (Fig. 4.1). This nearly symmetric environment results in almost identical radiation in the $+z$ and $-z$ directions, which hinders the over-coupling of light through one direction. As a result, using a single GMR or quasi-BIC mode hosted by the presented devices, it is very challenging to achieve large phase modulation of reflected light if there is no bottom mirror (see Fig. 4.A.4 for numerical study about the phase response of the single BIC resonance). In contrast, if there are multiple resonances in the frequency range of interest, the overall reflected phase response is affected by interference effects of the multiple resonant modes. Thus, the interference of dual modes can enable large phase shifts with non-zero reflection. It is worth mentioning here that a similar mechanism of the enhanced phase responses through dual modes has been investigated in the context of the Huygens metasurfaces or Huygens BIC metasurfaces [22, 186]. Figure 4.5**a** shows calculated reflection intensity and phase spectra of a device for which the design parameters are adjusted to place the narrow quasi-BIC mode resonance near the peak of the broad GMR (see Table. 4.A.1 for detailed designs of the device). In Fig. 4.5**a**, the minimum reflection at the resonance is 0.237 and the reflected phase shows strong phase response close to 2π. To numerically show the phase modulation via nanomechanical tuning, expressed by $g_2 - g_1$, the spectra of the reflected phase are plotted in Fig. 4.5**b** as a function of $g_2 - g_1$. In Fig. 4.5**b**, the mechanical tuning results in continuous blue-shift of the resonance while the strong phase response remains at the resonance. The blue-shifts of the quasi-BIC mode shown in Fig. 4.5**b** agree with the experimental observations in Figs. 4.3**b** and 4.3**c**. For the experimental demonstration, a new device is fabricated with the corresponding design parameters and its reflection spectra are plotted in Fig. 4.5**c**. The reflection spectra in Fig. 4.5**c** show electrical tuning of the resonances and a good agreement with the spectra shown in Fig. 4.5**a**. The measured Q-factor of the device used in Fig. 4.5**c** is ~244, which is less than simulated Q factor of ~1836. The difference could be explained by the small size of the array and imperfect fabrications. To experimentally characterize the phase response of the device used in 4.5**c** , we used a Michelson-type interferometer setup (see Method and Fig. 4.A.1). Due to the small size of the device, the incident laser beam illuminates the entire grating and the gold electrode at the same time and the interference patterns on both interfaces are simultaneously collected by a camera. At the resonant wavelength of 1556 nm, the fringes on the grating are shifted by external biases from 0 V to 4 V while the fringes on the electrode are unchanged (see Method and Fig. 4.A.5 for the details). The induced phase modulation is estimated by the observed shifts of the fringes on the grating and plotted in Fig. 4.5**d**. The largest phase shift of 144° is achieved at the external bias of 4V, which is smaller than the simulation result shown in Figs. 4.5**a** and 4.5**b**. The deviation from the simulation is primarily due to limited free-space coupling to the quasi-BIC mode. For example, the absolute reflection dip shown in Fig. 4.5**a** is much smaller than the measured dip in Fig. 4.5**c** indicating imperfect coupling to the quasi-BIC mode. We believe that this inefficient coupling dominantly results from the finite size effect.

Although it might be expected that the introduction of a spatially varying perturbation for each pair of the nanobars could allow electrically controlled wavefront shaping, it is worth explicitly noting that the presented resonance mode does not support efficient wavefront shaping at subwavelength scale. The introduction of the spatially varying perturbations at subwavelength scale may severely break the periodic condition of the structures, that the two modes necessitate to resonate. Thus, the interference effect of the two resonant modes is more suitable for spatial light phase-modulators having a pixel pitch of tens of micrometers than the pixel pitch of subwavelength scale. However, we expect that electrically controlled wavefront shaping in subwavelength or wavelength scale is possible with judicious engineering of various resonance modes hosted by an array of dielectric nanostructures [170, 187–189].

4.3 Summary and Conclusion

In summary, we demonstrate nano-electromechanical tuning of the leaky GMR and the quasi-BIC modes hosted by suspended silicon grating structures. With an external bias below 7 V, the devices experimentally achieve a spectral shift of the resonance over 5 nm, intensity modulation exceeding 40%, and modulation speed over 10 kHz in air. The required electrostatic bias can be further decreased by choosing the resonant modes that host large electric fields in the gaps [190]. In addition, co-optimization of both mechanical and optical properties is expected to improve the operating speed in air. With proper vacuum packaging, the devices may operate at high mechanical resonant frequency around several MHz. Moreover, we experimentally show that the interference between the GMR and quasi-BIC mode can enhance the phase response. The phase shift of 144° is measured at the external bias of 4V. Engineering of the resonant modes via structural tuning will improve the phase responses and enable dynamic wavefront shaping at subwavelength scale. Thus, this work paves the way of nano-electromechanical dynamic dielectric metasurfaces towards diverse applications such as spatial light modulators, lasers, nonlinear or structured light generation, pulse controller, polarization converters, and compact spectrometers for bio-sensing.

4.4 Methods

Simulation and design

The reflected spectra of the gratings with 6° tilted incidence light were calculated using the rigorous coupled wave analysis technique [95]. Assuming the infinite length of silicon nanobars, 2D simulations were performed. The silicon, air, and silicon oxide layers on a silicon substrate were 500nm, 300 nm, and 2700 nm thick, respectively. Refractive indices of Si and SiO_2 for the telecom wavelength in the simulation were 3.4 and 1.45, respectively. The width and lattice constant were varied in the simulation to achieve the desired reflection spectra (see Table. 4.A.1 for detailed information about the design parameters).

The mechanical resonance frequency is calculated by a commercial software based on the finite element method, COMSOL®. The eigenfrequency of the Si bar is extracted assuming that both ends of the suspended nanobars are fixed. In the mechanical simulation, Young's modulus and density values for silicon were 170 GPa and 2329 kgm^{-3}, respectively.

Device fabrication

The devices are fabricated using a silicon-on-insulator wafer with a device layer of 500 nm and a buffered oxide layer of 3 μm on a 1 mm thick silicon substrate. The fabrication includes two sequential e-beam lithography steps, the first one for the grating structures and another for the electrodes. For both lithography steps, a ~300-nm-thick positive electron resist (ZEP-520A, Zeon) is spin-coated on the device. The patterns are generated by 100 kV electron beam exposure (EBPG5200, Raith GmbH), and the resist is developed in a developer solution (ZED-N50, Zeon). For the silicon grating structures, the ZEP resist is utilized as a soft mask to etch the silicon device layer and then removed by remover PG (Microchem). Next, the electrodes are patterned by electron beam lithography, the deposition of chrome and gold (5nm and 95nm) layers, and liftoff. Buffered hydrofluoric acid is exploited to etch the buffered oxide layer under the gratings. The time of the under-cut process is carefully controlled such that the anchors are supported by the SiO_2 while the gratings are fully suspended. The device is dried by a critical point dryer. Finally, the device is bonded to a custom printed circuit board using a wire bonder (WestBond 7476D).

Measurement procedure

All of the reflection spectra presented in this paper are characterized using the set-ups shown schematically in Figure 4.A.1 [184]. A tunable laser (Photonetics, TUNICS-Plus) is used as the light source and the wavelength of the light is tuned from 1450 nm to 1580 nm. We use a beam splitter in front of the fiber collimator (Thorlabs, F260FC-1550) to capture the power from the source and send the light to the sample. For reference, the power from the source is captured by a InGaAs detector (Thorlabs, PDA10CS). Due to variation in polarization states from the laser, a quarter waveplate in front of a polarization beamsplitter (PBS) is used to prevent low transmission through PBS at specific wavelengths, increasing signal-to-noise ratio over the entire spectrum. The PBS, a half waveplate (HWP), and a polarizer are inserted to set the polarized state of the incident light to TE polarization. The sample at the object plane is imaged by a 20× infinity-corrected objective lens (Mitutoyo, M Plan Apo NIR) and a tube lens with a focal length of 200 mm. As the tube lens and the objective lens are forming a 4-f system, the movement of the tube lens in the x-axis enables adjustment of the angle of illuminated light. At the image plane, a pinhole with a diameter of 400 μm is inserted to select a region of interest with a diameter of 20 μm in the object plane. The spatially filtered light was either focused onto another InGaAs detector for the measurement of the spectra, or imaged on an InGaAs SWIR camera (Goodrich, SU320HX-1.7RT) using relay optics. All spectra in this paper were obtained by dividing the signal from the sample by the signal from the sources. Due to different input polarization states, the incidence power onto the sample varies in different wavelengths. Thus, the spectra are further normalized by the spectra from the gold electrode. For the measurement of dynamic responses shown in Figs. 4.3-4.5, bias voltages, both DC and AC, are applied with a function generator (FeelTech, FY6600-60M).

To measure the phase response shown in Fig. 4.5**d**, we use a Michelson-type interferometer setup. A part of the setup marked by a black dashed box in Fig. 4.A.1 is only utilized for the phase measurement. Specifically, the reference beam interferes with the reflected beam of the sample and forms fringe patterns at both image and camera planes enabling the measurement of reflected phase as a function of applied biases from 0V to 4V. As shown in Fig. 4.A.5**b** and 4.A.5**c**, the fringes are not shifted on the electrode but on the gratings under different external biases. The phase responses under the external biases are calculated by using the corresponding shifts of the fringes on the grating shown in Fig. 4.A.5**c**. We used the formula $2\pi\frac{\delta w}{w_0}$ to calculate the phase shifts, where δw is the averaged shift of the fringes in the unit of camera pixel number, and w_0 is the pixel number of a period of the fringe. The measured w_0 is 10 camera pixels. Finally, the phase shifts are averaged from all five pictures in Fig. 4.A.5**c** and plotted in Fig. 4.5**d**.

4.5 Appendix

Figure	$2l$ (nm)	w (nm)	g_1 (nm)	g_2 (nm)
Figures 4.3**b**, 4.3**d**, and 4.4	1400	495	245	165
Figures 4.3**c** and 4.3**e**	1320	495	185	145
Figure 4.5	1332	494	144	200
Figure 4.A.2**a**	1400	460	240	240
Figure 4.A.2**b**	1400	480	220	220

Table 4.A.1: **Design parameters for the blazed grating simulations shown in Fig. 5.3.**

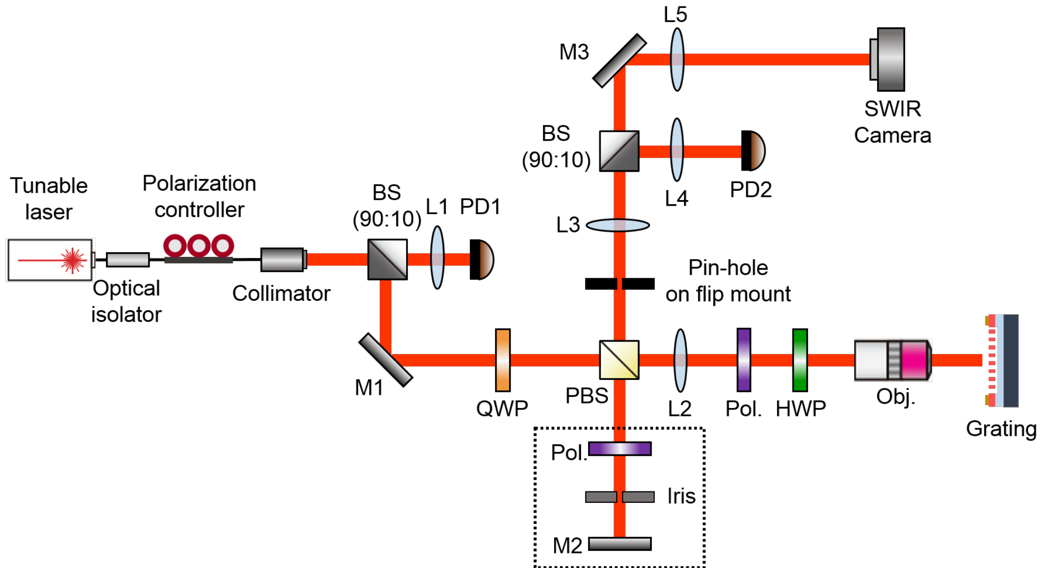

Figure 4.A.1: **Schematic illustration of the Experimental setup.** Red lines represent the paths of the light. To achieve the reflection spectra of the TE-polarized input light, Pol. and HWP in front of the objective lens are aligned to 45 and 67.5 degree, respectively. A black dashed box represents optical elements exploited to generate a reference beam for the phase measurement shown in Fig. 4.5**d** and Fig. 4.A.5. Pol.: linear polarizer. BS: beamsplitter. PBS: polarizing beamsplitter. L: lens. PD: photodetector. M: mirror. QWP: quarter waveplate. HWP: half waveplate. Obj.: microscope objective lens. SWIR camera: short-wave infrared camera.

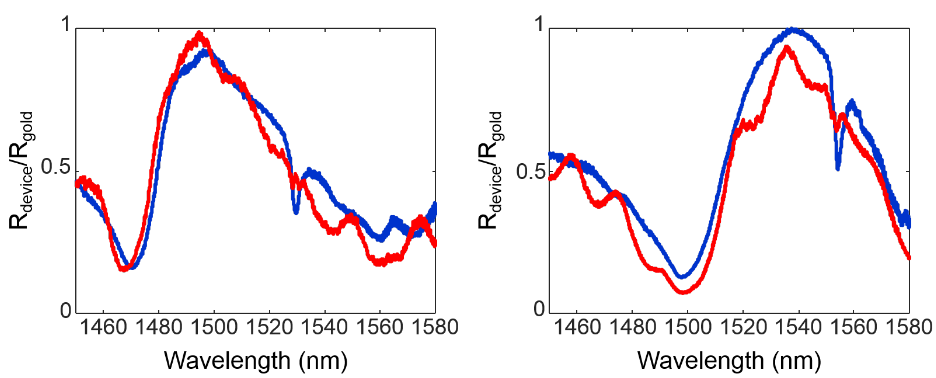

Figure 4.A.2: **Measurement of angle-sensitive reflection spectra. a** and **b** Red and blue curves show the reflection spectra for normal and 6 degree tilted TE polarized incident light, respectively. With 500 nm thickness and 700 nm period of the lattice, the design parameters of a and b are shown in Table 4.A.1.

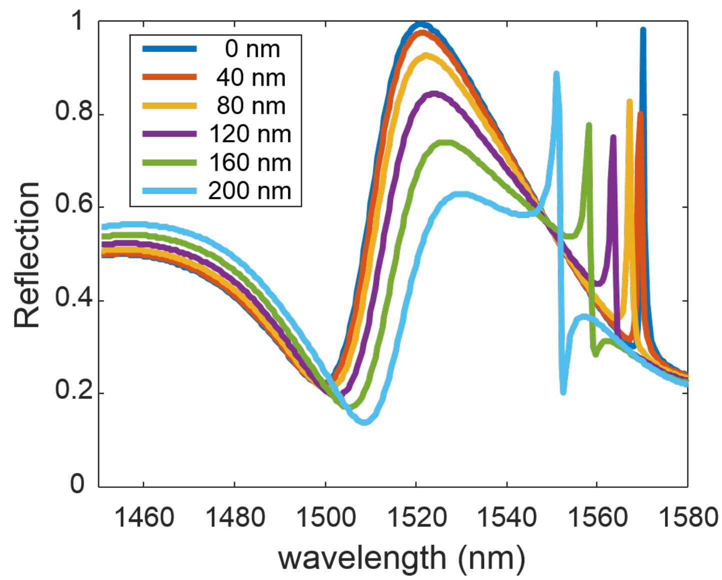

Figure 4.A.3: **Numerical investigation related to spectral shifts of the resonances induced by actuation.** The spectra are simulated under six different values of $g_2 - g_1$ and plotted in different colors. The value of $g_2 - g_1$ for each color is shown in the legends. The width and lattice constant of the device are 480 nm and 700 nm, respectively.

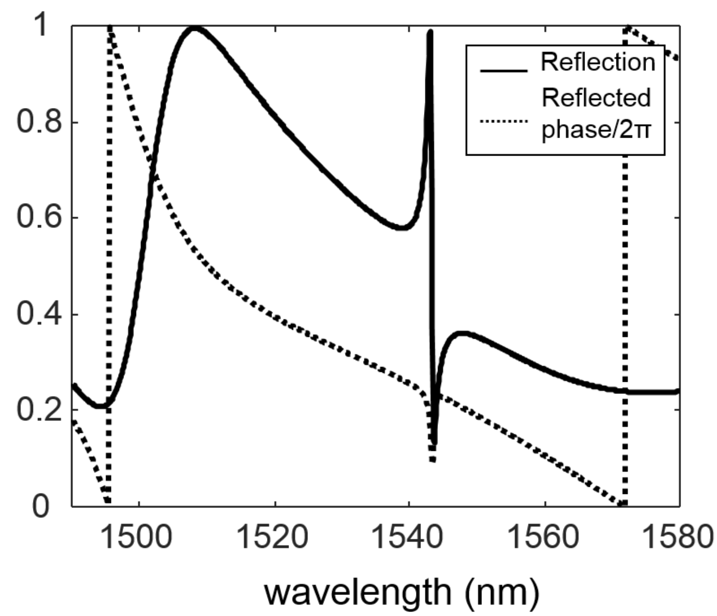

Figure 4.A.4: **Calculated reflection and reflected phase spectra for single BIC resonance.** The quasi-BIC mode is apart from the peak of the GMR. At the resonance wavelength of 1543 nm, the calculated phase response of the quasi-BIC mode is smaller than 55 deg. The width and the lattice of the structures are 475 nm and 666 nm, respectively.

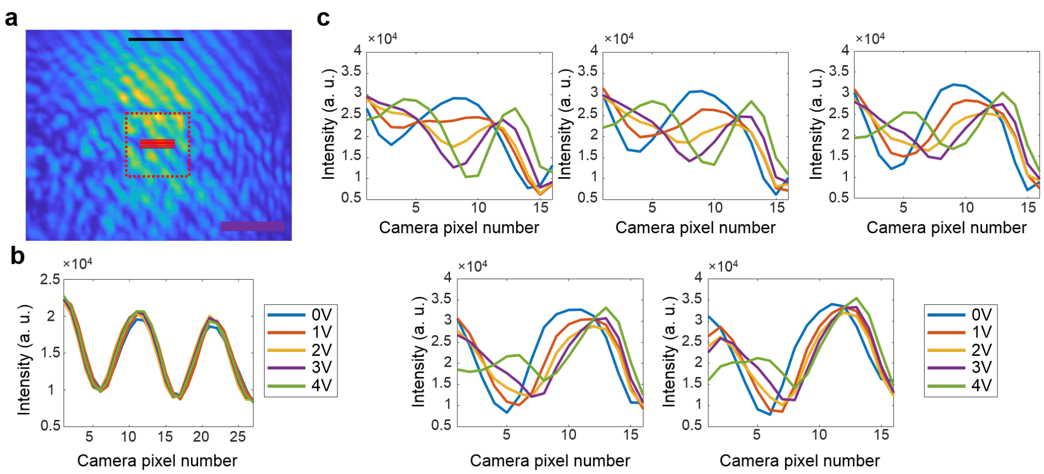

Figure 4.A.5: **Fringe analysis for phase response measurement.** **a** A camera image of the fringes on the measured device. The red dashed square shows the position of the measured device. Five solid red lines inside the red square and a black solid line show the places that we use to analyze the phase responses on the grating and the electrode, respectively. Scale bar denotes 30 μm. **b** The fringe patterns on the electrode under the external biases from 0V to 4V. The fringe patterns are captured along the black solid line in a. The fringes are nearly identical and not shifted for the different voltages. **c** The five fringe patterns on the grating under the external biases from 0V to 4V. The fringe patterns are captured at the center of the grating along the five red solid line in a. The five plots show the clear shifts of the fringes. In b and c, x- and y- axes are pixel number and pixel value of the camera, respectively. The applied biases for all colors are denoted in outsets in b and c.

Chapter 5

NANO-ELECTROMECHANICAL SPATIAL LIGHT MODULATOR ENABLED BY ASYMMETRIC RESONANT DIELECTRIC METASURFACES

Spatial light modulators (SLMs) play essential roles in various free-space optical technologies such as ranging, holographic display, and bio-imaging, offering spatiotemporal control of amplitude, phase, or polarization of light. Beyond conventional SLMs based on liquid crystal or micromechanical systems, active metasurfaces are considered as promising platforms for realization of advanced SLMs because they potentially provide high-speed, high-efficiency, small pixel size, and compact footprints simultaneously. However, the active metasurfaces reported so far have achieved either limited phase modulation or low efficiency. From the perspective of photonic structures, most of reflective active metasurfaces leverage mirrors to achieve strong phase response at resonances. Thus, the way to design efficient reflective active metasurfaces without mirrors has remained elusive. Here, we propose nano-electromechanically tunable asymmetric metasurfaces as a novel platform for reflective SLMs. Exploiting the strong asymmetric radiation of the perturbed high-order Mie reosnance, the proposed metasurfaces without mirrors experimentally achieve large phase shift over 300°, high absolute reflection over 50%, and a wavelength-scale pixel size. Furthermore, we demonstrate electrical control of diffraction patterns, manipulating the electrical biases applied into the nanostructures. This work paves the ways for future exploration of the asymmetric metasurfaces and for their application to the realization of the next-generation SLMs.

5.1 Introduction

Spatial light modulators (SLMs) enable spatiotemporal control of phase, amplitude, or polarization of input free-space light. In particular, phase-dominant SLMs realize efficient wavefront engineering and play essential roles in various applications such as LIDAR [48], holographic display [191], optical computing [192], and bio-imaging [103, 193]. Most of conventional SLMs rely on liquid crystals or micromechanical systems, which result in low speed and limited field of view [194]. On the other hand, metasurfaces have been developed as a new kind of diffractive optical elements, successfully realizing high-performance passive optical components [1, 2, 195]. Complementary to the great advancement of the passive metasurfaces, active metasurfaces may open new opportunities in the development of optical elements because they offer a new degree of freedom in time domain [45]. In particular, the phase-modulated active metasurfaces are considered as a promising platform for next-generation phase SLMs, enabling high-speed and high-resolution in compact footprint. Many seminal works have been proposed in the context of the active metasurfaces, using various active materials or mechanisms such as transparent conducting oxides [46–48], liquid crystal [55], phase-change materials [52], 2D materials [50, 51, 196], electromechanical system [49, 159], and semiconductors [54]. Among these various demonstrations, the most notable examples are active plasmonic metasurfaces based on the transparent conducting oxides [46–48]. The active plasmonic metasurfaces have successfully achieved complex modulation, ranging measurement, or arbitrary wavefront controls [47, 48]. However, as they operate near epsilon near zero regime where the light is critically coupled to lossy plasmonic resonant modes, most of the light is absorbed when large phase shift occurs so the efficiency is significantly limited [48]. Furthermore, the efficiency issue may be severe if scalable metals such as aluminium are used instead of noble metals such as gold. Regarding the photonic structures, most of the reflective active metasurfaces exploit mirrors to achieve strong phase response at optical resonances [46–48, 51, 52, 54]. The presence of the mirror ensures the radiation of the resonance is matched with the input light, enhancing the coupling between the resonance and the input light [183]. However, a way to achieve strong phase shift and high reflection without the mirror has remained illusive.

Here, we propose novel nano-electromechanically tunable asymmetric metasurfaces to realize phase-dominant SLMs. In particular, by exploiting the asymmetric high-Q Mie modes and nano-electromechanical system (NEMS), the active metasurfaces operate as efficient reflective SLMs without mirrors. First, we provide an analytical model that not only describes the physical picture of the proposed system, but also offers design intuitions. We numerically and experimentally verify that the proposed metasurfaces achieve strong phase modulation of 312°, high reflection over 50%, and a wavelength-scale pixel size of $2.186\mu m$. Finally, we demonstrate electrically controllable diffraction in experiment.

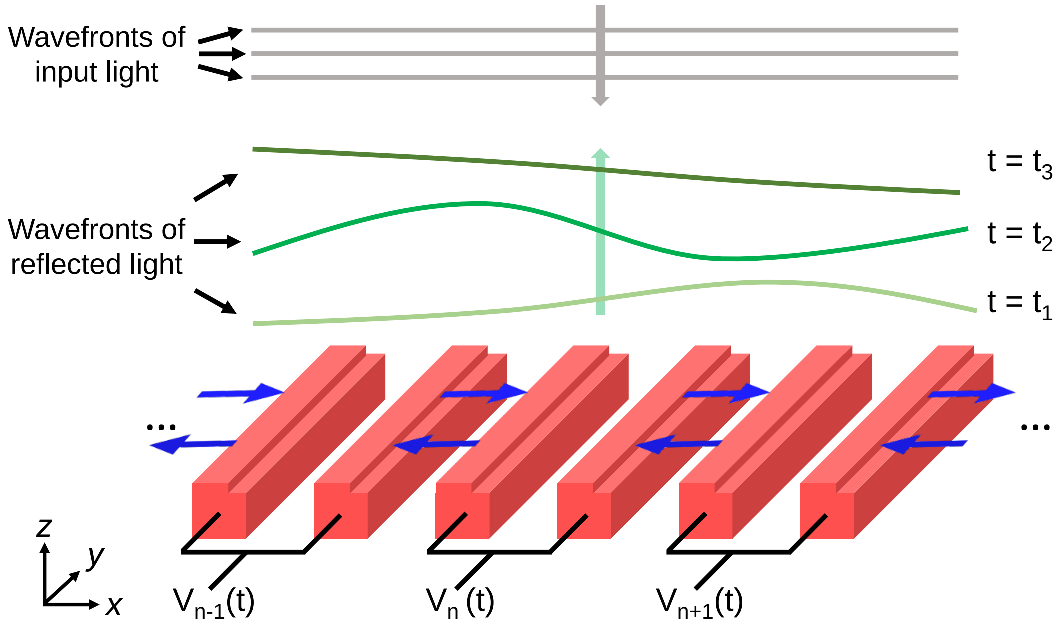

Figure 5.1: **Nano-electromechanically tunable asymmetric metasurfaces and their operation principle** Conceptual illustration of the nano-electromechanically tunable metasurfaces composed of asymmetric suspended nanostructures. Each pair of the nanostructures is connected to individually addressable electrodes. The electrical biases induce electrostatic forces between the neighboring bars, leading to lateral movements of the nanostructures in the x-axis. The blue arrows represent the induced movements. The asymmetric metasurface reflects normally an incident plane wave and dynamically manipulates the wavefront of the reflected light as a function of the applied biases.

5.2 Theoretical and numerical study of asymmetric resonant metasurfaces

Figure 5.1 shows a conceptual illustration of the proposed metasurface. The metasurface consists of suspended silicon (Si) nanostructures having notches at right top corners. Furthermore, each pair of the nanostructures is connected to an electrode enabling its lateral movements [159]. As a result, the metasurface actively manipulates wavefronts of reflected light as a function of the applied biases when the input plane wave is normally incident.

First, we model the suspended metasurface with the temporal coupled mode theory (TCMT) in order to get a rigorous physical picture of the system as well as design intuition [182, 183]. As shown in Fig. 5.2**a**, the metasurface under normal incidence can be generally modeled by a resonator coupled to two ports [197, 198]. When driving the metasurface with a continuous laser, whose frequency is w, the complex reflection coefficient for each port, r_1 and r_2, can be derived by (see Appendix for detailed derivation):

$$r_1 = \frac{i\left[r(w-w_0)\pm\sqrt{\frac{2}{\tau_1^2}+\frac{2}{\tau_2^2}-\frac{r^2}{\tau_{tot}^2}-\frac{1}{r^2\sigma^2}}\right]-\frac{1}{r\sigma}}{i(w-w_0)+\frac{1}{\tau_{tot}}}, \tag{5.1}$$

$$r_2 = \frac{i\left[r(w-w_0)\pm\sqrt{\frac{2}{\tau_1^2}+\frac{2}{\tau_2^2}-\frac{r^2}{\tau_{tot}^2}-\frac{1}{r^2\sigma^2}}\right]+\frac{1}{r\sigma}}{i(w-w_0)+\frac{1}{\tau_{tot}}}, \tag{5.2}$$

where r is the real reflection coefficient of the direct scattering process; w_0 is the resonant frequency; $\frac{1}{\tau_1}$ and $\frac{1}{\tau_2}$ are the resonator's radiative decay rates into port 1 and port 2, respectively; $\frac{1}{\tau_{tot}} = \frac{1}{\tau_1} + \frac{1}{\tau_2}$ and $\frac{1}{\sigma} = \frac{1}{\tau_1} - \frac{1}{\tau_2}$ represent total radiative decay rate and the difference between the two radiative decay rates, respectively. In general, the coupling condition between the port and the resonator determines the phase response of the reflected light [183]. Specifically, when a decay rate into a certain port is larger than the sum of other decay rates including radiative and non-radiative decay rates, the resonance is over-coupled to the port and the over-coupling results in almost 2π phase shift in reflection across the resonance frequency. In contrast, when a decay rate into a port is smaller than the sum of other decay rates, the resonance is under-coupled to the port such that the phase shift in reflection becomes negligible. To achieve the desired phase modulation, we aim to design the over-coupled resonator and tune its strong phase response near the resonance frequency [184, 199]. In Eqs. 5.1 and 5.2, the coupling conditions between the port and the resonator are determined by the $\frac{1}{\sigma}$. If $\frac{1}{\sigma} > 0$, the port 1 is over-coupled and the port 2 is under-coupled, and vice versa. Besides, strong asymmetric radiation leads to a large magnitude of $\frac{1}{\sigma}$, making the magnitude of $\frac{1}{r\sigma}$ comparable to the magnitude of $\frac{1}{\tau_{tot}}$ in Eqs. 5.1 and 5.2. As a result, the strong asymmetric radiation can make the reflection loss at the resonance and the variation in reflection spectra decrease [184]. Finally, the ratio between the two decay rates is bounded and the bound is determined by the direct scattering process [197]:

$$\frac{1-r}{1+r} \le \frac{\tau_2}{\tau_1} \le \frac{1+r}{1-r}. \tag{5.3}$$

In particular, Eq. 5.3 indicates that high r is necessary for the desired strong asymmetric radiation.

In contrast to the asymmetric cases, the symmetric resonators always have the same $\frac{1}{\tau 1}$ and $\frac{1}{\tau 2}$, which lead to $\frac{1}{\sigma}$ of zero. Therefore, critical coupling always occurs in

Eqs. 5.1 and 5.2, resulting in negligible reflection and π phase shift near the resonant frequency. Furthermore, this unwanted critical coupling even happens for oblique incident light when the resonator is symmetrically coupled to the available ports (See Appendix for details). As a result, the limited performance of the symmetric resonator explains why the asymmetry in the resonator is essential for high-efficient phase modulation when the surrounding environment is symmetric.

It is worth explicitly noting here that the TCMT describing the asymmetric resonators has been explored previously [197, 198]. Besides, the asymmetric photonic crystal resonator has been demonstrated very recently [200]. However, the phase responses of the resonances have been mostly overlooked. Up to our best knowledge, the asymmetric metasurfaces' potentials in active devices have not been explored yet.

To implement the model based on the TCMT, we first simulate the metasurfaces possessing the mirror symmetry in the z-direction. In Fig. 5.2**b**, the metasurface grating is composed of Si nanobars and surrounded by air. Specifically, the 841 nm wide and 838nm thick 2D nanostructures are periodically arranged with the lattice constant of 1093 nm. Referring to Eq. 5.3, we carefully select the thickness, width, and lattice constant of the unperturbed structures to make r higher than 0.9 in telecom wavelength range. Figure 5.2**c** shows an electrical field profile of the TE-polarized eigenmode at Γ point. The mode in Fig. 5.2**c** originates from the Mie mode hosted by individual Si nanostructures (see Fig. 5.A.1 for details). It is worth explicitly noting why we select the high-order Mie mode instead of the guided mode. Supported by the individual nanostructure instead of the periodic lattice, the Mie mode is potentially more robust against breaking of periodicity than the guided mode. As a result, in the scheme of the nano-electromechanical modulation shown in Fig. 5.1, each pair of the nanostructures individually hosts the resonance and works as an independent reflective resonant antenna [2]. Reflection and reflected phase spectra are calculated under 0° and 5° tilted incident lights and plotted in Figs. 5.2**d** and 5.2**e**. The resonance is not coupled to the normally incident light in Figs. 5.2**d** and 5.2**e**. That is due to the symmetry mismatch between the excitation and the eigenmode. In detail, the plane-wave excitation and the eigenmode in Fig. 5.2**c** are odd and even under C_2 rotation, 180° rotation around the z-axis, respectively. In contrast, the 5° tilted light excites the resonant mode by breaking the odd symmetry of the incident light. However, the critical coupling between the excitation and the resonant mode occurs, causing negligible reflection at the resonance in Fig. 5.2**d** and limited phase shifts smaller than 180° in Fig. 5.2**e**. Finally, the results shown in

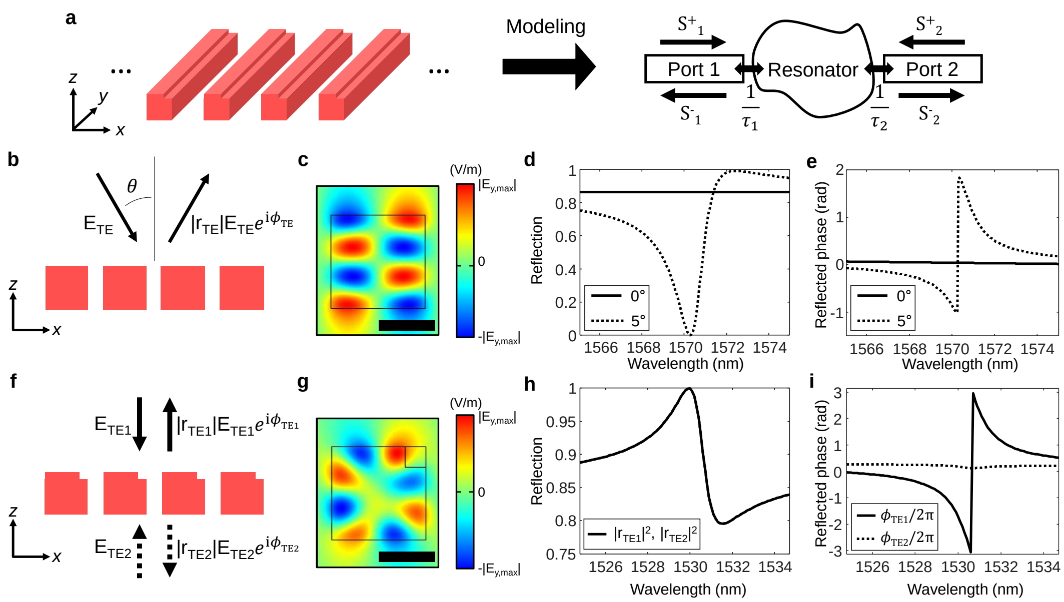

Figure 5.2: **Numerical investigations on resonant reflection behaviors of symmetric and asymmetric metasurfaces. a** Schematic of a periodic metasurface (left) and illustration of the corresponding analytical model based on an optical resonator coupled to two ports (right). The model describes the asymmetric metasurface under normal incident light. s_1^+ (s_2^+) and s_1^- (s_2^-) are incoming and outgoing waves through the port 1 (port 2), respectively. The resonance decays into the port 1 and 2 with decay rates, $\frac{1}{\tau 1}$ and $\frac{1}{\tau 2}$, respectively. **b** Schematic illustration of the suspended symmetric metasurfaces. The metasurface possesses mirror symmetry in the z-direction with respect to the middle of the nanostructure. The TE polarized light is incident on the metasurface. **c** Simulated electrical field profile of the eigenmode at Γ point. At the wavelength of 1568 nm, the y-components of the electrical fields are plotted. Scale bar denotes 500 nm. **d** and **e** Calculated reflection and reflected phase spectra of the symmetric metasurfaces. Solid and dashed curves show the spectra for 0° and 5° degree tilted TE polarized incident light, respectively. **f** Schematic illustration of the asymmetric metasurfaces. The structure is the same as the structure in **b**, except the notches placed at the right top corners. The notches have square cross-cessions and their side length is 143 nm. The TE polarized light is normally incident from either the top or the bottom side of the metasurface. $|r_{TE,1}|$ ($|r_{TE,2}|$) and $\phi_{TE,1}$ ($\phi_{TE,2}$) are reflected amplitude and phase for the top (bottom) illumination, respectively. **g** Simulated electrical field profile of the asymmetric metasurface's eigenmode at Γ point. At the wavelength of 1531 nm, the y-components of the electrical fields are plotted. Scale bar denotes 500 nm. **h** and **i** Calculated reflection and reflected phase spectra of the asymmetric metasurfaces for top and bottom illuminations. **h**: The reflection spectra are identical for both illumination condition, thus plotted by one solid black curve. **i**: Solid and dashed curves represent the reflected phase spectra for the top and bottom illuminations, respectively.

Figs. 5.2**d** and 5.2**e** agree with the previous discussion of the symmetric resonator.

To achieve strong phase response with high reflection, we break the symmetry of the nanostructures in Fig. 5.2**f**, making the notch at the right top corner of each nanostructure. Each notch has a square cross-section in the $x-z$ domain and its side length is 184 nm. In addition, the notches at the corners simultaneously break the mirror symmetry in the z-direction as well as the even symmetry of the resonant mode under C_2 rotation. The former aims to improve phase responses through asymmetric radiations, the later enables coupling between the Mie mode and normally incident light. Figure 5.2**g** shows the electrical field profile of the eigenmode of the asymmetric metasurface at Γ point. In Fig. 5.2**g**, the high-order Mie mode is preserved with some variations in the electrical fields compared to the symmetric field profile in Fig 5.2**c**. The spectra of the reflection and reflected phase are calculated for top and bottom illuminations and plotted in Figs. 5.2**h** and 5.2**i**. Specifically, the calculated reflection spectra are identical for both illumination conditions in Fig. 5.2**h**, whereas the phase responses in Fig. 5.2**i** show strong and negligible phase response for the top and bottom illuminations, respectively. The illumination-dependent phase responses in Fig. 5.2**i** result from the distinct coupling conditions determined by the two radiative decay rates. In particular, for the top illumination, the metasurfaces simultaneously achieve $\sim 2\pi$ phase shift and high reflection over 78% over the spectrum. We also fit the simulated spectra in Figs. 5.2**h** and 5.2**i** by using Eqs. 5.1 and 5.2 (see Fig. 5.A.2 for details). From the fitting in Fig. 5.A.2, we find the Q-factor and $\frac{\tau_2}{\tau_1}$ of 1004 and 17.52, respectively. The aforementioned values show good agreement with the numerical eigenmode analysis in Fig. 5.A.3.

5.3 Numerical investigations on nanomechanical phase modulation and beam steering

We numerically investigate the phase modulation, utilizing the nano-electromechanical movement in lateral directions [159]. For every two pairs of nanostructures, the asymmetric nanostructures are either grounded or connected to an external bias in Fig. 5.3**a**. g_1 and g_2 are gap distances between the nanostructures having different and same biases, respectively. The applied bias enables the continuous control of the nanomechanical movement, expressed by $\frac{g_1-g_2}{2}$. To numerically implement such nano-electromechanical tuning of the resonance, a pair of nanostructures is simulated by changing $\frac{g_1-g_2}{2}$. As the period of a pair of the nanostructures, 2Λ, is 657 nm larger than a design wavelength of 1529 nm in Fig. 5.3**a**, the induced nanome-

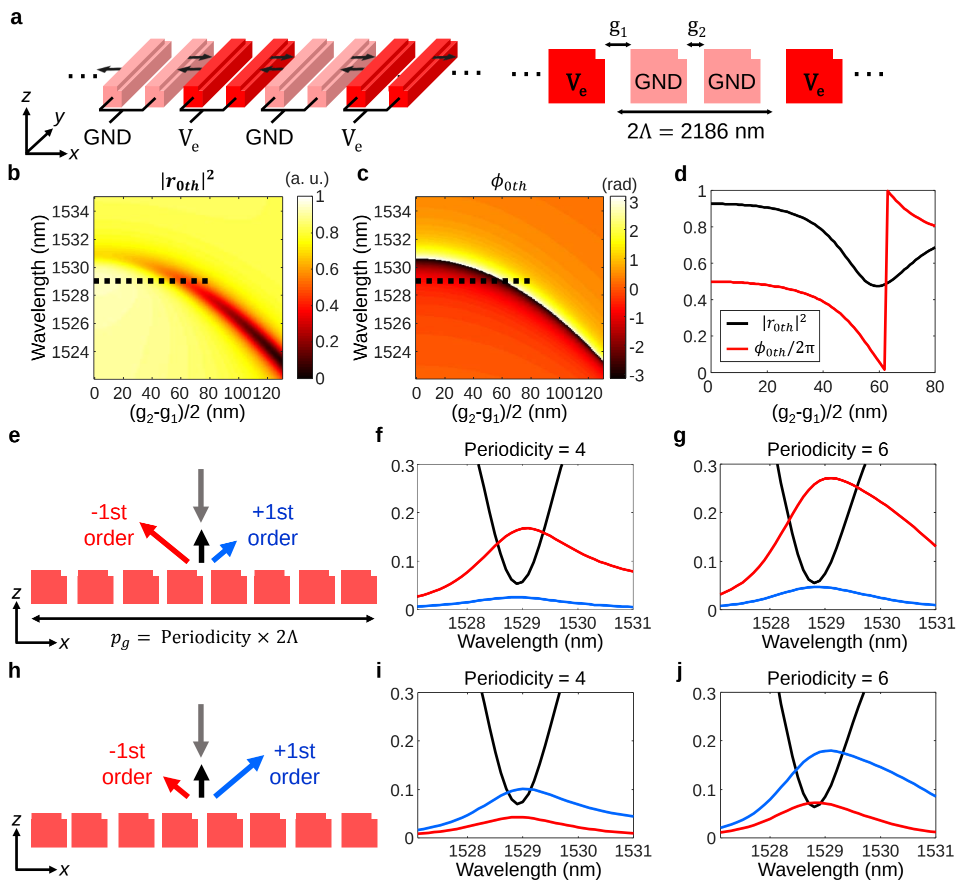

Figure 5.3: **Simulations on nano-electromechanical phase modulation and beam steering a** Schematic illustration of an array of pairs of the asymmetric nanostructures. For every two pairs of the nanostructures, one pair is connected to ground, GND, and the other pair is connected to an external bias, V_e. Pink and red colors represent GND and V_e, respectively. Left: When the external bias is applied, induced electrostatic forces result in lateral movements of the nanostructures. The black arrows show the corresponding movements. Right: The side view of the asymmetric metasurfaces is shown with design parameter definitions. **b** Calculated spectra of reflected power coefficient and phase of the 0th order diffraction, $|r_{0th}|^2$ and ϕ_{0th}. The spectra are plotted as a function of the nanomechanical tuning, $\frac{g_2-g_1}{2}$. **d** Calculated nanomechanical tuning of $|r_{0th}|^2$ and $\phi_{0th}/2\pi$ at the wavelength of 1524 nm. $|r_{0th}|^2$ and $\phi_{0th}/2\pi$ are plotted by black and red curves as a function of $\frac{g_2-g_1}{2}$, respectively. The corresponding data is noted by black dashed lines in **b** and **c**. **e** (**h**) Conceptual illustration of nanomechanical beam steering with negative (positive) phase gradients. In reflection, the -1st (1st) order diffraction is dominant over the 0th and +1st (-1st) order diffractions. **f** and **g** (**i** and **j**) Calculated reflected power coefficient spectra of the 0th and ± 1st order diffractions where phase-gradient is negative (postive). The spectra of the 0th, -1st and +1st order diffractions are plotted by black, red, and blue curves, respectively. The periodicities of the metasurface are 4 and 6 pairs in **f** (**i**) and **g** (**j**), respectively.

chanical movement causes unwanted diffraction orders at ±44°. Nevertheless, we expect that the high-order diffraction could be suppressed when we expand the periodic boundary for desired wavefront engineering. The reflected power coefficient and phase of the 0th-order, $|r_{0th}|^2$ and ϕ_{0th}, are calculated and plotted in Fig. 5.3**b** and 5.3**c**, respectively. In Fig. 5.3**b**, the blue shift of the resonances and the decrease of the minimum reflection are observed when the induced nanomechanical movement increases. Specifically, the decrease of the minimum reflection dominantly results from the ±1st order diffractions (see Fig. 5.A.4 for the calculated reflected power coefficient spectra of the ±1st order diffractions). In Fig. 5.3**c**, the mechanical tuning results in a continuous blue-shift of the resonance while the strong phase response remains at the resonance, indicating that the phase can be readily modulated by the nanomechanical tuning near the resonant wavelength. In particular, at the wavelength of 1529 nm, $|r_{0th}|^2$ and ϕ_{0th} are plotted in Fig.5.3**d** as a function of the nanomechanical tuning, revealing that the nanoscale movement within 80 nm can lead to phase modulation up to 252° with minimal $|r_{0th}|^2$ over 0.47. In Fig. 5.3**d**, we set the maximum mechanical movement at 80 nm to avoid irreversible stiction of the nanostructures, which is known as pull-in effect.

Next, we numerically investigate the metasurfaces' capability of beam steering, utilizing a pair of the nanostructure as a building block of the proposed active metasurfaces. Specifically, the gaps of the pairs of nanostructure are adjusted by the applied biases so that the metasurface manipulates the wavefronts of the reflected light. When assuming that the phase is locally determined by the gap of the two nanostructures, we can exploit the relationship between ϕ_{0th} and $\frac{g_1-g_2}{2}$ plotted in Fig 5.3**d** as a lookup table to design the metasurfaces. In other words, once the desired phase distribution is determined, the gaps of nanostructures can be inversely obtained from Fig. 5.3**d**. It is noteworthy to mention that this lookup table approach is widely used in passive and active metasurfaces. First, we investigate a blazed diffraction grating of which the linear phase gradient is negative. As shown in Fig. 5.3**e**, the period of the grating, p_g, is determined by periodicity and 2Λ, where the periodicity represents the number of the pairs in one period of the blazed grating. As the blazed grating is designed to have the negative phase gradient of $-\frac{2\pi}{p_g}$, the metasurfaces expect to cause the dominant −1st order diffraction at the angle of $-\theta_g = -sin^{-1}(\frac{\lambda}{p_g})$. We simulate negative phase gradient gratings having periodicity of 4 and 6. The spectra of reflected power coefficients for the 0th and ±1st and order diffractions are plotted in Figs. 5.3**f** and 5.3**g**. At 1529 nm, the reflected power coefficients of the −1st order diffraction are 16.7 and 27.0% in Figs. 5.3**f** and 5.3**g**, respectively. In contrast, the calculated reflected power coefficients of the +1 st (0th) order diffraction are 2.53% (5.69%) and 4.66%(7.47%) in Figs. 5.3**f** and 5.3**g**, respectively. Similarly, the blazed gratings with positive phase gradients are also investigated. In Fig. 5.3**h**, the arrangement of the gap sizes are simply reversed compared to the arrangement of the negative phase gradient blazed gratings shown in Fig 5.3**e**. Then, the reversed nanomehcanical displacements realize the positive phase gradient of $\frac{2\pi}{p_g}$, expecting to result in the dominant +1st order diffraction at the angle of θ_g. The reflected power coefficient spectra of the positive phase gradient blazed gratings are plotted in Figs. 5.3**i** and 5.3**j**. The dominant +1st order diffraction and the suppressed 0th and −1st order diffractions are observed in Figs 5.3**i** and 5.3**j**. At the design wavelength of 1529 nm, the reflected power coefficients of the +1st order diffraction are 10.1% and 18.0% in Figs. 5.3**i** and 5.3**j**, respectively. At the same wavelength, the calculated reflected power coefficients of the −1st (0th) diffraction order are 4.26% (7.46%) and 7.11%(8.49%) in Figs. 5.3**i** and 5.3**j**, respectively. For both periodicities of 4 and 6, the negative phase-gradient gratings used in Figs. 5.3**f** and 5.3**g** perform more efficiently than the positive phase-gradient gratings used in Figs. 5.3**i** and 5.3**j**. The same trend can be also found in the case of periodicity of 1 (see Fig. 5.A.4 for details). We expect that these differences inherently result from the asymmetry of the structure with respect to x-axis. Besides, at the design wavelength of 1529 nm, reflected power coefficients of all available diffraction orders are plotted in Fig. 5.A.5, showing that all high-order diffraction components are suppressed compared to the desired diffraction order.

5.4 Fabrication and optical characterization of the active metasurfaces

We fabricate the active metasurface using a standard silicon-on-insulator wafer and sequential nanofabrication process (see Methods for details). Figure 5.4**a** shows a photographic image of the device. In Fig. 5.4**a**, the fabricated device is wire-bonded to a custom-made printed circuit board for connections to the external electrical sources. Scanning electron microscope images of the devices are shown in Figs. 5.4**b-d**. The metasurface consists of 36 pairs of the asymmetric suspended nanostructures. In this paper, all of the nanostructures are 50 μm long in y-axis and both ends of the nanostructures are connected to either anchors or large silicon layers that are supported by the buffered oxide layers [159]. Furthermore, g_1 and g_2 are adjusted in the fabrication process to make g_1 120 nm smaller than g_2 such that the nano-electromechanical tuning leads to efficient tuning of the resonance. In Fig. 5.4**d**, the fabricated asymmetric nanostructures show great agreement with

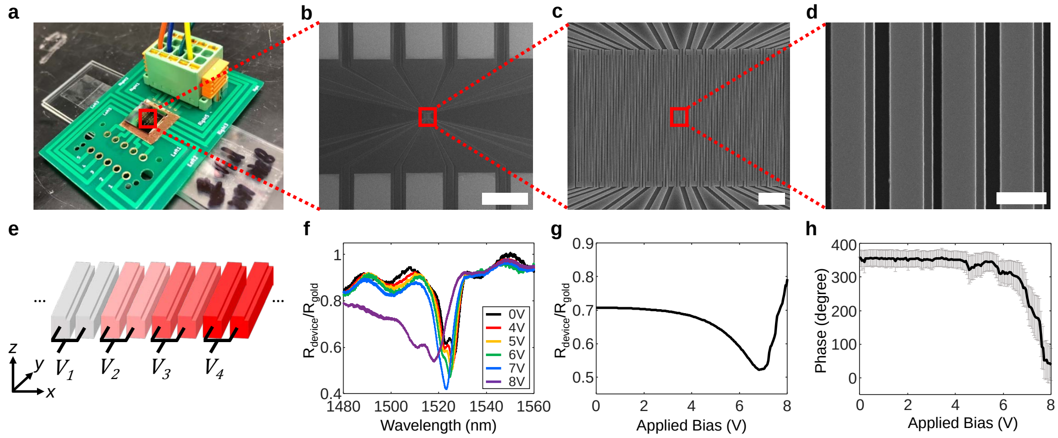

Figure 5.4: **Optical characterization of dynamic properties of the asymmetric nano-electromechanical metasurface. a** Optical image of the fabricated metasurface. Electrodes in the device are wire-bonded to a custom printed circuit board. **b-d** Scanning electron microscopy images of the metasurface. Every pair of the nanostructure is connected to the electrodes. Scale bars in b, c, and d denote 500, 10, and 1 μm, respectively. **e** Schematic of electrical configuration. Four different electrical biases, V_1, V_2, V_3, and V_4, are periodically applied to every four pairs of the nanostructures. In **f-h**, V_2 and V_4 are equally changed with V_1 and V_3 grounded. **f** Measured reflection spectra for TE-polarized normally incident light. The spectra are measured under six different biases and plotted in different colors. The applied bias for each color is shown in legend. The reflection spectra are normalized by the reflection from a gold electrode. **g** Measured intensity modulation under different biases at the wavelength of 1524 nm. The applied bias varies from 0V to 8V. **h** Measured phase shift of the metasurface at the wavelength of 1524 nm as a function of the applied biases from 0V to 8V. Error bars represent standard deviations of the estimated phase shifts.

the design shown in Fig. 5.1. Figure 5.4**e** illustrates the electrical configuration of the device, showing that every four pairs of nanostructures are connected to four different electrodes. In Fig. 5.4**e**, V_1, V_2, V_3, and V_4 denote the four different applied biases. The voltage differences between the neighboring nanostructures locally determine the gap sizes. The electrical configuration shown in Fig. 5.4**e** enables the nano-electromechanical modulation with periodicity of 4.

We characterize the tunable optical properties, implementing the scheme shown in Fig. 5.3**a**. While V_1 and V_3 are grounded, V_2 and V_4 are connected to the external biases. When the TE-polarized light is normally incident, the reflection spectra are measured under different external biases and plotted in Fig. 5.4**f** (see Methods and Fig. 5.A.6 for details). Without any bias, the resonance dip was observed around

1526 nm in Fig. 5.4**f**, showing good agreement with the simulated resonance dip at 1529 nm shown in Fig. 5.3**b**. We believe that the small deviation results from slight errors in fabrication. When the bias changes from 4V to 7V, blue-shift of the resonances and decrease of the minimum reflection are observed in Fig. 5.4**f**, showing great agreement with the simulated results in Fig. 5.3**b**. As an objective lens in the setup cannot capture the diffraction at ~44 degree, the decrease of minimum reflection in Fig. 5.4**f** can be explained by the increase of the ±1st-order diffractions (see Fig. 5.A.4 for details). However, the spectrum measured with the bias of 8V in Fig. 5.4**f** results in increase of the minimum reflection, abrupt broadening of the resonance, and a large spectral shift of −8nm, deviating from the simulation results in Fig. 5.3**b**. We believe that the deviation results from non-negligible bending of the nanostructures at the large applied bias.

We experimentally investigate electrical modulations of reflection and reflected phase. Like the measurements in Fig. 5.4**f**, we implement the electrical configuration shown in Fig. 5.3**a**. To measure the intensity as a function of the applied bias, the reflection is measured at 1524 nm by increasing the applied bias from 0 to 8V. The measured reflection is plotted as a function of the applied bias in Fig. 5.4**g**, showing that the measured reflection is higher than 50% (see Supplementary Fig. 5.A.7 for measured amplitude modulations at different wavelengths). Figure. 5.4**g** can be qualitatively explained by the blue shifts observed in Fig. 5.3**b** and Fig. 5.4**f**. In Fig. 5.4**f**, the resonance dip is placed at 1526 nm without any bias. As the applied bias increases, the resonance is continuously blue-shifted so the resonance dip moves towards the measured wavelength of 1524 nm. From the position of the dip in Fig. 5.4**g**, the resonance dip is placed at 1524 nm when the applied bias is around 6.91V. For the further increase of the bias, the resonance dip is blue-shifted below 1524 nm and the shift results in increase of the reflection. In addition, we measure the phase modulation at 1524 nm by varying the applied bias. For the measurement of the phase shifts, we employ a Michelson-type interferometer setup [159]. As the field of view of the objective lens is larger than the device size, the input light illuminates the metasurface and unpatterend regions at the same time and forms fringes with a reference beam at the image plane. The phase shift is mainly evaluated by the shift of the fringes on the metasurface, while we ensure that the fringes on the unpatterned regions are unchanged. Figure 5.4**h** shows measured phase shifts as a function of the applied bias at the wavelength of 1524 nm. First of all, the device achieves large phase modulation over 312° within the applied bias of 8V. Although the measured phase modulation is 61° larger than the simulated phase modulation shown in Fig. 5.3**d**, the enhanced phase modulation in the measurement may result from significant resonance shifts observed in Fig. 5.4**f** at the applied bias of 8V. As discussed before, the non-negligible bending effect at the large electrical bias may result in the large tuning of the resonance. In Fig. 5.4**h**, the phase shift mostly occurs over 6V and the phase shift of ~180° is observed with the applied bias of 7.37V.

5.5 Experimental demonstration of electrically controllable diffraction

After validating the wide phase tunability and high reflection, we demonstrate electrical control of the diffraction patterns. As shown in Fig. 5.4**e**, the device has the fixed periodicity of 4, so it realizes beam splitting into the ±1 st orders and beam deflection into the +1st or −1st order with the θ_g of 10.04°. While V_1 is connected to ground, the values of V_2, V_3, and V_4 are controlled to verify the dynamic diffraction patterns in experiment. We image a Fourier plane of the metasurface such that the diffraction patterns from the metasurface are directly measured (see Methods and Fig. 5.A.6 for details). First, we only increase V_4 from 0 to 8 V continuously and observe the changes in the Fourier plane. In Fig. 5.5**a**, the diffraction occurs near ±10° for the large bias over 6V. As shown in Figs. 5.5**a** and 5.5**b**, negligible signals are observed at 10° when no bias is applied. The strongest diffraction intensity is observed when V_4 is at 7.63V in Figs. 5.5**a** and 5.5**c**. Furthermore, the −1st order signal was stronger than the +1st order signal in Fig. 5.5**c**. This asymmetric diffraction mainly results from the inherent asymmetry of the structure, showing agreement in the numerical results shown in Fig. 5.3**d-i** and Fig. 5.A.4. Interestingly, when the V_4 further increases up to 8V, the devices achieve comparable ±1st order diffractions in Fig. 5.5**d** so nearly symmetric beam splitting is realized. Next, we start to control V_2, V_3, and V_4 for the demonstration of the beam deflection into the −1st or +1st order diffraction. In Fig. 5.5**e**, the device achieves the strong −1st order of which normalized intensity reaches 44%. Compared to the results shown in 5.5**c**. the +1st order diffraction is well suppressed in 5.5**e** and its normalized intensity is as small as 9 %. Likewise, the device can provide strong +1st order diffraction by adjusting the electrical bias reversely. In Fig. 5.5**f**, the strong +1st order diffraction is observed. Compared to the results in Fig. 5.5**d**, the −1st order is well suppressed but the peak intensity of the +1st order is rarely changed in Fig. 5.5**f**.

In addition to the electrical diffraction control, we should mention that the lobes near 0° in Figs. 5.5**a-e** are split. We believe that the finite size of the sample and the electric field profile in Fig. 5.2**g** result in the splitting of the main lobe. Although the

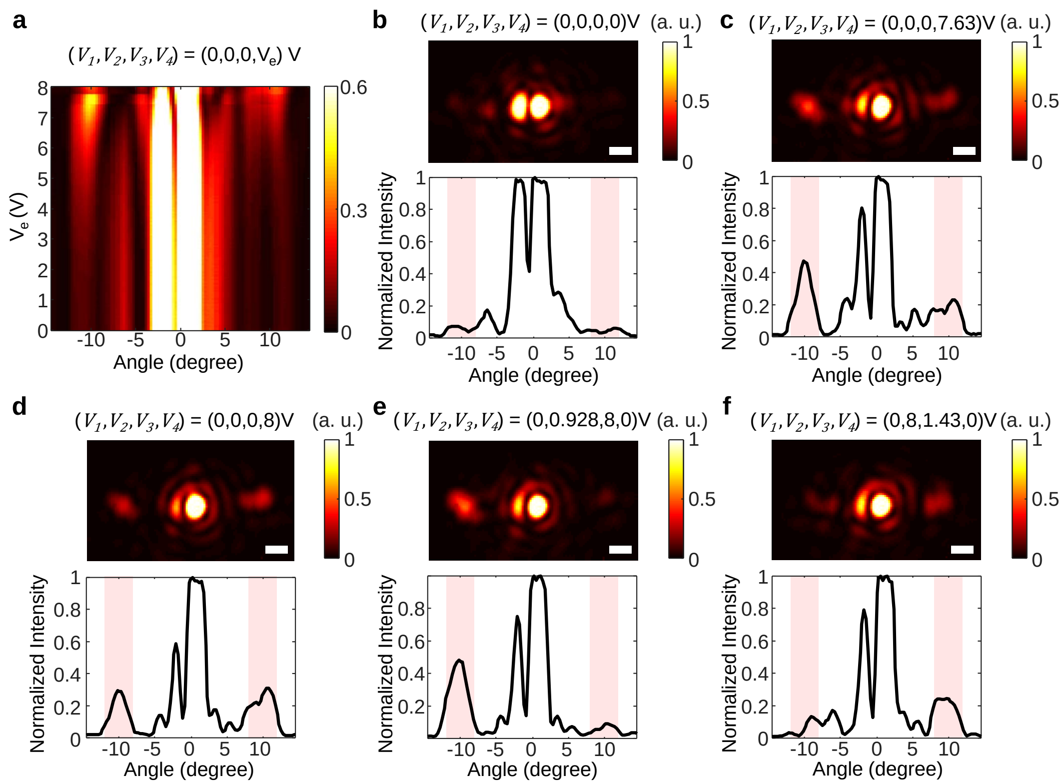

Figure 5.5: **Tunable diffraction with the asymmetric nano-electromechanical metasurface. a** Measured intensity at the Fourier plane of the metasurface. The intensity is measured at the 1524 nm as a function of the applied bias from 0V to 8V. At each bias, the intensity is normalized by the peak intensity near 0°. The ± 1st order diffractions start to appear near $+pm10°$ when the applied bias is over 6V. On top of the image, the values of V_1-V_4 are noted and V_4 is only changed. **b-f** Measured diffraction patterns at the wavelength of 1524 nm. The applied biases are changed for each result. (top) Normalized intensity images are measured at the Fourier plane of the metasurface. The values of V_1-V_4 are noted on top of the images. Scale bars are $0.05k_0$ where k_0 is a magnitude of wave vector in free-space. (bottom) Measured cross-sectional intensity profiles are plotted as a function of the diffraction angle. The intensities are normalized by the peak intensity at 0°. The diffracted signals near ±10° are denoted by pink shades.

notches break the symmetry in the x-axis, the field profile in Fig. 5.2**g** is nearly anti-symmetric along the x-axis from the center of the nanostrcuture, so we expect that the individual antenna weakly radiates into the 0°. Then, the finite size may allow non-zero angle radiation of the individual antenna even under normally incident light, potentially resulting in a dip around the center of the main lobe. Nonetheless, we can readily move the resonance away from the operating wavelength by inducing the large electrostatic forces and it shows the large lobe near 0° without any artifacts in experiment (see Fig. 5.A.8 for details).

Furthermore, the strong 0th order signals are observed in Fig. 5.5**a-e**, indicating that the diffraction efficiencies are not as good as the numerical results shown in Figs. 5.3**f**, 5.3**g**, 5.3**i**, and 5.3**j**. We expect that the low experimental efficiency mainly results from the imperfect fabrications and the finite size effect. To demonstrate efficient devices in experiment, we fabricate another array of the metasurfaces with changes in the electrical configuration (see Fig. 5.A.9 for details). The best device shows the ±1st order diffractions whose normalized intensities are larger than the 0th order diffraction (see Fig. 5.A.9 for details). It experimentally points out that further optimization in the nanofabrication process improves the diffraction efficiency of the device.

5.6 Discussion and outlook

We utilized the asymmetric dielectric metasurfaces for the realization of tunable phase SLMs, revealing that the asymmetric radiation is the key characteristic for the designs of the reflective SLMs without mirrors. The asymmetric metasurfaces have not just shown interesting physical properties such as a strong single-sided phase response, but also offered practical advantages. For example, the proposed asymmetric structure uniquely has allowed for the use of standard silicon-on-insulator wafers in which the mirrors are usually not included. Furthermore, the strong phase response of the asymmetric metasurfaces can be modulated by not only NEMS, but various active mechanisms in general. For example, one can employ thermo-optic [184], plasma-dispersion [201], DC-induced Kerr [202], and electro-optic [203, 204] effects for all-solid-state active metasurfaces without significant changes in the photonic design. Such all-solid-state active metasurfaces expect to overcome several limits of the mechanical systems such as fragility and limited aperture size.

In the numerical investigations on the beam steering capability of the active metasurfaces shown in Fig. 5.3**f**, 5.3**g**, 5.3**i**,and 5.3**j**, all of the structures are designed by using the lookup table in Fig. 5.3**d**. Although this intuitive approach enables large-scale designs with moderate efficiencies, the efficiencies of the metasurfaces can potentially be improved using optimization process [205]. Specifically, the parameterized adjoint optimization can be performed with arbitrary target wavefronts to determine optimal arrangement of the gap distances between the nanostructures [206]. For the moderate size of the device, we expect the parameterized adjoint optimization to yield significant improvement in efficiency.

In addition, it is worth noting that the tunable strong phase response shown in Fig. 5.3**c** is a necessary condition for wavefront shaping at wavelength scale. For example, in Ref. [159], interference of two guided mode resonances have led to similar nanomechanically tunable phase responses. However, the device could not support the wavefront engineering at wavelength or sub-wavelength scale. Therefore, the difference in performance makes the presented efficient beam steering performance unique. As explained before, we believe that the presented beam steering performance mainly results from the use of high-Q Mie mode resonance. The results presented here open up new questions about the design process of nano-electromechanical active metasurfaces: "What resonant modes can we use for high-resolution phase SLMs?" "What is a sufficient condition for the wavefront shaping?" etc. In general, we expect that the questions are fundamentally related to complicated interactions between non-periodic resonant nanostructures.

We employed two sequential nanofabrication processes to create asymmetric nanostructures shown in Fig. 5.4**d** (see Methods for details). Although the high-end CMOS fabrication process supports the multi-layer nanofabrication with high accuracy, the complexity of the multi-layer nanofabrication and the high accuracy required in the fabrication process may hinder scalable production of the proposed devices. However, we envision that slanted gratings can replace the proposed structures for the scalable production. In particular, it has been recently shown that the slanted gratings can achieve asymmetric radiations [200]. More importantly, the slanted gratings can be fabricated with a single lithography step and angled etching techniques [200]. Thus, the slanted structures potentially allow for integration of our asymmetric active metasurfaces in a scalable fashion using the mature standard optical MEMS foundry process.

In summary, we experimentally demonstrated the nano-electromechanically tunable phase SLMs, which are enabled by the asymmetric metasurfaces. Besides, a rigorous theoretical modeling based on temporal coupled mode theory was shown, offering detailed physical explanations and design intuitions. Furthermore, the active metasurfaces numerically and experimentally achieved wide phase tunability, high absolute reflection, and a wavelength scale pixel size. Finally, we demonstrated the nano-electromechanical control of diffraction patterns using the proposed metasurfaces. In general, this work experimentally showcases the potential of the asymmetric resonant dielectric metasurfaces in their applications to the next-generation SLMs.

5.7 Methods

Simulation and design

The reflected spectra are calculated using the rigorous coupled wave analysis technique [95]. Assuming the infinite length of silicon nanostructures, 2D simulations were performed. While we assume that the silicon structures are surround by air in Fig. 5.2, 700-nm air gap, 2300-nm thick silicon oxide layers and silicon substrate are added underneath the silicon structure in Fig. 5.3 to simulate the fabricated devices. The eigenmode analysis shown in Figs. 5.2**c**, 5.2**g**, **S1**, and **S3** are performed using a commercial software based on finite elements method, COMSOL®. Refractive indices of Si and SiO_2 for the telecom wavelength in the simulation are 3.4 and 1.45, respectively.

Device fabrication

We use a silicon-on-insulator wafer with a device layer of 1500 nm and a buffered oxide layer of 3 μm on a 1 mm thick silicon substrate. First of all, the device layer is thinned down to the target thickness of ~838 nm using reactive-ion-etching with a gas mixture of SF_6 and C_4F_8. The nanofabrication includes three sequential electron beam lithography steps, the first one for the grating structures, the second one for the notches, and the last one for the electrodes. For all electron beam lithography steps, a ~300-nm-thick positive electron resist (ZEP-520A, Zeon) is spin-coated on the device. The patterns are generated by 100 kV electron beam exposure (EBPG5200, Raith GmbH), and the resist is developed in a developer solution (ZED-N50, Zeon). To pattern the gratings and notches, the ZEP resist is utilized as a soft mask in the reactive ion etching steps and then removed by remover PG (Microchem). After the fabrication of the aysmmetric silicon nanostructures, the electrodes were patterned by electron beam lithography, the deposition of chrome and gold (5nm and 65nm) layers, and liftoff. To etch the buffered oxide layer under the gratings, we exploit buffered hydrofluoric acid. Like the under-cut process in [159], the time of the under-cut process is adjusted carefully such that the anchors are supported by the SiO_2 while the nanostructures are fully suspended. After the under-cut, the device is dried by a critical point dryer. Finally, the device is connected to a custom printed circuit board using a wire bonder (WestBond 7476D). In Fig. 5.4**e**, the device has four different sets of electrodes. The customized PCB is capable of providing four independent voltages to the sets of the electrodes in the device. The independent biases are produced by Arduino (Arduino Uno R3). Specifically, four different pulse width modulation (PWM) channels in Arduino are connected to four PWM to DC converter modules (LC-LM358-PWM2V) and a custom external circuit. As a result, the applied biases are individually controllable by updating the four PWM channels, which are programmed via a common laptop by using the Arduino software (IDE).

5.8 Appendix

Temporal coupled-mode theory on asymmetric resonant dielectric metasurfaces

For resonant metasurfaces or photonic crystals, it is known that temporal responses of the resonator can be described by temporal coupled mode theory (TCMT). As seen in Fig. 5.2**a**, with normally incident light, the resonant metasurface can be modeled by a single-mode resonator that is coupled to two ports. The dynamics of the optical resonance can be generally formulated by:

$$\frac{du}{dt} = (iw_0 - \frac{1}{\tau_1} - \frac{1}{\tau_2} - \frac{1}{\tau_{nr}})u + \begin{pmatrix} d_1 & d_2 \end{pmatrix} \begin{pmatrix} s_1^+ \\ s_2^+ \end{pmatrix}, \tag{5.4}$$

$$\begin{pmatrix} s_1^- \\ s_2^- \end{pmatrix} = C \begin{pmatrix} s_1^+ \\ s_2^+ \end{pmatrix} + \begin{pmatrix} d_1 \\ d_2 \end{pmatrix} u, \tag{5.5}$$

where u and w_0 correspond to complex amplitude of the resonance and the central resonance frequency, respectively; d_1 and d_2 are the coupling coefficients between the two ports and the resonances; the resonance radiatively decays into port 1 and 2 with decay rates of $\frac{1}{\tau_1}$ and $\frac{1}{\tau_2}$, respectively; $\frac{1}{\tau_{nr}}$ is the nonradiate decay rate; s_1^+ (s_1^-) and s_2^+ (s_2^-) are amplitudes of the incoming (outgoing) waves from the ports; C is a direct-transport scattering matrix, written by $C = e^{i\phi_d} \begin{pmatrix} t & it \\ it & r \end{pmatrix}$, where r, t, and ϕ_d are the real reflection coefficient, the real transmission coefficient, and the phase factor, respectively. C generally describes the direct coupling between the incoming and outgoing waves. In addition, as ϕ_d depends on the selection of reference planes in the model, ϕ_d can be set to 0 for simplicity. In addition, we here assume that $\frac{1}{\tau_{nr}}$ is negligible because silicon is almost lossless in the telecom wavelength range. According to the time-reversal symmetry and the energy conservation, the coupling coefficient satisfies

$$d_1^* d_1 = \frac{2}{\tau_1}, \qquad d_2^* d_2 = \frac{2}{\tau_2}, \tag{5.6}$$

$$C \begin{pmatrix} d_1^* \\ d_2^* \end{pmatrix} = - \begin{pmatrix} d_1 \\ d_2 \end{pmatrix}, \tag{5.7}$$

revealing that the coupling conditions are fundamentally related to the decay rates of the resonances as well as the direct-transport scattering [182, 197].

According to Refs. [197, 198], we could analytically solve Eqs. 5.4-5.7 to obtain the Eqs. 5.1 and 5.2. In detail, when the system is driven by a continuous laser, whose frequency is w, we can derive u as a function of w from Eq. 5.4

$$u = \frac{\begin{pmatrix} d_1 & d_2 \end{pmatrix} \begin{pmatrix} s_1^+ \\ s_2^+ \end{pmatrix}}{i(w - w_0) + \frac{1}{\tau_{tot}}}, \tag{5.8}$$

where $\frac{1}{\tau_{tot}} = \frac{1}{\tau_1} + \frac{1}{\tau_2}$. By inserting Eq. 5.8 into Eq. 5.5, the outgoing waves can be described by,

$$\begin{pmatrix} s_1^- \\ s_2^- \end{pmatrix} = C \begin{pmatrix} s_1^+ \\ s_2^+ \end{pmatrix} + \frac{\begin{pmatrix} d_1 \\ d_2 \end{pmatrix} \begin{pmatrix} d_1 & d_2 \end{pmatrix}}{i(w - w_0) + \frac{1}{\tau_{tot}}} \begin{pmatrix} s_1^+ \\ s_2^+ \end{pmatrix}. \tag{5.9}$$

From Eq. 5.9, we can derive the reflection spectra of port 1 and 2, r_1 and r_2:

$$r_1 = \left. \frac{s_1^-}{s_1^+} \right|_{s_2^+=0} = r + \frac{{d_1}^2}{i(w - w_0) + \frac{1}{\tau_{tot}}}, \tag{5.10}$$

$$r_2 = \left. \frac{s_2^-}{s_2^+} \right|_{s_1^+=0} = r + \frac{{d_2}^2}{i(w - w_0) + \frac{1}{\tau_{tot}}}. \tag{5.11}$$

Next, Eqs. 5.6 and 5.7 are employed to eliminate phase ambiguity of d_1 and d_2 in Eqs. 5.10 and 5.11. Specifically, from Eq. 5.6, d_1 and d_2 can be described by

$$d_1 = \sqrt{\frac{2}{\tau_1}} e^{i\theta_1}, \qquad d_2 = \sqrt{\frac{2}{\tau_2}} e^{i\theta_2}, \tag{5.12}$$

where θ_1 and θ_2 are phases of the coupling coefficients of d_1 and d_2, respectively. By inserting Eq. 5.12 into Eq. 5.7, $cos(2\theta_1)$ and $cos(2\theta_2)$ can be derived by

$$cos(2\theta_1) = \frac{\tau_1}{2r}\Big(- \frac{r^2}{\tau_{tot}} - \frac{1}{\sigma}\Big), \tag{5.13}$$

$$cos(2\theta_2) = \frac{\tau_2}{2r}\Big(- \frac{r^2}{\tau_{tot}} + \frac{1}{\sigma}\Big), \tag{5.14}$$

where $\frac{1}{\sigma} = \frac{1}{\tau_1} - \frac{1}{\tau_2}$. Then, $sin(2\theta_1)$ and $sin(2\theta_2)$ are expressed as:

$$sin(2\theta_1) = \pm\frac{\tau_1}{2r}\sqrt{\frac{4r^2}{\tau_1{}^2} - \frac{r^4}{\tau_{tot}{}^2} - \frac{1}{\sigma^2} - \frac{2r^2}{\tau_{tot}\sigma}}, \tag{5.15}$$

$$sin(2\theta_2) = \pm\frac{\tau_1}{2r}\sqrt{\frac{4r^2}{\tau_2{}^2} - \frac{r^4}{\tau_{tot}{}^2} - \frac{1}{\sigma^2} + \frac{2r^2}{\tau_{tot}\sigma}}. \tag{5.16}$$

As r_1 and r_2 in Eqs. 5.10 and 5.11 can be described by $cos(2\theta_1)$, $cos(2\theta_2)$, $sin(2\theta_1)$, and , $sin(2\theta_2)$, we can derive the Eqs. 5.1 and 5.2:

$$r_1 = r + \frac{\frac{2}{\tau_1}\Big(cos(2\theta_1) + isin(2\theta_1)\Big)}{i(w - w_0) + \frac{1}{\tau_{tot}}} = \frac{i\Bigg[r(w - w_0)\pm\sqrt{\frac{2}{\tau_1^2} + \frac{2}{\tau_2^2} - \frac{r^2}{\tau_{tot}^2} - \frac{1}{r^2\sigma^2}}\Bigg] - \frac{1}{r\sigma}}{i(w - w_0) + \frac{1}{\tau_{tot}}}, \tag{5.17}$$

$$r_2 = r + \frac{\frac{2}{\tau_2}\Big(cos(2\theta_2) + isin(2\theta_2)\Big)}{i(w - w_0) + \frac{1}{\tau_{tot}}} = \frac{i\Bigg[r(w - w_0)\pm\sqrt{\frac{2}{\tau_1^2} + \frac{2}{\tau_2^2} - \frac{r^2}{\tau_{tot}^2} - \frac{1}{r^2\sigma^2}}\Bigg] + \frac{1}{r\sigma}}{i(w - w_0) + \frac{1}{\tau_{tot}}}. \tag{5.18}$$

The two-port resonator model shown in Fig. 5.2**a** generally describes any single-mode resonant metasurfaces under normal incidence. When the light is obliquely incident and the metasurface is in sub-wavelength regime (i.e. there is no diffraction), the metasurface can be modeled by a four-port resonator. The general description of the four-port resonator model can be found in Ref. [198]. Here, we only deal with a fully symmetric case where the resonance equally decays into the four ports with the decay rate of $\frac{1}{\tau_0}$. The reflection spectrum of the symmetric resonator, r_s, can be expressed as [198]:

$$r_s = \frac{i\Big[r(w - w_0)\pm\frac{2}{\tau_0}\sqrt{1 - r^2}\Big]}{i(w - w_0) + \frac{2}{\tau_0}}. \tag{5.19}$$

We should note that Eq. 5.19 becomes identical to Eq. 5.17 or 5.18 when $\frac{1}{\tau_1} = \frac{1}{\tau_2} = \frac{1}{\tau_0}$. In other words, if the structures are symmetric with respect to all available ports and $\frac{1}{\tau_0} \neq 0$, the single-mode resonance is always critically coupled to the excitation.

Measurement procedure

All of the measurements presented in this paper are characterized using the set-ups shown schematically in Fig. 5.A.6 [159, 184]. We use a tunable laser (Photonetics, TUNICS-Plus) as the light source. A beam splitter is placed in front of the fiber collimator (Thorlabs, F260FC-1550) to capture the power from the source and send the light to the sample. For reference, the power from the source is measured by a InGaAs detector (Thorlabs, PDA10CS). The PBS, a half waveplate (HWP), and a polarizer are inserted to set the polarized state of the incident light to TE polarization. The sample at the object plane is imaged by a 20× infinity-corrected objective lens (Mitutoyo, M Plan Apo NIR) and a tube lens with a focal length of 200 mm. The position of tube lens and the mounting stage of the sample are adjusted to ensure normal incidence. At the image plane, an iris (Thorlabs,ID25) is inserted to select a region of interest with a diameter of 45 μm in the object plane. The spatially filtered light was either focused onto another InGaAs detector for the measurement of the spectra, or imaged on an InGaAs SWIR camera (Goodrich, SU320HX-1.7RT) using relay optics. All reflection signals were obtained by dividing the signal from the sample by the signal from the sources. Due to different input polarization states, the incident power onto the sample varies at different wavelengths. Thus, the signals are further normalized by the signals from the gold.

To measure the phase response shown in Fig. 5.4**h**, we use a Michelson-type interferometer setup [159]. A part of the setup marked by a black dashed box in Figure 5.A.6 is only utilized for the phase measurement.

To measure the diffracted signal shown in Figs. 5.5 and 5.A.9 , we image a Fourier plane of the metasurface [159]. Parts of the setup marked by a green solid box in Figure 5.A.6 are only utilized for the diffraction pattern measurement. Specifically, relay lenses, L6 and L7, and a filp mirror are used to image the Fourier plane with the InGaAs SWIR camera. Also, we built a custom microscope setup at the wavelength of 850 nm to align the sample when we image the Fourier focal plane.

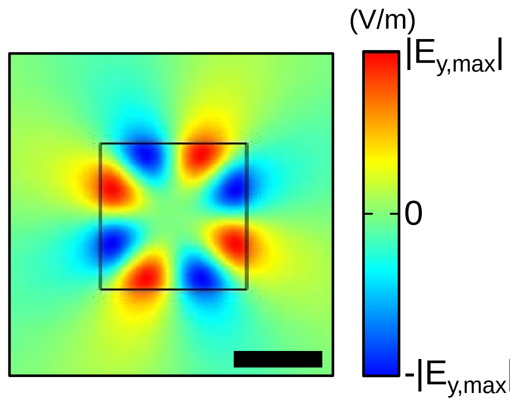

Figure 5.A.1: **Electric field profile of high-order Mie mode resonance in a symmetric Si nanobar.** y-components of electric fields are plotted. The eigenmode is found without the periodic boundary condition. The width and thickness are 841 and 838 nm, respectively. The calculated complex eigenfrequency is (191 + i0.291) THz, corresponding to the resonant wavelength of 1569 nm and Q-factor of 328. Scale bar denotes 500 nm.

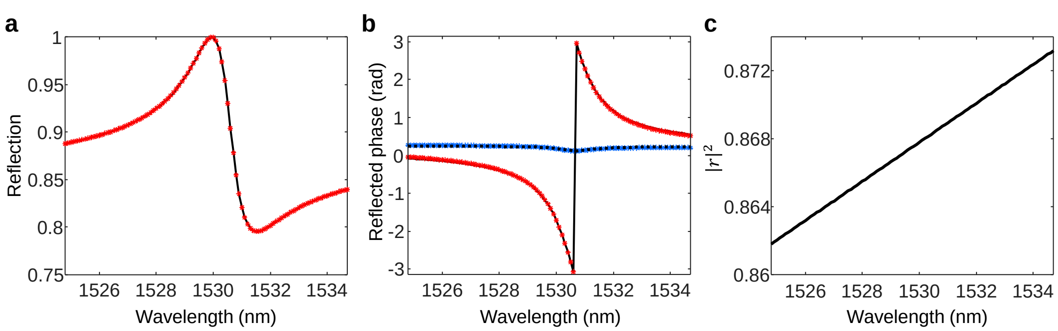

Figure 5.A.2: **Analytical fitting of calculated reflection and reflected phase spectra of the asymmetric metasurface.** **a** and **b** Numerical data shown in Figs. 5.2**h** and 5.2**i** is fitted by using Eqs. 5.1 and 5.2. As shown in Fig. 5.2**f**, $|r_{TE1}|^2$ ($|r_{TEw}|^2$) and ϕ_{TE1} (ϕ_{TE2}) represent reflection and reflected phase for top (bottom) illumination, respectively. **a**: Calculated and fitted spectra of $|r_{TE1}|^2$ and $|r_{TE2}|^2$. Red asterisks show the calculated spectra of $|r_{TE1}|^2$ or $|r_{TE2}|^2$. The fitted spectrum is plotted by a black solid line. **i**: Calculated and fitted spectra of ϕ_{TE1} and ϕ_{TE2}. Red and blue asterisks represent the calculated spectra of ϕ_{TE1} and ϕ_{TE2}, respectively. The fitted spectra of ϕ_{TE1} and ϕ_{TE2} are plotted by solid and dashed black lines, respectively. **c** Fitted reflection spectra of the direct-transport scattering process.

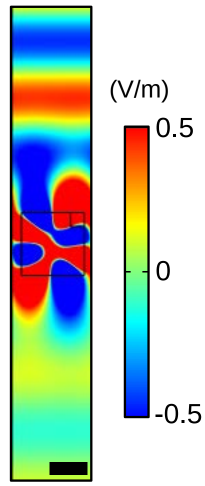

Figure 5.A.3: **Numerical investigation of asymmetric radiation of the proposed metasurface.** Calculated electric field profiles of the eigenmode at Γ point. The y-components of the electric field profiles of the eigenmode are plotted. Strong radiation toward top direction is observed. In simulation, the power ratio between the top and bottom radiations and Q-factor of the eigenmode are 17.54 and 1021, respectively.

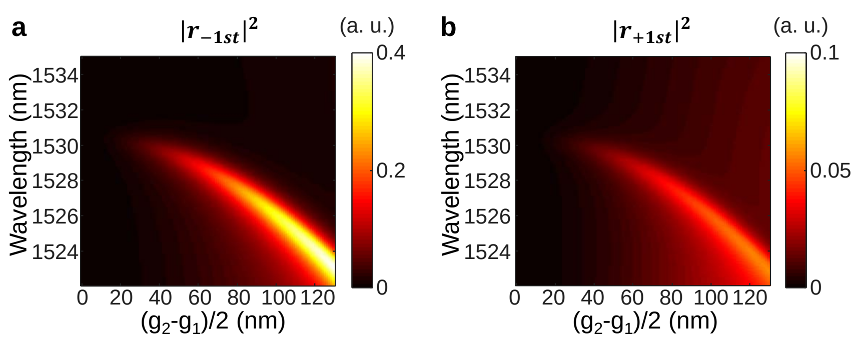

Figure 5.A.4: **Numerical investigations on high diffraction orders.** **a** and **b** Simulated reflected power spectra of the ±1st order diffractions. The reflected power coefficient spectra of the −1st and +1st order diffractions, $|r_{1st}|^2$ and $|r_{+1st}|^2$, are calculated as a function of the nanomechanical tuning, $\frac{g_2-g_1}{2}$, and plotted in **a** and **b**, respectively. It should be noted that the color bars are different in **a** and **b**. The calculated reflected power coefficient spectra of the 0th order diffraction is shown in Fig. 5.3**b**.

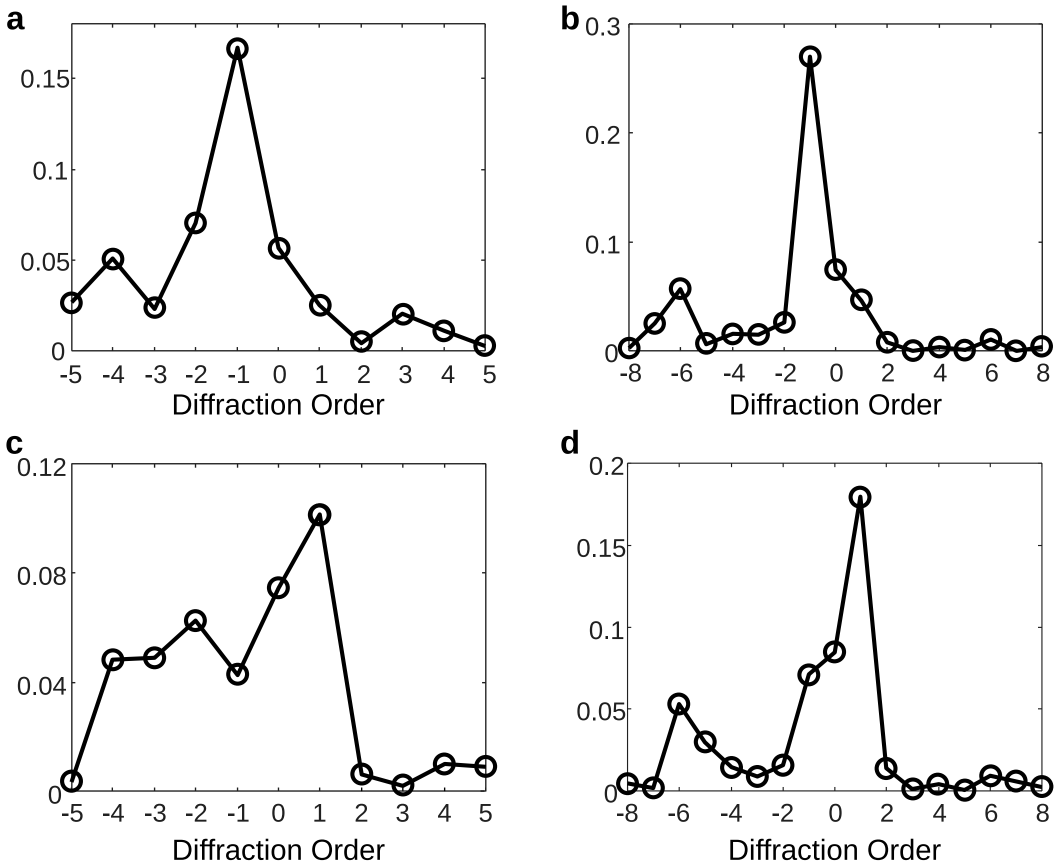

Figure 5.A.5: **Numerical investigation on reflected power coefficients of the asymmetric metasurface. a-d** Calculated reflected power coefficients of the metasurface grating at the design wavelength of 1529 nm. The simulated reflected power coefficients are plotted for all available diffraction orders. The designs used in Figs. 5.3**f**, 5.3**g**, 5.3**i** and 5.3**j** are employed for **a**, **b**, **c**, and **d**, respectively

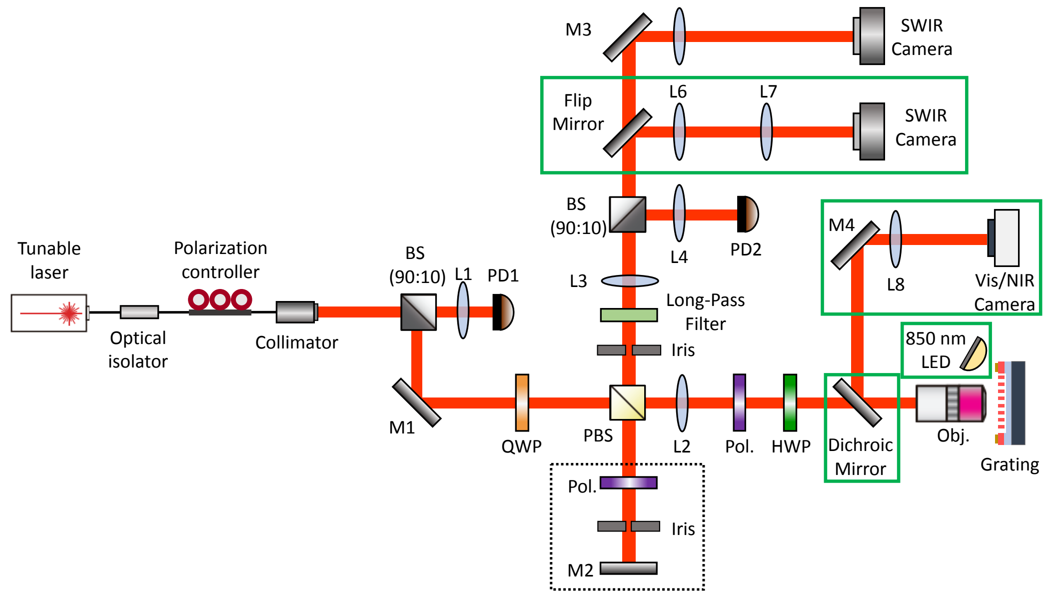

Figure 5.A.6: **Schematic illustration of the experimental setup.** Red lines represent the paths of the light. To achieve the reflection spectra of the TE-polarized input light, Pol. and HWP in front of the objective lens are aligned to 45 and 67.5 degree, respectively. A black dashed box represents optical elements exploited to generate reference beam for the phase measurement shown in Fig. 5.4**h**. Also, we use optical components in green boxes only for the measurements of the diffraction pattern shown in Figs. 5.5, 5.A.8, and 5.A.9. Pol.: linear polarizer. BS: beamsplitter. PBS: polarizing beamsplitter. L: lens. PD: photodetector. M: mirror. QWP: quarter waveplate. HWP: half waveplate. Obj.: microscope objective lens. SWIR camera: short-wave infrared camera.

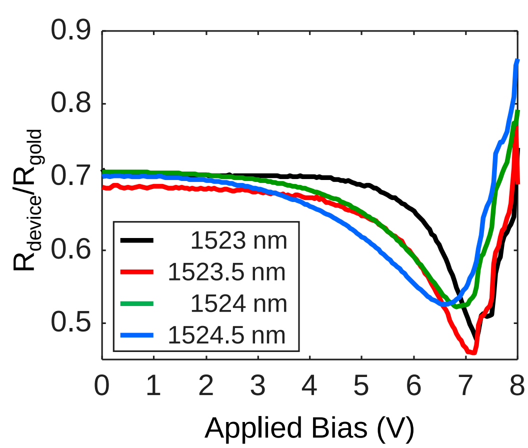

Figure 5.A.7: **Measured intensity modulations near the resonance wavelength.** Intensity modulation is measured at four different wavelengths and plotted in different colors as a function of the applied biases. The applied biases vary from 0V to 8V. The measured wavelength for each color is shown in legend.

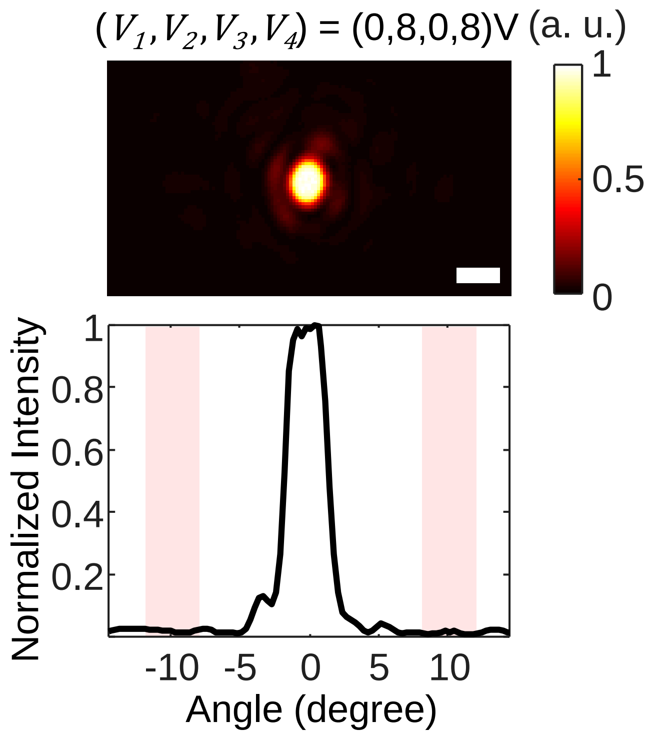

Figure 5.A.8: **Measured back focal plane image with large resonance shift.** Top: The normalized intensity image is measured at the Fourier plane of the metasurface. The values of V_1-V_4 are noted on top of the images. V_2 and V_4 increase up to 8 nm to move the resonance below the measured wavelength of 1524 nm. Scale bars are $0.05k_0$ where k_0 is a magnitude of wave vector in free-space. Bottom: The measured cross-sectional intensity profile is plotted as a function of the diffraction angle. The intensities are normalized by the peak intensity at 0°. The diffracted signals near ±10° are denoted by pink shades.

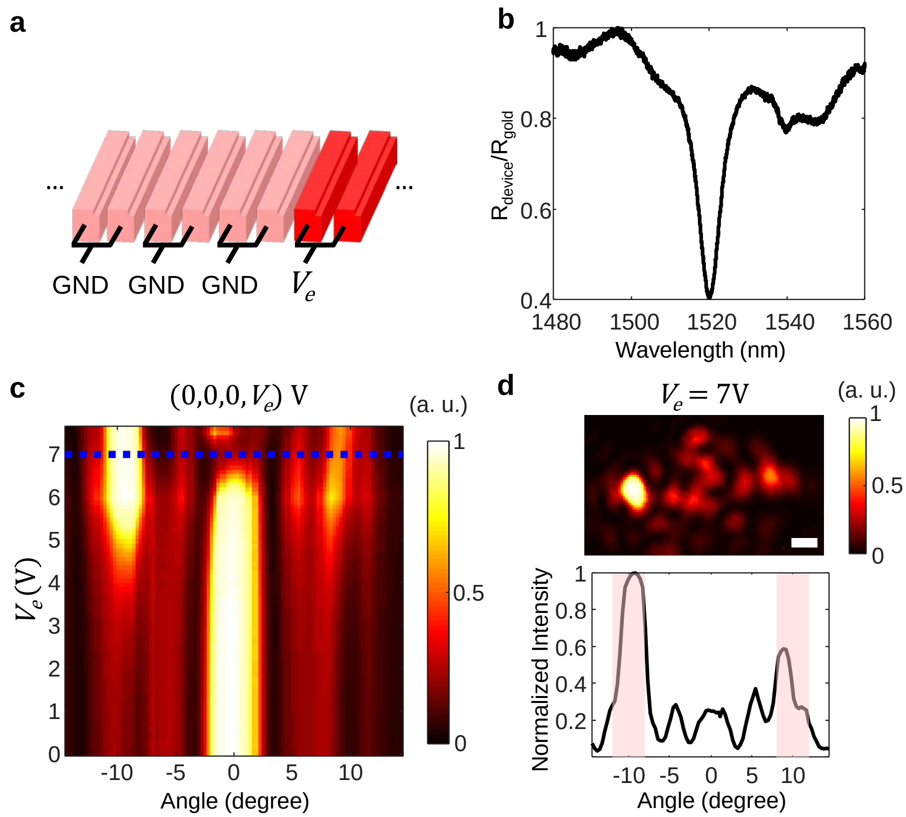

Figure 5.A.9: **Experimental demonstration of the efficient active metasurface.** **a** Schematic of electrical configuration. With three pairs of the asymmetric nanostructures grounded, only one pair is connected to external bias, V_e, for every four pairs of nanostructures. As two electrodes are required for this electrical bias, a large number of devices can be fabricated and modulated simultaneously [159]. **b** Measured reflection spectrum for TE-polarized normally incident light. The spectrum is measured without any bias and normalized by the reflection from a gold electrode. **c** Measured intensity at the Fourier plane of the metasurface. The intensity is measured at the 1519 nm as a function of the applied bias. V_e changes from 0V to 7.6V with a step size of 0.1 V. At each bias, the intensity is normalized by the maximum intensity. **d** Measured diffraction patterns at 1519 nm with V_e of 7V. The corresponding data is noted by a blue dashed line in **c**. Top: The normalized intensity image is measured at the Fourier plane of the metasurface. The value of V_e is noted on top of the image. Scale bar denotes $0.05k_0$ where k_0 is a magnitude of wave vector in free-space. Bottom: Measured cross-sectional intensity profile is plotted as a function of the diffraction angle. The intensities are normalized by the peak intensity around $-10°$. The diffracted signals near $\pm 10°$ are denoted by pink shades. Quantitatively, the -1st and $+1$st order signals are 6.06 dB and 3.75 dB larger than the 0th order signal, respectively

Chapter 6

NEMS-TUNABLE DIELECTRIC CHIRAL METASURFACES

Active control of strong chiroptical responses in metasurfaces can offer new opportunities for optical polarization engineering. Plasmonic active chiral metasurfaces have been investigated before, but their tunable chiroptical responses is limited due to inherent loss of plasmonic resonances, thus stimulating research in low loss active dielectric chiral metasurfaces. Among diverse tuning methods, electrically tunable dielectric chiral metasurfaces are promising thanks to their potential for on-chip integration. Here, we experimentally demonstrate nano-electromechanically tunable dielectric chiral metasurfaces with reflective circular dichroism (CD). We show a difference between absolute reflection under circulary polarized incident light with orthogonal polarization of over 0.85 in simulation and over 0.45 experimentally. The devices enable continuous control of CD by induced electrostatic forces from 0.45 to 0.01 with an electrical bias of 3V. This work highlights the potential of nano-electromechanically tunable metasurfaces for scalable optical polarization modulators.

6.1 Introduction

Chirality is an asymmetric feature describing structures that are not superimposed onto their mirror images. Chiral structures are known to interact differently with light polarized with different handedness and the optical responses that are sensitive to handedness are called by chiroptical responses. Although chirality is ubiquitous in various molecules, the chiroptical effects in natural materials are generally very weak, requiring considerable propagation distances to observe the chiropotical effects such as circular dichroism (CD) or circular birefringence. To overcome the limited amount of the natural chiroptical effects, chiral metatmaterials or metasurfaces have been investigated in past two decades [32–34]. First, plasmonic 3D-printed metamaterials or multilayers of patterned metasurfaces have been explored [207–210]. Despite their strong and broadband chiroptical properties, complicated fabrication procedures limit practical applications and extensions to tunable devices. Moreover, planar plasmonic chiral metasurfaces with a single patterned layer have been investigated. In particular, patterned plasmonic chiral metasurface on top of a flat back metallic mirror has achieved high circular dichroism [211–213]. Unlike conventional metallic mirrors which reflect circular polarized light with reversal of handedness, these plasmonic mirrors selectively reflect one circularly polarized light without changing the handedness while the other circular polarization is absorbed [211–213]. These polarization selective mirrors are often called chiral spin-preserving mirrors and have potential applications in valley exciton-polaritonics [214]. Complementary to plasmonic metastructures, all-dielectric chiral metasurfaces also have shown strong chiroptical effects [215–217]. In particular, it has been recently demonstrated that a single-layer dielectric metasurface is able to realize near-unity CD in reflection [217]. Unlike the aforementioned plasmonic chiral structures with back metallic mirrors [211–213], the single-layer dielectric chiral metasurface selectively reflects one circular polarized light with preserved handedness and transmits the other circular polarized light with flip of handedness [217].

Dynamical control of the strong chiroptical effects in metamaterials can boost development of devices for novel polarization control. During the last decade, reconfigurable plasmonic chiral metastructures have been extensively investigated in THz and microwave domain [218–221]. For example, diverse active platforms using optical tuning [218], global mechanical deformation [219], microelectromechanical systems [220], and electrical gating of graphene [221] have been proposed. In addition to the devices working in THz or microwave domain, dynamic plasmonic chiral metasurfaces have been also extensively studied in optical domain. For example, all-optical tuning of phase change materials [222] or DNA structures [223] has enabled switchable chiroptical responses. Also, global environmental tuning of liquid [224], pH [225], strain [226], and magnetic field [227] have been explored. However, these all-optical or global tuning methods generally require complicated setups hindering the development to on-chip integration. Thus, electrical control of the chirality can be more attractive than other methods for practical applications. We should note that Zhang et al reported cery recently nano-electromechanically tunable chiral plasmonic metasurfaces, thus enabling active control of polarization and chiroptical responses through nano-electromechanical actuation in vertical direction [228]. Nevertheless, all of the aforementioned tunable plasmonic chiral metasurfaces are inherently lossy which limit optical performance.

In contrast to the extensive works on tunable plasmonic chiral metasurfaces, investigations related to tunable dielectric chiral metasurfaces have been limited. For instance, optothermal moving of the nanoparticles [229] and all-optical tuning of nonlinearity of Si [230] have enabled tunable chiroptical responses. However, both systems still require additional optical systems to modulate the device optically, imposing considerable limits on compact integration [229, 230]. More broadly, optomechanical GaAs chiral metasurfaces have been demonstrated using excitation of global mechanical oscillation of the membrane through a bulky piezoelectric actuator [231]. However, the system has not just shown very weak tunable response mainly due to the limited movement of the membrane, but also only allowed the oscillation of the output signal [231]. Therefore, up to our knowledge, electrical tuning of dielectric chiral metasurfaces has not been explored and can be promising alternatives to that of the plasmonic chiral metasurfaces thanks to low-loss optical property of dielectric materials. Furthermore, from perspectives of devices, scalable material platforms such as silicon and low electrical bias within CMOS logic level can be important for the on-chip integration. In this work, we experimentally demonstrate nano-electromechanically tunable dielectric chiral metasurfaces in telecom wavelength. The metasurfaces resonantly work as the chiral spin-preserving mirrors, exhibiting selective reflection for one circular polarization without external bias. Furthermore, the resonances hosted by the metasurfaces can continuously tuned by induced electrostatic forces. Especially, the devices experimentally achieve transition of CD in reflection from 0.44 to 0.01 at the resonant wavelength. Finally, the devices are modulated within electrical bias of 3V and fabricated by using standard silicon-on-insulator platforms.

6.2 Main

Figure 6.1 shows conceptual illustrations of the proposed nano-electromechanically tunable chiral metasurface. In Fig. 6.1**a**, the illustrative schematic of top view of the suspended silicon chiral metasurface is displayed. The metasurface consists of two sets of pairs of doped silicon nanostructures and an electrode is deposited on each silicon layer for electrical bias. In Figs. 6.1**a** and 6.1**b**, different colors are used to explicitly visualize two sets of the nanostructures. Throughout this paper, all devices are composed of 675 nm thick and 45 μm long silicon nanostructures. Two pairs of the suspended nanostructures are shown in Fig. 6.1**b** with design parameters. Especially, period, p, is chosen to be 700 nm so that the period of the pair is smaller than the wavelength of interests to avoid unwanted diffraction under normal incidence. As shown in Fig. 6.1**b**, we intentionally breaks n-fold rotational symmetry for n>2 and any in-plane mirror symmetry to achieve strong chiroptical effects in reflection. It is worth noting here that this design approach has

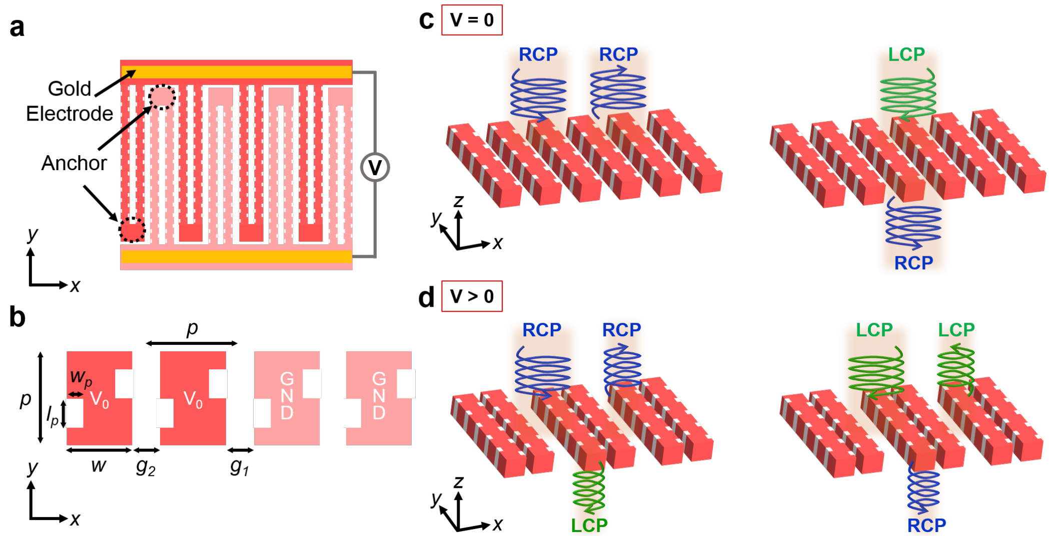

Figure 6.1: **nano-electromechanically tunable all-dielectric chiral metasurfaces** **a** Schematic illustration of a top view of the metasurface. The metasurface is composed of two sets of doped silicon nanostructures. Anchors and the gold electrodes are marked. Electrodes are deposited on each silicon layer for mechanical actuation. **b** Schematic illustration of two pairs of the nanostructures constituting to the metasurface. Geometric parameter definitions are shown in the illustration. In **a** and **b**, two different colors are employed to distinguish two sets of the nanostructures and visualize voltage difference between two sets. Pink and red colors represent ground, GND, and applied bias, V_0, respectively. **c** and **d** Illustrations of reflection behavior of the metasurfaces without and with external bias. **c**: Without external bias, the metasurface selectively reflects RCP light by keeping the handedness and transmits LCP light with change of handedness. **d** With actuation, the metasurface becomes achiral. The amounts of co- and cross-polarized reflection and transmission become symmetric for both RCP and LCP input lights.

been extensively used for the single layer dielectric chiral metasurfaces [217] and the plasmonic chiral metasurfaces having back metallic reflectors [211–213]. When the electrical bias is applied, all pairs of the neighboring nanostructures that are connected to the different electrodes have voltage difference and become capacitors. Thus, the induced electrostatic forces between the nanostructures enable continuous mechanical actuation as a function of the external bias. In other words, g_1 (g_2) decreases (increases) by applying the bias, where g_1 (g_2) is the gap size between the two neighboring bars in the different (same) set. In Fig. 6.1**c** and Fig. 6.1**d**, optical functions of the metasurface are schematically illustrated. In Fig. 6.1**c**, the structure without the actuation reflects right circular polarized (RCP) light without flip of the handedness while left circular polarized (LCP) light is transmitted with reversal of

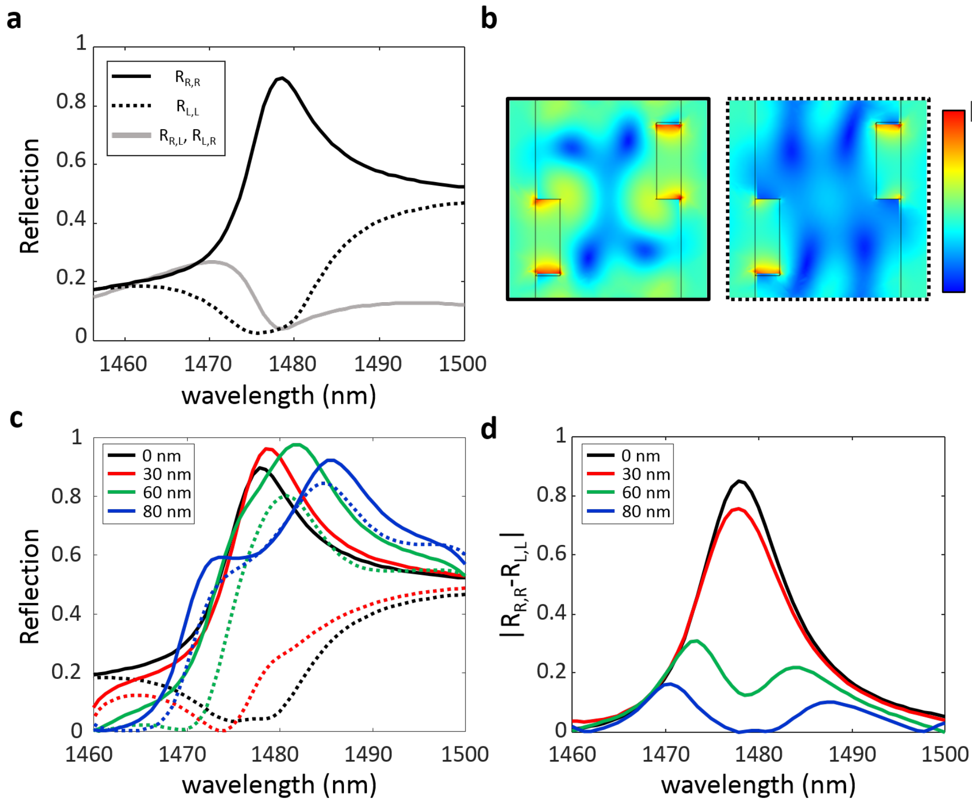

Figure 6.2: **Simulated mechanically tunable chiroptical responses.** **a** Simulated reflection spectra of co- and cross- polarized components under RCP and LCP illuminations. The spectra of $R_{L,L}$ and $R_{R,R}$ are plotted by dashed and solid black lines, respectively. $R_{R,L}$ and $R_{L,R}$ are identical and plotted together by a grey line. Geometric parameters used in the simulation: p = 700 nm, w = 505nm, g_1 = g_2 = 195 nm, w_p = 85nm, and l_p = 265nm. **b** Electric field distribution cuts from a middle plane of the nanostructure. The magnitude of the field profiles are plotted under LCP (left) and RCP (right) illuminations at the resonance wavelength of 1478 nm. **c** Calculated reflection spectra of $R_{L,L}$ and $R_{R,R}$ with mechanical movements. The spectra of $R_{L,L}$ and $R_{R,R}$ are plotted in dashed and solid lines, respectively. The mechanical movements, expressed by $\frac{g_1-g_2}{2}$, varies from 0 nm to 80 nm. The value of $\frac{g_1-g_2}{2}$ for each color is shown in the legend. **d** Spectra of circular dichroism in reflection, $|R_{L,L} - R_{R,R}|$, for the different mechanical movements. The spectra are calculated from c. The value of $\frac{g_1-g_2}{2}$ for each color is shown in the legend.

handedness. When the bias is applied, the suspended nanostructures are actuated and their chiroptical properties are continuously modulated. As shown in Fig. 6.1**d**, the metasurface can exhibit negligible chiroptical responses with the actuation so its co- and cross polarized reflection and transmission become identical for LCP and RCP illuminations at the target wavelength.

First, the proposed metasurfaces are numerically investigated by a commercial software based on the finite element method, COMSOL® (see Method for details). Polarization analysis of reflection from the metasurface is plotted in Fig 6.2**a**. The reflection coefficient $R_{L,L}$ ($R_{R,R}$) is defined as the reflection of the LCP (RCP) component from the metasurfaces to the LCP (RCP) input light. Similarly, $R_{R,L}$ ($R_{L,R}$) is defined as the reflection of the RCP (LCP) component from the metasurfaces to the LCP (RCP) input light. In Fig. 6.2**a**, the polarization-sensitive reflection is observed near the resonant wavelength of 1478 nm. The metasurface selectively reflects RCP light without flip of the handedness, while the LCP light is mostly transmitted. Specifically, $R_{L,L}$, $R_{R,R}$, and CD in reflection, defined by $|R_{L,L}$-$R_{R,R}|$ in this paper, are 0.04, 0.89, and 0.85, respectively. Moreover, $R_{R,L}$ and $R_{L,R}$ are identical due to the symmetry of the unit cell [232] and it is confirmed by a grey curve plotted in Fig.6.2**a**. In Fig. 6.2**b**, electric field profiles in the xy plane at the middle of the nanostructures (i.e. 337.5 nm above from the bottom) are plotted under LCP and RCP illuminations, showing that the metasurfaces interact with LCP and RCP lights differently at the resonance. The chiroptical responses in Fig. 6.2**a** and the two distinct electric field profiles in Fig. 6.2**b** can be qualitatively explained by spectral overlap of two leaky guided mode resonances hosted by the dielectric metasurfaces [217]. For example, the input polarization state determines the amplitude and phase of two leaky guided modes and the interference between the resonant modes results in the two distinct field profiles shown in Fig. 6.2**b**. The input polarization state also affects the phase and amplitude of the radiations from the two leaky guided modes, so the radiations from the guided modes interfere differently with directly transmitted or reflected light. Therefore, the reflection spectra shown in Fig. 6.2**a** highly depend on the handedness of the input polarization.

To simulate mechanical tuning of the chiroptical effects, the spectra of $R_{L,L}$ and $R_{R,R}$ are calculated by varying the mechanical movement, $\frac{g_2-g_1}{2}$, from 0 to 80 nm and plotted in Fig. 6.2**c**. In Fig. 6.2**c**, increase of $\frac{g_2-g_1}{2}$ causes red shift of peaks in the spectra of $R_{R,R}$ and blue shift of dips in the spectra of $R_{L,L}$. Furthermore, the amount of the spectral shift of the $R_{L,L}$ is larger than that of $R_{R,R}$. To visualize the change of the chiroptical effects clearly, $|R_{L,L} - R_{R,R}|$ is evaluated from Fig. 6.2**c** and plotted in Fig. 6.2**d**. In Fig. 6.2**d**, it is clearly shown that the mechanical movement in lateral direction causes the strong change of $|R_{L,L} - R_{R,R}|$ around the resonant wavelength of 1478 nm in Fig. 6.2**d**. In details, the 80 nm movement leads to change of $|R_{L,L} - R_{R,R}|$ from 0.85 to 8×10^{-4} at 1478 nm in Fig. 6.2**d**. Namely, the mechanical actuation in the lateral direction results in the transition from the strong

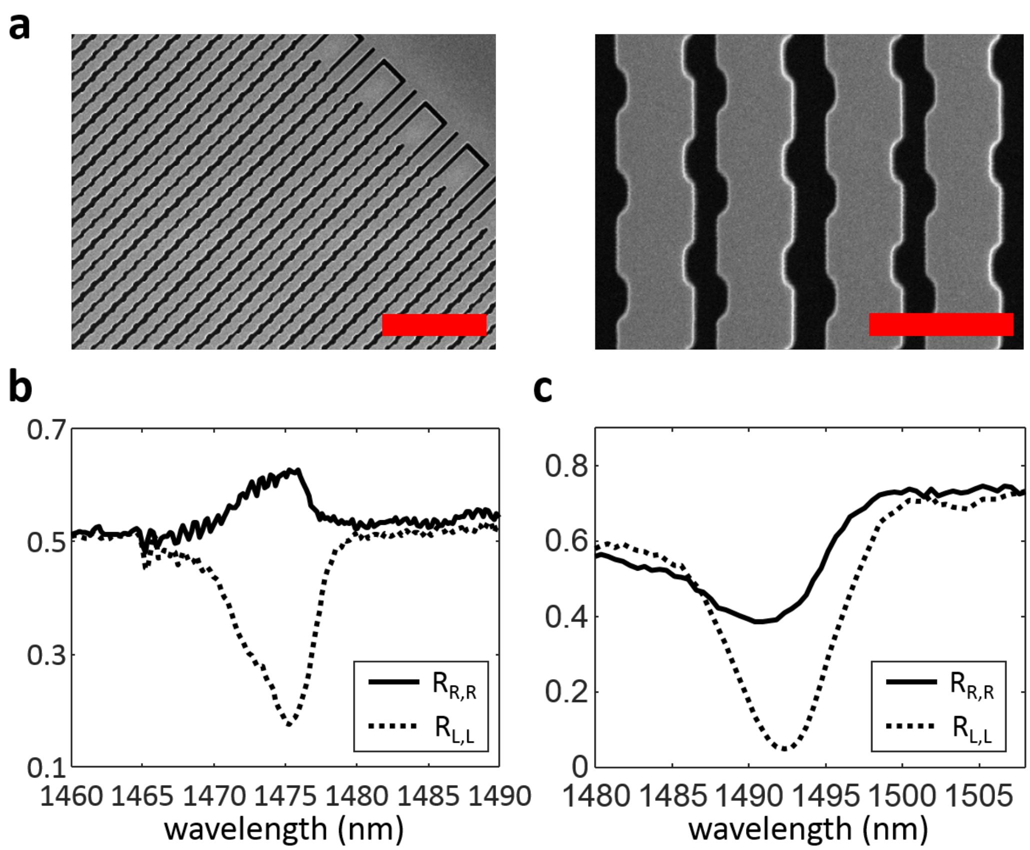

Figure 6.3: **Dielectric chiral metasurfaces and measurements of chiroptical repsonses in reflection.** **a** Scanning electron microscope images of the fabricated metasurfaces. Left : An array of the nanoabars. Right: Zoom-in scanning electron microscope image of the 2 pairs of the nanostructures. Scale bars in left and right denote 5 μm and 1 μm, respectively. **b** and **c** Measured reflection spectra of $R_{L,L}$ and $R_{R,R}$ for two different structures (see Table 6.A.1 for the measured design parameters). The spectra of $R_{L,L}$ and $R_{R,R}$ are plotted in dashed and solid lines, respectively.

chiroptical response to the negligible chiroptical response even with the presence of chirality in the structure.

To experimentally verify nano-electromechanically tunable chiroptical responses, the device is fabricated using the conventional nanofabrication process of standard silicon-on-insulator technology (see Methdo for details). We should mention here that g_1 and g_2 are adjusted in the fabrication process such that g_1 is 60 nm smaller than g_2. This adjustment allows for a large shift of the resonance with nano-electromechanical tuning of the gaps. Figure 6.3**a** shows scanning electron microscopy images, confirming good agreement with the illustrative schematics in Figs. 6.1**a** and 6.1**b**. To characterize chiroptical responses of the devices, spectra of $R_{L,L}$ and $R_{R,R}$ are measured using the setup in Fig. 6.A.1. is worth noting here that the measured spectra shown in this paper are normalized by the reflection from 65 nm gold electrode in order to estimate absolute reflection efficiency and remove fluctuations resulting from variations in polarization states of input tunable laser (see Method and Fig. 6.A.1 for details about measurement procedures). Considering reflection of the 65 nm of gold layer (~98% in simulation), the actual reflection can be a few percentage smaller than the values presented in the paper. Two different devices are measured and corresponding spectra of $R_{L,L}$ and $R_{R,R}$ are plotted in Figs. 6.3**b** and 6.3**c** (see Table 6.A.1 for the measured design parameters). Although the shape of the spectra in Fig. 6.3**b** shows good agreement with the shape of the simulated spectra in Fig. 6.2**a**, the dips in Fig. 6.3**c** are overlapped around the wavelength of 1492 nm. This deviation in Fig. 6.3**c** mainly results from the design parameters that are not perfectly matched. In specific, the value of l_p is slightly larger than the optimal value for other design parameters such as g_1, g_2, g_p, w, and l (see Fig. 6.A.2 for details). The spectra in Figs. 6.3**b** and 6.3**c** show maximal $|R_{L,L} - R_{R,R}|$ of 0.45 and 0.37 at the resonance wavelengths of 1475 nm and 1493 nm, respectively. Even with a few percentage reflection loss of the gold electrode used for the normalization, the maximal values calculated from Figs. 6.3**b** and 6.3**c** are still higher than 0.44 and 0.36, respectively. On the other hand, the ratios between $R_{L,L}$ and $R_{R,R}$ reach to 3.58:1 and 8.19:1 in Figs. 6.3**b** and 6.3**c**, respectively. The large ratio between $R_{L,L}$ and $R_{R,R}$ directly indicates potentials toward electromechanically tunable circular polarization filters. The measured values of $|R_{L,L} - R_{R,R}|$ are smaller than the simulated value shown in Fig. 6.2**a**. We believe that the deviation results from the finite length of the resonators, which may cause limited coupling between the resonance and the input light. We should note here that the optimized single-layer dielectric metasurfaces are able to reach near unity CD in reflection [217].

To demonstrate nano-electromechanical tuning of the chiroptical responses, static electrical bias is applied to the electrodes and the induced changes in the optical reflection are characterized. The spectra of $|R_{L,L} - R_{R,R}|$ are measured under several electrical biases and plotted in Figs. 6.4**a** and 6.4**b** (see Fig. 6.A.3 for the measured spectra of $R_{L,L}$ and $R_{R,R}$). The devices used in Fig. 6.3**b** and Fig. 6.3**c** are used for Figs. 6.4**a** and 6.4**b**, respectively. In both spectra, the CD in reflection is varied from the maximum value to nearly zero. For example, the external bias of 2.75 V

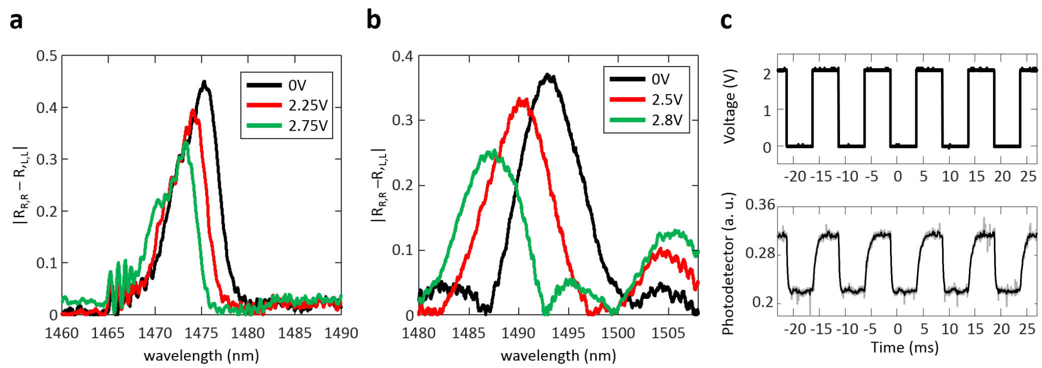

Figure 6.4: **nano-electromechanical tuning of chiroptical responses.** **a** and **b** Measured circular dichroism in reflection, $|R_{L,L} - R_{R,R}|$, under different external biases. The devices exploited in Fig. 6.3**b** and Fig. 6.3**c** are measured and plotted in **a** and **b**, respectively. The applied bias for each color is shown in legends. **c** Measured temporal response of the metasurfaces. Top: Input square wave signal of which duty cycle, frequency, and amplitude are 0.5, 100 Hz and 2V, respectively. Bottom: Measured output signals of $R_{L,L}$ by a photodetector. Raw and filtered reflection signals are plotted by grey and black curves, respectively.

(2.8 V) causes change of the CD from 0.45 (0.37) to 0.01 (1×10^{-4}) in Fig. 6.4**a** (Fig. 6.4**b**). The required electrical bias for the maximal change of the chiroptical response is smaller than 3V, which is already within CMOS logic level. Also, the static bias causes the blue shifts of main peaks of the $|R_{L,L} - R_{R,R}|$, which mainly resulting from the dominant blue shift of $R_{L,L}$ shown in Fig. 6.2**c**. To be specific, the peak shifts of $|R_{L,L} - R_{R,R}|$ shown in Fig. 6.4**a** and Fig. 6.4**b** are as large as -2 nm and -6 nm under the the bias of 2.75 V and 2.8 V, respectively. The large spectral shifts up to 6 nm indicate that the low-Q leaky guided resonances are sufficient to achieve considerable chiroptical tunablity. The large spectral shift is advantageous in terms of bandwidth and robustness in general, which are important from practical persepectives. Furthermore, the measured spectral shift is not the limit but the lower bound as the induced voltage up to 2.8V is smaller than pull-in voltage.

Finally, dynamic responses of the chiral metasurfaces are investigated in air. A periodic square-wave signal with a modulation frequency of 100 Hz, amplitude of 2V, and duty cycle of 50% is applied (see Method for details). The device used for Fig. 6.4**b** is measured with the input light at the wavelength of 1493 nm. The input electrical signals and the measured raw signals of $R_{L,L}$ are plotted in Fig. 6.4**c**. It clearly demonstrates that the optical responses are fully reconfigurable. In Fig. 6.4**c**, measured rise time (up to 90% power) and fall time (down to 10% power) are 1.48

ms and 460 μs, respectively. We believe that the low speed mainly results from the low-doping density of the Si layer of the silicon-on-insulator wafer.

6.3 Discussion and Summary

Many aspects of the proposed devices can be improved with further investigations. First of all, the modulation depths of CD in reflection shown in Figs. 6.4**a** and 6.4**b** are not limited by the spectral shifts but by the measured maximal CD in Figs. 6.3b and 6.3c. Considering the low loss of the dielectric metasurface, large sweep of design parameter spaces may result in near unity CD in reflection so improve the modulation depths of CD in reflection [217]. Furthermore, inverse-design of the tunable chiral metasurfaces can be of interest [205]. The inverse-design may not only improve CD in reflection, but also find other guided modes that are more robust against imperfect fabrication or more efficient for nano-electromechanical tuning. In specific, the inverse design may find two leaky guided mode resonances which similarly reacts to variations in design parameters. Thus, the large chiroptical responses resulting from the interfernce between two modes possibly become tolerant against imperfect fabrication. For efficient nano-electromechanical tuning in lateral direction, the optical modes can be optimized to store considerable electromagnetic energy at the gap between the nanostructures instead of inside of the nanostructures. In addition to optical aspects, considering the scale of the devices, we envision that high switching speed up to a few MHz is achievable with a highly-doped Si layer, co-optimization from both mechanical and optical perspectives, and proper packaging [49, 233]. With mechanical resonances supported by the metasurfaces, the proposed devices might provide efficient electromechanical platforms for polarization controlled optomechanical transduction [231].

In conclusion, we demonstrate nano-electromechanical tuning of the suspended silicon chiral metasurfaces. With an external bias below 3 V, the devices experimentally achieve continous tuning of CD in reflection from 0.45 to 0. This work paves the way of nano-electromechanically tunable dielectric chiral metasurfaces towards scalable and novel optical modulators, which can be used in diverse applications such as dynamic polarization engineering, stereoscopy, valleytronics, polarization optomechanics, and chiral sensing.

6.4 Methods

Simulation and design

The reflected spectra of the metasurface were calculated using a commercial software based on finite element method, COMSOL. Assuming infinite periodic array, the 3D silicon structure is simulated in air with normal incident light. Refractive indices of Si in the simulation was 3.5. The design parameters used in the simulation are shown in Fig. **2**.

Device fabrication

The devices are fabricated using a silicon-on-insulator SOI wafer. Detailed fabrication process can be found in Ref. []. We use a wafer having a device layer of 675 nm and a buffered oxide layer of 3 μm on a 1 mm thick silicon wafer. The fabrication includes two sequential e-beam lithography steps. First, the metasurfaces were fabricated with e-beam lithography and reactive ion etching. Subsequently, the electrodes are defined by the e-beam lithography, e-beam deposition of 65 nm gold/5 nm chromium layers, and lift-off process. Buffered hydrofluoric acid was used to etch the buffered oxide layer under the silicon layer. The time of the under-cut process is carefully controlled so that the metasurfaces are fully suspended while the anchors are supported by the SiO_2. In other words, one end of every suspended nanostructure is connected to anchors and the other end is connected to the silicon layer. That is because the connections on both sides prevent breaking during the undercut. To prevent destruction of the suspended device, the device is dried by a critical point dryer after the under-cut process. The device is bonded to a custom printed circuit board using a wire bonder (WestBond 7476D).

Measurement procedure

All of the reflection spectra presented in this paper are characterized using the set-ups shown schematically in Fig. 6.A.1 in Appendix. We use a tunable laser (Photonetics, TUNICS-Plus) as the light source and the wavelength of the light is tuned from 1450 nm to 1580 nm. A beam splitter is placed in front of the fiber collimator (Thorlabs, F260FC-1550) to capture the power from the source and send the light to the sample. For reference, the power from the source is captured by a InGaAs detector (Thorlabs, PDA10CS). a linear polarizer and a quarter waveplate (QWP) are inserted between a polarization beam splitter and a 20× infinity-corrected objective lens (Mitutoyo, M Plan Apo NIR) to set the polarized state of the incident light. Especially, the QWP is mounted on a rotation stage to set the input polarization state to LCP or

RCP. The sample at the object plane is imaged by the objective lens and a tube lens with a focal length of 200 mm. At the image plane, a pinhole with a diameter of 400 μm is inserted to select a region of interest with a diameter of 20 μm in the object plane. The spatially filtered light was simultaneously focused onto another InGaAs detector for the measurement of the spectra, or imaged on an InGaAs SWIR camera (Goodrich, SU320HX-1.7RT) using relay optics. All spectra in this paper were obtained by dividing the signal from the sample by the signal from the sources. To estimate absolute reflection and remove fluctuation resulting from variation in polarization states of input laser, the spectra are normalized by the spectra from the 65 nm gold electrode. For measured dynamic responses shown in Figs. 6.4, we use a function generator (FeelTech, FY6600-60M).

6.5 Appendix

Figure	$2p$ (nm)	w (nm)	g_1 (nm)	g_2 (nm)	w_p (nm)	l_p (nm)
Figures 3b	1400	505	165	225	53	275
Figures 3c	1400	520	150	210	70	270

Table 6.A.1: Measured design parameters of the devices used in Figs. 6.3**b** and 6.3**c**. The definitions of the design parameter are shown in Fig. 6.1**b**. $2p$: Period for a pair of the nanostructures. w: Width of the nano structure. g_1: Gap between the silicon bars having voltage difference. g_2: Gap between the silicon bars having same voltage. w_p: Perturbated width. l_p: Perturbated length.

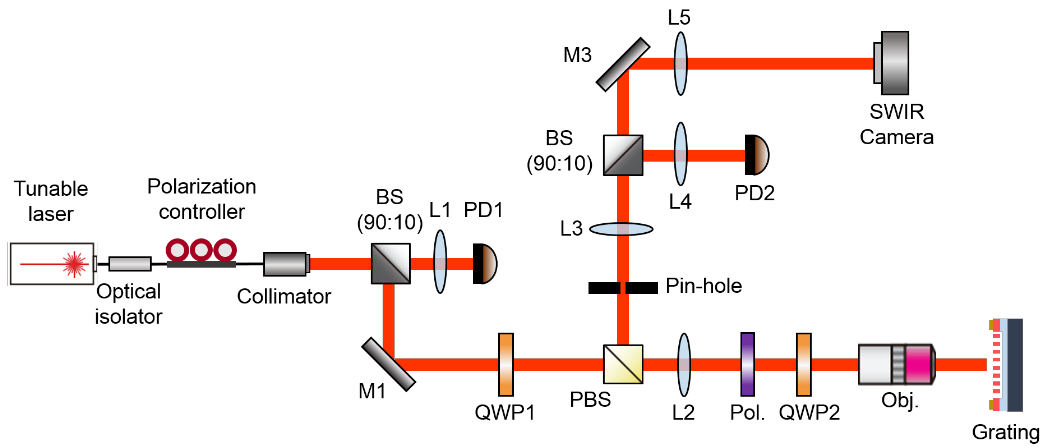

Figure 6.A.1: **Schematic illustration of the Experimental setup.** Red lines represent the paths of the light. Pol. of the objective lens are aligned to 45°. To achieve the reflection spectra of $R_{L,L}$ and $R_{R,R}$, the QWP2 is mounted on the rotation stage and aligned to 0° and 90°. Pol.: linear polarizer. BS: beamsplitter. PBS: polarizing beamsplitter. L: lens. PD: photodetector. M: mirror. QWP: quarter waveplate. HWP: half waveplate. Obj.: microscope objective lens. SWIR camera: short-wave infrared camera

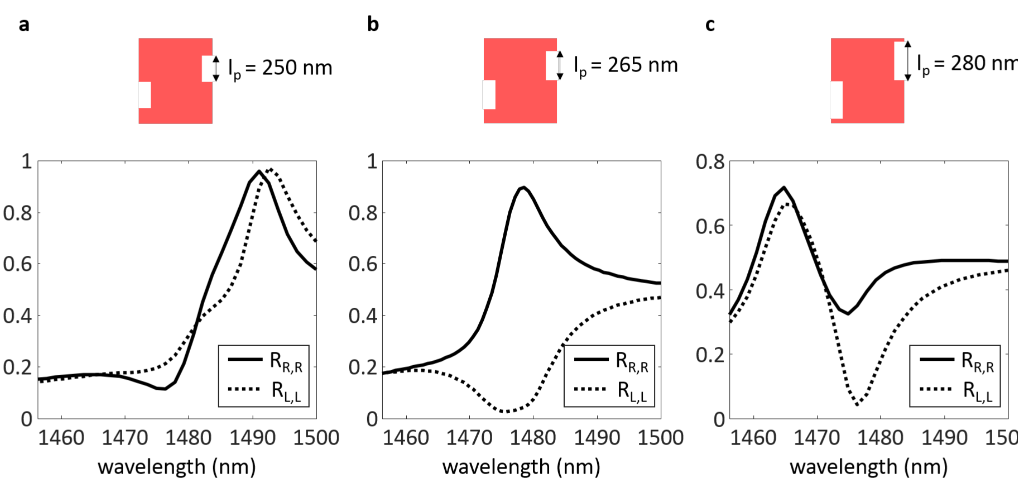

Figure 6.A.2: **Numerical investigation on fabrication errors. a-c** The simulated reflection spectra of $R_{L,L}$ and $R_{R,R}$ for different values of l_p. Other parameters are same with the parameters noted in Fig. 6.2 in the main text. Top: Schematic illustration of the nanostructures constituting to the metasurface. The values of l_p are shown in the illustration. Bottom: Calculated reflection spectra of $R_{L,L}$ and $R_{R,R}$. The spectra of $R_{L,L}$ and $R_{R,R}$ are plotted in dashed and solid lines, respectively.

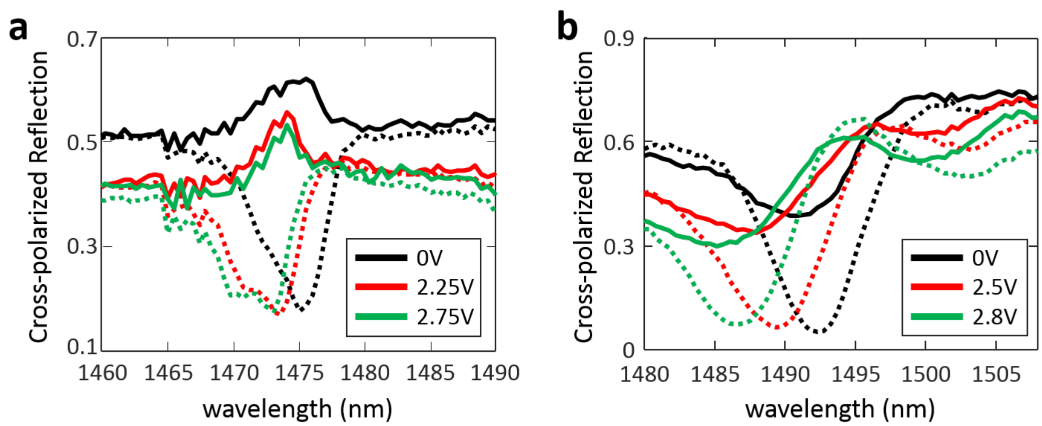

Figure 6.A.3: **Measured reflection spectra with electrical biases.** **a** and **b** Measured reflection spectra of $R_{L,L}$ and $R_{R,R}$ under different external biases. The devices exploited in Figs. 6.3**b** and 6.3**c** are measured and plotted in **a** and **b**, respectively. The spectra of $R_{L,L}$ and $R_{R,R}$ are plotted in dashed and solid lines, respectively. The applied bias for each color is shown in legends. The spectra of CD, $|R_{L,L} - R_{R,R}|$, are calculated from **a** and **b** and plotted in Fig. 6.4**a** and 6.4**b** in the main text.

Chapter 7

MULTILAYER METASTRUCTURES DESIGNED BY ADJOINT OPTIMIZATION

The material in this Chapter was in part presented in [206].

High-performance metasurfaces are important from a practical perspective. However, single-layer metasurfaces often show quick degradation in performance if the number of required optical functions increases. Thus, multi-layer metasurfaces, which are stacked layers of interacting metasurface layers, potentially provide sufficient degrees of freedom to implement efficient multifunctional devices. However, the design of the multi-layer metasurface is a complicated task due to considerable inter-layer coupling. Thus, the conventional design process used for the single-layer metasurfaces produces suboptimal devices. To address this challenge, we experimentally demonstrate the multi-layer metasurfaces that are designed by the adjoint optimization technique. Specifically, our technique considers the structure composed of more than 21,000 nanostructures as a whole and iteratively optimizes the structure. As proof of concept, we experimentally demonstrate a double-layered metasurface, designed using adjoint optimization, that has significantly higher efficiencies than a similar device designed with the conventional design approach. The multi-layer metasurfaces empowered by the optimization-based design technique and multi-layer nanofabrication is a general platform for high-performance multifunctional optical components and systems.

7.1 Introduction

Multilayer metasurfaces provide a significantly larger number of degrees of freedom and can be used for the implementation of multifunctional devices. Reference [81] recently demonstrated multiwavelength bilayer metasurfaces assuming layers to be non-interacting. However, considering interlayer interactions (evanescent coupling or unwanted diffracted propagating fields) allows one to leverage even more degrees of freedom for similarly-sized metasurfaces, promising higher-performing devices. Highly coupled multilayer metasurfaces can be considered as 2.5D aperiodic metamaterials [Fig. 7.1**a**]. Metamaterials and photonic crystals are periodic 3D arrangements of meta-atoms designed to achieve desired effective material properties or band structures, and are fully described by one of their unit cells. By contrast, 2.5D metastructures are composed of dissimilar interacting meta-atoms with a large number of design parameters. The methods that are conventionally used to design single-layer metasurfaces are not accurate for designing 2.5D devices due to multiple reflections and diffraction of light between the layers that lead to nonlocal interactions among meta-atoms in different layers. To address this issue, here we develop and use an adjoint optimization technique to design 2.5D metastructures.

Adjoint optimization [205, 234–237] is a versatile and powerful technique that has been used in the electromagnetics and optics communities to design various devices such as couplers and beam splitters [238], integrated components [239–242], and photonic crystals [234]. It has also been utilized to design single- [21, 243, 244] and multi-layer [245–247] metasurfaces; however, its applications have been mostly limited to periodic structures [21, 248] or 2D metasurfaces, resulting in a simpler formulation and implementation.

Here, we experimentally demonstrate 2.5D multifunctional metastructures designed using adjoint optimization. In contrast to most demonstrations so far that use a topological optimization scheme, we use parameterized meta-atoms that are more suitable for the layer-by-layer fabrication. The simulated and experimentally measured focusing efficiencies of the optimized device were found to be significantly higher than the simulated efficiency of the control, confirming the potential of the adjoint-based technique in designing high performance 2.5D multifunctional devices. We should mention that the detailed numerical study can be found in Ref. [206]. In this Chapter, we review the design method briefly and focus on the experimental demonstration.

7.2 Design process and numerical investigations

To describe the overall design process of the 2.5D metasurfaces, we use a bilayer metalens shown in Fig. 7.1**b** as an example. The bilayer structure in Fig. 7.1**b** is composed of more than 21,000 amorphous silicon meta-atoms arranged in two stacked layers. The bilayer meta-atoms are nano-posts with square cross-sections, and are placed on a periodic square lattice. The device has a diameter of 40 μm and focuses λ_1 = 780 nm and λ_2 = 915 nm light to two points 60 μm away from it. These two wavelengths were selected because of the availability of sources at these wavelengths. Although we use the bilayer metalens as an example in this study, we should explicitly mention that the proposed design (and fabrication) methods are generally applicable to 2.5D aperiodic metamaterials shown in Fig. 7.1**a**.

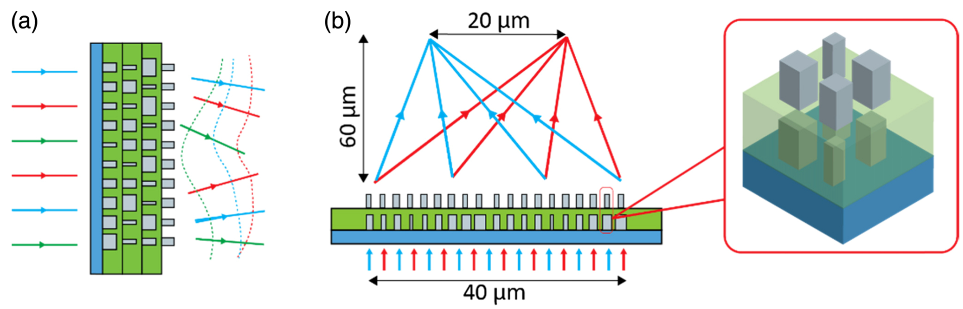

Figure 7.1: **Multifunctional 2.5D metastructure. a** Schematic of a metastructure with the ability to generate independent wavefronts for different wavelengths. **b** Illustration of one such metastructure which focuses two different wavelengths to two separate focal points. The blue and red arrows represent the light at the wavelength of 780 and 915 nm, respectively. The inset shows a closer picture of a part of the device.

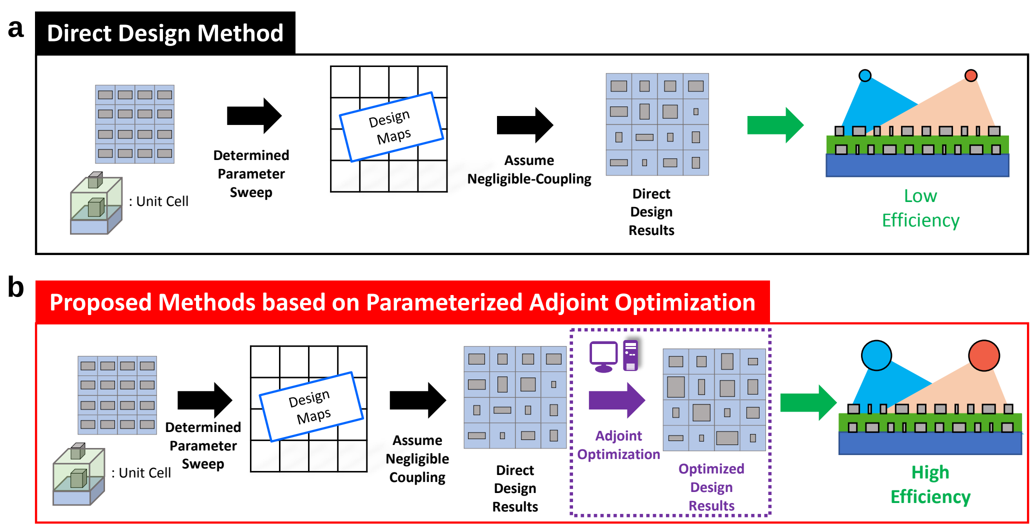

Figure 7.2: **Direct and optimized design methods of 2.5D metastructures. a** Illustration of the direct design method. First, the periodic unit cell is simulated by varying the design parameters to construct design maps. For the bilayer metasurfaces, the unit cell is composed of two nano-posts. With the desired optical transformation, the nanostructures in each unit cell can be chosen from the design maps. For the multi-layered structures, the direct design method often results in low efficiency. **b** Illustration of the proposed design method. The parameterized adjoint optimization is additionally performed after the direct design method shown in **a**. The additional optimization process improves the efficiency in general.

Figure 7.2**a** describes the direct design method. As shown in Fig. 7.2**a**, design maps are calculated with fully periodic conditions in the direct design method. The design maps relate the optical response of a unit cell to geometrical parameters of meta-atoms within it. Metastructures designed with this method use the design maps to determine the spatial arrangement of dissimilar unit cells that implement the desired optical transformation. An underlying assumption in the direct design is that the transmission amplitude of a unit cell in an aperiodic metasurface can be approximated by the transmission amplitude of the same unit cell in a periodic metasurface. The approximation is valid when the meta-atom geometries vary slowly and the metasurface is nearly periodic in the vicinity of each meta-atom. However, the accuracy of the approximation decreases as the interactions between neighboring unit cells deviate from those of a periodic structure. In the design of multilayer metasurfaces with conventional direct design, the deviation of the meta-atoms from perfect periodicity in one layer leads to scattering and diffraction of the waves in the spacer layers and non-local excitation of the meta-atoms in the following layers [81]. As a result, the accuracy of the direct technique for modeling and designing multilayer metasurfaces decreases as the number of layers increases.

Because of the inaccuracy of the underlying approximations of the direct design method, high-performance 2.5D metastructures cannot be designed using this method, and a new approach is required that accurately considers the complex interactions between meta-atoms. Thus, we employ the adjoint optimization technique to design such metastructures [21, 237, 238, 249, 250]. The newly proposed design method is shown in Fig. 7.2**b**. Compared to the direct design process shown in Fig. 7.2**a**, the additional parameterized adjoint optimization process is performed after the direct design process. In other words, we iteratively optimize the structure by using the directly designed metasurface as the initial design.

With the initial design, the adjoint optimization process starts by defining an objective function. Then, the device is optimized through an iterative procedure. Each iteration consists of two general steps: First, forward and adjoint simulations of the whole structure are performed. The results of these simulations are used to compute the gradient of the objective function with respect to the design parameters. Second, the design parameters are updated in small increments using the calculated gradient information. The iterations are continued until no further significant improvement to the objective function is observed.

For the proposed devices shown in Fig. 7.1**b**, the forward and adjoint simulations

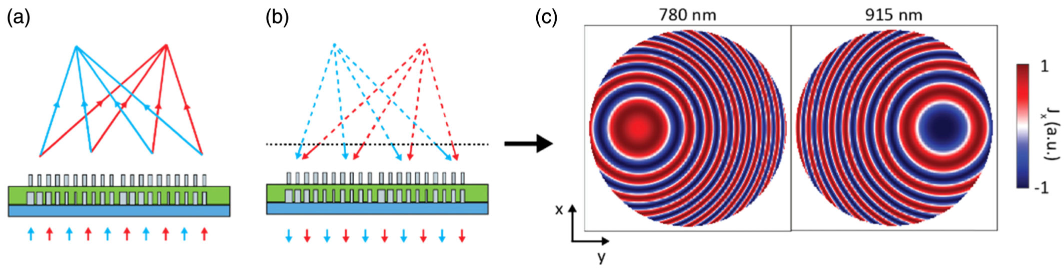

Figure 7.3: **Multiwavelength metalens design using adjoint technique. a** Schematic representation of the forward, and **b** the adjoint simulations in the adjoint optimization technique. In the forward simulation, the metalens is excited with the incident wave intended for the device operation, while in the adjoint simulation, it is excited by sources that are equal to the time-reversed (i.e., complex conjugate) of the desired output fields. **c** Color-coded plots of the surface electric current densities that are used as excitation sources in the adjoint simulation at the two wavelengths. The current densities are applied on the dotted plane shown in **b**.

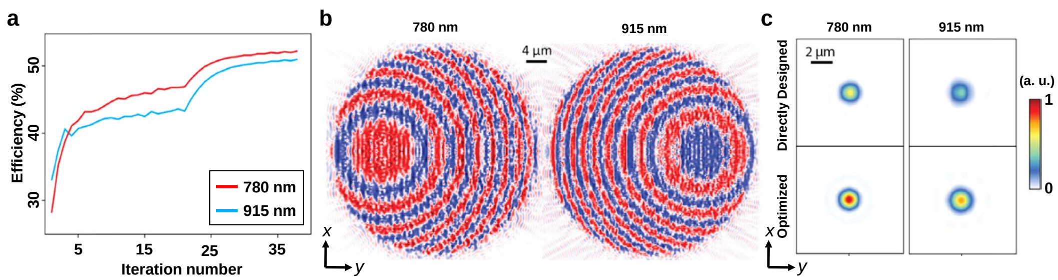

Figure 7.4: **Multifunctional metalens designed using adjoint optimization. a** Evolution of the focusing efficiencies of the device during the optimization process. **b** Electric field distribution on a plane 78 nm above the optimized metalens at 780 and 915 nm. **c** Simulated intensity distributions in the focal plane of the directly designed and optimized metalenses at 780 and 915 nm.

are conceptually illustrated in Figs. 7.3**a** and 7.3**b**, respectively. Specifically, in the forward simulations, normally incident plane waves at the wavelengths of 780 and 915 nm illuminate the metalens aperture [Fig. 7.3**a**]. In the adjoint simulation shown in Fig. 7.3**b**, the same structure is illuminated by adjoint sources that are equal to the complex conjugate of the desired output fields. A snapshot of the surface current densities that generate such illuminations are shown in Fig. 7.3**c**.

Figure 7.4**a** shows the evolution of the focusing efficiencies of the device, during the optimization process. The optimized device has simulated focusing efficiencies of 0.52 and 0.49 at 780 and 915 nm, respectively, for *x*-polarized incident light. Considering that the directly designed metasurface is used as an initial design, the results in Fig. 7.4**a** clearly show that the optimized efficiencies are significantly larger than the efficiencies of the directly designed metasurfaces. Snapshots of the electric fields in a plane ~80 nm above the optimized metalens' top surface are presented in Fig. 7.4**b**, showing great agreement of the adjoint sources shown in Fig. 7.3**c**. Figure 7.4**c** shows the focal plane intensities of the directly designed and optimized metalenses. Both devices are simulated with the same incident waves, and thus the focal spot intensities can be directly compared. In addition to the results shown in Fig. 7.4**a**, the focal plane intensities in Fig. 7.4**c** confirm that the proposed optimization method significantly improves the efficiency of the bilayer metasurfaces. Furthermore, it is worth noting that including additional degrees of freedom in the optimization (e.g., interlayer distance, post layer heights, additional layers of posts) can further increase the device efficiency [206].

7.3 Experimental results

We fabricated the 2.5D metalens using standard nano-fabrication techniques. A layer of amorphous silicon was deposited on a fused silica substrate, and the bottom layer meta-atom pattern was generated using electron beam lithography and dry etching. An SU-8 layer was then spin-coated to fill the gaps and cover the first metasurface, and to act as a spacer between the two layers. The top layer was then fabricated in a process mostly similar to the first one (see Methods for more details). Scanning electron micrographs of the fabricated devices showing top and cross-sectional views of the device are presented in Fig. 7.5**a**. By repeating the planarization and nano-post fabrication steps, an arbitrary number of layers can be incorporated.

The fabricated metalens was characterized using the setup shown schematically in Fig. 7.5**b** (see Methods for more details). Collimated beams from diode lasers at 780 and 915 nm were used to illuminate the device, and the intensity distribution after the device was measured using a custom-built microscope. The intensity distributions captured in the focal plane at both wavelengths are shown in Fig. 7.5**c** (logarithmic-scale intensity plots are shown in Fig. 7.A.2). Figure 7.5**d** shows the axial intensity distributions (in the y-z plane) at both wavelengths. As Figs. 7.5**c** and 7.5**d** show, the crosstalk between the two focal points is negligible. In Fig. 7.5**e**, the measured full width at half maximum (FWHM) spot sizes are 1.33 and 1.54 μm at 780 and 915 nm, respectively. For comparison, the corresponding FWHMs values for ideal phase profiles are 1.30 and 1.50 μm, respectively, and thus the device shows near-diffraction-limited focusing. To confirm that the device is polarization

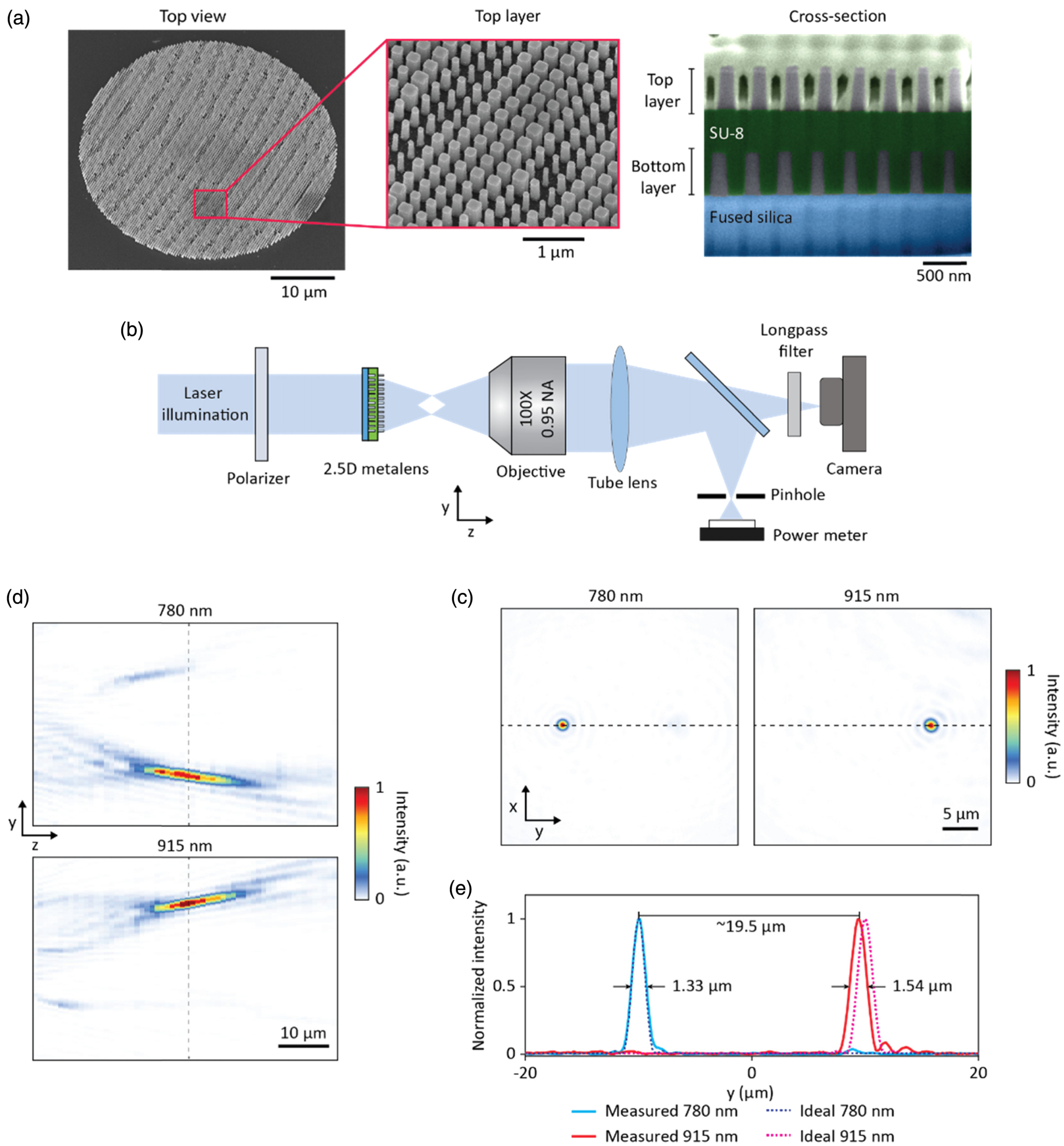

Figure 7.5: **Experimental results of the inverse-designed 2.5D metasurface. a** Scanning electron micrographs of the top and cross-sectional view of the 2.5D metalens. A thin, protective platinum layer (light green) was deposited on the top nano-post layer during cross-sectioning. **b** Schematic of the measurement setup used to characterize the bilayer metalens. **c** Intensity distributions measured in the y-z plane at 780 and 915 nm. **d** Intensity distributions measured in the focal plane of the device at 780 and 915 nm. **e** Intensity profile along the dashed lines shown in **c** and **d** at 780 and 915 nm.

insensitive, we measured the device with both x- and y-polarized input light and observed a negligible polarization dependence (see Fig. 7.A.1).

We measured the focusing efficiency of the device at both wavelengths, which is the ratio of optical power focused to a 3.6 μm diameter circle to the power incident on the device, at both wavelengths (see Methods for details). The measured efficiencies were found to be 30.3 ± 0.7% (33 ± 1.2%) and 38.2 ± 1% (36.5 ± 1%) for x-polarized(y-polarized) light at 780 and 915 nm, respectively. We attribute the lower measured efficiencies (in comparison to full-wave simulated values of about 50%) to fabrication imperfections, and especially to the difference between the fabricated spacer layer thickness of 800 nm from its designed value of 500 nm. To confirm this, we performed further full-wave simulations of the optimized metalens, but with the actual spacer thickness of 800 nm that resulted in efficiencies of 42% and 38%. Another source of imperfection in 2.5D metasurfaces is misalignment between registered layers. The device characterized in this Chapter was one of a large array of devices written with deliberate shifts (up to 200 nm in both x- and y-directions) in an effort to produce a device with minimal misalignment between layers. We experimentally characterized devices with a relative shift between layers to study this effect (see Fig. 7.A.3 for the measured efficiencies with several different lateral shifts.). A device with a 56 nm shift along the x-axis exhibited a -0.8% (-4.8%) change in efficiency for 780 (915) nm light, while a device with the same lateral shift along the y-axis exhibited changes of -7.2% (+1%). For reference, the misalignment between layers patterned using electron beam lithography is typically on the order of tens of nanometers.

7.4 Discussion and conclusion

The versatile 2.5D metastructure platform presented here provides more degrees of freedom than ordinary single layer metasurfaces, enabling the implementation of efficient multifunctional optical devices. By increasing the number of layers or by using more complicated meta-atoms, one can imagine the possibility of integrating additional functionalities by accommodating more wavelengths, different polarizations, or angles of incidence. The conventional direct methods used in designing metasurfaces have a few built-in approximations, making them inaccurate even for designing bilayer metastructures. The problem is exacerbated as the number of layers increases because the interactions between different layers become increasingly complex and thus cannot be captured by the simple unit cell model.

The adjoint optimization technique provides an effective approach for overcoming most of these design limitations. The cost, however, is the significantly increased computational resource requirements, resulting in demonstrations of either very small or 2D devices. The use of parameterized meta-atoms (instead of the conventionally used topological schemes) lays out a way of overcoming the design limitations while decreasing the computation time through reducing the design domain dimensionality. This compromise allows for optimization of 3D structures with volumes as large as a few thousand cubic wavelengths. However, the efficiencies achieved might be lower than what might be possible with a freeform device.

Although the fabrication process of 2.5D metastructures involves more steps than single-layer metasurfaces, the significant performance improvement is large enough to justify the more involved fabrication process. Multilayer structures with tens of nanometer tolerances are routinely fabricated in CMOS foundries, and similar processes can be potentially used to manufacture practical 2.5D multifunctional metastructures such as color-splitting filters for image sensors.

7.5 Methods

Device fabrication

A 578-nm-thick layer of α-Si was deposited using plasma-enhanced chemical vapor deposition (PECVD) on a 1-mm-thick fused silica substrate. For nano-patterning, we spincoated a positive electron-beam (e-beam) resist (ZEP520A) on the sample (~300 nm). In addition, a charge-dissipating polymer (aquaSave, Mitsubishi Rayon) was spin-coated on the e-beam resist layer to avoid electrostatic charging during the e-beam lithography. The first meta-atom layer and alignment marks were patterned by an e-beam lithography system (Vistec EBPG5000+) and developed in ZED-N50 developer. A ~60-nm Al_2O_3 layer was deposited by e-beam evaporation and then the nano-pattern was transferred to the Al_2O_3 layer by a lift-off process. The Al_2O_3 layer was used as a hard mask to etch the α-Si layer in a mixture of C_4F_8 and SF_6 gases. The Al_2O_3 was then removed by a mixture of NH_4OH and H_2O_2 at 100^oC.

To make a spacer between the first and second meta-atom layers, we spin-coated the SU-8 2002 at 5300 rpm and performed photo-lithography so that the alignment markers on the first layer were exposed. Subsequently, thermal reflow at 250^oC was performed for the planarization of the SU-8 layer, resulting in an ~1.38 μm spacer layer. We deposited the second 550-nm thick α-Si layer, and then the second layer was patterned using a procedure similar to the one used for the first layer. Finally, the removal process of Al_2O_3 is avoided because the mixture of NH_4OH and H_2O_2 could attack the SU-8 spacer layer.

Measurement

A schematic of the optical setup used to measure the two focal points is shown in Fig. 7.5. A 780-nm or 915-nm semiconductor laser was coupled to a single-mode fiber for illumination. The fiber was connected to a fiber polarization controller and a collimator package (Thorlabs, F220APC-850). A linear polarizer (Thorlabs, LPVIS100-MP2) was placed in front of the collimator to confirm the polarization of the input light, and the fiber polarization controller was used to maximize the power passing through the polarizer. A custom-built microscope setup, which was used to capture the focal plane intensity distributions, consisted of a 100× objective lens (Olympus, UNPlanFl) with an NA of 0.95, a tube lens with a focal length of 15 cm (Thorlabs, AC254-150-B-ML), and a CCD camera (CoolSNAP K4, Photometrics). The objective lens was mounted on the three-axis stage. To decrease the background noise, an optical longpass filter (Thorlabs, FEL0700) was placed in front of the camera. Furthermore, a flip mirror and a pinhole with a diameter of 300 μm (Thorlabs, P300D) in the image plane of the microscope were used to measure the focusing efficiency. The pinhole was mounted on the axial stage for alignment. To calculate the focusing efficiency, we divided the optical power focused by the device and passed through the pinhole by the power incident on the device. The power incident on the device was measured by placing an iris instead of the pinhole and removing the sample and adjusting the iris diameter to effectively have a 40-μm diameter at the sample plane. Moreover, the objective lens is moved along the z-axis in steps of 1 μm for obtaining the axial plane measurements shown in Figs. 7.5**d** and 7.A.1**c**.

7.6 Appendix

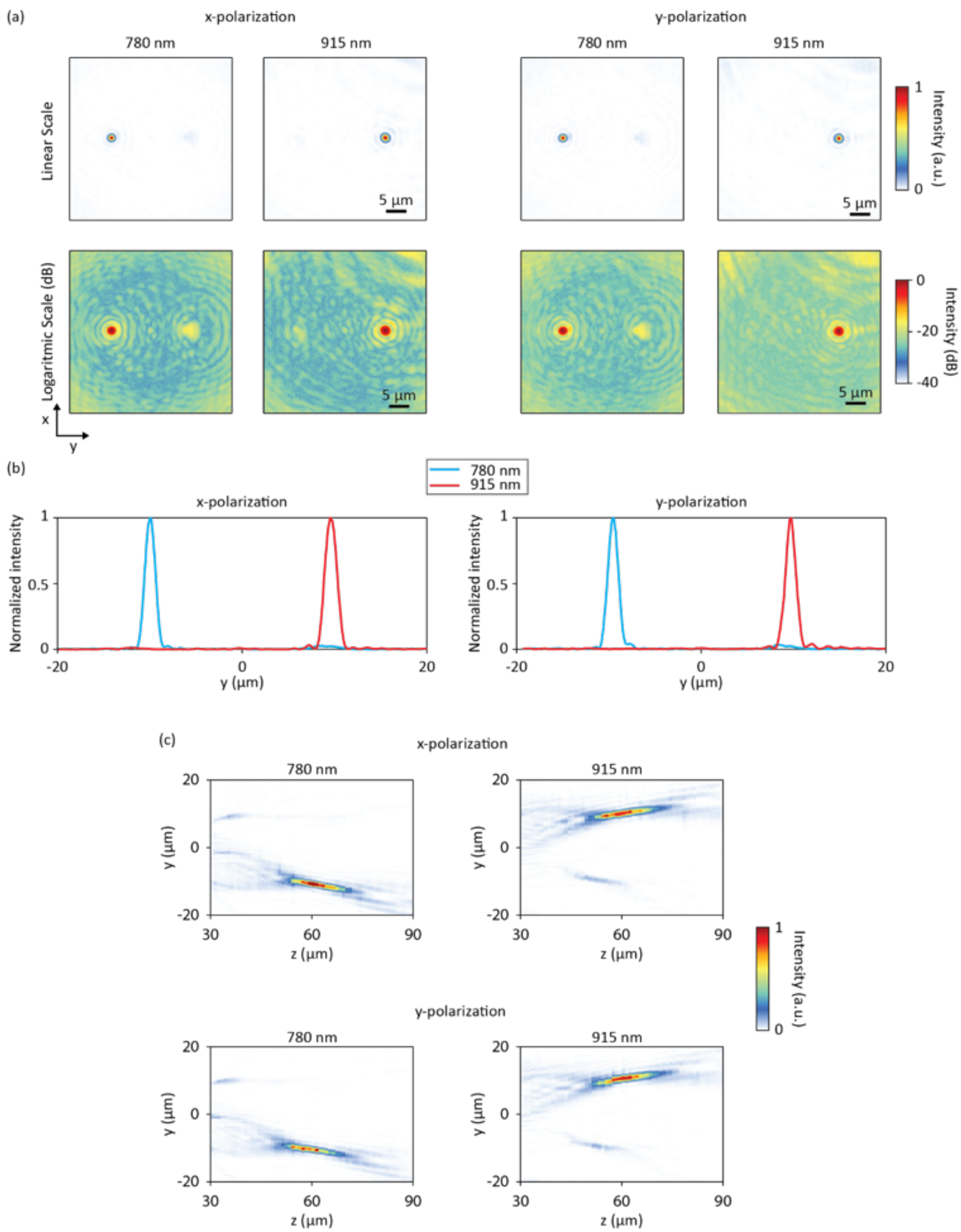

Figure 7.A.1: **Polarization-resolved measurements of the optimized metalens.** **a** Measured focal plane intensity distributions for x- and y-polarized incident light on linear and logarithmic scales. **b** Focal plane intensity profiles along the $x = 0$ line for x- and y-polarized incident light. **c** Measured intensity distributions in the y-z plane for x- and y-polarized incident light.

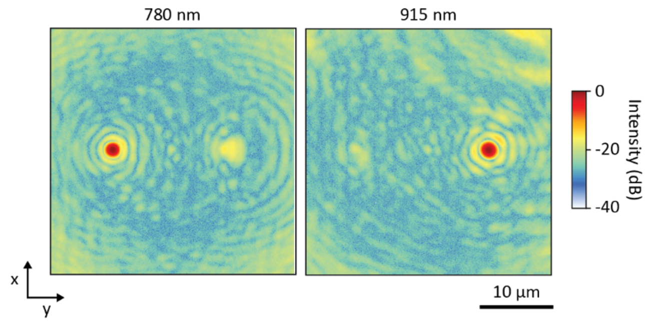

Figure 7.A.2: **Measured focal plane intensity distributions of the optimized metalens on a logarithmic scale at 780 nm and 915 nm.**

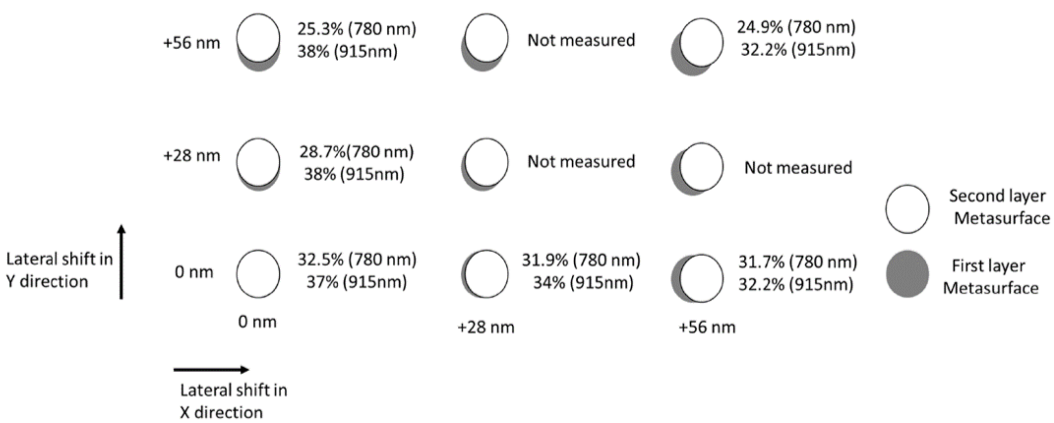

Figure 7.A.3: **Schematic diagram of measured efficiencies for different inter-layer shifts.**

Chapter 8

CONCLUSION AND OUTLOOK

8.1 Summary and Contributions

In this thesis, I investigated dielectric metastructures for optical field imaging systems, reconfigurable optical elements, and high-performance multi-layered optical devices. In Chapter 1, we first introduced the concept of optical metasurfaces and briefly reviewed the history of metasurfaces. Then, we focused on the recent advancements of high-contrast dielectric metasurfaces. In addition to passive metasurfaces, a brief overview of active metasurfaces was also introduced. In Chapter 2 and 3, we proposed and explored optical field imaging devices using high-contrast dielectric metasurfaces. In particular, we extensively employed the high-contrast metasurfaces' unique capability to control phase and polarization simultaneously. In Chapter 2, we demonstrated novel single-shot quantitative phase gradient microscopes inspired by conventional differential interference microscopes. The proposed quantitative phase gradient microscope was composed of two dielectric metasurface layers. The quantitative phase gradient microscope simultaneously captured three phase-shifted interference patterns to generate a quantitative phase gradient image in a single shot. Also, the volumes of the metasurface optical systems was on the order of 1-mm^3 volume. Imaging experiments with various phase samples verified their capability to capture quantitative phase gradient data, with phase gradient sensitivity better than 92.3 mrad/μm, single cell resolution, and low spatial and temporal noise level. In Chapter 3, we proposed a computational holographic imaging system based on metasurface diffusers and the speckle-correlation scattering matrix method. We experimentally showed holographic reconstruction of USAF resolution targets. Furthermore, we explored the mathematical properties of the metasurface's transmission matrix such as correlation between columns and singular value spectrum, which elucidate the metasurfaces' properties in the aspect of random media. Compared to the conventional random media, the metasurface diffusers provided a large noise tolerance, reliable reproducibility, and robustness against misalignments. More importantly, the metasurface diffusers (or the random metasurface) allowed for replacing the laborious experimental characterization procedure of the conventional random media with a simple simulation process. In Chapters 4-6, we proposed nano-electromechanically tunable metasurfaces as a new platform for active metasurfaces. Three different types of nano-electromechanically tunable metasurfaces were experimentally demonstrated. For example, we exploited two resonant eigenmodes to showcase the intensity and phase modulators in Chapter 4. Particularly, the metasurfaces hosted two different types of resonances, leaky guided mode resonances and quasi-bound states in the continuum, enabling efficient nano-electromechanical tuning of the optical responses. The devices experimentally achieved intensity modulation over 40 % with >10kHz modulation speed in air. More importantly, we showed that the phase response at the resonance can be enhanced by the interference between the two resonant modes. The devices experimentally achieved 144° phase modulation. In Chapter 5, we exploited the high-order Mie resonance in the dielectric nanostructures instead of the guided mode resonances discussed in Chapter 4 such that the metasurfaces efficiently supported wavefront-engingeering. Specifically, we intentionally broke the mirror symmetry in the z-axis and this broken symmetry uniquely enabled the large phase response in reflection without mirrors. The metasurfaces showed the large phase modulation over 300° and the electrically controllable diffraction in experiment. In Chapter 6, we showcased the novel chiroptical modulators based on the dielectric chiral metasurfaces and NEMS. In experiment, the devices achieved the reconfigurable transition from strong to negligible chiroptical responses within the electrical bias of 3V. This work generally showed that the metasurfaces could realize a new type of spatial light modulators. In Chapter 7, we experimentally demonstrated the double-layered metastructures for highly efficient multifunctional optical elements. In general, the design of multi-layered metastructures is a complicated task because of considerable inter-layer coupling. Therefore, we addressed this issue by designing the layered metastructures using the parameterized adjoint optimization technique. The optimized devices had significantly higher efficiencies than a similar device designed with the conventional unit-cell approach. The multi-layered metastructures empowered by the optimization-based design technique and multi-layer nanofabrication is a general platform for the realization of high-performance multifunctional optical components and systems.

8.2 Outlook

In the last two decades, the dielectric metasurfaces have shown great potentials beyond bulky refractive optical elements or conventional diffractive optical elements. These metasurfaces have not only outperformed conventional diffractive optical elements in terms of the efficiencies, but also offered novel optical functionalities, planar form factor, compatibility with conventional semiconductor fabrication processes, and potentials for system-level free-space optical engineering. With those advantages, we believe that metasurfaces are promising candidates for the realization of the next-generation free-space optical systems. On the other hand, several fundamental and practical challenges have still remained unsolved. Thus, we will discuss the opportunities and the challenges of metasurfaces in various aspects.

Metasurfaces may offer great opportunities in free-space optical imaging and sensing applications. First of all, the high-contrast metasurfaces have already shown superior imaging performance for narrow-band applications compared to conventional assembly of polymer-based lenses which are widely used in CMOS camera modules [251]. These narrow-band cameras have great applications in autonomous vehicles, eye-tracking for AR/VR headsets, and face/fingerprint recognition system in smartphones. Moreover, the single-layered or volumetric metasurfaces are promising candidates for next-generation color filters thanks to their small foot-print and superior optical functionality [252–254]. In addition to the intensity imaging and the color filters, we expect that the metasurfaces' unprecedented optical functionality can play pivotal roles for optical functional imaging system such as phase imaging [56, 101], polarization imaging [255–257], spectrometer [40] or spectral imaging [258], edge detection [17, 83], and other multidimensional imaging. In this context, the works presented in Chapters 2 and 3 showcased the metasurfaces' potentials for the phase imaging [56, 101]. Despite the metasurfaces' great potentials in the field of optical imaging and sensing, severe chromatic aberration of the metasurfaces has resulted in narrow operating bandwidth and become critical issues for the real-world applications. For instance, the narrow bandwidth primarily hinders the metasurfaces' applications for lenses in ubiquitous color camera modules. Although several seminar works have demonstrated dispersion-engineered achromatic metasurfaces [14, 15, 259], the sizes and numerical apertures of the demonstrated devices are very limited. Recently, it was theoretically shown that the dispersion-engineering method cannot realize high-NA large-size achromatic lenses [14, 260]. In contrast to the aforementioned dispersion engineering method, a novel way to overcome the narrow bandwidth issue has been proposed recently, utilizing cascade metasurfaces [261]. Specifically, the sophisticatedly designed cascaded metasurfaces leverage the propagation between the two metasurface layers to significantly enlarge the bandwidth [261]. However, the imaging quality of the proposed metasurface lenses has not been experimentally explored yet. Therefore, the achromatic metasurfaces lenses having a large diameter over a few millimeter and moderate numerical apertures have not been demonstrated. Furthermore, the broadband functional imaging such as white-light polarization or phase imaging might be of great interests for applications in remote sensing, computer vision, and point-of-care. Finally, instead of improving the metasurfaces in the classical optical systems, co-design of the metasurfaces and computational algorithms may open up new opportunities over the classical imaging systems based on the metasurfaces [101, 129, 262, 263].

Low-cost mass-production of metasurfaces is also important for real-world applications. Including all the works presented in this thesis, most of the works in the academic literature still rely on expensive electron beam lithography rather than conventional photolithography so far. However, it is worth noting that a company in the USA (Applied Materials) and a national laboratory in Singapore (A-Star) have already demonstrated metasurface lenses on 12-inch glass wafers by using standard semiconductor fabrication technology [264]. Also, nano-imprinting [265, 266] and roll-to-roll [267] fabrication techniques have shown great potentials as alternative scalable fabrication methods. In addition to the high-volume production, the uses of the semiconductor fabrication techniques, the planar features, and the high refractive indices of optical materials can be beneficial for the integration of multiple metasurfaces. Considering that the alignment process of the separate optical elements in conventional optical systems often costs more than the optical elements themselves, the integration of the multiple metasurfaces with the accuracy of the conventional multi-layer nanofabrication may ease the complicated optical alignment process and provide scalable ways to realize the complicated free-space optical systems. It is worth noting here that the concept of the folded metasurfaces suggests promising methods to fabricate multiple elements in a single lithography step [40, 258, 268]. Unlike the conventional optical elements, the metasurface is suitable for the co-integration of the photonic and electronic components because both the metasurfaces and the electronic chips can be produced by the same foundry process in principle. This aspect is potentially advantageous for the high volume low-cost optical sensors and on-chip active metasurfaces.

High efficiency of the metasurfaces is very important for realizing high-performance optical devices. Furthermore, the high efficiency is a prerequisite for system-level engineering. That is because the total efficiency of the system is rapidly degraded if the systems are composed of inefficient optical elements. In this regard, new design methods to optimize efficiencies are critically needed. To overcome the conventional design approaches that utilize a limited design space, various inverse designed methods [205] such as gradient-free optimization [269], adjoint-optimization [21, 270], and deep learning [271] have been proposed. These inverse designed methods may not only improve the efficiency significantly, but also provide general design methods for multi-layered or volumetric metastructures as we discussed in Chapter 7 [206, 254]. However, general optimization platforms to design efficient metastructures have not been introduced yet and the experimental demonstrations of the optimized performance are still very limited. Thus, we believe that there is a lot of room for optimization of high-performance metadevices. In this regard, high-speed parallelized electromagnetic solvers for large-scale photonic simulations are particularly important in the field of metasurfaces as well as integrated photonic systems. On the other hand, fundamental limits of the metastructures' performance still remain unknown. Theory on the fundamental limits of the metasurface device is of great interest. This theoretical intuition will help to shed light on questions that have not been fully answered: "What is the fundamental limit of the efficiencies of the metasurface-based optical elements such as metalenses or metagratings?" "Do metasurfaces fundamentally outperform the conventional diffractive optical elements or holographic optical elements?" "How large does the number of available degree of freedom exist in a specific volume?", and so on.

Reliable modulators are essential to build high-end optical systems. In the field of silicon photonics, fast and efficient integrated phase modulators have played an essential role in many applications of the silicon photonics technology. For example, integrated phase modulators have enabled transceivers, optical phased arrays, and optical computing. Likewise, active metasurfaces in many spectral ranges are of great need for the next-generation free-space optical systems. Especially, high-efficiency, ultra-fast, high-resolution, electrically controllable wavefront tuning will open up new opportunities in many technologies such as LIDAR, holographic displays, bio-imaging, quantum optics, Li-Fi, and so on. As we demonstrated in Chapters 4 and 5, NEMS is one of the promising active platforms for high-performance spatial light phase modulators thanks to low energy consumption, compatibility with the foundry process, and large tuning range compared to weak optical nonlinear effects. Particularly, the relatively large tunability enables large optical bandwidth and low modulation voltage level. Despite these advantages, NEMS also has several limitations. First, the nanostructures in NEMS are usually suspended, so the devices are inherently fragile to external forces, and it is hard to achieve a large aperture size. While unsuspended nanostructures can be actuated in a stable manner and fabricated with a large aperture size, they usually require high-aspect ratios and considerable increase of the modulation voltages. Furthermore, the fundamental limit of the modulation speed is on the order of a few MHz, which is orders of magnitudes slower than electro-optic effects. Also, NEMS based on the silicon-on-insulator technology is not suitable for wavelength ranges below 1100 nm due to absorption of the silicon layers. In addition to NEMS, we can think of various active mechanisms. Particularly, the electro-optic materials such as lithium niobate, barium titanate, aluminum nitride, electro-optic polymer, and 2D materials are promising platforms for the high-speed active metasurfaces thanks to their high modulation speed up to tens of GHz. Although the nonlinearity of the electro-optic materials is very small in nature, we can significantly boost the weak light-matter interaction through high-Q free-space coupled resonators described in Chapters 5 and 6. As lithium niobate, barium titanate, and aluminum nitride achieve a large bandgap and large second-order optical nonlinearity at the same time, the resonant metasurfaces composed of those materials may realize high-speed (up to tens of GHz) spatial light modulators in a visible frequency range, which have potential applications to bio-imaging and quantum optics. Finally, the type of the spatial light modulators is not limited to the phase-dominant spatial light modulators. For example, we have demonstrated chiroptical modulators in Chapter 7. With diverse new optical functions provided by the metasurfaces, novel types of the spatial light modulators may be conceived for new technology.

In conclusion, we envision that the metasurfaces may provide unprecedented advantages over conventional free-space optical elements. So far, it is hard to say that the metasurfaces have changed a paradigm of optical engineering yet. We believe that they are still in the early stage towards the realization of a real-world technology. As we discussed above, much research is critically needed on how to realize the next-generation free-space optical systems using metasurfaces.

BIBLIOGRAPHY

[1]S. M. Kamali, E. Arbabi, A. Arbabi, and A. Faraon, "A review of dielectric optical metasurfaces for wavefront control", Nanophotonics **7**, 1041–1068 (2018) (cit. on pp. 1, 72, 91).

[2]A. I. Kuznetsov, A. E. Miroshnichenko, M. L. Brongersma, Y. S. Kivshar, and B. Luk'yanchuk, "Optically resonant dielectric nanostructures", Science **354** (2016) (cit. on pp. 1, 72, 91, 94).

[3]N. Yu and F. Capasso, "Flat optics with designer metasurfaces", Nature materials **13**, 139–150 (2014) (cit. on pp. 1, 2, 41).

[4]S. Jahani and Z. Jacob, "All-dielectric metamaterials", Nature nanotechnology **11**, 23–36 (2016) (cit. on pp. 1, 8, 41).

[5]F. Ding, A. Pors, and S. I. Bozhevolnyi, "Gradient metasurfaces: a review of fundamentals and applications", Reports on Progress in Physics **81**, 026401 (2017) (cit. on pp. 1, 41).

[6]H.-H. Hsiao, C. H. Chu, and D. P. Tsai, "Fundamentals and applications of metasurfaces", Small Methods **1**, 1600064 (2017) (cit. on pp. 1, 41).

[7]P. Genevet, F. Capasso, F. Aieta, M. Khorasaninejad, and R. Devlin, "Recent advances in planar optics: from plasmonic to dielectric metasurfaces", Optica **4**, 139–152 (2017) (cit. on pp. 1, 8, 41).

[8]N. Yu, P. Genevet, M. A. Kats, F. Aieta, J.-P. Tetienne, F. Capasso, and Z. Gaburro, "Light propagation with phase discontinuities: generalized laws of reflection and refraction", science **334**, 333–337 (2011) (cit. on pp. 1, 2).

[9]J. Huang, "Reflectarray antenna", Encyclopedia of RF and Microwave Engineering (2005) (cit. on p. 1).

[10]D. Pozar and T. Metzler, "Analysis of a reflectarray antenna using microstrip patches of variable size", Electronics Letters **29**, 657–658 (1993) (cit. on p. 1).

[11]P. Lalanne and P. Chavel, "Metalenses at visible wavelengths: past, present, perspectives", Laser & Photonics Reviews **11**, 1600295 (2017) (cit. on p. 2).

[12]M. Decker et al., "Imaging performance of polarization-insensitive metalenses", Acs Photonics **6**, 1493–1499 (2019) (cit. on p. 2).

[13]A. Arbabi, Y. Horie, M. Bagheri, and A. Faraon, "Dielectric metasurfaces for complete control of phase and polarization with subwavelength spatial resolution and high transmission", Nature nanotechnology **10**, 937–943 (2015) (cit. on pp. 2–4, 8–11, 18, 42, 54).

[14]E. Arbabi, A. Arbabi, S. M. Kamali, Y. Horie, and A. Faraon, "Controlling the sign of chromatic dispersion in diffractive optics with dielectric metasurfaces", Optica **4**, 625–632 (2017) (cit. on pp. 2, 8, 53, 148).

[15]W. T. Chen, A. Y. Zhu, V. Sanjeev, M. Khorasaninejad, Z. Shi, E. Lee, and F. Capasso, "A broadband achromatic metalens for focusing and imaging in the visible", Nature nanotechnology **13**, 220–226 (2018) (cit. on pp. 2, 8, 53, 148).

[16]S. M. Kamali, E. Arbabi, A. Arbabi, Y. Horie, M. Faraji-Dana, and A. Faraon, "Angle-multiplexed metasurfaces: encoding independent wavefronts in a single metasurface under different illumination angles", Physical Review X **7**, 041056 (2017) (cit. on pp. 2, 8).

[17]Y. Zhou, H. Zheng, I. I. Kravchenko, and J. Valentine, "Flat optics for image differentiation", Nature Photonics **14**, 316–323 (2020) (cit. on pp. 2, 148).

[18]C. W. Hsu, B. Zhen, A. D. Stone, J. D. Joannopoulos, and M. Soljačić, "Bound states in the continuum", Nature Reviews Materials **1**, 1–13 (2016) (cit. on pp. 2, 71, 74, 75).

[19]G. Quaranta, G. Basset, O. J. Martin, and B. Gallinet, "Recent advances in resonant waveguide gratings", Laser & Photonics Reviews **12**, 1800017 (2018) (cit. on pp. 2, 71).

[20]D. Lin, P. Fan, E. Hasman, and M. L. Brongersma, "Dielectric gradient metasurface optical elements", science **345**, 298–302 (2014) (cit. on pp. 2, 8).

[21]D. Sell, J. Yang, S. Doshay, R. Yang, and J. A. Fan, "Large-angle, multifunctional metagratings based on freeform multimode geometries", Nano letters **17**, 3752–3757 (2017) (cit. on pp. 2, 134, 136, 150).

[22]M. Decker et al., "High-efficiency dielectric huygens' surfaces", Advanced Optical Materials **3**, 813–820 (2015) (cit. on pp. 2, 80).

[23]Y. F. Yu, A. Y. Zhu, R. Paniagua-Domınguez, Y. H. Fu, B. Luk'yanchuk, and A. I. Kuznetsov, "High-transmission dielectric metasurface with 2π phase control at visible wavelengths", Laser & Photonics Reviews **9**, 412–418 (2015) (cit. on pp. 2, 41).

[24]C. Gigli, Q. Li, P. Chavel, G. Leo, M. Brongersma, and P. Lalanne, "Fundamental limitations of huygens' metasurfaces for optical beam shaping", arXiv e-prints, arXiv–2011 (2020) (cit. on p. 2).

[25]P. Lalanne, S. Astilean, P. Chavel, E. Cambril, and H. Launois, "Blazed binary subwavelength gratings with efficiencies larger than those of conventional échelette gratings", Optics letters **23**, 1081–1083 (1998) (cit. on pp. 2, 8).

[26]D. Fattal, J. Li, Z. Peng, M. Fiorentino, and R. G. Beausoleil, "Flat dielectric grating reflectors with focusing abilities", Nature Photonics **4**, 466–470 (2010) (cit. on pp. 2, 3).

[27]A. Arbabi, Y. Horie, A. J. Ball, M. Bagheri, and A. Faraon, "Subwavelength-thick lenses with high numerical apertures and large efficiency based on high-contrast transmitarrays", Nature communications **6**, 1–6 (2015) (cit. on pp. 2–4, 41).

[28]M. Khorasaninejad, W. T. Chen, R. C. Devlin, J. Oh, A. Y. Zhu, and F. Capasso, "Metalenses at visible wavelengths: diffraction-limited focusing and subwavelength resolution imaging", Science **352**, 1190–1194 (2016) (cit. on pp. 2, 41).

[29]N. I. Landy, S. Sajuyigbe, J. J. Mock, D. R. Smith, and W. J. Padilla, "Perfect metamaterial absorber", Physical review letters **100**, 207402 (2008) (cit. on p. 3).

[30]Y. Horie et al., "Visible wavelength color filters using dielectric subwavelength gratings for backside-illuminated cmos image sensor technologies", Nano letters **17**, 3159–3164 (2017) (cit. on p. 3).

[31]Y. Horie, A. Arbabi, E. Arbabi, S. M. Kamali, and A. Faraon, "Wide bandwidth and high resolution planar filter array based on dbr-metasurface-dbr structures", Optics express **24**, 11677–11682 (2016) (cit. on p. 3).

[32]M. Hentschel, M. Schäferling, X. Duan, H. Giessen, and N. Liu, "Chiral plasmonics", Science advances **3**, e1602735 (2017) (cit. on pp. 3, 118).

[33]X. Ma, M. Pu, X. Li, Y. Guo, P. Gao, and X. Luo, "Meta-chirality: fundamentals, construction and applications", Nanomaterials **7**, 116 (2017) (cit. on pp. 3, 118).

[34]J. Mun et al., "Electromagnetic chirality: from fundamentals to nontraditional chiroptical phenomena", Light: Science & Applications **9**, 1–18 (2020) (cit. on pp. 3, 118).

[35]J. Lee et al., "Giant nonlinear response from plasmonic metasurfaces coupled to intersubband transitions", Nature **511**, 65–69 (2014) (cit. on p. 3).

[36]Y. Yang et al., "Nonlinear fano-resonant dielectric metasurfaces", Nano letters **15**, 7388–7393 (2015) (cit. on p. 3).

[37]G. Li, S. Zhang, and T. Zentgraf, "Nonlinear photonic metasurfaces", Nature Reviews Materials **2**, 1–14 (2017) (cit. on p. 3).

[38]C. J. Chang-Hasnain and W. Yang, "High-contrast gratings for integrated optoelectronics", Advances in Optics and Photonics **4**, 379–440 (2012) (cit. on p. 3).

[39]S. M. Kamali, E. Arbabi, A. Arbabi, Y. Horie, and A. Faraon, "Highly tunable elastic dielectric metasurface lenses", Laser & Photonics Reviews **10**, 1002–1008 (2016) (cit. on pp. 4, 17, 54).

[40]M. Faraji-Dana, E. Arbabi, A. Arbabi, S. M. Kamali, H. Kwon, and A. Faraon, "Compact folded metasurface spectrometer", Nature communications **9**, 4196 (2018) (cit. on pp. 4, 8, 15, 148, 149).

[41]S. J. Byrnes, A. Lenef, F. Aieta, and F. Capasso, "Designing large, high-efficiency, high-numerical-aperture, transmissive meta-lenses for visible light", Optics express **24**, 5110–5124 (2016) (cit. on p. 4).

[42]D. Sell, J. Yang, E. W. Wang, T. Phan, S. Doshay, and J. A. Fan, "Ultra-high-efficiency anomalous refraction with dielectric metasurfaces", Acs Photonics **5**, 2402–2407 (2018) (cit. on p. 4).

[43]A. Arbabi, E. Arbabi, M. Mansouree, S. Han, S. M. Kamali, Y. Horie, and A. Faraon, “Increasing efficiency of high numerical aperture metasurfaces using the grating averaging technique”, Scientific reports **10**, 1–10 (2020) (cit. on p. 4).

[44]N. A. Rubin, A. Zaidi, A. Dorrah, Z. Shi, and F. Capasso, “Jones matrix holography with metasurfaces”, arXiv preprint arXiv:2012.14874 (2020) (cit. on p. 5).

[45]A. M. Shaltout, V. M. Shalaev, and M. L. Brongersma, “Spatiotemporal light control with active metasurfaces”, Science **364** (2019) (cit. on pp. 5, 72, 91).

[46]Y.-W. Huang et al., “Gate-tunable conducting oxide metasurfaces”, Nano letters **16**, 5319–5325 (2016) (cit. on pp. 5, 91).

[47]G. K. Shirmanesh, R. Sokhoyan, P. C. Wu, and H. A. Atwater, “Electro-optically tunable multifunctional metasurfaces”, ACS nano **14**, 6912–6920 (2020) (cit. on pp. 5, 91).

[48]J. Park et al., “All-solid-state spatial light modulator with independent phase and amplitude control for three-dimensional lidar applications”, Nature Nanotechnology **16**, 69–76 (2021) (cit. on pp. 5, 90, 91).

[49]A. L. Holsteen, A. F. Cihan, and M. L. Brongersma, “Temporal color mixing and dynamic beam shaping with silicon metasurfaces”, Science **365**, 257–260 (2019) (cit. on pp. 5, 72, 91, 127).

[50]N. Dabidian et al., “Electrical switching of infrared light using graphene integration with plasmonic fano resonant metasurfaces”, Acs Photonics **2**, 216–227 (2015) (cit. on pp. 5, 91).

[51]M. C. Sherrott et al., “Experimental demonstration of> 230 phase modulation in gate-tunable graphene–gold reconfigurable mid-infrared metasurfaces”, Nano letters **17**, 3027–3034 (2017) (cit. on pp. 5, 91).

[52]Y. Kim, P. C. Wu, R. Sokhoyan, K. Mauser, R. Glaudell, G. Kafaie Shirmanesh, and H. A. Atwater, “Phase modulation with electrically tunable vanadium dioxide phase-change metasurfaces”, Nano letters **19**, 3961–3968 (2019) (cit. on pp. 5, 91).

[53]A. Leitis, A. Heßler, S. Wahl, M. Wuttig, T. Taubner, A. Tittl, and H. Altug, “All-dielectric programmable huygens’ metasurfaces”, Advanced Functional Materials **30**, 1910259 (2020) (cit. on p. 5).

[54]P. C. Wu et al., “Dynamic beam steering with all-dielectric electro-optic iii–v multiple-quantum-well metasurfaces”, Nature communications **10**, 1–9 (2019) (cit. on pp. 5, 91).

[55]S.-Q. Li, X. Xu, R. M. Veetil, V. Valuckas, R. Paniagua-Domınguez, and A. I. Kuznetsov, “Phase-only transmissive spatial light modulator based on tunable dielectric metasurface”, Science **364**, 1087–1090 (2019) (cit. on pp. 5, 91).

[56]H. Kwon, E. Arbabi, S. M. Kamali, M. Faraji-Dana, and A. Faraon, "Single-shot quantitative phase gradient microscopy using a system of multifunctional metasurfaces", Nature Photonics **14**, 109–114 (2020) (cit. on pp. 7, 148).

[57]F. Zernike, "How i discovered phase contrast", Science **121**, 345–349 (1955) (cit. on p. 7).

[58]W. Lang, *Nomarski differential interference-contrast microscopy* (Carl Zeiss, 1982) (cit. on p. 7).

[59]G. Popescu, *Quantitative phase imaging of cells and tissues* (McGraw Hill Professional, 2011) (cit. on pp. 7, 53).

[60]Y. Park, C. Depeursinge, and G. Popescu, "Quantitative phase imaging in biomedicine", Nature Photonics **12**, 578–589 (2018) (cit. on pp. 7, 8).

[61]R. Alford et al., "Toxicity of organic fluorophores used in molecular imaging: literature review", Molecular imaging **8**, 341–354 (2009) (cit. on p. 7).

[62]K. Lee et al., "Quantitative phase imaging techniques for the study of cell pathophysiology: from principles to applications", Sensors **13**, 4170–4191 (2013) (cit. on pp. 7, 53).

[63]P. Marquet, B. Rappaz, P. J. Magistretti, E. Cuche, Y. Emery, T. Colomb, and C. Depeursinge, "Digital holographic microscopy: a noninvasive contrast imaging technique allowing quantitative visualization of living cells with subwavelength axial accuracy", Optics letters **30**, 468–470 (2005) (cit. on p. 8).

[64]W. Choi, C. Fang-Yen, K. Badizadegan, S. Oh, N. Lue, R. R. Dasari, and M. S. Feld, "Tomographic phase microscopy", Nature methods **4**, 717 (2007) (cit. on p. 8).

[65]T. Kim, R. Zhou, M. Mir, S. D. Babacan, P. S. Carney, L. L. Goddard, and G. Popescu, "White-light diffraction tomography of unlabelled live cells", Nature Photonics **8**, 256–263 (2014) (cit. on p. 8).

[66]G. Zheng, R. Horstmeyer, and C. Yang, "Wide-field, high-resolution fourier ptychographic microscopy", Nature photonics **7**, 739–745 (2013) (cit. on pp. 8, 14).

[67]A. Greenbaum, Y. Zhang, A. Feizi, P.-L. Chung, W. Luo, S. R. Kandukuri, and A. Ozcan, "Wide-field computational imaging of pathology slides using lens-free on-chip microscopy", Science translational medicine **6**, 267ra175 (2014) (cit. on pp. 8, 17).

[68]K. K. Ghosh, L. D. Burns, E. D. Cocker, A. Nimmerjahn, Y. Ziv, A. El Gamal, and M. J. Schnitzer, "Miniaturized integration of a fluorescence microscope", Nature methods **8**, 871–878 (2011) (cit. on p. 8).

[69]F. Helmchen, M. S. Fee, D. W. Tank, and W. Denk, "A miniature head-mounted two-photon microscope: high-resolution brain imaging in freely moving animals", Neuron **31**, 903–912 (2001) (cit. on p. 8).

[70] Y. Ziv et al., “Long-term dynamics of ca1 hippocampal place codes”, Nature neuroscience **16**, 264–266 (2013) (cit. on p. 8).

[71] A. Zhan, S. Colburn, R. Trivedi, T. K. Fryett, C. M. Dodson, and A. Majumdar, “Low-contrast dielectric metasurface optics”, ACS Photonics **3**, 209–214 (2016) (cit. on p. 8).

[72] E. Maguid, I. Yulevich, D. Veksler, V. Kleiner, M. L. Brongersma, and E. Hasman, “Photonic spin-controlled multifunctional shared-aperture antenna array”, Science, aaf3417 (2016) (cit. on pp. 8, 9, 23).

[73] E. Arbabi, A. Arbabi, S. M. Kamali, Y. Horie, and A. Faraon, “Multiwavelength polarization-insensitive lenses based on dielectric metasurfaces with meta-molecules”, Optica **3**, 628–633 (2016) (cit. on pp. 8, 9, 23).

[74] Z. Shi et al., “Single-layer metasurface with controllable multiwavelength functions”, Nano letters **18**, 2420–2427 (2018) (cit. on p. 8).

[75] E. Arbabi et al., “Two-photon microscopy with a double-wavelength metasurface objective lens”, Nano letters **18**, 4943–4948 (2018) (cit. on p. 8).

[76] A. Y. Zhu et al., “Compact aberration-corrected spectrometers in the visible using dispersion-tailored metasurfaces”, Advanced Optical Materials, 1801144 (2018) (cit. on p. 8).

[77] H. Pahlevaninezhad et al., “Nano-optic endoscope for high-resolution optical coherence tomography in vivo”, Nature Photonics **12**, 540–547 (2018) (cit. on pp. 8, 18).

[78] A. Arbabi, E. Arbabi, S. M. Kamali, Y. Horie, S. Han, and A. Faraon, “Miniature optical planar camera based on a wide-angle metasurface doublet corrected for monochromatic aberrations”, Nature communications **7**, 13682 (2016) (cit. on pp. 8, 17, 53).

[79] A. Arbabi, E. Arbabi, Y. Horie, S. M. Kamali, and A. Faraon, “Planar metasurface retroreflector”, Nature Photonics **11**, 415–420 (2017) (cit. on pp. 8, 41).

[80] O. Avayu, E. Almeida, Y. Prior, and T. Ellenbogen, “Composite functional metasurfaces for multispectral achromatic optics”, Nature communications **8**, 14992 (2017) (cit. on p. 8).

[81] Y. Zhou, I. I. Kravchenko, H. Wang, J. R. Nolen, G. Gu, and J. Valentine, “Multilayer noninteracting dielectric metasurfaces for multiwavelength metaoptics”, Nano letters **18**, 7529–7537 (2018) (cit. on pp. 8, 133, 136).

[82] C. Guo, M. Xiao, M. Minkov, Y. Shi, and S. Fan, “Photonic crystal slab laplace operator for image differentiation”, Optica **5**, 251–256 (2018) (cit. on p. 8).

[83] H. Kwon, D. Sounas, A. Cordaro, A. Polman, and A. Alù, “Nonlocal metasurfaces for optical signal processing”, Physical review letters **121**, 173004 (2018) (cit. on pp. 8, 148).

[84]P. S. Huang and S. Zhang, “Fast three-step phase-shifting algorithm”, Applied optics **45**, 5086–5091 (2006) (cit. on pp. 10, 25).

[85]E. Arbabi, S. M. Kamali, A. Arbabi, and A. Faraon, “Full stokes imaging polarimetry using dielectric metasurfaces”, ACS Photonics **5**, 3132–3140 (2018) (cit. on p. 10).

[86]T. H. Nguyen, M. E. Kandel, M. Rubessa, M. B. Wheeler, and G. Popescu, “Gradient light interference microscopy for 3d imaging of unlabeled specimens”, Nature communications **8**, 210 (2017) (cit. on pp. 10, 15).

[87]Z. Wang et al., “Spatial light interference microscopy (slim)”, Optics express **19**, 1016–1026 (2011) (cit. on p. 10).

[88]N. T. Shaked, “Quantitative phase microscopy of biological samples using a portable interferometer”, Optics letters **37**, 2016–2018 (2012) (cit. on p. 10).

[89]P. Bon, G. Maucort, B. Wattellier, and S. Monneret, “Quadriwave lateral shearing interferometry for quantitative phase microscopy of living cells”, Optics express **17**, 13080–13094 (2009) (cit. on p. 10).

[90]Y. Baek, K. Lee, J. Yoon, K. Kim, and Y. Park, “White-light quantitative phase imaging unit”, Optics express **24**, 9308–9315 (2016) (cit. on p. 10).

[91]P. Bouchal, L. Štrbková, Z. Dostál, R. Chmelık, and Z. Bouchal, “Geometric-phase microscopy for quantitative phase imaging of isotropic, birefringent and space-variant polarization samples”, Scientific reports **9**, 1–11 (2019) (cit. on p. 10).

[92]D. Paganin and K. A. Nugent, “Noninterferometric phase imaging with partially coherent light”, Physical review letters **80**, 2586–2589 (1998) (cit. on p. 17).

[93]E. Arbabi, A. Arbabi, S. M. Kamali, Y. Horie, M. Faraji-Dana, and A. Faraon, “Mems-tunable dielectric metasurface lens”, Nature communications **9**, 812 (2018) (cit. on p. 17).

[94]A. She, S. Zhang, S. Shian, D. R. Clarke, and F. Capasso, “Adaptive metalenses with simultaneous electrical control of focal length, astigmatism, and shift”, Science Advances **4**, eaap9957 (2018) (cit. on p. 17).

[95]V. Liu and S. Fan, “S4: a free electromagnetic solver for layered periodic structures”, Computer Physics Communications **183**, 2233–2244 (2012) (cit. on pp. 18, 53, 82, 106).

[96]D. Lin, A. L. Holsteen, E. Maguid, G. Wetzstein, P. G. Kik, E. Hasman, and M. L. Brongersma, “Photonic multitasking interleaved si nanoantenna phased array”, Nano letters **16**, 7671–7676 (2016) (cit. on p. 23).

[97]C. J. Cogswell, N. I. Smith, K. G. Larkin, and P. Hariharan, “Quantitative dic microscopy using a geometric phase shifter”, in Three-dimensional microscopy: image acquisition and processing iv, Vol. 2984 (International Society for Optics and Photonics, 1997), pp. 72–81 (cit. on p. 28).

[98] X. Meng, L. Cai, X. Xu, X. Yang, X. Shen, G. Dong, and Y. Wang, "Two-step phase-shifting interferometry and its application in image encryption", Optics letters **31**, 1414–1416 (2006) (cit. on p. 28).

[99] J.-P. Liu and T.-C. Poon, "Two-step-only quadrature phase-shifting digital holography", Optics letters **34**, 250–252 (2009) (cit. on p. 28).

[100] Y. Zhang, X. Tian, and R. Liang, "Random two-step phase shifting interferometry based on lissajous ellipse fitting and least squares technologies", Optics express **26**, 15059–15071 (2018) (cit. on p. 28).

[101] H. Kwon, E. Arbabi, S. M. Kamali, M. Faraji-Dana, and A. Faraon, "Computational complex optical field imaging using a designed metasurface diffuser", Optica **5**, 924–931 (2018) (cit. on pp. 40, 148, 149).

[102] D. Huang et al., "Optical coherence tomography", science **254**, 1178–1181 (1991) (cit. on p. 40).

[103] R. Horstmeyer, H. Ruan, and C. Yang, "Guidestar-assisted wavefront-shaping methods for focusing light into biological tissue", Nature photonics **9**, 563–571 (2015) (cit. on pp. 40, 90).

[104] P. Berto, H. Rigneault, and M. Guillon, "Wavefront sensing with a thin diffuser", Optics Letters **42**, 5117–5120 (2017) (cit. on pp. 40, 41).

[105] O. Katz, P. Heidmann, M. Fink, and S. Gigan, "Non-invasive single-shot imaging through scattering layers and around corners via speckle correlations", Nature photonics **8**, 784–790 (2014) (cit. on p. 40).

[106] S. Popoff, G. Lerosey, M. Fink, A. C. Boccara, and S. Gigan, "Image transmission through an opaque material", Nature communications **1**, 1–5 (2010) (cit. on pp. 40, 47).

[107] K. T. Takasaki and J. W. Fleischer, "Phase-space measurement for depth-resolved memory-effect imaging", Optics express **22**, 31426–31433 (2014) (cit. on pp. 40, 41).

[108] H.-Y. Liu, E. Jonas, L. Tian, J. Zhong, B. Recht, and L. Waller, "3d imaging in volumetric scattering media using phase-space measurements", Optics express **23**, 14461–14471 (2015) (cit. on pp. 40, 41).

[109] A. K. Singh, D. N. Naik, G. Pedrini, M. Takeda, and W. Osten, "Exploiting scattering media for exploring 3d objects", Light: Science & Applications **6**, e16219–e16219 (2017) (cit. on pp. 40, 41).

[110] R. Horisaki, R. Egami, and J. Tanida, "Single-shot phase imaging with randomized light (spiral)", Optics express **24**, 3765–3773 (2016) (cit. on pp. 40, 41).

[111] N. Antipa, G. Kuo, R. Heckel, B. Mildenhall, E. Bostan, R. Ng, and L. Waller, "Diffusercam: lensless single-exposure 3d imaging", Optica **5**, 1–9 (2018) (cit. on pp. 40, 41, 58).

[112] X. Xie, H. Zhuang, H. He, X. Xu, H. Liang, Y. Liu, and J. Zhou, "Extended depth-resolved imaging through a thin scattering medium with psf manipulation", Scientific reports **8**, 1–8 (2018) (cit. on pp. 40, 41).

[113] K. Lee and Y. Park, "Exploiting the speckle-correlation scattering matrix for a compact reference-free holographic image sensor", Nature communications **7**, 1–7 (2016) (cit. on pp. 40, 41, 46, 48, 50, 56, 58).

[114] Y. Baek, K. Lee, and Y. Park, "High-resolution holographic microscopy exploiting speckle-correlation scattering matrix", Physical Review Applied **10**, 024053 (2018) (cit. on pp. 40, 41).

[115] B. Redding, S. F. Liew, R. Sarma, and H. Cao, "Compact spectrometer based on a disordered photonic chip", Nature Photonics **7**, 746–751 (2013) (cit. on pp. 40, 41).

[116] M. Chakrabarti, M. L. Jakobsen, and S. G. Hanson, "Speckle-based spectrometer", Optics letters **40**, 3264–3267 (2015) (cit. on pp. 40, 41).

[117] M. Mazilu, T. Vettenburg, A. Di Falco, and K. Dholakia, "Random super-prism wavelength meter", Optics letters **39**, 96–99 (2014) (cit. on pp. 40, 41).

[118] S. K. Sahoo, D. Tang, and C. Dang, "Single-shot multispectral imaging with a monochromatic camera", Optica **4**, 1209–1213 (2017) (cit. on pp. 40, 41).

[119] K. Lee and Y. Park, "Interpreting intensity speckle as the coherency matrix of classical light", Physical Review Applied **12**, 024003 (2019) (cit. on pp. 40, 41).

[120] L. Gong, Q. Zhao, H. Zhang, X.-Y. Hu, K. Huang, J.-M. Yang, and Y.-M. Li, "Optical orbital-angular-momentum-multiplexed data transmission under high scattering", Light: Science & Applications **8**, 1–11 (2019) (cit. on pp. 40, 41).

[121] H. Yilmaz, E. G. van Putten, J. Bertolotti, A. Lagendijk, W. L. Vos, and A. P. Mosk, "Speckle correlation resolution enhancement of wide-field fluorescence imaging", Optica **2**, 424–429 (2015) (cit. on pp. 40, 41).

[122] Y. Kashter, A. Vijayakumar, and J. Rosen, "Resolving images by blurring: superresolution method with a scattering mask between the observed objects and the hologram recorder", Optica **4**, 932–939 (2017) (cit. on pp. 40, 41).

[123] I. M. Vellekoop and A. Mosk, "Focusing coherent light through opaque strongly scattering media", Optics letters **32**, 2309–2311 (2007) (cit. on p. 41).

[124] A. Goetschy and A. Stone, "Filtering random matrices: the effect of incomplete channel control in multiple scattering", Physical review letters **111**, 063901 (2013) (cit. on p. 41).

[125] M. Jang et al., "Wavefront shaping with disorder-engineered metasurfaces", Nature photonics **12**, 84–90 (2018) (cit. on pp. 41, 42, 47, 54, 58).

[126] P. Moitra, B. A. Slovick, W. Li, I. I. Kravchencko, D. P. Briggs, S. Krishnamurthy, and J. Valentine, "Large-scale all-dielectric metamaterial perfect reflectors", Acs Photonics **2**, 692–698 (2015) (cit. on p. 41).

[127]L. Wang, S. Kruk, H. Tang, T. Li, I. Kravchenko, D. N. Neshev, and Y. S. Kivshar, "Grayscale transparent metasurface holograms", Optica **3**, 1504–1505 (2016) (cit. on p. 41).

[128]S. M. Kamali, A. Arbabi, E. Arbabi, Y. Horie, and A. Faraon, "Decoupling optical function and geometrical form using conformal flexible dielectric metasurfaces", Nature communications **7**, 1–7 (2016) (cit. on p. 41).

[129]S. Colburn, A. Zhan, and A. Majumdar, "Metasurface optics for full-color computational imaging", Science advances **4**, eaar2114 (2018) (cit. on pp. 41, 149).

[130]H.-C. Liu et al., "Single-pixel computational ghost imaging with helicity-dependent metasurface hologram", Science advances **3**, e1701477 (2017) (cit. on p. 41).

[131]A. Pors, F. Ding, Y. Chen, I. P. Radko, and S. I. Bozhevolnyi, "Random-phase metasurfaces at optical wavelengths", Scientific reports **6**, 28448 (2016) (cit. on p. 41).

[132]M. Castro-Lopez, M. Gaio, S. Sellers, G. Gkantzounis, M. Florescu, and R. Sapienza, "Reciprocal space engineering with hyperuniform gold disordered surfaces", APL Photonics **2**, 061302 (2017) (cit. on p. 41).

[133]E. Maguid, M. Yannai, A. Faerman, I. Yulevich, V. Kleiner, and E. Hasman, "Disorder-induced optical transition from spin hall to random rashba effect", Science **358**, 1411–1415 (2017) (cit. on p. 41).

[134]M. S. Asif, A. Ayremlou, A. Veeraraghavan, R. Baraniuk, and A. Sankaranarayanan, "Flatcam: replacing lenses with masks and computation", in 2015 ieee international conference on computer vision workshop (iccvw) (IEEE, 2015), pp. 663–666 (cit. on p. 42).

[135]R. Horisaki, R. Egami, and J. Tanida, "Experimental demonstration of single-shot phase imaging with a coded aperture", Optics express **23**, 28691–28697 (2015) (cit. on p. 42).

[136]J. K. Adams et al., "Single-frame 3d fluorescence microscopy with ultraminiature lensless flatscope", Science advances **3**, e1701548 (2017) (cit. on p. 42).

[137]R. W. Gerchberg, "A practical algorithm for the determination of phase from image and diffraction plane pictures", Optik **35**, 237–246 (1972) (cit. on pp. 43, 54).

[138]J. R. Fienup, "Phase retrieval algorithms: a comparison", Applied optics **21**, 2758–2769 (1982) (cit. on p. 43).

[139]R. Piestun, B. Spektor, and J. Shamir, "Wave fields in three dimensions: analysis and synthesis", JOSA A **13**, 1837–1848 (1996) (cit. on p. 43).

[140]S. Popoff, G. Lerosey, R. Carminati, M. Fink, A. Boccara, and S. Gigan, "Measuring the transmission matrix in optics: an approach to the study and control of light propagation in disordered media", Physical review letters **104**, 100601 (2010) (cit. on p. 47).

[141]C. W. Hsu, S. F. Liew, A. Goetschy, H. Cao, and A. D. Stone, "Correlation-enhanced control of wave focusing in disordered media", Nature Physics **13**, 497–502 (2017) (cit. on p. 47).

[142]S. Popoff, G. Lerosey, M. Fink, A. C. Boccara, and S. Gigan, "Controlling light through optical disordered media: transmission matrix approach", New Journal of Physics **13**, 123021 (2011) (cit. on p. 47).

[143]V. A. Marchenko and L. A. Pastur, "Distribution of eigenvalues for some sets of random matrices", Matematicheskii Sbornik **114**, 507–536 (1967) (cit. on p. 47).

[144]H. Yu, T. R. Hillman, W. Choi, J. O. Lee, M. S. Feld, R. R. Dasari, and Y. Park, "Measuring large optical transmission matrices of disordered media", Physical review letters **111**, 153902 (2013) (cit. on p. 47).

[145]A. Greenbaum et al., "Imaging without lenses: achievements and remaining challenges of wide-field on-chip microscopy", Nature methods **9**, 889–895 (2012) (cit. on p. 53).

[146]B. Groever, W. T. Chen, and F. Capasso, "Meta-lens doublet in the visible region", Nano letters **17**, 4902–4907 (2017) (cit. on p. 53).

[147]F. Aieta, M. A. Kats, P. Genevet, and F. Capasso, "Multiwavelength achromatic metasurfaces by dispersive phase compensation", Science **347**, 1342–1345 (2015) (cit. on p. 53).

[148]S. Wang et al., "Broadband achromatic optical metasurface devices", Nature communications **8**, 1–9 (2017) (cit. on p. 53).

[149]S. Wang et al., "A broadband achromatic metalens in the visible", Nature nanotechnology **13**, 227–232 (2018) (cit. on p. 53).

[150]A. Sinha, J. Lee, S. Li, and G. Barbastathis, "Lensless computational imaging through deep learning", Optica **4**, 1117–1125 (2017) (cit. on p. 53).

[151]Y. Rivenson, Y. Zhang, H. Günaydın, D. Teng, and A. Ozcan, "Phase recovery and holographic image reconstruction using deep learning in neural networks", Light: Science & Applications **7**, 17141–17141 (2018) (cit. on p. 53).

[152]Y. Wu, Y. Rivenson, Y. Zhang, Z. Wei, H. Günaydin, X. Lin, and A. Ozcan, "Extended depth-of-field in holographic imaging using deep-learning-based autofocusing and phase recovery", Optica **5**, 704–710 (2018) (cit. on p. 53).

[153]H. Lee et al., "An endoscope with integrated transparent bioelectronics and theranostic nanoparticles for colon cancer treatment", Nature communications **6**, 1–10 (2015) (cit. on p. 53).

[154]H. Zhu, S. O. Isikman, O. Mudanyali, A. Greenbaum, and A. Ozcan, "Optical imaging techniques for point-of-care diagnostics", Lab on a Chip **13**, 51–67 (2013) (cit. on p. 53).

[155]D. Gabor, *A new microscopic principle*, 1948 (cit. on p. 53).

[156]R. Pappu, B. Recht, J. Taylor, and N. Gershenfeld, “Physical one-way functions”, Science **297**, 2026–2030 (2002) (cit. on p. 53).

[157]R. Horstmeyer, B. Judkewitz, I. M. Vellekoop, S. Assawaworrarit, and C. Yang, “Physical key-protected one-time pad”, Scientific reports **3**, 3543 (2013) (cit. on p. 53).

[158]J. W. Goodman, *Introduction to fourier optics* (Roberts and Company Publishers, 2005) (cit. on p. 55).

[159]H. Kwon, T. Zheng, and A. Faraon, “Nano-electromechanical tuning of dual-mode resonant dielectric metasurfaces for dynamic amplitude and phase modulation”, Nano Letters (2021) (cit. on pp. 71, 91, 92, 96, 99, 101, 105, 107, 111, 117).

[160]A. Hessel and A. Oliner, “A new theory of wood’s anomalies on optical gratings”, Applied optics **4**, 1275–1297 (1965) (cit. on p. 71).

[161]R. Magnusson and Y. H. Ko, “Guided-mode resonance nanophotonics: fundamentals and applications”, in Nanoengineering: fabrication, properties, optics, and devices xiii, Vol. 9927 (International Society for Optics and Photonics, 2016), p. 992702 (cit. on p. 71).

[162]K. Koshelev, A. Bogdanov, and Y. Kivshar, “Engineering with bound states in the continuum”, Optics and Photonics News **31**, 38–45 (2020) (cit. on p. 71).

[163]K. Hirose, Y. Liang, Y. Kurosaka, A. Watanabe, T. Sugiyama, and S. Noda, “Watt-class high-power, high-beam-quality photonic-crystal lasers”, Nature photonics **8**, 406–411 (2014) (cit. on p. 72).

[164]A. Kodigala, T. Lepetit, Q. Gu, B. Bahari, Y. Fainman, and B. Kanté, “Lasing action from photonic bound states in continuum”, Nature **541**, 196–199 (2017) (cit. on p. 72).

[165]Z. Liu et al., “High-q quasibound states in the continuum for nonlinear metasurfaces”, Physical Review Letters **123**, 253901 (2019) (cit. on pp. 72, 77).

[166]K. Koshelev, Y. Tang, K. Li, D.-Y. Choi, G. Li, and Y. Kivshar, “Nonlinear metasurfaces governed by bound states in the continuum”, ACS Photonics **6**, 1639–1644 (2019) (cit. on p. 72).

[167]N. Karl, P. P. Vabishchevich, S. Liu, M. B. Sinclair, G. A. Keeler, G. M. Peake, and I. Brener, “All-optical tuning of symmetry protected quasi bound states in the continuum”, Applied Physics Letters **115**, 141103 (2019) (cit. on p. 72).

[168]S. Han et al., “All-dielectric active terahertz photonics driven by bound states in the continuum”, Advanced Materials **31**, 1901921 (2019) (cit. on p. 72).

[169]K. Fan, I. V. Shadrivov, and W. J. Padilla, “Dynamic bound states in the continuum”, Optica **6**, 169–173 (2019) (cit. on p. 72).

[170]S. C. Malek, A. C. Overvig, S. Shrestha, and N. Yu, “Active nonlocal metasurfaces”, Nanophotonics **10**, 655–665 (2020) (cit. on pp. 72, 81).

[171]A. Tittl et al., "Imaging-based molecular barcoding with pixelated dielectric metasurfaces", Science **360**, 1105–1109 (2018) (cit. on p. 72).

[172]Y. Kanamori, N. Matsuyama, and K. Hane, "Resonant-wavelength tuning of a pitch-variable 1-d photonic crystal filter at telecom frequencies", IEEE Photonics Technology Letters **20**, 1136–1138 (2008) (cit. on p. 72).

[173]M. J. Uddin and R. Magnusson, "Guided-mode resonant thermo-optic tunable filters", IEEE Photonics Technology Letters **25**, 1412–1415 (2013) (cit. on p. 72).

[174]A. Sharon, D. Rosenblatt, A. Friesem, H. Weber, H. Engel, and R. Steingrueber, "Light modulation with resonant grating–waveguide structures", Optics letters **21**, 1564–1566 (1996) (cit. on p. 72).

[175]T. Katchalski, G. Levy-Yurista, A. A. Friesem, G. Martin, R. Hierle, and J. Zyss, "Light modulation with electro-optic polymer-based resonant grating waveguide structures", Optics Express **13**, 4645–4650 (2005) (cit. on p. 72).

[176]A. Karvounis, B. Gholipour, K. F. MacDonald, and N. I. Zheludev, "Giant electro-optical effect through electrostriction in a nanomechanical metamaterial", Advanced Materials **31**, 1804801 (2019) (cit. on pp. 72, 77, 78).

[177]N. I. Zheludev and E. Plum, "Reconfigurable nanomechanical photonic metamaterials", Nature nanotechnology **11**, 16 (2016) (cit. on p. 72).

[178]S.-G. Lee and R. Magnusson, "Band flips and bound-state transitions in leaky-mode photonic lattices", Physical Review B **99**, 045304 (2019) (cit. on p. 74).

[179]K. Koshelev, S. Lepeshov, M. Liu, A. Bogdanov, and Y. Kivshar, "Asymmetric metasurfaces with high-q resonances governed by bound states in the continuum", Physical review letters **121**, 193903 (2018) (cit. on p. 75).

[180]H. Honma, K. Takahashi, M. Ishida, and K. Sawada, "A low-voltage and high uniformity nano-electro-mechanical system tunable color filter based on sub-wavelength grating", Japanese Journal of Applied Physics **51**, 11PA01 (2012) (cit. on p. 77).

[181]Y. Jin, Z. Wang, P. Lim, D. Pan, J. Wei, and C. Wong, "Mems vacuum packaging technology and applications", in Proceedings of the 5th electronics packaging technology conference (eptc 2003) (IEEE, 2003), pp. 301–306 (cit. on p. 78).

[182]S. Fan, W. Suh, and J. D. Joannopoulos, "Temporal coupled-mode theory for the fano resonance in optical resonators", JOSA A **20**, 569–572 (2003) (cit. on pp. 78, 92, 108).

[183]H. A. Haus, *Waves and fields in optoelectronics* (Prentice-Hall, 1984) (cit. on pp. 78, 91–93).

[184]Y. Horie, A. Arbabi, E. Arbabi, S. M. Kamali, and A. Faraon, "High-speed, phase-dominant spatial light modulation with silicon-based active resonant antennas", ACS Photonics **5**, 1711–1717 (2017) (cit. on pp. 78, 79, 83, 93, 104, 111).

[185] J. Park, J.-H. Kang, S. J. Kim, X. Liu, and M. L. Brongersma, “Dynamic reflection phase and polarization control in metasurfaces”, Nano letters **17**, 407–413 (2017) (cit. on pp. 78, 79).

[186] M. Liu and D.-Y. Choi, “Extreme huygens’ metasurfaces based on quasi-bound states in the continuum”, Nano letters **18**, 8062–8069 (2018) (cit. on p. 80).

[187] A. C. Overvig, S. C. Malek, M. J. Carter, S. Shrestha, and N. Yu, “Selection rules for quasibound states in the continuum”, Physical Review B **102**, 035434 (2020) (cit. on p. 81).

[188] K. Koshelev, S. Kruk, E. Melik-Gaykazyan, J.-H. Choi, A. Bogdanov, H.-G. Park, and Y. Kivshar, “Subwavelength dielectric resonators for nonlinear nanophotonics”, Science **367**, 288–292 (2020) (cit. on p. 81).

[189] A. Forouzmand and H. Mosallaei, “A tunable semiconductor-based transmissive metasurface: dynamic phase control with high transmission level”, Laser & Photonics Reviews, 1900353 (cit. on p. 81).

[190] J. S. Ginsberg et al., “Enhanced harmonic generation in gases using an all-dielectric metasurface”, Nanophotonics **10**, 733–740 (2020) (cit. on p. 81).

[191] J. An et al., “Slim-panel holographic video display”, Nature communications **11**, 1–7 (2020) (cit. on p. 90).

[192] G. Wetzstein et al., “Inference in artificial intelligence with deep optics and photonics”, Nature **588**, 39–47 (2020) (cit. on p. 90).

[193] T.-L. Liu et al., “Observing the cell in its native state: imaging subcellular dynamics in multicellular organisms”, Science **360** (2018) (cit. on p. 90).

[194] N. Savage, “Digital spatial light modulators”, Nature Photonics **3**, 170–172 (2009) (cit. on p. 90).

[195] F. Ding, Y. Yang, R. A. Deshpande, and S. I. Bozhevolnyi, “A review of gap-surface plasmon metasurfaces: fundamentals and applications”, Nanophotonics **7**, 1129–1156 (2018) (cit. on p. 91).

[196] J. van de Groep, J.-H. Song, U. Celano, Q. Li, P. G. Kik, and M. L. Brongersma, “Exciton resonance tuning of an atomically thin lens”, Nature Photonics, 1–5 (2020) (cit. on p. 91).

[197] K. X. Wang, Z. Yu, S. Sandhu, and S. Fan, “Fundamental bounds on decay rates in asymmetric single-mode optical resonators”, Optics letters **38**, 100–102 (2013) (cit. on pp. 92–94, 108).

[198] H. Zhou, B. Zhen, C. W. Hsu, O. D. Miller, S. G. Johnson, J. D. Joannopoulos, and M. Soljačić, “Perfect single-sided radiation and absorption without mirrors”, Optica **3**, 1079–1086 (2016) (cit. on pp. 92, 94, 108, 109).

[199] W. Yang et al., “High speed optical phased array using high contrast grating all-pass filters”, Optics express **22**, 20038–20044 (2014) (cit. on p. 93).

[200]X. Yin, J. Jin, M. Soljačić, C. Peng, and B. Zhen, "Observation of topologically enabled unidirectional guided resonances", Nature **580**, 467–471 (2020) (cit. on pp. 94, 105).

[201]C. Qiu, J. Chen, Y. Xia, and Q. Xu, "Active dielectric antenna on chip for spatial light modulation", Scientific reports **2**, 1–7 (2012) (cit. on p. 104).

[202]E. Timurdogan, C. V. Poulton, M. Byrd, and M. Watts, "Electric field-induced second-order nonlinear optical effects in silicon waveguides", Nature Photonics **11**, 200–206 (2017) (cit. on p. 104).

[203]S. Koeber et al., "Femtojoule electro-optic modulation using a silicon–organic hybrid device", Light: Science & Applications **4**, e255–e255 (2015) (cit. on p. 104).

[204]D. Barton III, M. Lawrence, and J. Dionne, "Wavefront shaping and modulation with resonant electro-optic phase gradient metasurfaces", Applied Physics Letters **118**, 071104 (2021) (cit. on p. 104).

[205]S. Molesky, Z. Lin, A. Y. Piggott, W. Jin, J. Vucković, and A. W. Rodriguez, "Inverse design in nanophotonics", Nature Photonics **12**, 659–670 (2018) (cit. on pp. 105, 127, 134, 150).

[206]M. Mansouree, H. Kwon, E. Arbabi, A. McClung, A. Faraon, and A. Arbabi, "Multifunctional 2.5 d metastructures enabled by adjoint optimization", Optica **7**, 77–84 (2020) (cit. on pp. 105, 133, 134, 138, 150).

[207]J. K. Gansel et al., "Gold helix photonic metamaterial as broadband circular polarizer", Science **325**, 1513–1515 (2009) (cit. on p. 118).

[208]K. Dietrich, D. Lehr, C. Helgert, A. Tünnermann, and E.-B. Kley, "Circular dichroism from chiral nanomaterial fabricated by on-edge lithography", Advanced Materials **24**, OP321–OP325 (2012) (cit. on p. 118).

[209]A. Rogacheva, V. Fedotov, A. Schwanecke, and N. Zheludev, "Giant gyrotropy due to electromagnetic-field coupling in a bilayered chiral structure", Physical review letters **97**, 177401 (2006) (cit. on p. 118).

[210]Y. Zhao, M. Belkin, and A. Alù, "Twisted optical metamaterials for planarized ultrathin broadband circular polarizers", Nature communications **3**, 1–7 (2012) (cit. on p. 118).

[211]E. Plum and N. I. Zheludev, "Chiral mirrors", Applied Physics Letters **106**, 221901 (2015) (cit. on pp. 119, 121).

[212]L. Kang et al., "Preserving spin states upon reflection: linear and nonlinear responses of a chiral meta-mirror", Nano letters **17**, 7102–7109 (2017) (cit. on pp. 119, 121).

[213]W. Li, Z. J. Coppens, L. V. Besteiro, W. Wang, A. O. Govorov, and J. Valentine, "Circularly polarized light detection with hot electrons in chiral plasmonic metamaterials", Nature communications **6**, 1–7 (2015) (cit. on pp. 119, 121).

[214] H. Hübener, U. De Giovannini, C. Schäfer, J. Andberger, M. Ruggenthaler, J. Faist, and A. Rubio, "Engineering quantum materials with chiral optical cavities", Nature Materials, 1–5 (2020) (cit. on p. 119).

[215] F. Zhang et al., "All-dielectric metasurfaces for simultaneous giant circular asymmetric transmission and wavefront shaping based on asymmetric photonic spin–orbit interactions", Advanced Functional Materials **27**, 1704295 (2017) (cit. on p. 119).

[216] A. Y. Zhu et al., "Giant intrinsic chiro-optical activity in planar dielectric nanostructures", Light: Science & Applications **7**, 17158–17158 (2018) (cit. on p. 119).

[217] B. Semnani, J. Flannery, R. Al Maruf, and M. Bajcsy, "Spin-preserving chiral photonic crystal mirror", Light: Science & Applications **9**, 1–12 (2020) (cit. on pp. 119, 121, 123, 125, 127).

[218] S. Zhang et al., "Photoinduced handedness switching in terahertz chiral metamolecules", Nature communications **3**, 1–7 (2012) (cit. on p. 119).

[219] Z. Wang et al., "Origami-based reconfigurable metamaterials for tunable chirality", Advanced materials **29**, 1700412 (2017) (cit. on p. 119).

[220] L. Cong, P. Pitchappa, N. Wang, and R. Singh, "Electrically programmable terahertz diatomic metamolecules for chiral optical control", Research **2019** (2019) (cit. on p. 119).

[221] T.-T. Kim, S. S. Oh, H.-D. Kim, H. S. Park, O. Hess, B. Min, and S. Zhang, "Electrical access to critical coupling of circularly polarized waves in graphene chiral metamaterials", Science advances **3**, e1701377 (2017) (cit. on p. 119).

[222] X. Yin, M. Schäferling, A.-K. U. Michel, A. Tittl, M. Wuttig, T. Taubner, and H. Giessen, "Active chiral plasmonics", Nano letters **15**, 4255–4260 (2015) (cit. on p. 119).

[223] A. Kuzyk, R. Schreiber, H. Zhang, A. O. Govorov, T. Liedl, and N. Liu, "Reconfigurable 3d plasmonic metamolecules", Nature materials **13**, 862–866 (2014) (cit. on p. 119).

[224] Z. Wu, X. Chen, M. Wang, J. Dong, and Y. Zheng, "High-performance ultrathin active chiral metamaterials", ACS nano **12**, 5030–5041 (2018) (cit. on p. 119).

[225] A. Kuzyk, M. J. Urban, A. Idili, F. Ricci, and N. Liu, "Selective control of reconfigurable chiral plasmonic metamolecules", Science Advances **3**, e1602803 (2017) (cit. on p. 119).

[226] Y. Kim, B. Yeom, O. Arteaga, S. J. Yoo, S.-G. Lee, J.-G. Kim, and N. A. Kotov, "Reconfigurable chiroptical nanocomposites with chirality transfer from the macro-to the nanoscale", Nature materials **15**, 461–468 (2016) (cit. on p. 119).

[227] I. Zubritskaya, N. Maccaferri, X. Inchausti Ezeiza, P. Vavassori, and A. Dmitriev, "Magnetic control of the chiroptical plasmonic surfaces", Nano letters **18**, 302–307 (2018) (cit. on p. 119).

[228] Q. Zhang, E. Plum, J.-Y. Ou, H. Pi, J. Li, K. F. MacDonald, and N. I. Zheludev, "Electrogyration in metamaterials: chirality and polarization rotatory power that depend on applied electric field", Advanced Optical Materials, 2001826 (2020) (cit. on p. 119).

[229] J. Li et al., "Tunable chiral optics in all-solid-phase reconfigurable dielectric nanostructures", Nano Letters (2020) (cit. on pp. 119, 120).

[230] L. Kang, C.-Y. Wang, X. Guo, X. Ni, Z. Liu, and D. H. Werner, "Nonlinear chiral meta-mirrors: enabling technology for ultrafast switching of light polarization", Nano letters **20**, 2047–2055 (2020) (cit. on p. 120).

[231] S. Zanotto et al., "Optomechanics of chiral dielectric metasurfaces", Advanced Optical Materials **8**, 1901507 (2020) (cit. on pp. 120, 127).

[232] C. Menzel, C. Helgert, C. Rockstuhl, E.-B. Kley, A. Tünnermann, T. Pertsch, and F. Lederer, "Asymmetric transmission of linearly polarized light at optical metamaterials", Physical review letters **104**, 253902 (2010) (cit. on p. 123).

[233] T. J. Seok, K. Kwon, J. Henriksson, J. Luo, and M. C. Wu, "Wafer-scale silicon photonic switches beyond die size limit", Optica **6**, 490–494 (2019) (cit. on p. 127).

[234] R. Matzen, J. S. Jensen, and O. Sigmund, "Topology optimization for transient response of photonic crystal structures", JOSA B **27**, 2040–2050 (2010) (cit. on p. 134).

[235] J. S. Jensen and O. Sigmund, "Topology optimization for nano-photonics", Laser & Photonics Reviews **5**, 308–321 (2011) (cit. on p. 134).

[236] A. Y. Piggott, J. Lu, K. G. Lagoudakis, J. Petykiewicz, T. M. Babinec, and J. Vučković, "Inverse design and demonstration of a compact and broadband on-chip wavelength demultiplexer", Nature Photonics **9**, 374–377 (2015) (cit. on p. 134).

[237] P. D. Miller, "From fundamental solar cell physics to computational inverse design", PhD thesis (Thesis, 2012) (cit. on pp. 134, 136).

[238] C. M. Lalau-Keraly, S. Bhargava, O. D. Miller, and E. Yablonovitch, "Adjoint shape optimization applied to electromagnetic design", Optics express **21**, 21693–21701 (2013) (cit. on pp. 134, 136).

[239] A. C. Niederberger, D. A. Fattal, N. R. Gauger, S. Fan, and R. G. Beausoleil, "Sensitivity analysis and optimization of sub-wavelength optical gratings using adjoints", Optics express **22**, 12971–12981 (2014) (cit. on p. 134).

[240] L. H. Frandsen, A. Harpøth, P. I. Borel, M. Kristensen, J. S. Jensen, and O. Sigmund, "Broadband photonic crystal waveguide 60 bend obtained utilizing topology optimization", Optics Express **12**, 5916–5921 (2004) (cit. on p. 134).

[241] A. Iguchi, Y. Tsuji, T. Yasui, and K. Hirayama, "Efficient topology optimization of optical waveguide devices utilizing semi-vectorial finite-difference beam propagation method", Optics Express **25**, 28210–28222 (2017) (cit. on p. 134).

[242] Y. Lefevre, P. Wahl, N. Vermeulen, and H. Thienpont, "Adjoint-enabled optimization of optical devices based on coupled-mode equations", Optics express **22**, 19423–19439 (2014) (cit. on p. 134).

[243] M. Mansouree and A. Arbabi, "Large-scale metasurface design using the adjoint sensitivity technique", in Cleo: qels_fundamental science (Optical Society of America, 2018), FF1F–7 (cit. on p. 134).

[244] M. Mansouree and A. Arbabi, "Metasurface design using level-set and gradient descent optimization techniques", in 2019 international applied computational electromagnetics society symposium (aces) (IEEE, 2019), pp. 1–2 (cit. on p. 134).

[245] Z. Lin, B. Groever, F. Capasso, A. W. Rodriguez, and M. Lončar, "Topology-optimized multilayered metaoptics", Physical Review Applied **9**, 044030 (2018) (cit. on p. 134).

[246] Z. Lin and S. G. Johnson, "Overlapping domains for topology optimization of large-area metasurfaces", Optics express **27**, 32445–32453 (2019) (cit. on p. 134).

[247] A. Zhan, T. K. Fryett, S. Colburn, and A. Majumdar, "Inverse design of optical elements based on arrays of dielectric spheres", Applied optics **57**, 1437–1446 (2018) (cit. on p. 134).

[248] J. Yang and J. A. Fan, "Topology-optimized metasurfaces: impact of initial geometric layout", Optics Letters **42**, 3161–3164 (2017) (cit. on p. 134).

[249] M. Mansouree and A. Arbabi, "Multi-layer multifunctional metasurface design using the adjoint sensitivity technique (conference presentation)", in High contrast metastructures viii, Vol. 10928 (International Society for Optics and Photonics, 2019), 109281N (cit. on p. 136).

[250] H. Chung and O. D. Miller, "High-na achromatic metalenses by inverse design", Optics Express **28**, 6945–6965 (2020) (cit. on p. 136).

[251] D. Coldewey, *Metalenz reimagines the camera in 2d and raises 10m to ship it*, (2021) `https://techcrunch.com/2021/02/04/metalenz-reimagines-the-camera-in-2d-and-raises-10m-to-ship-it/` (cit. on p. 148).

[252] W.-J. Joo et al., "Metasurface-driven oled displays beyond 10,000 pixels per inch", Science **370**, 459–463 (2020) (cit. on p. 148).

[253] J. S. Smalley et al., "Subwavelength pixelated cmos color sensors based on anti-hermitian metasurface", Nature communications **11**, 1–7 (2020) (cit. on p. 148).

[254] P. Camayd-Muñoz, C. Ballew, G. Roberts, and A. Faraon, "Multifunctional volumetric meta-optics for color and polarization image sensors", Optica **7**, 280–283 (2020) (cit. on pp. 148, 150).

[255]E. Arbabi, S. M. Kamali, A. Arbabi, and A. Faraon, "Full-stokes imaging polarimetry using dielectric metasurfaces", Acs Photonics **5**, 3132–3140 (2018) (cit. on p. 148).

[256]N. A. Rubin, G. D'Aversa, P. Chevalier, Z. Shi, W. T. Chen, and F. Capasso, "Matrix fourier optics enables a compact full-stokes polarization camera", Science **365** (2019) (cit. on p. 148).

[257]Z. Yang et al., "Generalized hartmann-shack array of dielectric metalens subarrays for polarimetric beam profiling", Nature communications **9**, 1–7 (2018) (cit. on p. 148).

[258]M. Faraji-Dana, E. Arbabi, H. Kwon, S. M. Kamali, A. Arbabi, J. G. Bartholomew, and A. Faraon, "Hyperspectral imager with folded metasurface optics", ACS Photonics **6**, 2161–2167 (2019) (cit. on pp. 148, 149).

[259]S. Shrestha, A. C. Overvig, M. Lu, A. Stein, and N. Yu, "Broadband achromatic dielectric metalenses", Light: Science & Applications **7**, 85 (2018) (cit. on p. 148).

[260]F. Presutti and F. Monticone, "Focusing on bandwidth: achromatic metalens limits", Optica **7**, 624–631 (2020) (cit. on p. 148).

[261]A. McClung, M. Mansouree, and A. Arbabi, "At-will chromatic dispersion by prescribing light trajectories with cascaded metasurfaces", Light: Science & Applications **9**, 1–9 (2020) (cit. on p. 148).

[262]L. Huang, J. Whitehead, S. Colburn, and A. Majumdar, "Design and analysis of extended depth of focus metalenses for achromatic computational imaging", Photonics Research **8**, 1613–1623 (2020) (cit. on p. 149).

[263]E. Tseng, S. Colburn, J. Whitehead, L. Huang, S.-H. Baek, A. Majumdar, and F. Heide, "Neural nano-optics for high-quality thin lens imaging", arXiv preprint arXiv:2102.11579 (2021) (cit. on p. 149).

[264]N. Li et al., "Large-area metasurface on cmos-compatible fabrication platform: driving flat optics from lab to fab", Nanophotonics **9**, 3071–3087 (2020) (cit. on p. 149).

[265]G.-Y. Lee et al., "Metasurface eyepiece for augmented reality", Nature communications **9**, 1–10 (2018) (cit. on p. 149).

[266]G. Yoon, K. Kim, S.-U. Kim, S. Han, H. Lee, and J. Rho, "Printable nanocomposite metalens for high-contrast near-infrared imaging", ACS nano (cit. on p. 149).

[267]X. Yin, J.-S. Park, K. K. Stensvad, R. L. Brott, N. Rubin, M. B. Wolk, and F. Capasso, "Roll-to-roll dielectric metasurfaces", in Metamaterials, metadevices, and metasystems 2020, Vol. 11460 (International Society for Optics and Photonics, 2020), 114600S (cit. on p. 149).

[268]J. Jahns and A. Huang, "Planar integration of free-space optical components", Applied Optics **28**, 1602–1605 (1989) (cit. on p. 149).

[269]S. Jafar-Zanjani, S. Inampudi, and H. Mosallaei, “Adaptive genetic algorithm for optical metasurfaces design”, Scientific reports **8**, 1–16 (2018) (cit. on p. 150).

[270]T. Phan, D. Sell, E. W. Wang, S. Doshay, K. Edee, J. Yang, and J. A. Fan, “High-efficiency, large-area, topology-optimized metasurfaces”, Light: Science & Applications **8**, 1–9 (2019) (cit. on p. 150).

[271]J. Jiang, M. Chen, and J. A. Fan, “Deep neural networks for the evaluation and design of photonic devices”, Nature Reviews Materials, 1–22 (2020) (cit. on p. 150).